Università degli Studi di Bari Aldo Moro
Dipartimento Interateneo di Fisica
"Michelangelo Merlin"

Dottorato di Ricerca in Fisica XXX ciclo

Settore Scientifico Disciplinare: FIS/02

MODELLING AND STUDY OF COMPLEX FLUIDS AND LIQUID CRYSTAL DROPLETS

Dottorando:
Federico Fadda

Coordinatore:
Ch.mo Prof. Gaetano Scamarcio

Supervisori:
Ch.mo Prof. Giuseppe Gonnella
Ch.mo Dott. Antonio Lamura

Anno Accademico 2017-2018

To my family

Unthinking respect for authority is the greatest enemy of truth–Albert Einstein

There are two possible outcomes: if the result confirms the hypothesis, then you've made a measurement. If the result is contrary to the hypothesis, then you've made a discovery–Enrico Fermi

Study hard what interests you the most in the most undisciplined, irreverent and original manner possible.–Richard Feynman

My goal is simple. It is a complete understanding of the universe, why it is as it is and why it exists at all–Stephen Hawking

It is important to do everything with passion, it embellishes life enormously.–Lev Landau

It's an experience like no other experience I can describe, the best thing that can happen to a scientist, realizing that something that has happened in his or her mind exactly corresponds to something that happens in Nature. One is surprised that a construct of one's own Mind can actually be realised in the honest-to-goodness World out there. A great shock, and a great, great joy.–Leo Kadanoff

Research group members

(a) Prof. Giuseppe Gonnella

(b) Doct. Antonio Lamura

(c) Prof. Davide Marenduzzo

(d) Prof. Enzo Orlandini

(e) Doct. Adriano Tiribocchi

(a) Università degli Studi di Bari Aldo Moro, Dipartimento Interateneo di Fisica Michelangelo Merlin e Sezione INFN, Italy.
(b) Istituto Applicazioni Calcolo, CNR, Bari, Italy.
(c) SUPA School of Physics and Astronomy, Università di Edinburgo, UK.
(d)-(e) Università degli Studi di Padova, Dipartimento di Fisica e Astronomia e Sezione INFN, Italy.

Publications

The results of this thesis were published or will be published in these papers:

- F. Fadda, G. Gonnella, A. Lamura and A. Tiribocchi, "*Lattice Boltzmann study of chemically-driven self-propelled droplets*", Eur. Phys. J. E, submitted.

- F. Fadda, G. Gonnella, A. Lamura, D. Marenduzzo, E. Orlandini and A. Tiribocchi, "*Shear dynamics of an inverted cholesteric emulsion*", Fluids, in preparation.

- F. Fadda, G. Gonnella, A. Lamura, D. Marenduzzo, E. Orlandini and A. Tiribocchi, "*Interacting rotating cholesteric liquid crystal droplets*", in preparation.

- F. Fadda, G. Gonnella, D. Marenduzzo, E. Orlandini and A. Tiribocchi "*Switching dynamics in cholesteric liquid crystal emulsions*", J. Chem. Phys. **147**, 064903 (2017).

Contents

Introduction

Generally the matter is presented in the three fundamental states such as solid, liquid and gas. In a crystalline solid the molecules are fixed in the space and located in the positions of the sites of the crystalline lattice. They have therefore a positional and an orientational order. In the other physical state, the liquid state, the molecules have lost any orientational and positional order. Between these two states there is a world of systems which belong to a branch of Physics known as *Soft Condensed Matter Physics* or *Soft Matter Physics* which studies systems with intermediate properties between solids and liquids. In general colloids, polymer solutions, emulsions, foams, surfactants, liquid crystals and similar materials are gathered in the *Soft Matter Physics*. People have daily experience of "soft materials" like mayonnaise, detergents, shaving foams etc.
An interesting example of *Soft Matter Physics* studied in this Ph.D. thesis is represented by liquid crystals. As mentioned in the name, they are liquid because they flow like liquids but they are also "crystals" because like solids they possess molecules, typically with rod-like or disk-like shape, with orientational but not positional order. Nowdays they find industrial applications in the construction of screens for monitors, computers, televisions etc. The basic element behind these applications is the so called twisted nematic cell in which nematic liquid crystal molecules between two plates have an helicoidal orientation. They also find important applications in photonics, optics, cosmetics etc. In this sense it is understandable the necessity to study the response of liquid crystals under electric fields of various types. Generally the experiments are permormed on films where the liquid crystal is placed. However it can be of great importance studying liquid crystals in different geometries and situations like the liquid crystal droplets.
Another important theme abundantly studied in recent Soft Matter Physics deals with the self-propulsion of droplets and particles realized in various ways. One possibility is the Marangoni effect in which liquid droplets self-propel due to an imbalance of surface tension caused by anisotropies in the system which can consist in gradient of temperature or inhomogeneous concentration of a tensioactive material or surfactant. Literature is rich of past works on the Marangoni effect in different variants but a lot more can be studied for example the interaction of more self-propelled droplets and their related collective phenomena.

A possible way to study these systems consists in defining a set of coarse-grained quantities which can be the total density, the temperature, the velocity and the concentration field. These quantities are generally called fields and consist in functions of the points in the space and time and evolve through particular equations for example, the continuity equation for the total density field and the Navier-Stokes equation for the velocity field. In this approach the molecular microscopic details of the system are neglected and the attention is focused on mesoscopic elements of the system which are little compared to the macroscopic scales but big enough to contain a huge number of molecules.
As long as the equations mentioned before are partial differential equations and are also coupled, an analytical treatment is difficult and so a good choice to solve them is a numerical procedure through computer simulations with a certain tecnique. One of the most used in the scientific panorama consists in the *Lattice Boltzmann method* or simply *LBM method*. It is widely used for various reasons such as the portability, the attitude to be parallelized in order to study bigger systems and the possibility to simulate complex systems with various geometries. As the term says, it is a lattice method in which the physical space is discretized through convenient lattices in which the physical quantities are functions of these lattice sites. The term "Boltzmann" is related to the fact that the main ingredient of the method is the introduction of a set of distribution functions, related to the physical quantities such as the total density field and the velocity field, which evolve through the Boltzmann equation conveniently simplified for this algorithm.
The theme of this Ph.D. thesis deals with the study of single or emulsions of simple fluid and liquid crystal droplets through computer simulations with Lattice Boltzmann method whose main results are here collected.
The thesis is organized as follows.

- In Chapter 1 a theoretical frame for the study of complex fluids is presented. The continuity and the Navier-Stokes equations which represent the conservation laws of mass and momentum of the fluid are mathematically derived. In the case of fluid mixture, the order parameter is scalar and consists in the concentration field which evolve according to the convection-diffusion equation. In the case of liquid crystals, instead, the description requires a tensorial order parameter which evolves through the Beris-Edwards equation. In the last part of the Chapter brief elements of the Landau theory and non equilibrium thermodynamics, used for the studies collected in this thesis, are remembered.

- Chapter 2 is dedicated to a general description of liquid crystals. It starts with a general historical overview with a presentation of the most famous

mesophases like the nematic, cholesteric, the smectic etc. The Chapter proceeds with the definition of the tensor order parameter which consists in a second rank, symmetric and traceless tensor. It is a powerful tool to describe liquid crystals because it takes into account the type of alignment and also the strenght of this one. The degree of alignment of the molecules of a liquid crystal is defined by a vector called director which indicates the average direction of the molecules. Particular factors such as elasticity of the material, the type of anchoring of the director, the presence of colloidal impurities and external fields can cause the rise of topological defects which are regions in which the order parameter is ill defined and the local orientation of the director becomes ambiguous. They are briefly described in particular the defects of cholesteric liquid crystals (λ, τ and χ) are presented. In the last part of the Chapter 2, the Landau-de Gennes free energy functional for liquid crystals is introduced and all the important energetic contributions related to the bulk, interfaces and external fields are described in detail.

- In Chapter 3 the Lattice Boltzmann method used to simulate the systems, studied in this thesis, is described. The Chapter deals with specifically a variant of the method called hybrid Lattice Boltzmann in which the equations of the system are divided in two groups: the continuity and the Navier-Stokes equations are solved in the standard way instead the equation for the order parameter of the system and other scalar fields are solved apart with a finite difference scheme. In the first part the Lattice Boltzmann method for fluid mixtures is described and then the version for the the study of liquid crystals is presented. The Chapter also contains some numerical details concerning the up-wind scheme to solve numerically the convection-diffusion equation for the scalar concentration field for fluid mixtures and also the implementation of the rigid walls.

- In Chapter 4 the results of the simulations of a cholesteric liquid crystal droplet under electric fields are collected. These results belong to the paper "*Switching dynamics in cholesteric liquid crystal emulsions*", J. Chem. Phys. **147**, 064903 (2017). The Chapter starts with the introduction of the free-energy functional of the studied system, a brief description of the typical values of the parameters used and then moves to the presentation of the results. At first the equilibrium structures of the cholesteric droplets are described without the electric field varying the pitch of the helix and the anchoring condition of the director on the droplet. Then the results of the application of an electric field are introduced firstly considering a continuous electric field and a rotating electric field. The dynamics of topological defects of the cholesteric droplet

is studied in detail. As regards the continuous electric field, the switching on-off is performed at first switching on the field and letting the system relax towards a first equilibrium state and then switching off it observing if the system regains or not the original state. This kind of analysis is also compared to another situation in which a whole cholesteric channel is considered and compared to the case of the droplet. Another quantitative analysis consists in evaluating the threholds of the electric field which cause a nematization of the droplet destroying the cholesteric order as function of the elastic constant for various anchorings and pitches. Then the analysis of a rotating electric field is considered computing the angular velocity of the rotating droplet as function of the frequency of the applied field and also investigating the periodicity of the topological defects to observe if they are periodic or not with the rotating field. The final part of the Chapter contains also the initial results of a system of two cholesteric droplets under rotatig electric fields with surfactant of the paper in preparation, "*Interacting rotating cholesteric liquid crystal droplets*". This system seems to be characterized by an interaction consisting in a mutual rotation of the two droplets around a common centre above a threshold value of the frequency of the applied field. The evaluation of the angular velocity of each rotating droplet and the angular velocity of the axis joining the two droplets as function of the frequency of the applied field is performed.

- Chapter 5 contains the initial results of the study of a cholesteric emulsion under shear of the paper in preparation "*Shear dynamics of an inverted cholesteric emulsion*". At first the numerical model with the free-energy functional is introduced and then the results are discussed. At first the simple case of a channel of isotropic fluid is considered; the system initially relaxes towards the equilibrium, then a symmetric shear is applied and then the system reaches the final stationary state. This simple case is used in order to establish a unit time in function of which all the other times of the other cases will be expressed. Another situation analyzed is the one with an isotropic droplet in cholesteric phase subjected to a symmetric shear which slightly elongates the droplet and reorganizes the defects in the bulk. The configurations of the director and the velocity fields are inserted.

- In Chapter 6 the results of the simulations of simple fluid self-propelled droplets through Marangoni effect will be presented. These results belong to the paper "*Lattice Boltzmann study of chemically-driven self-propelled droplets*" submitted to the journal *European Physical Journal E*. At first the basic concept of the Marangoni effect for fluids in general and for droplets is defined. After that, the system studied is introduced and the results are discussed first start-

ing with the equilibrium properties of the system dealing the analysis of the one dimensional profiles of the concentration fields, the surface tension and the interface width. Then the results of the self-propelled motion of a single droplet are discussed. The motion of the droplet through Marangoni effect is achieved inserting specific terms of production and consumption of surfactants in the dynamic equation of the surfactant. In particular producing the surfactant in a circular region internally tangent to the droplet and consuming the surfactant in the system creates the requested imbalance of surface tension and the droplet finally moves. The final analysis consists in exploring two interacting droplets in different configurations. Both the cases of two self-propelled droplets and one self-propelled and the other motionless are considered.

Chapter 1

Hydrodynamics of complex fluids

A continuum dynamic description requires a thermodynamic model for the studied system. The common approach for the results presented in this thesis is based on a Ginzburg-Landau method which consists in the definition of a free-energy expressed as a polynomial function of the invariants of the the order parameter respect to a particular group of symmetry. From this free-energy functional it is possibile to derive some quantities such as the chemical potential which figures in the dynamic equations of the system. The nature of this order parameter can be scalar, vectorial or tensorial depending by the system and by the symmetries involved.
In the case of binary fluid mixtures, for example, there are translational and rotational symmetries and the order parameter is chosen as scalar defined as the difference of the chemical concentrations between the two phases. In liquid crystals, instead, the order parameter must take into account the orientation of the molecules and the strenght of the alignment so in this case the order parameter is tensorial. In this latter case the study is complicated by the fact that in the liquid crystal systems there can be regions, the topological defects, where the order parameter is not well defined, which play an important role in the evolution of the system. When one defect moves, the coupling between the velocity field and the variation of the orientation of the molecules becomes important. This effect is called backflow and the moviment of the defect generates a variation in the orientation of molecules which produces a variation in the velocity field [1]. These topological defects will be better introduced in Chapter 2 which is dedicated to the description of liquid crystals and their general aspects. In case of the fluid mixtures there is something quite similar shown in Fig. 1.1. In this figure a typical velocity field along and interface which separates two different phases is shown. Along interfaces tangential forces rise due to different curvatures and this generates velocity fields particularly intense where the interface is convex. Passing time the curvature is reduced until the regions are spherical and the system reaches a

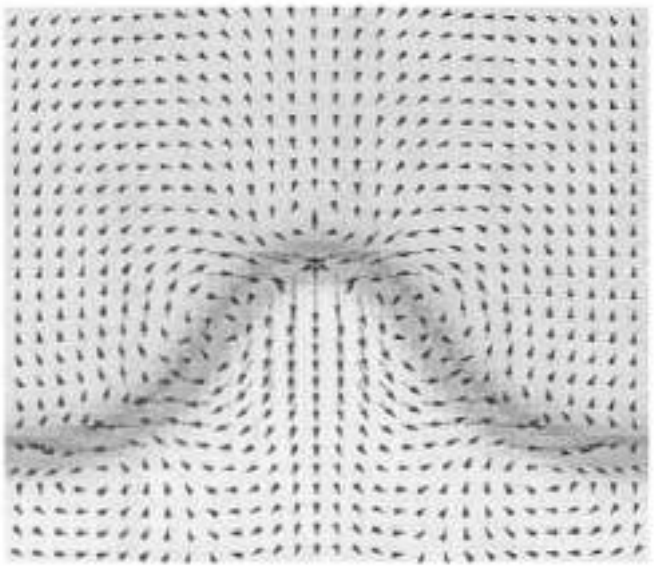

Figure 1.1: Velocity field along a flat interface which separates two different regions of a binary mixture which acts to equalize the curvature [3].

final state where the two phases are separated. Defects are thus the sources of the velocity field. Hydrodynamics plays an important role in leading systems towards equilibrium removing, if possibile, defects. There are systems, for example liquid crystal blue phases, where this is not always possible and hydrodynamics doesn't succeed in removing defects which remain and slow down the evolution of the system [2].
What is important to say now is the fact that what makes some systems such as the fluid mixtures and liquid crystals interesting is the fact that the coupling between the quantities of the system can generate important effects. In this Chapter the hydrodynamic equations such as the continuity equation, the Navier-Stokes equation, the convection-diffusion equation and the Beris-Edwards equation are introduced.

1.1 Hydrodynamic equations

In this section the hydrodynamic equations are shown.
The description of a simple fluid, for example, requires five functions with their correspondent equations. These functions are respectively the three components of the velocity field $\mathbf{u}(x, y, z, t)$, the total density field and the energy. The corrispondent equations are respectively the Navier-Stokes equation for the velocity field and the continuity equation for the total density field. It is also necessary to define an equation for the evolution of the order parameter; it is scalar for fluid mixtures and consists in the concentration field instead it is tensorial for liquid crystals and evolves through the Beris-Edwards equation.

1.1.1 The continuity equation

The first equation described is the continuity equation which prescribes the conservation of the mass of fluid [4].
If n is the density of fluid, the conservation of mass imposes that the variation in the unit time of the mass in a volume V equals the flux of mass in the unit time across the surface $S(V)$ which surrounds the volume V

$$\partial_t \int_V n dV = - \int_{S(V)} n\mathbf{u} \cdot d\mathbf{l} \tag{1.1}$$

in which $\mathbf{u}(x, y, z, t)$ is the velocity of fluid in a point (x, y, z) at time t and $d\mathbf{l}$ is a vector in the normal direction of the surface element with area equals to the modulus of $d\mathbf{l}$. The positive verse is assumed the outgoing verse from the surface. In the differential form the equation becomes

$$\partial_t n = -\partial_\alpha (n u_\alpha) \tag{1.2}$$

with index α which represents the three possibile cartesian directions and the sum on the index α is assumed. The term $n\mathbf{u}$ is the density mass flux. The continuity equation (1.2) shown above is the first hydrodynamic equations and establishes that the total mass in every element of the system can change only if matter fluxes across the element to the outside or from the outside.

1.1.2 The Navier-Stokes equation

The second equation is the Navier-Stokes equation related to the conservation of the momentum [3, 4]. It can be seen as the Newton equation for an element of fluid.
Starting neglecting all the dissipative effects, the total force acting on an element of fluid is

$$-\int p d\mathbf{l} \tag{1.3}$$

where p is the pressure on the surface which surrounds the volume of the fluid. Changing (1.3) into a volume integral it is

$$-\int p d\mathbf{l} = -\int \nabla p dV. \tag{1.4}$$

So on the volume element there is a force equals $-\nabla p$. Now it is possibile to equalize the force to the mass per unit volume (the density) times the acceleration $d\mathbf{u}/dt$

$$n\frac{d\mathbf{u}}{dt} = -\nabla p. \tag{1.5}$$

The operator $d\mathbf{u}/dt$ which appears in the left hand side of (1.5) is the material derivative. It does not indicate the variation of the fluid velocity in a fixed point in space but the variation of the velocity of a particle of fluid that moves in the space. In this sense one can observe that that the variation $d\mathbf{u}$ of the velocity of a particle of fluid, in the interval time dt, is determined by two contributions: the variation of the velocity in a fixed point in the space in the time dt and the difference between the velocity (in the same instant) in two points of the space distant $d\mathbf{r}$ where $d\mathbf{r}$ is the distance described by the particle in the time dt [4]. The first contribution is

$$\frac{\partial \mathbf{u}}{\partial t} dt \tag{1.6}$$

where $\frac{\partial \mathbf{u}}{\partial t}$ is calculated with x, y, and z costants in a certain point in the space. The second contribution is

$$dx\frac{\partial \mathbf{u}}{\partial x} + dy\frac{\partial \mathbf{u}}{\partial y} + dz\frac{\partial \mathbf{u}}{\partial z} = (d\mathbf{r}\cdot\nabla)\mathbf{u} \tag{1.7}$$

So expressing the material derivative $d\mathbf{u}/dt$ in this way

$$\frac{d\mathbf{u}}{dt} = \frac{\partial \mathbf{u}}{\partial t} + \mathbf{u}\cdot\nabla\mathbf{u} \tag{1.8}$$

(1.5) becomes

$$n\partial_t u_\alpha + n u_\beta \partial_\beta u_\alpha = -\partial_\alpha p \tag{1.9}$$

which allows to obtain the Cauchy equation

$$\partial_t(nu_\alpha) = -\partial_\beta T_{\alpha\beta}. \tag{1.10}$$

This equation describes the reversible transfer of momentum due only to pressure forces and mechanical movement of particle fluid. The term $T_{\alpha\beta}$ is the density flux momentum tensor and represents the momentum in the direction β which moves across a surface element perpendicular to the α direction. In case of an ideal fluid the explicit expression of the tensor is

$$T_{\alpha\beta} = p\delta_{\alpha\beta} + nu_\alpha u_\beta \tag{1.11}$$

in which p is the pressure that surrounds the element of fluid volume. If dissipative effects are present it is necessary the presence of a term in the tensor which deals with these effects. This is called viscous stress tensor and its expression is

$$S_{\alpha\beta} = \eta\left(\partial_\alpha u_\beta + \partial_\beta u_\alpha - \frac{2\delta_{\alpha\beta}}{d}\partial_\gamma u_\gamma\right) + \zeta\delta_{\alpha\beta}\partial_\gamma u_\gamma \tag{1.12}$$

in which η and ζ are, respectively, the dynamic viscosity and the bulk viscosity or second viscosity. They are both poistive and d is the dimension of the problem. Inserting this new tensor in the Cauchy equation (1.10) one obtains the Navier-Stokes equation with expression

$$\partial_t(nu_\beta) + \partial_\alpha(nu_\alpha u_\beta) = -\partial_\alpha p + \partial_\alpha\left[\eta\left(\partial_\alpha u_\beta + \partial_\beta u_\alpha - \frac{2\delta_{\alpha\beta}}{d}\partial_\gamma u_\gamma\right) + \zeta\delta_{\alpha\beta}\partial_\gamma u_\gamma\right]. \tag{1.13}$$

If the fluid is not homogeneous, like multiphase mixtures, concentration gradients must be taken into account. In this case pressure will not be equal in the zones of the fluid and it could be dependent by concentration and its gradients. Thus the term $p\delta_{\alpha\beta}$ shown before in (1.13) is changed with the pressure tensor $P_{\alpha\beta}$ and the Navier-Stokes equation becomes

$$\partial_t(nu_\beta) + \partial_\alpha(nu_\alpha u_\beta) = -\partial_\alpha P_{\alpha\beta} + \partial_\alpha\left[\eta\left(\partial_\alpha u_\beta + \partial_\beta u_\alpha - \frac{2\delta_{\alpha\beta}}{d}\partial_\gamma u_\gamma\right) + \zeta\delta_{\alpha\beta}\partial_\gamma u_\gamma\right]. \tag{1.14}$$

In the special case of incompressible fluids, $\partial_\alpha u_\alpha = 0$ and the Navier-Stokes equations simplifies in

$$\partial_t u_\alpha + u_\beta\partial_\beta u_\alpha = -\frac{1}{n}\partial_\alpha P_{\alpha\beta} + \nu\nabla^2 u_\alpha \tag{1.15}$$

where $\nu = \eta/n$ is the cinematic viscosity.
In the case of liquid crystals the Navier-Stokes equation expression is

$$n(\partial_t + u_\beta\partial_\beta)u_\alpha = \partial_\beta\sigma^{total}_{\alpha\beta} \tag{1.16}$$

where $\sigma_{\alpha\beta}^{total}$ is the total stress tensor for liquid crystals [5, 6]

$$\sigma_{\alpha\beta}^{total} = \sigma_{\alpha\beta}^{visc} + \sigma_{\alpha\beta}^{lc} + \sigma_{\alpha\beta}^{int} \tag{1.17}$$

where $\sigma_{\alpha\beta}^{visc}$, $\sigma_{\alpha\beta}^{lc}$ and $\sigma_{\alpha\beta}^{int}$ are respectively the viscous term, the liquid crystal term and the last one takes into account the presence of interfaces. The viscuous term is

$$\sigma_{\alpha\beta}^{visc} = \eta(\partial_\alpha u_\beta + \partial_\beta u_\alpha) \tag{1.18}$$

with η dynamical viscosity. The liquid crystal stress term is:

$$\sigma_{\alpha\beta}^{lc} = \sigma_{\alpha\beta} + \tau_{\alpha\beta} \tag{1.19}$$

where

$$\sigma_{\alpha\beta} = -P_0\delta_{\alpha\beta} - \xi H_{\alpha\gamma}\left(Q_{\gamma\beta} + \frac{1}{3}\delta_{\gamma\beta}\right) - \xi\left(Q_{\alpha\gamma} + \frac{1}{3}\delta_{\alpha\gamma}\right)H_{\gamma\beta} + 2\xi\left(Q_{\alpha\beta} - \frac{1}{3}\delta_{\alpha\beta}\right)Q_{\gamma\mu}H_{\gamma\mu} \tag{1.20}$$

is the symmetric part of the stress tensor for liquid crystals instead

$$\tau_{\alpha\beta} = Q_{\alpha\nu}H_{\nu\beta} - H_{\alpha\nu}Q_{\nu\beta} \tag{1.21}$$

is the antisymmetric part of the stress tensor. The final term of the total stress tensor is

$$\sigma_{\alpha\beta}^{int} = -\left(\frac{\delta\mathcal{F}}{\delta\phi}\phi - \mathcal{F}\right)\delta_{\alpha\beta} - \frac{\delta\mathcal{F}}{\delta(\partial_\beta\phi)}\partial_\alpha\phi - \frac{\delta\mathcal{F}}{\delta(\partial_\beta Q_{\gamma\mu})}\partial_\alpha Q_{\gamma\mu} \tag{1.22}$$

where $Q_{\alpha\beta}$ is the **Q** tensor order parameter for liquid crystals, **H** is the molecular field, P_0 the isotropic pressure and $\mathcal{F}$ is the free-energy functional of the given system and ϕ is concentration field. ξ is a constant which takes into account the aspect ratio of the molecules and is related to the rheological answer of the director under shear. If $\xi \geq 0.6$ the liquid crystal is in the flow aligning regime and there is a stable response (the molecules form a fixed angle respect to direction of the flow as the Leslie angle [7]) instead for $\xi < 0.6$ the liquid crystal is in the flow tumbling regime and there is an unstable response (molecules continuously change their orientation in chaotic way) [7, 8].

1.2 The convection-diffusion equation

As introduced before, the thermodynamics of a system can be described by an order parameter; in the case for example of a binary fluid mixture it consists in a scalar quantity corresponding to the density difference between the components. The evolution of the order parameter is described by a convection-diffusion equation in which there is the coupling with the velocity field. In this paragraph the convection-diffusion equation will be introduced for the simple case of binary fluid mixtures.
In general there are two ways of variation of concentration in a mixture: the first is mechanical and consists in the movement of little portions of fluid and the second is the diffusion consisting in the moviment of fluid molecules due to termic or chemical gradients [3, 9]. In case of absence of diffusion the composition of each element of fluid doesn't change and for each component of fluid the continuity equation is valid

$$\partial_t n_k + \partial_\alpha (n_k u_\alpha) = 0 \tag{1.23}$$

with $k = 1, 2$. Passing in the integral form and including the diffusive terms it is

$$\partial_t \int_{V_0} n_k dV_0 = -\int_{S(V_0)} n_k \mathbf{u} \cdot d\mathbf{l} - \int_{S(V_0)} \mathbf{J}_k \cdot d\mathbf{l} \tag{1.24}$$

which in differential form becomes

$$\partial_t n_k + \partial_\alpha (n_k u_\alpha) = -\partial_\alpha J_{\alpha,k} \tag{1.25}$$

where the term $\mathbf{J}_k$ is the flux of diffusion and it depends only by termal and chemical potential gradients. Writing $\mathbf{J} = \mathbf{J}_1 = -\mathbf{J}_2$ and, remembering that $\phi = n_1 - n_2$, subtracting the equation for $k = 1$ (1.25) with the one for $k = 2$ it results

$$\partial_t \phi + \partial_\alpha (\phi u_\alpha) = -2\partial_\alpha J_\alpha. \tag{1.26}$$

The term $\mathbf{J}$ represents the current of diffusion which, under the assumption of little termal or concentration gradients, can be expressed as linear function of $\nabla\mu$ where μ is the chemical potential [10].
So the typical expression of the convection-diffusion equation, also called Cahn-Hilliard equation, for binary fluid mixtures becomes

$$\partial_t \phi + \nabla \cdot (\phi \mathbf{u}) = D\nabla^2 \mu_\phi \tag{1.27}$$

with D diffusion coefficient. The chemical potential μ depends from the order parameter and by its gradient and represents the strenght which drives the system towards the equilibrium. In the mean-field theories it is calculated as functional derivative of the free energy $\mathcal{F}$ respect to the concentration field [3]:

$$\mu = \frac{\delta \mathcal{F}}{\delta \phi}. \tag{1.28}$$

1.3 The Beris-Edwards equation

In the case of liquid crystals the order parameter, which will be better described in Chapter 2, is a second-rank, symmetric and traceless tensor with five indipendent components which evolve through the Beris-Edwards equation [5]

$$(\partial_t + \mathbf{u} \cdot \nabla)\mathbf{Q} - \mathbf{S}(\mathbf{W}, \mathbf{Q}) = \Gamma \mathbf{H} \tag{1.29}$$

where Γ is the collective rotational diffusion constant. The left hand side of equation represents the material derivative which describes the temporal dependence of a quantity shifted by the fluid with velocity $\mathbf{u}$. The term $\mathbf{S}(\mathbf{W}, \mathbf{Q})$ takes into account the possibility that molecules can be rotated and stretched by fluxes. The explicit expression of $\mathbf{S}$ is this

$$\mathbf{S}(\mathbf{W}, \mathbf{Q}) = (\xi \mathbf{D} + \mathbf{\Omega})(\mathbf{Q} + \mathbf{I}/3) + (\mathbf{Q} + \mathbf{I}/3)(\xi \mathbf{D} - \mathbf{\Omega}) - 2\xi(\mathbf{Q} + \mathbf{I}/3)Tr(\mathbf{Q}\mathbf{W}) \tag{1.30}$$

where $\mathbf{D} = (\mathbf{W} + \mathbf{W}^T)/2$ and $\mathbf{\Omega} = (\mathbf{W} - \mathbf{W}^T)/2$ are respectively the symmetric and antisymmetric parts of the tensor velocity gradient $W_{\alpha\beta} = \partial_\beta u_\alpha$ and $\mathbf{I}$ is the unit matrix. At the right hand side of (1.29) there is the molecular field

$$\mathbf{H} = -\frac{\delta \mathcal{F}}{\delta \mathbf{Q}} + \frac{\mathbf{I}}{3} Tr \frac{\delta \mathcal{F}}{\delta \mathbf{Q}} \tag{1.31}$$

which, in this case, can be interpreted as the thermodynamic force which drives the system towards the equilibrium state with $\mathcal{F}$ free-energy functional of the system in which all the thermodynamics is encoded, $\mathbf{I}$ identity matrix and Tr the trace of $\delta \mathcal{F}/\delta \mathbf{Q}$.

1.4 Brief summary of Landau theory

The Ginzburg-Landau theory is a powerful tool to study phase-transitions in the systems [11]. When a physical system is affected by a phase-transition, once a critical value of a certain control parameter (for example the temparature) is reached, a value of a physical quantity, defined as order parameter becomes zero passing in the disordered phase. In the case of a binary mixtures, for example, the order parameter is assumed as the scalar concentration field which is non-zero in the ordered phase, under the critical point where the two phases are separated, and zero above it where the phases are mixed in a unique phase.
As long as the order parameter of a system is zero in the disordered phase above the critical point, in the vicinity of the critical point it is small and the simplest expression of the free-energy can be written as an expansion in power-series of the order parameter requiring particular simmetries by the system. This free-energy is

defined as $\mathcal{F} = E - TS$ with E internal energy of the system, T temperature and S entropy of the system. At equilibrium this free-energy must be minimized.
In case of the binary mixture, for example, the expression of the free-energy should contain only even power-series terms of the concentration field ϕ because the symmetry for transormation $\phi \to -\phi$ is requested. Speaking in physical terms, if the oil droplet in water phase is being studied, the energy must be the same of the inverse situation of a water droplet in the oil phase. Taking into account these aspects, the expression of the free-energy functional for binary fluid mixtures is:

$$\mathcal{F} = \int dV f = \int dV \left(\frac{a}{2}\phi^2 + \frac{b}{4}\phi^4 + \frac{K}{2}|\nabla\phi|^2 \right) \tag{1.32}$$

where f is the free-energy density. The power-series, as said previously, contains only even terms and is truncated to the fourth order. The last term takes into account the energetic penalty for the presence of interfaces with coefficient K [12].
From the expression of the free-energy functional, which contains all the thermodynamic information of the system, it is also possible to calculate other physical quantities such as the chemical potential μ calculated as the functional derivative of the free-energy respect to ϕ [3]

$$\mu = \frac{\delta\mathcal{F}}{\delta\phi} = a\phi + b\phi^3 - K\nabla^2\phi. \tag{1.33}$$

The surface tension is defined as

$$\sigma = \int_{-\infty}^{+\infty} dz \left[f(n,\phi,T) - f(n,\phi_\pm,T) + \frac{K}{2}\left(\frac{d\phi}{dz}\right)^2 \right] \tag{1.34}$$

$$= \int_{\phi_-}^{\phi_+} d\phi \sqrt{2K[f(n,\phi,T) - f(n,\phi_\pm,T)]} \tag{1.35}$$

in which the integral is calculated in the direction normal to the interface between the two bulk phases $\phi_\pm$ at temperature T [3]. Another important quantity is the pressure tensor in which there is the information of the interactions of the components of the mixture [13]:

$$P_{\alpha\beta} = \left\{ \frac{\delta\mathcal{F}}{\delta\phi}\phi + \frac{\delta\mathcal{F}}{\delta n}n - f \right\} \delta_{\alpha\beta} + D_{\alpha\beta}(\phi) \tag{1.36}$$

in which $D_{\alpha\beta}(\phi)$ is a symmetric tensor added ad hoc to ensure the condition of mechanical equilibrium $\partial_\alpha P_{\alpha\beta} = 0$ [14, 15].
Generally a physical system can be subjected to various stimuli for example an electric field, an external force, chemical reactions etc. which drive the system out of equilibrium. In this case all the treatment described before is always valid in

the hypothesis of local equilibrium [10] in a certain element of the system[1]. One then writes all the conservation laws such as the conservation of mass, momentum, energy etc. and also relations which relate the fluxes in the system to the thermodynamic forces or gradients.

[1]This element in which a local equilibrium is supposed is small compared to the macroscopic scales of the system but big from a microscopic point of view because it contains a large number of atoms and molecules of the order of the Avogadro number $N_A = 6.022 \times 10^{23} mol^{-1}$.

Chapter 2

Introduction to liquid crystals

This chapter introduces the general aspects of the liquid crystals theory as a state of matter with properties intermediate between solids and liquids.
Nowadays liquid crystals are used in a pletora of applications such as the production of TV screens, computer monitors, temperature sensors, optical instruments and cosmetics [16–25]. The variety of this fields of application and the continuous evolution of the technology based on them justifies the continuous necessity to study their properties.
After a brief initial historical overview about the most important dates that mark the first discoveries of the liquid crystals, the Chapter proceeds describing briefly the most important and known structures such as the nematic, cholesteric, smectic and columnar phases also mentioning the cholesteric fingers and recent structures such as the twist-bend liquid crystal [26, 27].
The concepts of director and tensor order parameter will be then introduced. Liquid crystals are characterized by a second rank, symmetric, traceless tensor order parameter with five independent components in the simplest case.
After that, topological defects will be treated. They are in general regions which can be points, lines and surfaces where the local orientation of the director becomes ambiguous and the order parameter is ill defined. They can rise by the competition and combination of different factors such as the elasticity of the liquid crystal, presence of boundaries and external fields, colloidal impurities etc. Thus the formalism of the tensor order parameter becomes a powerful way to detect and study them. They will be introduced in general also defining the concept of topological charge to quantify and qualify them.
In final part of the Chapter the Landau-De Gennes theory formalism for liquid crystals will be analyzed describing all the energetic terms related to the bulk of the system, the interfaces, the interaction between the liquid crystal and the external fields, the elastic distortions etc.

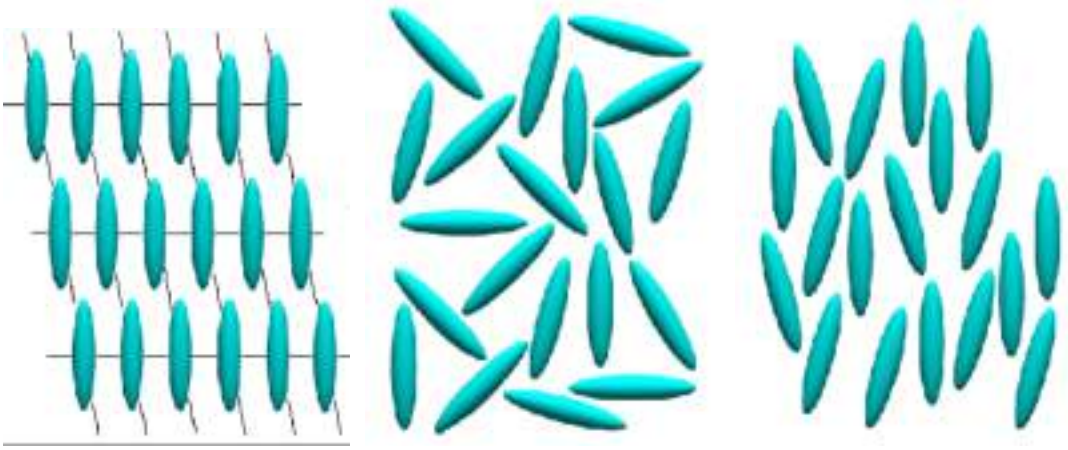

(a) Solid state (b) Liquid state (c) Liquid crystal state

Figure 2.1: Schematic representation of molecules in a solid (a) with perfect positional and orientational order, in a liquid or isotropic fluid (b) without any positional and orientational order and in a liquid crystal (c) where only orientational order survives.

2.1 Historical overview

The first experimental observation of the liquid crystals is dated to late 19th century, precisely in 1888, with the austrian botanist Friedrich Reinitzer who investigated the melting transition of an organic compound (today known as cholesteril benzoate) and observed curious things. The solid melted in a cloudy liquid at $145.5°C$ but then "melted" again in a clear liquid at $178.5°C$. Reinitzer then reported this result to his collegue physicist Otto Lehmann who continued the obserations through a polarizing microscope and found other substances with a similar behaviour. In the end Lehmann and Reinetzer understood that the cloudy liquid, which was also birifrangent, was a new state of matter Lehmann baptized "liquid crystal". Although liquid crystals had been discovered already in the 19th century, the sistematic study of this new state of matter started only in 1920 with G. Friedel, followed by 50 years of inactivity. Only by 1970's with the influence of the Nobel prized physicist P.G. de Gennes, the study of liquid crystals became an important and recognized field of research today still in continuous expansion even advantaged by the introduction of the computer in the science [28, 29].
Usually physics or chemistry introductory books write that matter consist in the three states of solid, liquid and gas but this is not completely true because there are intermediate situations between them and one interesting exemple are, indeed, the liquid crystals.

With this term usually it is indicated a state of matter with intermediate properties between solids and liquids [5, 30–34]. As shown in Fig. 2.1 in a cristalline solid atoms and molecules are disposed in the cristalline lattice in an ordered way with positional and orientational order. The opposite situation, instead, is that of an isotropic fluid or liquid where the molecules have lost any positional and orientational order and are distributed randomly in the space. Therefore liquid crystals are "crystals" because their molecules don't have any positional order but preserve an orientational order like solids but they are also "liquids" because they flow under a shear like isotropic fluids.

2.2 General classification and mesophases

Starting with a chemical point of view, liquid crystal molecules have an anistropic shape which can be oblate or prolate and have some rigidity conferred by biphenyl or terphenyl groups. Liquid crystals structures can also form when amphiphilic molecules associate to form anisotropic structures which, in turn, spontaneously order into liquid-crystalline phases [29, 30]. Fig. 2.2 shows some examples of liquid crystal moelecules such as N-(p-methoxybenzilidene)-p-butylaniline (MBBA), p-n-hexyloxybenzilidene-p'-aminobenzonitrile (HBAB) and 4-cyano-4' alkylbiphenyl series, or nCB, where n is the number of carbons (typically 5-12) in the flexible "tail" of the molecule [29]. Liquid crystals, in general, can be classified in different ways depending by the point of view. If one consideres the shape of the molecules, they can be classified as *calamitics*, with rod-like molecules, or *discotics*, with disk-shape molecules. Another important difference deals with the control parameter which induces a phase transtion; if that is triggered by a change in temperature, liquid crystals are called *thermotropic*, in case of a change in the molecular concentration they are called *lyotropic* [30–32].[1] As regards the disposition of the molecules, liquid crystals can give rise to different and exotic structures also called *mesophases* which will be introduced in the following subsections.

[1] In last years the new class of *metallotropic* liquid crystals or metallomesogens has been investigated. They are formed exploiting cationic surfactant templating of molten divalent metal halides. [35]

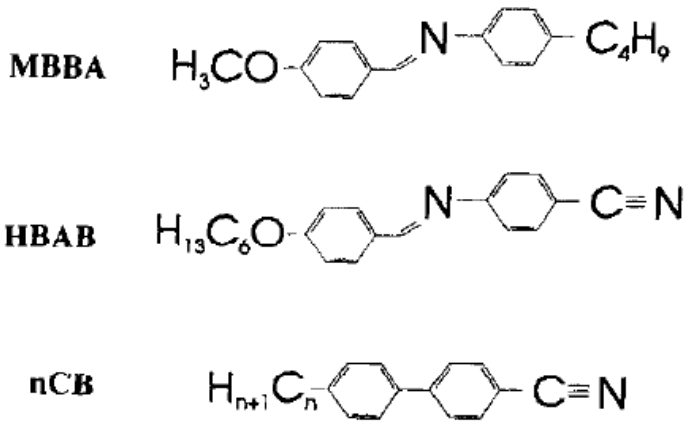

Figure 2.2: Molecules that form liquid crystals. N-(p-methoxybenzilidene)-p-butylaniline (MBBA), p-n-hexyloxybenzilidene-p'-aminobenzonitrile (HBAB) 4-cyano-4' alkylbiphenyl (nCB) [29].

2.2.1 Nematic mesophase

The *nematic phase* is maybe the most famous and simplest of the liquid crystal structures. The molecules, generally with rod-like shape, are on average directed towards a common direction, Fig. 2.3, specified by the director, a unit vector, $|\mathbf{n}| = 1$, with head-to-tail simmetry (a vector with no arrow such that $\mathbf{n} = -\mathbf{n}$) [30–32].

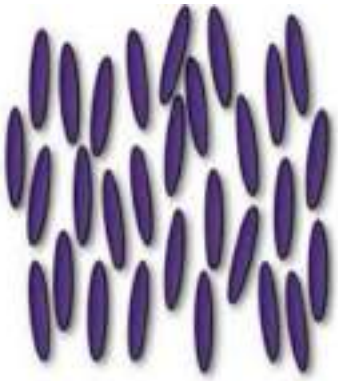

Figure 2.3: Nematic phase in which rod-like molecules are on average oriented towards the common direction of the director.

Molecules such as p-azoxyanisole (PAA) or N-(p-methoxybenzylidene)-p-butylaniline

(MMBA) shown in Fig. 2.4 are examples of nematogens. This word means that they give rise to the nematic mesophase.

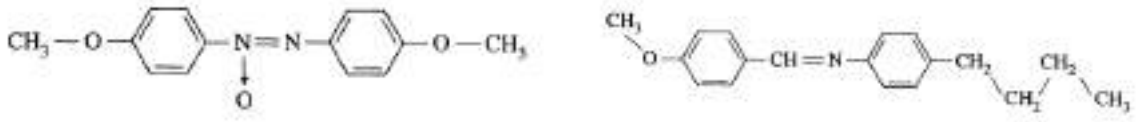

(a) (b)

Figure 2.4: Chemical structure of p-azoxyanisole (PAA) (a) and N-(p-methoxybenzylidene)-p-butylaniline (MMBA) (b) [30].

2.2.2 Cholesteric mesophase

The *cholesteric* or *chiral nematic phase* is another important mesophase which is locally equivalent to a nematic one but not globally because molecules are arranged in an helical structure like in Fig. 2.5. This mesophase occurs for chiral molecules[2] but it is also obtained experimentally starting from a nematic liquid crystal adding a chiral dopant. The helix is characterized by a pitch which represent the spacial distance over that the director rotates of 2π. The wave vector q_0 is defined so that the pitch $p_0 = 2\pi/q_0$. However, as long as the two orientations of the director are equivalent ($\mathbf{n} = -\mathbf{n}$), it is also possible to define $L = p_0/2 = \pi/q_0$ with pitch p_0 defined as the length for which the director rotates of π or makes a twist as Fig. 2.5-(a). This scale lenght has dimensions (≈ 3000Å) comparable with the wavelenght of visible light so that cholesteric liquid crystals are well fit to be used for optical instruments [16, 36, 37]. Finally it is important the aspect of the sign: if the xyz frame is righ-handed, then $q_0 > 0$ and the helix will be right-handed. This situation is verified in the cholesterol chloride. If $q_0 < 0$, the helix will be left-handed. Most of the aliphatic esters of cholesterol belong to this class [30–32].
Cholesterol esters, with structure shown in Fig. 2.6, are examples of twisted structures. This is the reason why the chiral nematic liquid crystals are so called "cholesterics".
Cholesteric fingers are a typical structure which appears if the liquid crystal is confined between two plates, treated anchoring the director to the plates perpendicularly or homeotropically [28]. While the director is planar the boundary conditions are satisfied by orienting the axis of the helix normal to the plates, instead no orientation is compatible when the director is perpendicular and therefore this leads

[2] A chiral molecule has a non-superposable mirror image.

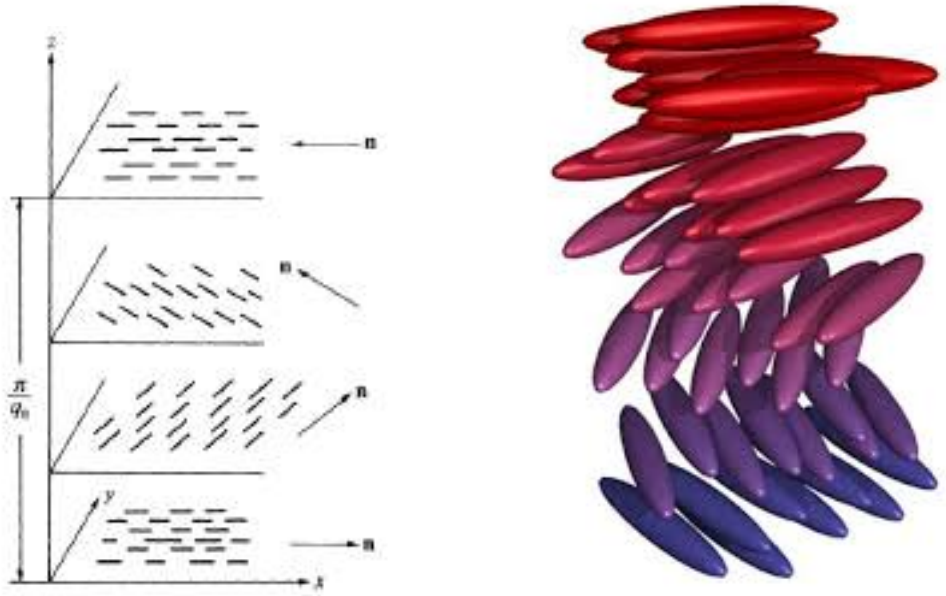

(a) (b)

Figure 2.5: Cholesteric phase with pitch $p_0 = \pi/q_0$ so that the director makes a rotation of π or a twist [30] (a) and 3D view of a cholesteric liquid crystal molecules (b).

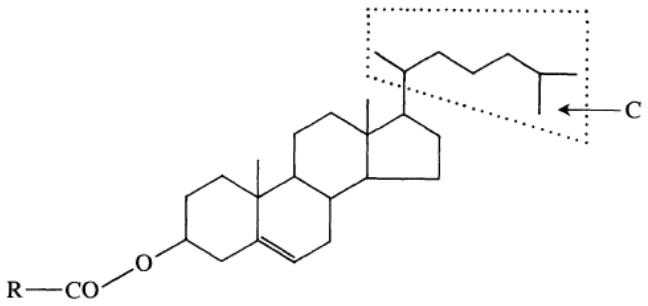

Figure 2.6: General structure of cholesterol esters. The rings are not aromatic and the structure is not planar, hydrogens are not reported [30].

to a frustrated situation.
Experiments confirm that the texture strongly depends by an adimensional param-

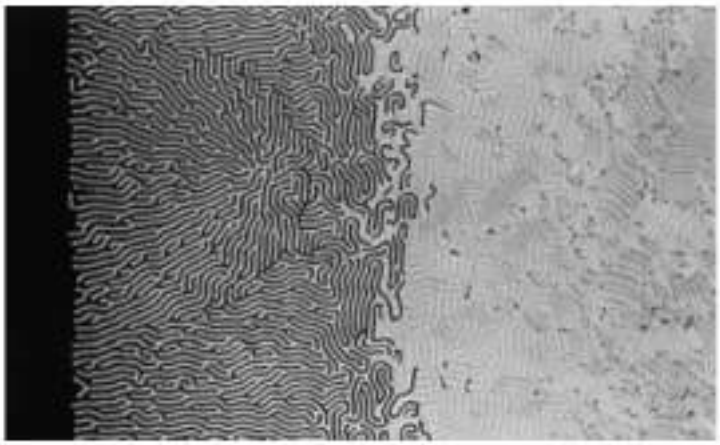

Figure 2.7: Cholesteric fingers in a wedge between crossed polarizers. From left to right three zones are distinguishable: a black zone (homeotropic nematic), the fingers separated by homeotropic nematic and finally adhering fingers [28].

eter $C = h/p$, called confinement ratio [38], where h is the thickness of the sample and p is the pitch of the cholesteric helix. The situation reported in [28] consists in a mixture of 96.5 wt% $ZLI1981$ nematic and 3.5 wt% cholesteryl nonanoate with a pitch of 6.7 μm at room temperature placed between two plates and reported in Fig. 2.7.
Experiments show the existence of a critical confinement ratio $C_c \approx 1.25$ such that for $C < C_c$ the cholesteric structure is completely unwound and the director is always parallel to the axis normal to the plates whereas for $C > C_c$ a "fingerprint" texture appears composed of so called *cholesteric fingers* separated one another by hometropic nematic for $C_c < C < C^*$ and adhering together for $C > C^*$ (with $C^* \approx 1.65$). Other experiments have been performed through the years [28] in which the confinement ratio can be modified by changing either the thickness of the sample or the pitch. The first one has reveled not applicable because strongly perturbs the director instead the second way is simpler and has two variants. The first consists in modifying the pitch changing the temperature or using an electric field which requires the sample being prepared between two electrodes [28, 38].

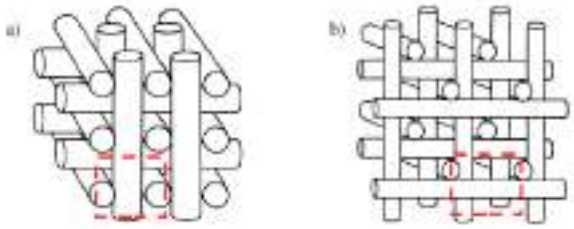

Figure 2.8: Three-dimensional periodic structure of cylinders for $BPII$ (a) and BPI (b) [39].

2.2.3 Blue phases

Blue phases are particular structures of liquid crystals which live in a narrow temperature range (about $1K$) between isotropic and cholesteric structure [30, 31, 39]. However more recent studies have extended this temperature range of stability of about $60K$ through the introduction of colloidal impurities [40–42]. Three blue phases are known without the action of an electric field: blue phase I (BPI), blue phase II ($BPII$), shown in Fig. 2.8, and blue phase III ($BPIII$). BPI and $BPII$ are characterized by a three dimensional cubic array with period of the same magnitude of wave lenght of the visible light. BPI has a face centered cubic pattern; $BPIII$, instead, is different because has an amorphous structure called "blue fog". The physical reason of the formation of the blue phases is due to the fact that when the temperature of the system raises towards the critical point of transition isotropic-cholesteric, the cholesteric helix in the system is a configuration no longer energetically advantagious. So blue phases occur because the local double-twisted structure, shown in Fig. 2.9, (i.e. local twisting in two directions, as opposed to the single twist of cholesteric) is more energetically favoured.

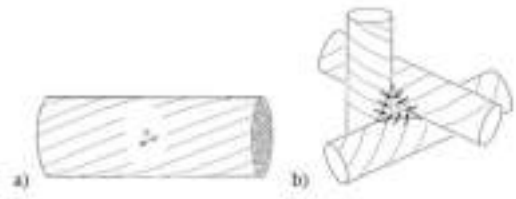

Figure 2.9: The stable cylindrical region of a blue phase (a). A topological defect casued by the double-twist of the cylinders (b). The arrows indicate the local direction of the director [43].

As long as this structure is incompatible with the requirement of continuity, this

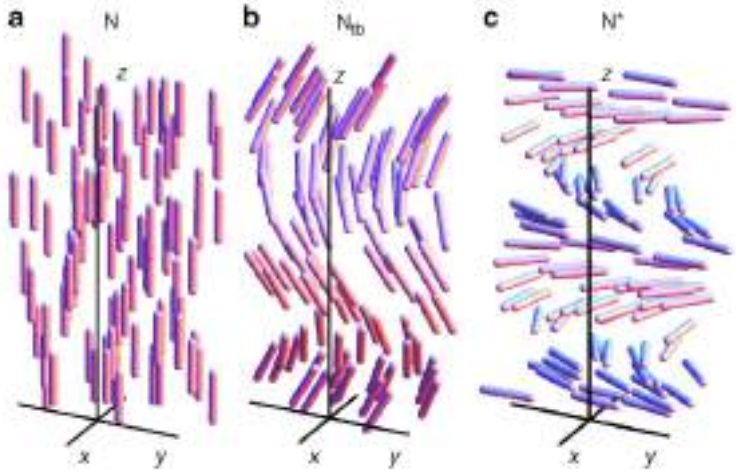

Figure 2.10: (a) Nematic phase with uniaxial alignment $\theta_0 = 0$, (b) twist-bend structure with $0 < \theta_0 < \pi/2$, (c) cholesteric structure $\theta_0 = \pi/2$ [26].

results in the formation of networks of defects that separate isolated stable regions [39, 44]. So it can be concluded that blue phases are interesting and elegant three dimensional structures of topological defects in nature. Another important feature of these structures is the fact that the defects have a lattice period of several hundred nanometers of the same magnitude of wave lenght of the visible light. For this reason they exhibit Bragg reflection in the range of visible light and find important applications in the production of light modulators or tunable photonic crystals [44–46]. The first experimental optical observation of a blue phase was with a blue colour, which justifies the name, but it can vary in the visible range.

2.2.4 Twist-bend structure

As reported in paragraph 2.2.1 and 2.2.2, in the uniaxial nematic the rod-like molecules are, on averege, parallel to the director **n**, instead in a cholesteric liquid crystal the molecules are rearranged in an helical structure. However in 1973 Meyer predicted that polar molecules interactions that favoured bend deformations could lead to twist-bend nematic phase, in Fig. 2.10, in which the director draws an oblique helicoid manteining a constant oblique angle $0 < \theta_0 < \pi/2$ with the helical axis z [26, 27][3]:

$$\mathbf{n} = (sin\theta_0 cos\phi, sin\theta_0 sin\phi, cos\theta_0) \tag{2.1}$$

[3]All these mesophases are generally identified as nematic family divided in uniaxial nematic, biaxial nematic, chiral nematic or cholesteric, blue phase and twist-bend. The latter in [27] is identified as the recent "fifth nematic phase".

(a) smectic-A (b) smectic-C

Figure 2.11: Case of smectic-A (a) in which molecules are perpendicular to the planes and smectic-C (b) in which molecules are tilted.

where $\phi = t_{tb}z$ is the azimuthal angle, $t_{tb} = 2\pi/p_{tb}$ with p_{tb} pitch of the helicoid. In this way the nematic and cholesteric phase can be considered the limiting cases of the twist-bend structure respectively with $\theta_0 = 0$ and $\theta_0 = \pi/2$. A series of studies demonstrate that this twist-bend structure seems to be facilitated by bent (banana-like) shaped molecules [26]. Another aspect is the fact that the pitch of the twist-bend helicoid is of the order of magnitude of $10nm$ instead of a cholesteric in which the length of the pitch is of the order of $100nm$ [27].

2.2.5 Smectic and columnar mesophases

The smectic phase is the liquid crystal phase which is the closest to a solid structure [30, 31]. Differently from the nematic phase in which the molecules are, on average, oriented towards a common direction, smectics are ordered in two directions. Precisely the smectic molecules are arreanged in a layered structure, as shown in Fig. 2.11, with two different orientations. In a smectic-A, Fig. 2.11-(a), the orientation of the molecules is perpendicular to the planes whereas in a smectic-C, Fig. 2.11-(b), the molecules have a tilted orientation. The columnar phase is the dis-

Figure 2.12: Molecules arranged in stacks in the columnar phase.

cotic equivalent of the smectic phase in which the disk-like molecules are arranged in stacks [30, 31] as shown in Fig. 2.12:

2.3 Order parameter for liquid crystals

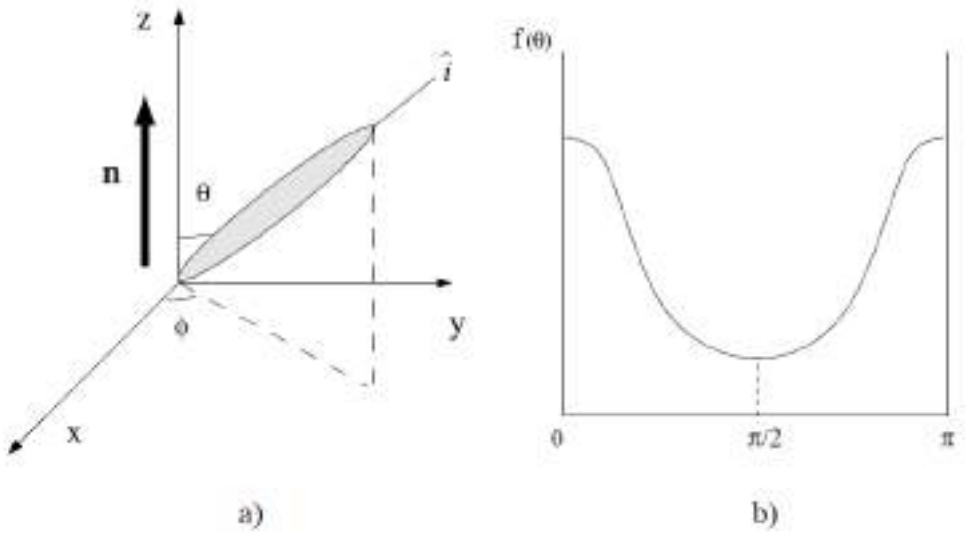

Figure 2.13: Position of the molecule, along the direction **i** respect to the director **n** directed along z axis; θ and ϕ are the angles that the molecule forms with z and x axis (a). (b) Probability distribution function of the molecular orientation dependent from the angle θ, symmetric respect to $\pi/2$ with two maxima in 0 and π [30, 43].

As previously said, in the nematic phase the molecules are, on averege, oriented towards a common direction identified by the director **n**, a unite vector with head-to-tail symmetry (it means that directions **n** and $-\mathbf{n}$ are equivalent), whereas in the isotropic phase the molecules are oriented randomly in the space without nor positional nor orientational order. This concept can be better expressed saying that the nematic phase is "more ordered" than the isotropic one or has a lower symmetry. In order to express these concepts in a more quantitative way it is necessary to introduce an order parameter which is non-zero in the nematic phase and vanishes in the isotropic phase. This research of an order parameter can start with a simple case [5, 30, 31, 47].
As long as liquid crystal molecules have an anisotropic structure similar to a rod, the axis of a rod can be labelled with **i**. The direction of the director **n** is assumed coincident to the z axis in a xyz frame. The orientation of **i**, respect to **n**, is identified by the polar angles θ and ϕ, as in Fig. 2.13-(a), so that its components are

$$i_x = sin\theta cos\phi, \tag{2.2}$$

$$i_y = sin\theta sin\phi \tag{2.3}$$

and

$$i_z = cos\theta. \tag{2.4}$$

The state of alignment of these rods can be described by a distribution function $f(\theta, \phi)d\Omega$ which represents the probability of finding a rod in the solid angle $d\Omega = sin\theta d\theta d\phi$ around the direction (θ, ϕ). According to the properties of nematics it is possible to impose some constraints to this function: $f(\theta, \phi)$ is independent of ϕ because of the cylindrical symmetry around $\mathbf{n}$ and $f(\theta) = f(\theta - \pi)$ because the directions $\mathbf{n}$ and $-\mathbf{n}$ are equivalent. The functions has, also, two maxima in $\theta = 0$ and π and a minimum in $\theta = \pi/2$, as shown in Fig. 2.13-(b), because in the first cases the axis of the molecule is parallel to the director $\mathbf{n}$, instead in the last case is perpendicular. Now the function $f(\theta)$ alone can't give information to the state of the alignment of the molecules so it is necessary to define a numerical associated quantity. The first possibility could be

$$< cos\theta >=< \mathbf{i} \cdot \mathbf{n} >= \int_0^\pi f(\theta) cos\theta sin\theta d\theta \tag{2.5}$$

but this function vanishes because it's a product of symmetric function $f(\theta)sin\theta$ for an antysimmetric one $cos\theta$ in the interval $[0; \pi]$. Thus the first non trivial information on the state of alignment of molecules can be found in the quadrupole term

$$S = \frac{1}{2} < (3cos^2\theta - 1) >= \int f(\theta)\frac{1}{2}(3cos^2\theta - 1)d\Omega. \tag{2.6}$$

This choice in non trivial as before because if $\theta = 0$ or π (situation of complete alignment), $S = 1$ instead if $\theta = \pi/2$ (perpendicular alignment) $S = -1/2$. If the molecules are randomly oriented as in an isotropic fluid ($f(\theta)$ independent form θ), $< cos^2\theta >= 1/3$ and so $S = 0$. Therefore this S quantity gives a measure of the alignment of the molecules [5, 30, 31].
This approach in defining a scalar order parameter could be useful because it gives a measure of the alignment of the molecules respect to the director but it doesn't give information about the orientation of the director itself which has been supposed parallel to the z axis. It's important to generalize the definition of the order parameter which must be independent from the choice of the frame of reference. The approach consists in defining a tensorial order parameter related to the direction of the individual molecules

$$Q_{\alpha\beta} = \left\langle n_\alpha n_\beta - \frac{1}{3}\delta_{\alpha\beta} \right\rangle \tag{2.7}$$

where the angular brackets denote a coarse-grained average. This tensor order parameter, the $\mathbf{Q}$ tensor, has the following form suitable for an uniaxial nematic

[30, 31]:

$$Q_{\alpha\beta} = q\left(n_\alpha n_\beta - \frac{1}{3}\delta_{\alpha\beta}\right) = q\begin{pmatrix} n_x^2 - 1/3 & n_x n_y & n_x n_z \\ n_x n_y & n_y^2 - 1/3 & n_y n_z \\ n_x n_z & n_y n_z & n_z^2 - 1/3 \end{pmatrix} \tag{2.8}$$

where $0 \leq q \leq 2/3$ represents the magnitude of the alignment. It is a 3×3 real matrix, symmetric and traceless with only five independet components. However it is possible to find a suitable coordinate system where the tensor is diagonal.[4]

$$Q_{\alpha\beta} = \begin{pmatrix} -\frac{q}{3} & 0 & 0 \\ 0 & -\frac{q}{3} & 0 \\ 0 & 0 & \frac{2q}{3} \end{pmatrix} \tag{2.9}$$

If $\mathbf{n}$ is along the z axis of the coordinate system. From the previous expression it is clear that the diagonalized tensor has eigenvalues $-q/3$, $-q/3$ and $2q/3$ and its largest eigenvalue, $\frac{2}{3}q$, represents a measure of the alignement and its correspondent eigenvector defines the direction of the director $\mathbf{n}$. In [48] it is demonstrated that if q remains constant it is possible to obtain back the equations of Ericksen, Leslie and Parodi for an uniaxial nematic.
The most general form of the $\mathbf{Q}$ tensor, valuable to describe the biaxial[5] nematics, is similar to the previous one but the three eigenvalues are different [28, 32, 34, 47]. In the eigenvector space ($\mathbf{l}$,$\mathbf{m}$,$\mathbf{n}$) one writes:

$$Q_{\alpha\beta} = \begin{pmatrix} \frac{-q+\eta}{3} & 0 & 0 \\ 0 & \frac{-q-\eta}{3} & 0 \\ 0 & 0 & \frac{2q}{3} \end{pmatrix} \tag{2.10}$$

which becomes, in an arbitrary frame of reference

$$Q_{\alpha\beta} = -\frac{1}{3}(q-\eta)l_\alpha l_\beta - \frac{1}{3}(q+\eta)m_\alpha m_\beta + \frac{2}{3}q n_\alpha n_\beta \tag{2.11}$$

The tensor now has five independent components: the amplitudes q and η and three out of the nine components of the basis vectors $(\mathbf{l}, \mathbf{m}, \mathbf{n})$. It is also invariant for transformation $\mathbf{l} \to -\mathbf{l}$, $\mathbf{m} \to -\mathbf{m}$ and $\mathbf{n} \to -\mathbf{n}$. Setting $\eta = 0$ one returns to the uniaxial form is restored.

[4] It must be enphasized that the $\mathbf{Q}$ tensor written in (2.8) is function of the spatial coordinates.

[5] A uniaxial molecule can be thought as rod or disk with rotation symmetry about the axis of the molecule (which explains the term uniaxial). A biaxial nematic can be thought with a shape of a plank of wood; in this case there is not rotation axis along the long axis of the plank but there are three axis of reflective symmetry (the long, intermediate and the short axis) [47]. In an uniaxial arrangement the molecules are oriented, on averege, along the direction of the director whereas for biaxial liquid crystals, with molecules of a shape of plank of wood, the long axis align in one direction and the short axis along another direction.

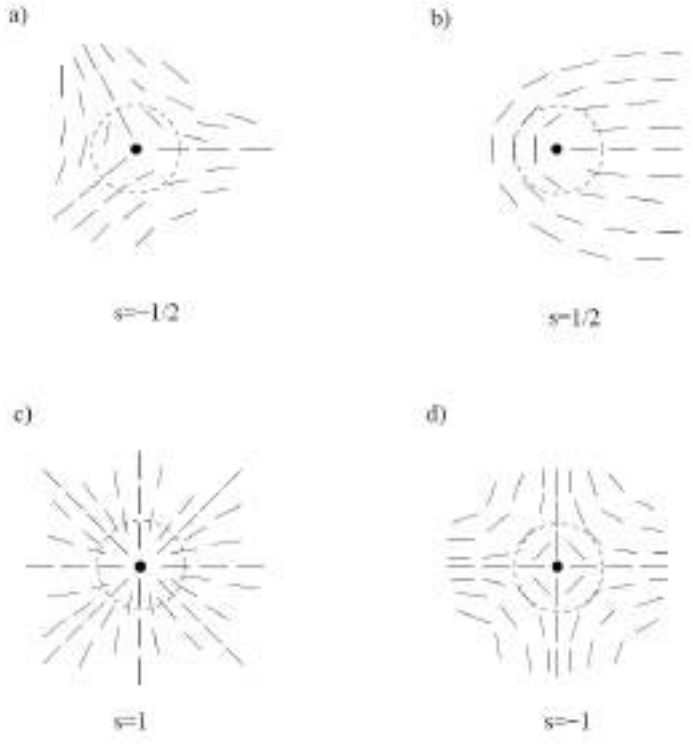

Figure 2.14: Exemples of topological defects and relative topological charges. (a) $s = -1/2$, (b) $s = 1/2$, (c) the radial hedgehog with $s = +1$ and (d) with $s = -1$.

2.4 Topological defects in liquid crystals

2.4.1 General aspects

Topological defects in liquid crystals are regions where the order parameter is not well defined and the orientation of the director becomes ambiguous [30, 31, 49, 50]. They can form by the combination and competition of different factors such as the elasticity of the liquid crystal, the type of anchoring of the director, the presence of boundaries in the system, external fields, colloidal impurities etc. To every topological defects it is possible to associate a topological charge s defined as the number of rotation of the director around a closed curve which surrounds the defect. As long as the rotation cannot be of 2π the topological charge can be integer or semi-integer. Fig. 2.14 shows tipical defects with relative topological charge. For exemple in Fig. 2.14-(a) the director rotates of an angle equals π so this corrisponds to a topological charge $s = -1/2$ whereas in Fig. 2.14-(b) the rotation happens in opposite verse so the sign becomes positive, $s = 1/2$. In Fig. 2.14-(c) it is shown the tipical "hedgehog" defect in which the director sweeps out in all directions and

makes a complete rotation of 2π thus in this case the topological charge is $s = 1$. The formation of a topological defect in liquid crystals can be understood in terms of the Volterra process also used to study topological defects in solids [30–32, 34]. It is shown the case for the defect with topological charge $s = -1/2$ in a nematic in Fig. 2.15.

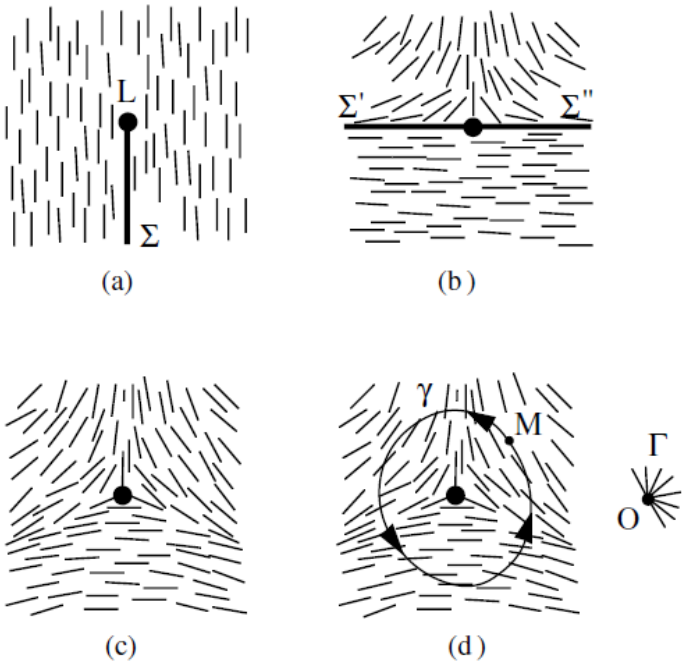

Figure 2.15: Volterra process to obtain the topological defect with charge $s = -1/2$. (a) a cut of surface Σ and length L is made, (b) the lips of the cut $\Sigma^{'}$ and $\Sigma^{''}$ are opened of π and extra material is added, (c) the system relaxes. (d) Burger circuit γ which surrounds the defect and hodograph Γ [32].

Initially a piece of nematic material is considered and a cut of surface Σ with length L is performed, Fig. 2.15-(a). Then the lips of the cut Σ, $\Sigma^{'}$ and $\Sigma^{''}$, are opened of an angle π and extra matter is introduced, Fig. 2.15-(b). The system is let to relax, Fig. 2.15-(c), and the final configuration of Fig. 2.15-(d) is obtained. As noticed the topological charge can have a sign and the origin of it is justified considering the travelling direction along the so called Burger circuit γ which surrounds the defect and the so called hodograph Γ of the director. In Fig. 2.15-(d) the Burger circuit is considered as a circle on which an arbitrary verse is fixed starting from a point M. Each director $\mathbf{n}$ that is met when traversing γ is now parallel transported to an origin O. The set of extremities traverses a circular arc oriented according

to the construction. This is the hodograph Γ. In the case shown in Fig. 2.15-(d) Γ and γ are oriented in opposite directions and this justifies the $-$ sign. Usually, for basic studying or practical application, liquid crystal is filled in between two glass substrates. A certain treatment of the substrate surfaces allows one to obtain different types of liquid crystal orientation. In the case of heterogeneous planar orientation of nematics, the director **n** is parallel to substrates but points in different directions. Such a structure appears as a *Schlieren texture* (*Schliere* means streak in German) between crossed polarizers in a polarizing microscope as shown in Fig. 2.16.

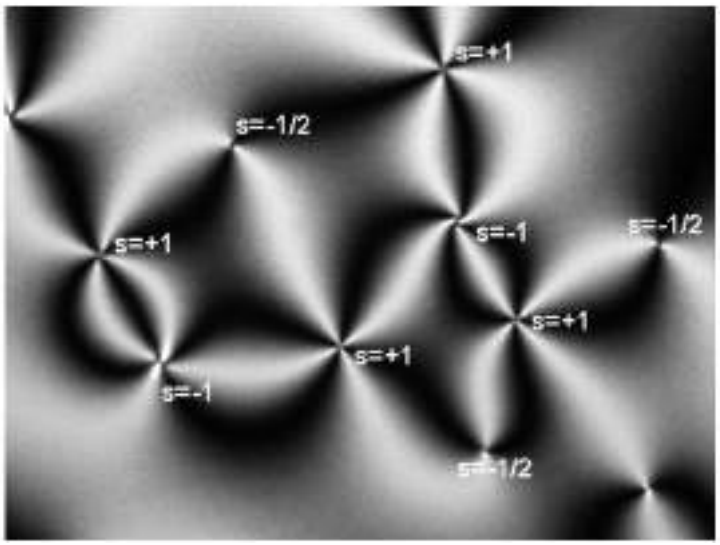

Figure 2.16: Typical Schlieren texture of a nematic liquid crystal; s is the topological charge associated to the defects [45].

The schlieren texture shows dark brushes, which correspond to the extinction orientation of the nematic liquid crystal. Accordingly, the director **n** lies either parallel or perpendicular to the polarizer or analyzer axes. The points, where two or four brushes meet, correspond to the director singularities and are called disclinations in the structure. The disclination is characterized by its strength s, which shows how much the director rotates in each point on the closed curve around the singularity point. The disclinations with $s = \pm 1/2, \pm 1$ can be found in nematics. The points where four brushes meet correspond to the disclinations with $s = \pm 1$, and, the points with two brushes correspond to the disclinations with $s = \pm 1/2$. Usually, neighboring singularities which are connected by brushes have opposite signs [45]. To distinguish between the disclinations of different sign, one can use, for example, the rotation of the sample with schlieren texture between the fixed

crossed polarizers. When the liquid crystal sample is rotated, the black brushes move continuously indicating a continuous change of the director **n**. Both two- and four-brush disclinations with a negative sign rotate in the same sense as the sample, but the brushes of positive two-brush disclinations rotate in the opposite sense.

2.4.2 Topological defects in presence of colloids

As introduced before a factor that can cause the rise of topological defects in a liquid crystal is the presence of colloidal intrusions in the medium. In this paragraph the main topological defects of this situation are briefly introduced. If a colloidal particle is placed in a liquid crystal host according to the orientation of the director different kinds of defects can rise [49]. A particle with perpendicular or homeotropic anchoring of the director is topologically equivalent to a radial hedgehog as shown in Figure 2.17:

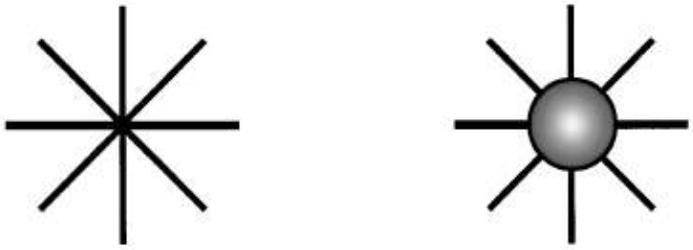

Figure 2.17: Schematic representation of a radial hedgehog (left) and a particle with normal boundary condition (right) [49].

Hedgehogs are point defects where the director sweeps out all directions an inreger number of times.
A satellite *hyperbolic hedgehog* can also occur when a colloidal particle with normal boundary conditions is placed in a liquid crystal host with director aligned far from the particle as shown in Figure 2.18:

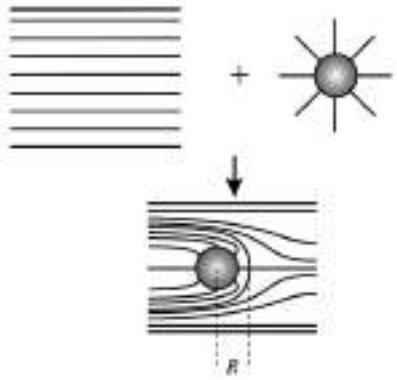

Figure 2.18: Hyperbolic hedgehog when a particle with normal boundary condition is introduced in a homegeneously aligned liquid crystal [49].

A *Saturn ring* is a topological defect with a disclination loop of strenght $-\frac{1}{2}$ shown in Fig. 2.19.

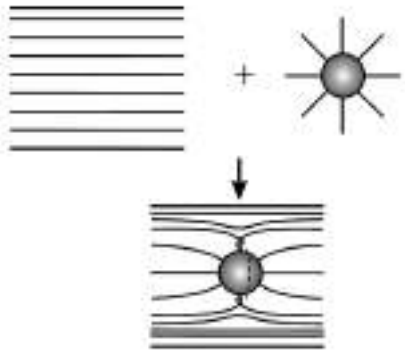

Figure 2.19: Saturn ring defect representation [49].

In general if the anchoring is weak the Saturn ring configuration is more favoured instead if the anchoring is strong the hyperbolic hedgehog configuration occurs. If a colloidal particle with tangential boundary conditions is placed in a liquid crystal two defects at the poles of the particle can rise and are called *boojums* shown in Fig. 2.20:

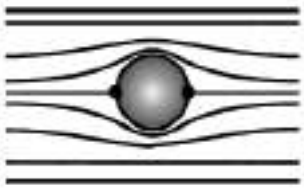

Figure 2.20: Two boojum defects are induced on the surface of the particle for tangential anchoring [49].

2.4.3 Topological defects in cholesteric liquid crystals

Topological defects in cholesteric liquid crystals are usually divided in $\lambda^{\pm m}$, $\tau^{\pm m}$ and $\chi^{\pm m}$ with m topological charge [30–32]. These are reported in Fig. 2.21: The λ, τ and χ are related to the three mutual perpendicular directions of the space. λ states for longitudinal because is associated to the local longitudinal direction of the molecules, χ instead is associated to the direction parallel or coincident to the cholesteric helix and τ states for transverse perpendicular to the first two.
The concept of "longitudinal" and "transverse" can be understood in terms of the Volterra process for creating them. If the cut of the material is along the molecular axis, the disclinations which result are the λ^+ or λ^- with sign $+$ or $-$ according if material has to be removed or added to arrive to the final configuration. If the cut is made in the direction perpendicular to the molecular axis, instead, τ^+ and τ^- occur [30, 31]. λ and τ are point defects instead χ is a line defect in particular a singular line parallel or coincident to the cholesteric axis.
As seen in Fig. 2.21 the λ defect is the only one among the three which is non singular because the director avoids the singularity escaping in the third direction; τ and χ, instead, are singular because in the cores, depicted with the red spots in Fig. 2.21, there is the singularity and the director is undefined. For this reason λ defects, which are coreless, possess lower energy than the correspondent τ.

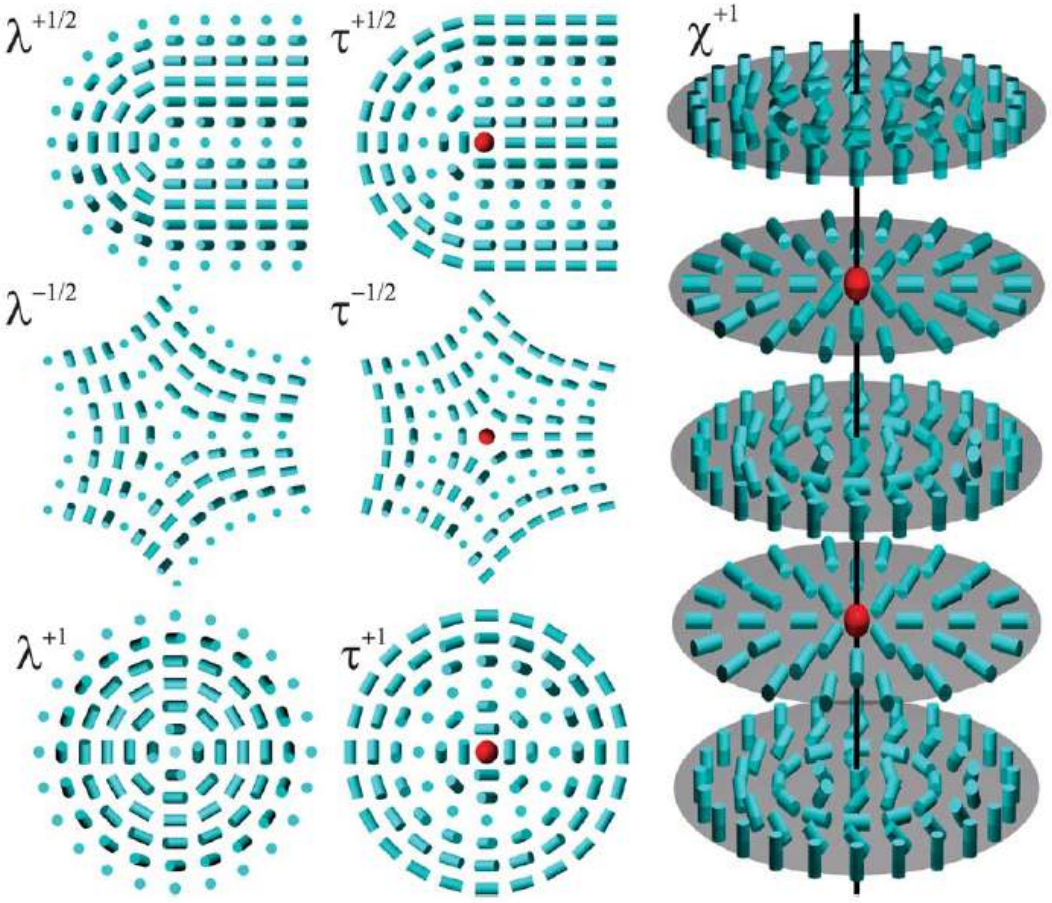

Figure 2.21: Representation of $\lambda^{\pm m}$, $\tau^{\pm m}$ and $\chi^{\pm m}$ defects. The director is depicted as blue cylinders while red spheres characterize regions with lower order parameters. The core of the χ disclination is drawn as a black line. [51].

2.4.4 Twist-disclinations

Twist disclinations occur when following the Burger circuit enclosing the defect, the director, **n**, is viewed continuosly rotating about a direction perpendicoular to the line. In general they rise when the twist constant K_2 is smaller than the splay and bend constants K_1 and K_3 which will be treated in the paragraph 2.5.2.
A schematic view of a twist disclination can be the following: attaching to each point of the circuit the director that meets it at that point and considering the ribbon formed by the circuit and those attached directors. This is the Möbius ribbon with charge $|s| = 1/2$ with total rotation $\pm\pi$ as shown in Fig 2.22 [32].

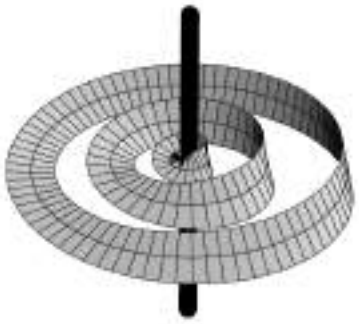

Figure 2.22: A schematic view of twist disclination of charge $s = 1/2$ [32].

The concept of twist disclination can again be understood in terms of the Volterra process. A piece of the liquid cystal material of cylindrical form is considered like in Fig. 2.23 associating the vertical axis with the z direction and the section of the cylinder as the xy plane and is cut.

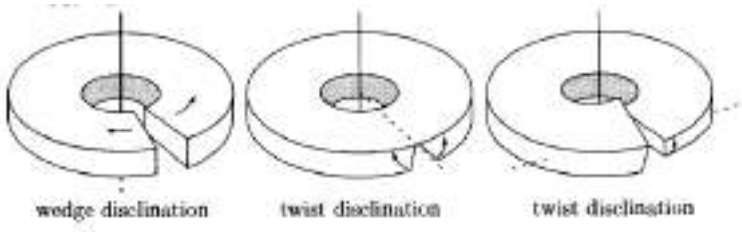

Figure 2.23: Volterra construction of wedge and twist disclinations [34].

If the two phases of the cut rotate or move in the xy plane a wedge disclination will be formed; in contrast if the the moviment of the two faces of the cut is no longer in the xy plane a twist disclination will be formed [30–32, 34].

2.5 Free energy of liquid crystals

The properties of liquid crystals can be described, following a Landau-de Gennes approach, building a free energy functional obtained with a series expansion of terms of the order parameter invariant respect to rotations with terms related to energetic costs of elastic deformations, anchoring conditions, presence of boundaries and external fields. In the following subsection the various terms of the free energy density are considered in details and are suitable to describe the phase-transition liquid crystal isotropic phase which is an example of first order transition.[6]

2.5.1 The Q bulk, the scalar field and the interface terms

The request in the construction of a free energy density is the invariance of the system for rotations. A scalar is surely a rotation invariant but the order parameter described before is a tensor so the simplest way to pass from a matrix to a scalar is considering the trace of the tensor. Remembering that **Q** tensor is traceless and expanding the free energy density in terms of powers of the traces of **Q** tensor the expression becomes [30, 32, 34]

$$f_{bulk} = \frac{A_0}{2}\left(1 - \frac{\gamma}{3}\right) Q_{\alpha\beta}Q_{\beta\alpha} - \frac{A_0\gamma}{3}Q_{\alpha\beta}Q_{\beta\gamma}Q_{\gamma\alpha} + \frac{A_0\gamma}{4}(Q_{\alpha\beta}Q_{\beta\alpha})^2 \tag{2.12}$$

which is the most general form of the free energy functional which describes the isotropic-nematic or the isotropic-cholesteric transition. A_0 is a pressure and the parameter γ corresponds to a temperature or a concentration.
In the bulk free energy term there are respectively the traces of $\mathbf{Q}^2$, $\mathbf{Q}^3$ and $\mathbf{Q}^4$ which are:

$$Tr\mathbf{Q}^2 = \frac{2}{3}q^2, Tr\mathbf{Q}^3 = \frac{2}{9}q^3, (Tr\mathbf{Q}^2)^2 = \frac{4}{9}q^4 \tag{2.13}$$

So the bulk free energy becomes

$$f_{bulk} = \frac{A_0}{3}\left(1 - \frac{\gamma}{3}\right) q^2 - \frac{2}{27}A_0\gamma q^3 + \frac{A_0\gamma}{9}q^4 \tag{2.14}$$

The first-order isotropic-nematic transition takes place at the critical temperature $\gamma = \gamma_c$. Now the critical values of γ_c and q_c can be calculated analitically assuming that the isotropic and nematic free energies are equal at the critical point and at the

[6] A *first-order transition* is a kind of phase transition in which the order parameter is a discontinuos function of the control parameter like the temperature while *second-order phase transitions* are characterized by a continuous order parameter. The classic examples of first order phase transitions are the transitions liquid/gas/solid while the ferromagnetic/paramagnetic transition is a second-order one.

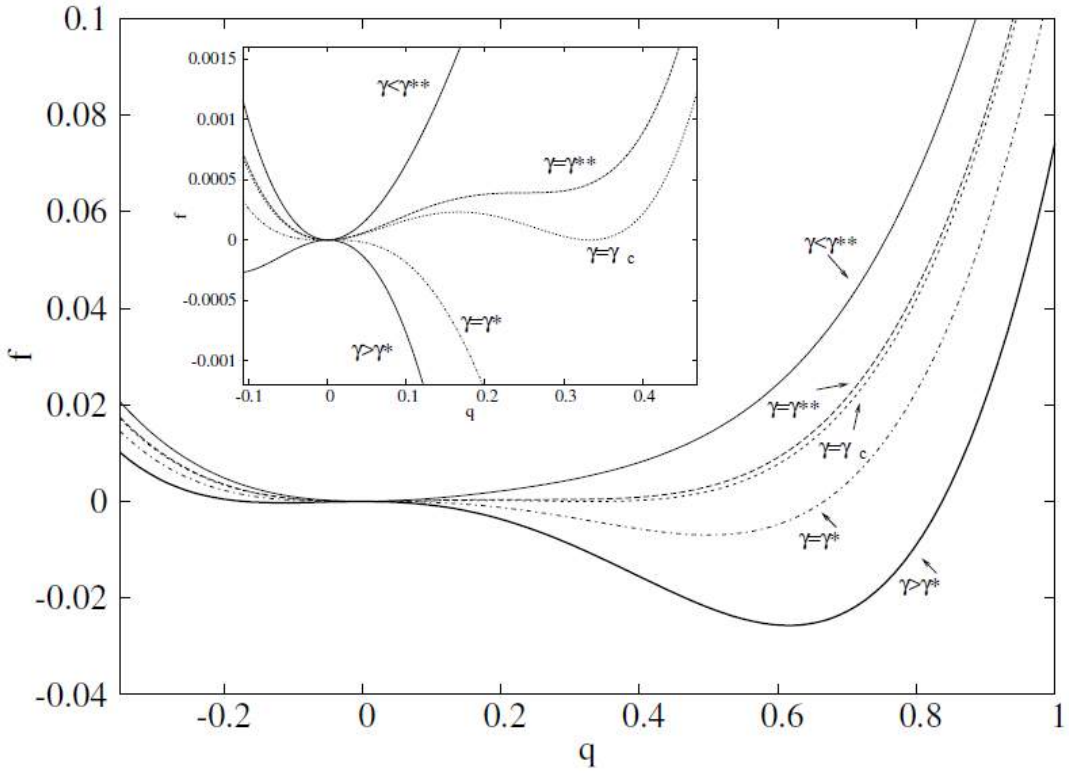

Figure 2.24: Free energy as function of the order parameter q for various temperatures. The values γ^* and γ^{**} represent respectively the metastability limits of isotropic and nematic phase. γ_c is the coexistence line of liquid crystal and isotropic phase with two minima of the density free energy one for $q = 0$ and $q = 1/3 = 0.33$ [43].

equilibrium the free energy is minimized so the free energy is minimal respect to q. These two conditions give rise to a system of two equations in varibales γ and q

$$\frac{A_0}{3}\left(1-\frac{\gamma}{3}\right)q^2 - \frac{2}{27}A_0\gamma q^3 + \frac{A_0\gamma}{9}q^4 = 0, \tag{2.15}$$

$$\frac{\partial f_{bulk}}{\partial q} = \frac{2A_0}{3}\left(1-\frac{\gamma}{3}\right)q - \frac{2}{9}A_0\gamma q^2 + \frac{4A_0\gamma}{9}q^3 = 0 \tag{2.16}$$

One trivial solution of the system is for $q = 0$ which identically satisfies the system but it must be avoided because it physically correponds to the isotropic phase. The non trivial solution of the system is for

$$q_c = \frac{1}{3} = 0.33, \tag{2.17}$$

$$\gamma_c = \frac{27}{10} = 2.7. \tag{2.18}$$

The value of γ for which the quadratic term, q^2, vanishes is $\gamma^* = 3$. This value physically represents the metastability limit of the isotropic phase; for values $\gamma > \gamma^*$ there is only the liquid crystal nematic phase as shown in Fig. 2.24. For $\gamma > \gamma^*$ the free energy density has only one minimum whereas for $\gamma = \gamma^*$ there is a stationary point in $q = 0$. When $\gamma < \gamma^*$ the isotropic phase starts to form which substitutes the nematic phase at $\gamma = \gamma^{**}$. This value $\gamma^{**} = 8/3$ corresponds to the metastability limit of the ordered phase. For values of $\gamma < \gamma^{**}$ the free-energy density has only one minimum at $q = 0$. The values of the order parameter correspondent to the two minima for $\gamma^{**} \leq \gamma \leq \gamma^*$ are:

$$q_{iso} = 0, \tag{2.19}$$

$$q_{nem} = \frac{1}{4} + \frac{3}{4}\left(1 - \frac{8}{3\gamma}\right)^{1/2}. \tag{2.20}$$

The value γ^{**} defined above mathematically corresponds to the annulment of the square root in. For $\gamma_c = 2.7 < \gamma < \gamma^* = 3$, q_{nem} is a global minimum of the free energy and for $\gamma > \gamma^*$ is the only minimum of the free-energy [30, 34].
As previously said, the liquid crystal system is characterized by the tensor order parameter $\mathbf{Q}$ with a corrispondent bulk term in the free energy density but if a system like a liquid crystal droplet in an isotropic phase is considered one must introduce a scalar field $\phi(\mathbf{r})$ which represents the liquid crystal fraction with a corrispondent bulk term similar to the Landau free-energy of fluid mixtures [8]:

$$f_\phi = \frac{a}{4}\phi^2(\phi - \phi_0)^2 \tag{2.21}$$

where ϕ_0 the value of the concentration field of the liquid crystal phase with also an energetic penalty related to the presence of the interface which separates the liquid crystal region from the isotropic host

$$f_i = \frac{\kappa_\phi}{2}(\partial_\alpha \phi)^2. \tag{2.22}$$

As said in the previously, the parameter γ can be a temperature or a concentration. In the particular case of lyotropic liquid crystal γ must be related to the scalar concentartion field in a certain manner. The analitical expression which relates γ with ϕ is generally assumed linear following [6, 8].

$$\gamma = \gamma_0 + \gamma_s \phi. \tag{2.23}$$

where γ_0 and γ_s are constants controlling the coexistence region.

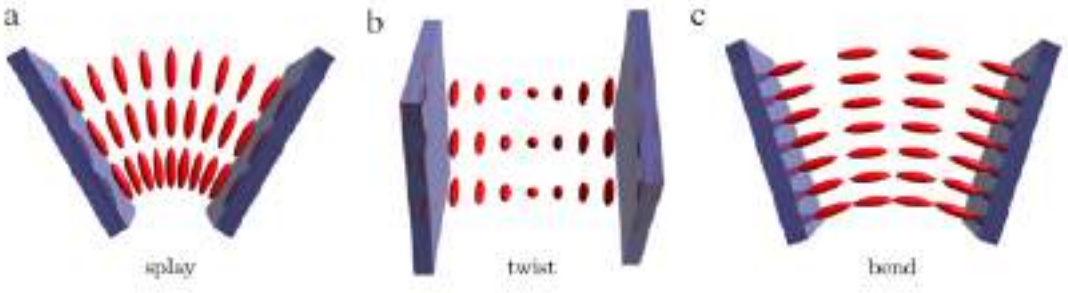

Figure 2.25: Representation of the three elastic distortions in liquid crystals [52]. The director is depicted with red rods.

2.5.2 Elastic distortions in liquid crystals

The presence of surfaces in the system originates elastic distortions in the bulk known as *splay*, *twist* and *bend*, portayed in Fig. 2.25, so they must be represented by and energetic penalty in the free-energy system [5, 30, 31]. This free energy term is built assuming that the variations of $\mathbf{n}$ are small on molecular scales i.e. $a\nabla\mathbf{n} << 1$ where a represents the tipical dimension of a molecule.
The free energy term must be even in $\mathbf{n}$, as long as states with $\mathbf{n}$ and $-\mathbf{n}$ are energetically equivalent, and must contain power series of $\nabla\mathbf{n}$. Terms linear in $\nabla\mathbf{n}$ are absent. The only terms that are invariant for rotations are $\nabla \cdot \mathbf{n}$ and $\mathbf{n} \cdot \nabla \times \mathbf{n}$; the first is ruled out because it is not even in $\mathbf{n}$ and the second one too because it changes sign for parity transformations ($x \to -x$, $y \to -y$, $z \to -z$). Therefore summing all these aspects the final expression of the free energy density for elastic distortions is:

$$f_{EL} = \frac{1}{2}K_1(\nabla \cdot \mathbf{n})^2 + \frac{1}{2}K_2(\mathbf{n} \cdot \nabla \times \mathbf{n})^2 + \frac{1}{2}K_3(\mathbf{n} \times \nabla \times \mathbf{n})^2 \tag{2.24}$$

where K_1, K_2 and K_3 are respectively *splay*, *twist* and *bend* constants. Dimensionally they are energies for unitary length or forces (energy/cm or dynes) with tipical values of the same magnitude.
For PAA (p-azoxyanisole), for example, at temperature of $120°C$ the elastic constants are:

$$K_1 = 0.7 \times 10^{-6} dyn, \tag{2.25}$$

$$K_2 = 0.43 \times 10^{-6} dyn \tag{2.26}$$

and

$$K_3 = 1.7 \times 10^{-6} dyn \tag{2.27}$$

It must be emphasized that the bend constant K_3 is greater than the two others.[7]

[7] In the cgs system unit the dyn is the unit of the force. Respect to SI unit $1\ dyn = 10^{-5}N$.

These elastic constants decrease with the increase of the temperature but their ratio is almost independent by the temperature [30]. As long as the three elastic constants are of the same magnitude order, in simulations and other studies it is commonly used the one constant approximation in which all the elastic constants are set equal each other

$$K_1 = K_2 = K_3 = K \tag{2.28}$$

In terms of gradients of the tensor order parameter **Q** the expression mostly used is

$$f_{EL} = \frac{1}{2}K(\partial_\alpha Q_{\beta\gamma})^2 \tag{2.29}$$

This treatment here is particularly suitable with nematic liquid crystals. However cholesteric liquid crystals are locally nematic but globally different with a director which describes an helix in the space so this is traduced in a supplementary term in the free energy density

$$f_{EL} = \frac{1}{2}K_1(\nabla \cdot \mathbf{n})^2 + \frac{1}{2}K_2(\mathbf{n} \cdot \nabla \times \mathbf{n} + q_0)^2 + \frac{1}{2}K_3(\mathbf{n} \times \nabla \times \mathbf{n})^2 \tag{2.30}$$

where $q_0 = 2\pi/p_0$ and p_0 is the pitch of the helix. The correspondent expression in terms of gradients of the **Q** tensor is [7, 53]

$$f_{EL} = \frac{1}{2}K[(\partial_\alpha Q_{\alpha\beta})^2 + (\varepsilon_{\alpha\xi\delta}\partial_\xi Q_{\delta\beta} + 2q_0 Q_{\alpha\beta})^2] \tag{2.31}$$

where $\varepsilon_{\alpha\beta\gamma}$ is the completely antisymmetric Levi-Civita tensor. It must be noted that a nematic can be considered as the limit case of cholesteric with infinite pitch so for nematics the term $q_0 = 2\pi/p_0 = 0$.

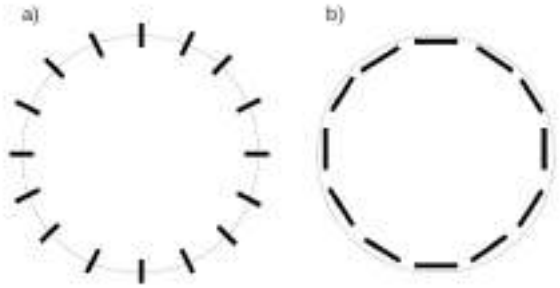

Figure 2.26: Schematic representation of homeotropic (perpendicular) (a) and tangential (b) anchoring of the director (black bars) on the surface of a circular droplet.

2.5.3 The anchoring energy

In the case of the study of a liquid crystal droplet, a term which represents the energetic cost to anchor the director to the interface of the droplet must be considered with the following expression which couples the **Q** tensor to the interface $\nabla\phi$ [6, 8]:

$$f_a = W(\partial_\alpha\phi)Q_{\alpha\beta}(\partial_\beta\phi) \tag{2.32}$$

with constant W which represents the strength of the anchoring of the director to the interface of the droplet with dimensions of an energy per unit area. The sign of W, also, suggests the type of anchoring which can be planar or tangential, if $W > 0$, or homeotropic or perpendicular, if $W < 0$. Fig. 2.26 shows a schematic representation of the director in the hometropic and tangential cases. The system considered can also present boundaries represented by rigid walls the director could be anchored to, so another anchoring term must be considered of this type:

$$f_{aw} = \frac{W_0}{2}(Q_{\alpha\beta} - Q^0_{\alpha\beta})^2 \tag{2.33}$$

where the physical meaning of W_0 is similar to the previous constant W and $Q^0_{\alpha\beta} = q^w_0(n^0_\alpha n^0_\beta - \frac{1}{3}\delta_{\alpha\beta})$ which is the **Q** tensor to the wall with q^w_0 the magnitude of the surface order and n^0_α the director to the boundary. In this case the anchoring is said to be strong if $W_0 >> 1$.
In the study of a liquid crystal droplet in an isotropic host for example, following [6], one could define an adimensional parameter to quantify how much strong or weak is the anchoring of the director to the interface of the droplet. The expression is

$$WR/K \tag{2.34}$$

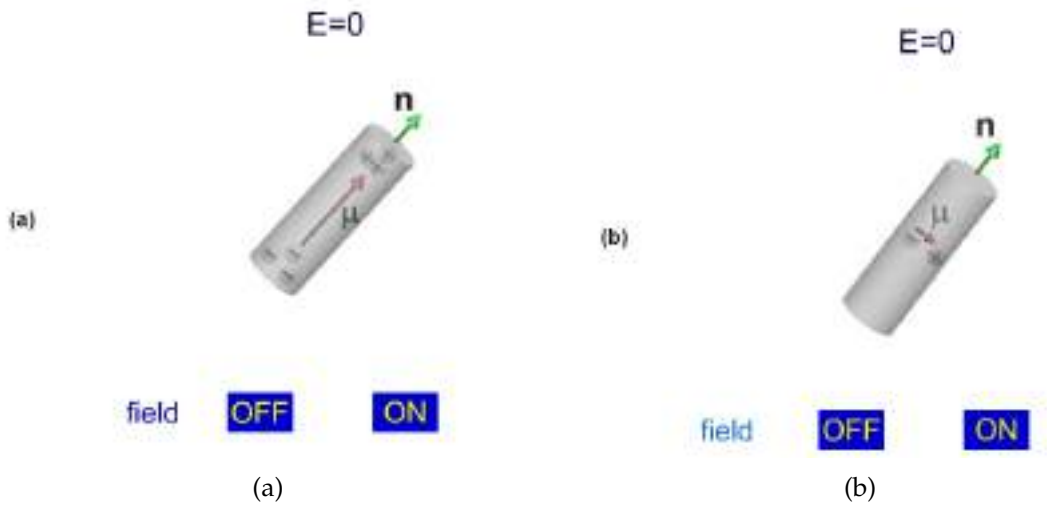

(a) (b)

Figure 2.27: A molecule of liquid crystal with positive (a) and negative dielectric constant (b) [45]. μ indicates the electic dipole.

where W is the anchoring strengt defined bove, R is the radius of the droplet and K is the elastic constant for the bulk elastic deformations. If $WR/K < 1$ the anchoring is defines weak whereas if $WR/K >> 1$ the anchoring is said to be strong. A limiting case is when the adimensional quantity $WR/K = 0$ which correspond to the physical situation in which the director is completely decoupled from the interface [6, 50].

2.5.4 Interaction with an electric field

Another important energetic term comes from the presence of external magnetic or electric fields the liquid crystal could interact with [7, 30, 53]. The cause of the interaction, for example with an electric field, is due to the fact that liquid crystal molecules are electric dipoles and they answer to the presence of an eventual electric field. The contribution to the free energy is:

$$f_E = -\frac{\varepsilon}{12\pi} E_\alpha Q_{\alpha\beta} E_\beta \tag{2.35}$$

where E is the electric field and ε is the dielectric constant calculated as $\varepsilon = \varepsilon_{||} - \varepsilon_\perp$ where the last two terms in the difference are the dielectric constants in the direction parallel and perpendicular to the field respectively. The sign of ε suggests the answer of the director to the applied electric field. If $\varepsilon > 0$, the director orientates parallel to the field whereas if, $\varepsilon < 0$, the director orientates perpendicular to the

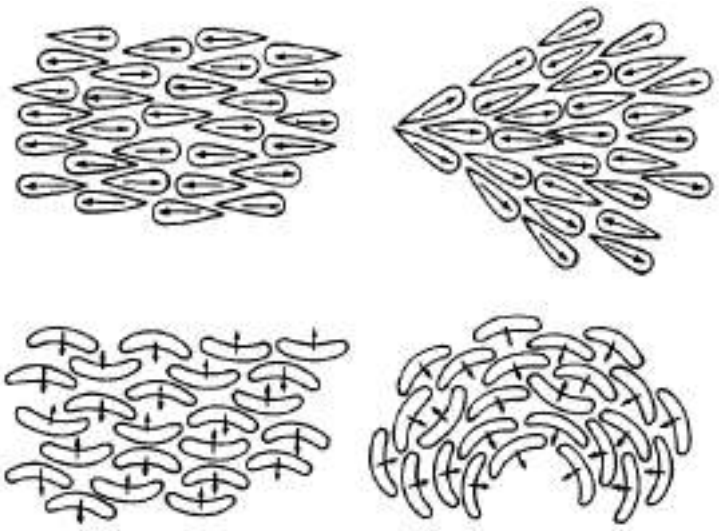

Figure 2.28: Pear and banana shaped molecules in which flexoelectric effect occurs [31].

field [30, 31]. The reason of this behaviour can be found exploring the microscopic details of the liquid crystals molecules. They possess, in fact, an electric dipole, μ, along or across the molecular axis as shown in Fig. 2.27. If this electric dipole is parallel or nearly parallel to the molecular axis $\varepsilon_{\parallel} > \varepsilon_{\perp}$, $\varepsilon = \varepsilon_{\parallel} - \varepsilon_{\perp} > 0$ and thus the director aligns parallel to the field as long as the effect of an electric field is orienting the electric dipole. If instead the electric dipole is perpendicular to the axis it is $\varepsilon_{\parallel} < \varepsilon_{\perp}$, $\varepsilon = \varepsilon_{\parallel} - \varepsilon_{\perp} < 0$ and the director aligns perpendicular to the field [45].

2.5.5 Flexoelectricity in liquid crystals

Flexoelectricity of liquid crystals is a phenomenon in which an elastic deformation such as splay or bend can polarize the material and conversely an electric field can induce a deformation. This situation, which resembles the piezoelectric effect in solids, occurs for liquid crystal molecules which have a polar shape, for example a banana or a pear, as in Fig. 2.28, in addition to the permanent electric dipole [30, 31].
To take into account the flexoelectricity in liquid crystals one must add to the free energy density a flexoelectric term which couples the **Q** tensor to the external field **E** with the following expression [7, 53, 54]:

$$f_{fl} = \varepsilon^{b}_{fl} Q_{\alpha\beta}(E_{\alpha}\partial_{\gamma} - E_{\gamma}\partial_{\alpha})Q_{\beta\gamma} \tag{2.36}$$

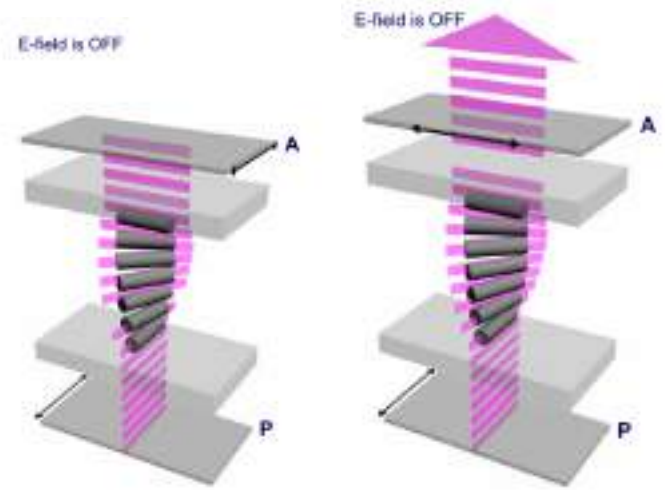

(a) (b)

Figure 2.29: Twisted nematic display device in normally black mode (a) and in normally white mode (b). Black arrows show transmission axes of polarizers; violet stripes represent polarized light [45].

where $\varepsilon_{fl}^{b} > 0$ is the bulk flexoelectric constant. In this expression each term of the flexoelectric coupling is linear in E_α and quadratic in $\mathbf{Q}$. This term in the free energy density is important when one wants to take into account the flexoelectricity in liquid crystals. In most applications this term is absent and it will not be considered in this thesis.

2.6 The twisted nematic cell

The development of the principles of operation of the twisted nematic (TN) liquid crystal display device made a crucial impact on the development of the liquid crystal displays technology of the present days. The TN device, Fig. 2.29-(a)-(b), consists of the twisted nematic liquid crystal confined between two glass substrates with homogeneous planar orientation: the orientation of the director $\mathbf{n}$ on one substrate is rotated by 90° with respect to $\mathbf{n}$ on another substrate. Such a design induces 90° twist of the nematic liquid crystal. The cell with twisted nematic liquid crystal is placed between two polarizers: the polarizer P on the input end and the analyzer A on the output end of the TN device. The director $\mathbf{n}$ on the input end is parallel to the transmission axis of the polarizer. Two operation modes of the TN device are possible depending on the orientation of the analyzer transmission axis. If the analyzer is parallel to the polarizer it is called a *normally black* (NB) mode Fig.

2.29-(a). If the analyzer is perpendicular to the polarizer it is called a *normally white* (NW) mode, Fig. 2.29-(b).

- *TN display device in normally black mode*
  When no voltage is applied, the polarized light after polarizer enters the TN cell and, following the twisted orientation of the liquid crystal molecules, change its polarization by 90° Fig. 2.29-(a). On the TN cell output the light polarization is perpendicular to the analyzer transmission axis; therefore, the light is blocked on the device exit by the analyzer. When voltage is applied, the liquid crystal molecules align along the electric field and the polarization of the light passing through the TN cell does not change. Thus, light passes through the device because its polarization is parallel to the analyzer transmission axis.

- *TN display device in normally white mode*
  When no voltage is applied to the TN device, the polarized light after the polarizer enters the TN cell and, following the twisted orientation of the LC molecules, change its polarization by 90° Fig. 2.29-(b). On the exit from the TN cell, the light polarization is parallel to the analyzer transmission axis, therefore, the light passes through the system. When voltage is applied, the LC molecules align along the electric field and the polarization of the light passing through the TN cell does not change and is perpendicular to the analyzer transmission axis. Thus, light is blocked by the analyzer on the device output.

2.7 Summary

In this Chapter an introductory description of the physics of liquid crystals and the theoretical model to describe them were presented.
At first the most important mesophases were presented, the most important of which is the cholesteric one which is the theme of the results collected in Chapter 4. Liquid crystals in general are characterized by a tensorial order parameter which is a powerful tool to describe them because it takes into account the orientation of the director and also the strenght of alignment. For this reason with the **Q** tensor formalism it is possibile to detect the dynamics of topological defects which can arise in the systems.
The type of description which is widely used and was presented in this thesis and was also used in the work "*Switching dynamics in cholesteric liquid crystal emulsions*", whose results will be described in detail in Chapter 4, consists in building a

Landau-de Gennes free energy functional in terms of the power series of the trace of the **Q** tensor parameter with the addition of other terms which take into account various aspects such as the interfaces, the elastic distortions, the presence of boundaries and external fields.
Chapter 3 is dedicated to the introduction of the Lattice Boltzmann method for both fluid mixtures and liquid crystals instead Chaper 4 collects the main results related to the study of a cholesteric liquid crystal droplet under electric fields.

Chapter 3

Lattice Boltzmann Method

In this Chapter the Lattice Boltzmann method, or simply the LBM method, used in computer simulations is presented [3, 55]. Lattice Boltzmann is a modern and powerful tool to study fluid and soft matter systems for its attitude to allow simulations of systems with different geometries, to solve correctly the hydrodynamics of the velocity field, for its portability and its possibility to be parallelized in order to study very large systems.
LBM method, through the years, has been developed in many contests: for multiphase fluids [55–59], domain growth in separation process in binary mixtures [60], porous media [61, 62], thermal fluids [63, 64], magnetohydrodynamics [65–67], quantum fluids [68–72], relativistic hydrodynamics [72–76], holographic fluids [77–81], and liquid crystals [48] as examples. Through the years hybrid versions of this method have been developed and widely used which solve hydrodynamics in the standard way and the convection-diffusion equations with finite-different schemes; this variant of the LBM method allows a significative saving in computational memory [14, 82]. This variant has also been used in my research for the results collected in this thesis. A very interesting recent paper which summarizes the state of the art and presents the future challenges of LBM method is [83].
The Chapter is divided in two parts: after a brief historical backgroud to clarify the steps which carried the rise of this metod, in the first one the general aspects of the hybrid Lattice Boltzmann method are presented for the study of fluid mixtures and in the second one, the corrispondent method for the study of liquid crystals is described.

3.1 Brief historical background

The Lattice Boltzmann method is an algorithm used to solve the Navier-Stokes equation and is a mesoscopic tecnique that avoids the analysis of microscopic details of the system. The main advantages of this tecnique are the portability of the code, the possibility to be parallelized in order to study very large systems and the possibility to study complex geometries.
Historically the LBM method is an upgrade of the *Lattice-Gas Automaton* [84] in which the Navier-Stokes equation could be obtained, in the continuum limit, exploiting the mass and momentum conservation during the collision steps of the model dynamics. This method consists of particles that move on lattice sites, indicated with index i, and collide when two or more of them are on the same site. There is a boolean field $n(\mathbf{r}, t)$ that assumes two different values associated to presence of absence of the particle in a site of position $\mathbf{r}$ at time t. The equation that governs the evolution of the particles is

$$n_i(\mathbf{r} + \mathbf{e}_i, t + 1) - n_i(\mathbf{r}, t) = \Omega_i(n(\mathbf{r}, t)) \tag{3.1}$$

where $\Omega(n(\mathbf{r}, t))$ is the collisional operator and vectors $\mathbf{e}_i$ are lattice velocities. The evolution happens in two steps: the propagation in which each particle moves towards an adiacent site in the direction of lattice velocity $\mathbf{e}_i$ and the collision in which two or more particles in the same site scatter changing velocities and directions according to certain rules. The main drawback of this method was the excessive noise of statistical fluctuations associated to the boolean variables later changed with average values [85].
Indeed, successively Higuera and others [86, 87] introduced a new model in which distribution functions, f_i, were defined and in which the collision operator is linearized around an equilibrium value f_i^{eq} written as $\Omega_i = H_{ij}(f_j - f_j^{eq})$ where H_{ij} is the scattering matrix that defines the type of collision and chosen to conserve mass and momentum. A simplified version is the one in which the collision operator is written as $\Omega_i(\mathbf{r}, t) = -(f_i - f_i^{eq})/\tau$ [87] where τ is the relaxation time for the distribution functions f_i to relax towards the equilibrium f_i^{eq} always chosen to conserve mass and momentum [88, 89]. The models of this kind have been introduced to study for example immiscible binary fluids [90] and miscible ones [91].
A generalization and upgrade of this approach consists in introducing a free energy functional which encodes the thermodynamics of the system so that the equilibrium state can be identified as the minimum of this energy [92–96]. The main advantage of these, so called free-energy based methods, is the fact that one can calculate analitically the equilibrium state of the system and keeping under control the system equilibrium features.

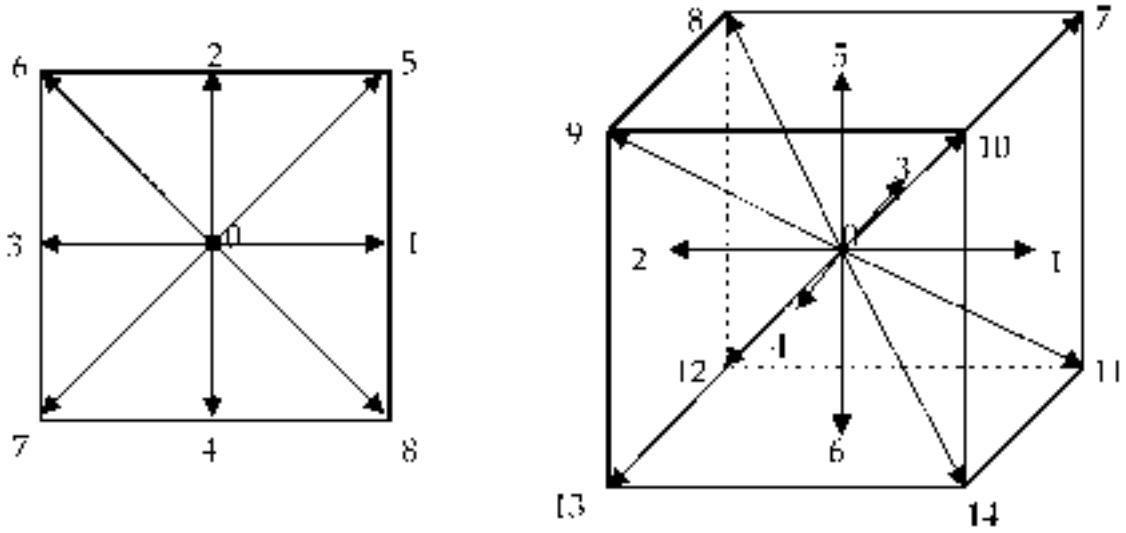

Figure 3.1: Typical lattices mostly used in Lattice Boltzmann simulations: $D2Q9$ (left) and $D3Q15$ cells (right). In the $D2Q9$ 0 site is the center of the cell, $1,2,3,4$ sites are the first neighbours and $5,6,7,8$ sites the second neighbours. In the $D3Q15$ 0 site is the center of the cell, $1,2,3,4,5,6$ sites are the first neighbours and $7,8,9,10,11,12,13,14$ sites the second neighbours.

3.2 Lattice Boltzmann method for a single fluid

The basic idea of the LBM method, for the simple case of a single fluid, is discretizing the physical space with lattices with convenient geometry. Fig. 3.1 shows two typical lattices: the lattice $D2Q9$, in the bidimensional case, in which the square elementary cell has nine sites first and second neighbours and the lattice $D3Q15$, in the tridimensional space, with cubic elementary cell with fifteen sites first and second neighbours. A set of distribution functions $f_i(\mathbf{r}, t)$ defined on sites of position $\mathbf{r}$ and t that move along the directions of a lattice fixed by the velocity vectors is then introduced. The sum of the distribution functions along the directions i represents the density of fluids whereas the first order momentum is related to the velocity of the fluid

$$n = \sum_i f_i, \qquad n\mathbf{u} = \sum_i f_i \mathbf{e}_i. \tag{3.2}$$

These distribution functions evolve with the lattice Boltzmann equation

$$f_i(\mathbf{r} + \mathbf{e}_i \Delta t, t + \Delta t) - f_i(\mathbf{r}, t) = -\frac{(f_i - f_i^{eq})}{\tau} \tag{3.3}$$

where Δt is the time step of the simulation and the right hand side of the equation is the collision operator in the BGK approximation [88]. The $\mathbf{e}_i$ (with $i = 0, 1, .., 8$) denote the nine velocity vectors in the $D2Q9$ lattice connecting first and second neighbours:

$$\mathbf{e}_i = \begin{cases} (0,0) & i = 0 \\ (\pm e, 0), (0, \pm e) & i = 1,2,3,4 \\ (\pm e, \pm e) & i = 5,6,7,8. \end{cases} \tag{3.4}$$

They have modulus $|\mathbf{e}_i| = \frac{\Delta x}{\Delta t} = e$ for $i = 1,2,3,4$ and $|\mathbf{e}_i| = \sqrt{2}e$ for $i = 5,6,7,8$ where Δx and Δt are the spatial and time steps of the lattice, respectively. The null vector velocity in the center of the cell e_0 is also considered.
f_i^{eq} are the equilibrium distribution functions chosen to guarantee mass and momentum conservation laws

$$\sum_i (f_i^{eq} - f_i) = 0 \Rightarrow \sum_i f_i^{eq} = n, \tag{3.5}$$

$$\sum_i (f_i^{eq} - f_i) e_{i\alpha} = 0 \Rightarrow \sum_i f_i^{eq} e_{i\alpha} = n u_\alpha. \tag{3.6}$$

τ, in (3.3), is the time for the f_i to relax towards f_i^{eq}. A suitable choice for the expression of these f_i^{eq} consists in expanding them to the second order in the velocity

$$f_i^{eq} = A^\sigma + B^\sigma e_{i\alpha} u_\alpha + C^\sigma u^2 + D^\sigma (e_{i\alpha} u_\alpha)^2 \tag{3.7}$$

in which the index σ denotes, for the case $D2Q9$ here reported, the coefficients correspondent to the velocity moduli 0, e and $\sqrt{2}e$ in particular

$$\sigma = \begin{cases} 0 & \text{if } i = 0 \\ 1 & \text{if } i = 1,2,3,4 \text{ (first neighbours)} \\ 2 & \text{if } i = 5,6,7,8 \text{ (second neighbours)} \end{cases}$$

The calculus of the coefficients is now neglected but the general idea is using the (3.7) and imposing the relations of (3.5)-(3.6). After some algebra, the complete list of coefficients will be [3]

$$A^0 = n - 20A^2; \qquad A^1 = 4A^2; \qquad A^2 = \frac{n}{36}, \tag{3.8}$$

$$B^0 = 0; \qquad B^1 = 4B^2; \qquad B^2 = \frac{n}{12e^2}, \tag{3.9}$$

$$C^0 = -\frac{2n}{3e^2}; \qquad C^1 = 4C^2; \qquad C^2 = -\frac{n}{24e^2}, \tag{3.10}$$

$$D^0 = 0; \qquad D^1 = 4D^2; \qquad D^2 = \frac{n}{8e^4}. \tag{3.11}$$

3.3 Hybrid Lattice Boltzmann for fluid mixtures

In this paragraph the hybrid Lattice Boltzmann method for fluid mixtures is discussed considering the lattice $D2Q9$. The distribution functions $f_i(\mathbf{r}, t)$ are always related to the physical quantities the total density and the momentum in a different way

$$n = \sum_i f_i, \qquad n\mathbf{u} = \sum_i f_i \mathbf{e}_i + \frac{1}{2}\mathbf{F}\Delta t \tag{3.12}$$

where $\mathbf{u}$ is the velocity field and $\mathbf{F}$ is the density force which acts on the fluid and contains as well as of any external force information of the interactions among the component of the mixtures [14, 97]. The distribution functions evolve according the lattice Boltzmann equation, previously seen, but now modified adding a forcing term F_i in the right hand side of the equation [14]

$$f_i(\mathbf{r} + \mathbf{e}_i\Delta t, t + \Delta t) - f_i(\mathbf{r}, t) = -\frac{(f_i - f_i^{eq})}{\tau} + \Delta t F_i(\mathbf{r}, t) \tag{3.13}$$

to be properly determined. The evolution of the distribution functions proceeds in two different steps. In the first phase, the collision, the distribution functions collide in the same lattice sites and evolve as

$$f_i^c(\mathbf{r}, t) = f_i(\mathbf{r}, t) - \frac{\Delta t}{\tau}(f_i(\mathbf{r}, t) - f_i^{eq}(\mathbf{r}, t)) + \Delta t F_i(\mathbf{r}, t), \tag{3.14}$$

in the second moment they propagate to the neighbour sites as

$$f_i(\mathbf{r} + \mathbf{e}_i\Delta t, t + \Delta t) = f_i^c(\mathbf{r}, t) \tag{3.15}$$

The choice of the equilibrium distribution functions is made in order to ensure that the density and momentum conservation laws are verified. This requires to fix the first two moments of the equilibrium distribution functions

$$\sum_i (f_i^{eq} - f_i) = 0 \Rightarrow \sum_i f_i^{eq} = n, \tag{3.16}$$

$$\sum_i (f_i^{eq} - f_i) e_{i\alpha} = 0 \Rightarrow \sum_i f_i^{eq} e_{i\alpha} = n u_\alpha. \tag{3.17}$$

The second order moment is chosen so that the hydrodynamic equations are correctly obtained in the continuum limit

$$\sum_i f_i^{eq} e_{i\alpha} e_{i\beta} = n c_s^2 \delta_{\alpha\beta} + n u_\alpha u_\beta \tag{3.18}$$

where $c_s = e/\sqrt{3}$ is the sound speed in this model.
The explicit expression of the equilibrium distribution functions in the $D2Q9$ model is obtanied from a second order expansion in the velocity of the Maxwell-Boltzmann distribution

$$f_i^{eq} = \omega_i n \left[1 + \frac{\mathbf{e}_i \cdot \mathbf{u}}{c_s^2} + \frac{\mathbf{uu} : (\mathbf{e}_i\mathbf{e}_i - c_s^2\mathbf{I})}{2c_s^4}\right] \tag{3.19}$$

where $\mathbf{I}$ is the unit matrix and ω_i are weights with values $\omega_0 = 4/9$, $\omega_i = 1/9$ for $i = 1, 2, 3, 4$, and $\omega_i = 1/36$ for $i = 5, 6, 7, 8$.
The force term is written as power series of the lattice velocity to the second order [98]

$$F_i = \omega_i \left[A + \frac{\mathbf{B} \cdot \mathbf{e}_i}{c_s^2} + \frac{\mathbf{C} : (\mathbf{e}_i\mathbf{e}_i - c_s^2\mathbf{I})}{2c_s^4}\right] \tag{3.20}$$

where $\mathbf{A}$, $\mathbf{B}$ and $\mathbf{C}$ are functions of $\mathbf{F}$ to be determined requiring that the hydrodynamic equations are correctly recovered in the continuum limit.
By performing the Chapman-Enskog expansion (Appendix A for details), the continuity and Navier-Stokes equations are obtained. The density force has to be

$$F_\beta = \partial_\alpha(nc_s^2\delta_{\alpha\beta} - P_{\alpha\beta}) \tag{3.21}$$

where nc_s^2 is the ideal gas pressure and $P_{\alpha\beta}$ is the pressure tensor which appears in the right hand side of the Navier-Stokes equation and whose analytical expression is [3, 14]

$$P_{\alpha\beta} = \left[\phi\frac{\delta\mathcal{F}}{\delta\phi} + n\frac{\delta\mathcal{F}}{\delta n} - f(\phi)\right]\delta_{\alpha\beta} + D_{\alpha\beta}. \tag{3.22}$$

where $\mathcal{F}$ is the free energy functional which encodes the thermodynamics of the system, f is the free energy density such that $\mathcal{F} = \int f dV$ and $D_{\alpha\beta}$ is a symmetric tensor inserted in order to ensute the condtion of mechanical equilibrium $\partial_\alpha P_{\alpha\beta} = 0$ [3, 14].The expressions of the coefficents of the force F_i are

$$A = 0, \qquad \mathbf{B} = \left(1 - \frac{\Delta t}{2\tau}\right)\mathbf{F}, \qquad \mathbf{C} = \left(1 - \frac{\Delta t}{2\tau}\right)(\mathbf{uF} + \mathbf{Fu}) \tag{3.23}$$

which appropriately inserted in (3.20) give

$$F_i = \left(1 - \frac{\Delta t}{2\tau}\right)\omega_i \left[\frac{\mathbf{e_i} - \mathbf{u}}{c_s^2} + \frac{\mathbf{e}_i \cdot \mathbf{u}}{c_s^4}\mathbf{e}_i\right] \cdot \mathbf{F}. \tag{3.24}$$

3.4 Up-wind scheme for convection-diffusion equation in 2D lattice

Particular attention must be spent on the numerical implementation of the convection-diffusion equations like the one presented in Chapter 1

$$\partial_t \phi + \nabla \cdot (\phi \mathbf{u}) = D\nabla^2 \mu_\phi. \tag{3.25}$$

In this paragraph the most important aspects are considered following [99]. Let $g(x_i, y_i, t^n) = g_{ij}^n$ be a generic function discretized at time $t^n = n\Delta t$ with $n = 1, 2, 3, ...$, on the node (x_i, y_j) of a $2D$ lattice where $i = 1, 2, .., L_x$ and $j = 1, 2, ..., L_y$ with L_x and L_y the dimensions of the lattice. Here Δt and Δx are the same space and time steps of the LBM. The update of ϕ from time t^n to time t^{n+1} goes in two steps in which the convective part is first integrated and then the diffusive one; this approach allows a better numerical stability of the simulation. The convective part is integrated with the Euler method [100]

$$\phi^{n+1/2} = \phi^n - \Delta t(\phi^n \partial_\alpha u_\alpha^n + u_\alpha^n \partial_\alpha \phi^n) \tag{3.26}$$

where the velocity $\mathbf{u}$ comes from the Navier-Stokes equation. The derivatives are discretized as

$$\partial_x u_x|_{ij}^n = \frac{u_{x,(i+1)j}^n - u_{x,(i-1)j}^n}{2\Delta x}, \tag{3.27}$$

$$\partial_x \phi|_{ij}^n = \frac{\phi_{ij}^n - \phi_{(i-1)j}^n}{\Delta x}, u_{x,ij}^n > 0, \tag{3.28}$$

$$\partial_x \phi|_{ij}^n = \frac{\phi_{(i+1)j}^n - \phi_{ij}^n}{\Delta x}, u_{x,ij}^n < 0, \tag{3.29}$$

and the same procedure applies for the derivative along the y direction. The next step consists adding the diffusive part

$$\phi^{n+1} = \phi^{n+1/2} + \Delta t D\nabla^2(\mu^{n+1/2}). \tag{3.30}$$

3.4.1 Boundary conditions for fluid mixtures

In some systems rigid walls can be present and for this reason, the definition of the distribution functions along the walls and in the angles must be wise and careful [101–103]. In this section the implementation of the bottom wall, the left wall, and the angle within is considered.
In the case of the bottom wall after the propagation the distribution functions f_0, f_1, f_3, f_4, f_7, f_8 are known instead f_2, f_5 and f_6 are unknown. Requiring the conservation mass of the fluid and the velocity along the wall to be zero, it is

$$f_2(t) + f_5(t) + f_6(t) = n - [f_0(t) + f_1(t) + f_3(t) + f_4(t) + f_7(t) + f_8(t)] \tag{3.31}$$

$$f_1(t) - f_3(t) + f_5(t) - f_6(t) - f_7(t) + f_8(t) = -\frac{1}{2}\Delta t F_x \tag{3.32}$$

$$f_2(t) - f_4(t) + f_5(t) + f_6(t) - f_7(t) - f_8(t) = -\frac{1}{2}\Delta t F_y \tag{3.33}$$

Adopting the bounce-back-rule, $f_2(t) = f_4(t)$ for the distribution functions normal to the boundary while mass conservation requires that

$$\begin{aligned} \hat{n}(t-\Delta t) = f_0(t-\Delta t) + f_4(t-\Delta t) + f_7(t-\Delta t) \\ + f_8(t-\Delta t) + f_1(t) + f_3(t) + f_4(t) + f_7(t) + f_8(t) \end{aligned} \tag{3.34}$$

where the quantities at time $t - \Delta t$ are computed at the previous time step and have not been propagated over the lattice. Requiring $n = \hat{n}$ and introducing $f_0(t)$ as independent variable, solving (3.31)-(3.33), one obtains a set of solutions for the unknown distribution functions

$$f_0(\mathbf{r}, t) = \hat{n} - [f_1(\mathbf{r}, t) + f_3(\mathbf{r}, t)] - 2[f_4(\mathbf{r}, t) + f_7(\mathbf{r}, t) + f_8(\mathbf{r}, t)] + \frac{\Delta t}{2} F_y, \tag{3.35}$$

$$f_5(\mathbf{r}, t) = f_7(\mathbf{r}, t) - \frac{1}{2}[f_1(\mathbf{r}, t) - f_3(\mathbf{r}, t)] - \frac{\Delta t}{4}(F_x + F_y), \tag{3.36}$$

$$f_6(\mathbf{r}, t) = f_8(\mathbf{r}, t) + \frac{1}{2}[f_1(\mathbf{r}, t) - f_3(\mathbf{r}, t)] + \frac{\Delta t}{4}(F_x - F_y), \tag{3.37}$$

$$f_2(\mathbf{r}, t) = f_4(\mathbf{r}, t). \tag{3.38}$$

The implementation of the distribution functions at the left vertical wall is similar to the previous one. In this case the functions f_1, f_5 and f_8 are unknown. Adopting here the bounce-back rule $f_1 = f_3$ it is

$$\begin{aligned} \hat{n}(t-\Delta t) = f_0(t-\Delta t) + f_3(t-\Delta t) + f_6(t-\Delta t) \\ + f_7(t-\Delta t) + f_2(t) + f_3(t) + f_4(t) + f_6(t) + f_7(t), \end{aligned} \tag{3.39}$$

$$f_1(\mathbf{r}, t) = f_3(\mathbf{r}, t), \tag{3.40}$$

$$f_5(\mathbf{r},t) = f_7(\mathbf{r},t) + \frac{1}{2}[f_4(\mathbf{r},t) - f_2(\mathbf{r},t)] - \frac{\Delta t}{4}(F_x + F_y), \tag{3.41}$$

$$f_8(\mathbf{r},t) = f_6(\mathbf{r},t) - \frac{1}{2}[f_4(\mathbf{r},t) - f_2(\mathbf{r},t)] - \frac{\Delta t}{4}(F_x - F_y), \tag{3.42}$$

$$f_0(\mathbf{r},t) = \hat{n} - [f_2(\mathbf{r},t) + f_4(\mathbf{r},t)] - 2[f_3(\mathbf{r},t) + f_6(\mathbf{r},t) + f_7(\mathbf{r},t)] + \frac{\Delta t}{2}F_x. \tag{3.43}$$

In the case of the angle between the walls considered before, the functions f_1, f_2, f_5, f_6, and f_8 are unkwown. Requiring that $f_2 = f_4$ and $f_1 = f_3$ it is now

$$\begin{aligned} \hat{n}(t-\Delta t) = {} & f_0(t-\Delta t) + f_6(t-\Delta t) + f_3(t-\Delta t) \\ & + f_4(t-\Delta t) + f_8(t-\Delta t) + f_7(t-\Delta t) \\ & + f_3(\mathbf{r},t) + f_7(\mathbf{r},t) + f_4(\mathbf{r},t), \end{aligned} \tag{3.44}$$

$$f_2(\mathbf{r},t) = f_4(\mathbf{r},t), \tag{3.45}$$

$$f_1(\mathbf{r},t) = f_3(\mathbf{r},t), \tag{3.46}$$

$$f_5(\mathbf{r},t) = f_7(\mathbf{r},t) - \frac{\Delta t}{4}(F_x + F_y), \tag{3.47}$$

$$f_8(\mathbf{r},t) = \frac{\hat{n}}{2} - \frac{1}{2}f_0(\mathbf{r},t) - f_3(\mathbf{r},t) - f_4(\mathbf{r},t) - f_7(\mathbf{r},t) + \frac{\Delta t}{4}F_y, \tag{3.48}$$

$$f_6(\mathbf{r},t) = \frac{\hat{n}}{2} - \frac{1}{2}f_0(\mathbf{r},t) - f_3(\mathbf{r},t) - f_4(\mathbf{r},t) - f_7(\mathbf{r},t) + \frac{\Delta t}{4}F_x. \tag{3.49}$$

3.5 Hybrid Lattice Boltzmann for liquid crystals

Computer simulations for the study of liquid crystal have been performed using a hybrid LBM method analogous to the one used for fluid mixtures. In this paragraph the most important features are presented [48, 82, 104].
As the previous method, introduced for fluid mixtures, it is called hybrid because the continuity and Navier-Stokes equations are solved by LBM whereas the scalar concentration field and the **Q** tensor equations are solved with a finite-difference scheme.
The hybrid Lattice Boltzmann method for liquid crystals is built considering a three dimensional lattice with geometry D3Q15 and introducing a set of distribution function $f_i(\mathbf{r},t)$ along with a set of velocity vectors:

$$\mathbf{e}_i = \begin{cases} (0,0,0) & i = 0 \\ (\pm e,0,0),(0,\pm e,0),(0,0,\pm e) & i = 1,...,6 \\ (\pm e,\pm e,\pm e) & i = 7,...,14. \end{cases} \tag{3.50}$$

with moduli $|\mathbf{e}_0| = 0$, $|\mathbf{e}_i| = \frac{\Delta x}{\Delta t} = e$ for $i = 1, 2, ..6$ and $|\mathbf{e}_i| = \sqrt{3}e$ for $i = 7, 8, ..., 14$ where Δx and Δt are the spatial and the time lattice steps. The distribution functions are, as usual, related to total density fluid and velocity by the relations

$$n = \sum_i f_i, \qquad n\mathbf{u} = \sum_i f_i \mathbf{e}_i \tag{3.51}$$

and evolve according to the lattice Boltzmann equation

$$f_i(\mathbf{r} + \mathbf{e}_i\Delta t, t + \Delta t) - f_i(\mathbf{r}, t) = \frac{\Delta t}{2}[\mathcal{C}_{f_i}(\mathbf{r}, t, f_i) + \mathcal{C}_{f_i}(\mathbf{r} + \mathbf{e}_i\Delta t, t + \Delta t, f_i^*)] \tag{3.52}$$

where $\mathcal{C}_{f_i}$ is the collision operator with single relaxation time τ

$$\mathcal{C}_{f_i} = -\frac{1}{\tau}(f_i(\mathbf{r}, t) - f_i^{eq}(\mathbf{r}, t)) + F_i(\mathbf{r}, t, f_i) \tag{3.53}$$

with F_i driving force in the right hand side of the equation. In this case the resolution of the Boltzmann equation is supplemented by the predictor-corrector method [100]. In the first step, the predictor phase, the distribution function f_i^* is calculated as first order approximation

$$f_i^*(\mathbf{r} + \mathbf{e}_i\Delta t, t + \Delta t) = f_i(\mathbf{r} + \mathbf{e}_i\Delta t, t + \Delta t) = f_i(\mathbf{r}, t) + \Delta t\mathcal{C}_{f_i}(\mathbf{r}, t, f_i) \tag{3.54}$$

and with the trapezoid rule

$$f_i(\mathbf{r} + \mathbf{e}_i\Delta t, t + \Delta t) = f_i(\mathbf{r}, t) + \frac{\Delta t}{2}(\mathcal{C}_{f_i}(\mathbf{r} + \mathbf{e}_i\Delta t, t + \Delta t, f_i^*) + \mathcal{C}_{f_i}(\mathbf{r}, t, f_i)). \tag{3.55}$$

The value f_i^*, calculated in (3.54), at time $t + \Delta t$ has been used to calculate $\mathcal{C}_{f_i}$ at time $t + \Delta t$. This last passage is called corrector because it improves or corrects the iterated value f_i^*.
As already seen for fluid mixtures, the LBM method requires a proper definition of the equilibrium distribution functions which must satisfy the constraints of conservation of mass and momentum. This requires

$$\sum_i f_i^{eq} = n, \qquad \sum_i f_i^{eq} e_{i\alpha} = nu_\alpha \tag{3.56}$$

whereas for the second-order moment it has to be

$$\sum_i f_i^{eq} e_{i\alpha} e_{i\beta} = \sigma_{\alpha\beta} + nu_\alpha u_\beta \tag{3.57}$$

with $\sigma_{\alpha\beta}$ symmetric part of the liquid crystals stress tensor presented in Chapter 1. A constraint of the third order moment is also necessary to get an isotropic Navier-Stokes equation via the Chapman-Enskog approximation

$$\sum_i f_i^{eq} e_{i\alpha} e_{i\beta} e_{i\gamma} = \frac{n\tau}{3}(u_\alpha\delta_{\beta\gamma} + u_\beta\delta_{\alpha\gamma} + u_\gamma\delta_{\alpha\beta}). \tag{3.58}$$

The contraints on the force F_i are

$$\sum_i F_i = 0; \qquad \sum_i F_i e_{i\alpha} = \partial_\beta \tau_{\alpha\beta} - \partial_\beta \left(\partial_\alpha Q_{\gamma\nu} \frac{\delta f}{\delta \partial_\beta Q_{\gamma\nu}} \right) - \partial_\alpha f \equiv b_\alpha, \tag{3.59}$$

$$\sum_i F_i e_{i\alpha} e_{i\beta} = 0; \qquad \sum_i F_i e_{i\alpha} e_{i\beta} e_{i\gamma} = 0 \tag{3.60}$$

where $\tau_{\alpha\beta}$ and f are the antisymmetric part of the liquid crystal stress tensor and the free-energy density of the system. The equilibrium distribution functions are chosen as a opwer series expansion truncated to the second order in velocities

$$f_i^{eq} = A_\sigma + B_\sigma u_\alpha e_{i\alpha} + C_\sigma u^2 + D_\sigma u_\alpha u_\beta e_{i\alpha} e_{i\beta} + E_{\sigma,\alpha\beta} e_{i\alpha} e_{i\beta} + G_\sigma b_\alpha e_{i\alpha} \tag{3.61}$$

where $\sigma = 0, 1, 2$ if $e_i^2 \in \{0, 1, 3\}$ identifies separate coefficients for different square absolute values of velocities. The coefficients are determined required the (3.56)-(3.60). A possible adopted choice of coefficients is [82]

$$A_2 = \frac{nT}{10}; \qquad A_1 = A_2; \qquad A_2 = n - 14A_2, \tag{3.62}$$

$$B_2 = \frac{n}{24}; \qquad B_1 = 8B_2, \tag{3.63}$$

$$C_2 = -\frac{n}{24}, \qquad C_1 = 2C_2; \qquad C_0 = -\frac{2n}{3}, \tag{3.64}$$

$$D_2 = \frac{n}{16}; \qquad D_1 = 8D_2, \tag{3.65}$$

$$E_{2\alpha\beta} = -\frac{1}{16}\sigma_{\alpha\beta}; \qquad E_{1\alpha\beta} = 8E_{2\alpha\beta}, \tag{3.66}$$

$$G_2 = \frac{1}{24}; \qquad G_1 = 8G_2. \tag{3.67}$$

By a Chapman-Enskog expansion, in the continuum limit it is possible to obtain the continuity and Navier-Stokes equations [48].

3.5.1 Boundary conditions for liquid crystals

In this section the implementation of the boundary conditions for a system confined between two horizontal parallel walls is illustrated following [104]. The vertical direction is assumed the z direction with walls at $z = 0$ and $z = L_z$.
No flux across the wall at $z = 0$ implies $\sum_i f_i e_{iz} = 0$ and hence

$$f_5 + f_7 + f_8 + f_9 + f_{10} = f_6 + f_{11} + f_{12} + f_{13} + f_{14}. \tag{3.68}$$

For no slip along the x direction it has to be $\sum_i f_i e_{ix} = 0$ or

$$f_1 + f_7 + f_{10} + f_{11} + f_{14} = f_3 + f_8 + f_9 + f_{12} + f_{13}. \tag{3.69}$$

Fixing the velocity u_y along y direction $\sum_i f_i e_{iy} = n u_y$ or

$$f_2 + f_7 + f_8 + f_{11} + f_{12} - f_4 - f_9 - f_{10} - f_{13} - f_{14} = n u_y. \tag{3.70}$$

At the wall $z = 0$ there are five unknown distributions f_5, f_7, f_8, f_9 and f_{10}. To determine them, two constraints are required. Simmetry suggests:

$$f_7 - f_8 = f_{10} - f_9 \tag{3.71}$$

The conservation of mass is easily obtained by choosing

$$f_5 = f_6 \tag{3.72}$$

Solving the equations (3.68)-(3.72), one obtains

$$\begin{cases} f_5 = f_6, \\ f_7 = \frac{1}{4}(-f_1 - f_2 + f_3 + f_4 - f_{11} + f_{12} + 3f_{13} + f_{14} + n u_y), \\ f_8 = \frac{1}{4}(f_1 - f_2 - f_3 + f_4 + f_{11} - f_{12} + f_{13} + 3f_{14} + n u_y), \\ f_9 = \frac{1}{4}(f_1 + f_2 - f_3 - f_4 + 3f_{11} + f_{12} - f_{13} + f_{14} - n u_y), \\ f_{10} = \frac{1}{4}(-f_1 + f_2 + f_3 - f_4 + f_{11} + 3f_{12} + f_{13} - f_{14} - n u_y). \end{cases} \tag{3.73}$$

3.6 Summary

In this Chapter the Lattice Boltzmann method for fluid mixtures and liquid crystals was introduced.
The particular type of the method here presented and adopted for simulations, was the so called hybrid version. The adjective hybrid is related to the fact that the method is used to solve the fluid at the Navier-Stokes level and is coupled to a finite-difference method to solve the equations for the order parameters. The main advantage of this version is a considerable saving in computational resources and a better numerical stability. As previously described, the basic idea of the method is to discretize the physical space with lattices and definig a set of distribution functions for the fluid which evolve in time with a discretized Boltzmann equation. These distribution functions are related to the density and velocity of the fluid. A full treatement of the full set of equations by the Lattice Boltzmann method, would require to define more increasing memory storage and time of the simulation. Solving apart the equations for the order parameters, allows bigger or three dimensional systems to be studied more easily.

Chapter 4

Cholesteric liquid crystal droplet under electric fields

This chapter collects the main results of the study of a cholesteric liquid crystal droplet in isotropic host subjected to the action of electric fields of the work "*Switching dynamics in cholesteric liquid crystal emulsions*" published on *The Journal of Chemical Physics*. As described in Chapter 2, liquid crystals, due to polar nature of their molecules, answer to electric fields in different ways with the director which orientates for the field. During the evolution of the system, the presence of electric fields, boundaries such as rigid walls, anchoring and elasticity can induce the rise of topological defects. The goal of the work has been the detection of these defects when the cholesteric droplet feels the action of different types of electric fields. The chapter is organized as follows.
At first the free-energy of the system is introduced. Then some aspects related to cholesteric liquid crystals are introduced such as the phase diagram which marks the cholesteric, isotropic and blue phases regions which must be always kept in mind in order to choose the parameters of the system wisely so that the cholesteric region is correctly considered. After that, the results of the computer simulations are considered and analyzed in detail. At first the equilibrium structure, before switching on the field, of cholesteric droplets are shown and then the results of the application of continuous and rotating fields are described. In the former case the switching on-off of the field has been considered, describing the evolution of the topological defects, also comparing the situation of the droplet with a different geometry represented by a channel of cholesteric and analyzing the field tresholds that break the helix and turn the cholesteric droplet into a nematic one. In the latter case the effect of rotating fields is considered computing quantitatively the angular velocity of the droplet and analyzing the periodicity of the topological defects.

4.1 Liquid crystals droplets

Chapter 2 introduced the general aspects of liquid crystals presenting the most important mesophases such as the nematic, the cholesteric, the recent twist-bend structure, the smectic and columnar phases. The cholesteric phase, in particular, in which the molecules are arranged in a three-dimensional helix with a certain pitch will be the theme of the results collected in this Chapter. As also reported liquid crystals are of fundamental importance in technological applications in the production of TV, calculator, computer screens bases on the TN cell element, optical instruments, sensors etc.
In the years the attention has moved to the study of liquid crystal droplets and the discoveries to possibile practical applications related to them. The possibile applications are various [105]; liquid crystal droplets can be used as microresonators, droplets with concentric package of cholesteric layers can be used as tunable onion-like Bragg microresonators and cholesteric droplets prepared as polymer dispersed liquid cystals can also be used for lasing [25, 37] also droplets used for the production of filaments [105]. This pletora of possible applications explains why studying liquid crystal droplets is useful and important.
Various studies were performed about liquid crystal droplets in various situations: isotropic droplet in nematic host under electric fields [6], isotropic droplets in nemtaic host under shear [8] and typical structures of cholesteric droplets at equilibrium [51, 105–108] without electric fields.
Another important study on which scientists are focusing deals with the Lehmann effect in cholesteric liquid crystals [109–126] consisting in a rotation of a cholesteric liquid crystal droplet due to a thermal gradient first observed by Lehmann in 1900 [30, 31]. In [109] in particular the inverse Lehmann-type effect is described. It, inversly, consists in a process in which a molecular field associated with orientational degrees of freedom arises when there is a pattern forming non-equilibrium situation. This molecular field, in turn, gives rise, to concentration, heat or electric currents across a freely suspended film of liquid crystals. As final result of this kind of process a pumping force arises which can be used to push particles and ions for length scales of the micron.
Starting from [51] in particular, the goal of the work, whose results are collected in this Chapter, is to explore the dynamics of topological defects and the typical structures of cholesteric liquid crystal droplets under electric fields for different pitches of the helix, for different anchoring situations and different types of electric fields.

4.2 The numerical model

The free-energy functional, $\mathcal{F} = \int f dV$, which encodes all the thermodynamics of the problem, whose energetic terms were already considered in Chapter 2, adopted in this system is:

$$\begin{aligned} f &= \frac{a}{4}\phi^2(\phi-\phi_0)^2 + \frac{\kappa_\phi}{2}|\nabla\phi|^2 \\ &+A_0\left[\frac{1}{2}\left(1-\frac{\gamma(\phi)}{3}\right)Q_{\alpha\beta}^2 - \frac{\gamma(\phi)}{3}Q_{\alpha\beta}Q_{\beta\gamma}Q_{\gamma\alpha} + \frac{\gamma(\phi)}{4}(Q_{\alpha\beta}^2)^2\right] \\ &+\frac{K}{2}\left[(\partial_\beta Q_{\alpha\beta})^2 + (\varepsilon_{\alpha\zeta\delta}\partial_\zeta Q_{\delta\beta} + 2q_0 Q_{\alpha\beta})^2\right] \\ &+W(\partial_\alpha\phi)Q_{\alpha\beta}(\partial_\beta\phi) - \frac{\varepsilon}{12\pi}E_\alpha Q_{\alpha\beta}E_\beta \end{aligned} \tag{4.1}$$

with $\gamma(\phi) = \gamma_0 + \gamma_s\phi$ with constants γ_0 and γ_s which mark the stable phase.
The variables of interest in this situation are the total density field $n(x,y,z,t)$, the velocity field $\mathbf{u}(x,y,z,t)$, the scalar concentration field $\phi(x,y,z,t)$ and the $\mathbf{Q}(x,y,z,t)$ tensor order parameter [48, 104]. The dynamic equations of the system, already presented in Chapter 1, are the Beris-Edwards equation for the $\mathbf{Q}$ tensor order parameter [5]

$$(\partial_t + \mathbf{u}\cdot\nabla)\mathbf{Q} - \mathbf{S}(\mathbf{W},\mathbf{Q}) = \Gamma\mathbf{H} \tag{4.2}$$

with molecular field

$$\mathbf{H} = -\frac{\delta\mathcal{F}}{\delta\mathbf{Q}} + \frac{\mathbf{I}}{3}Tr\frac{\delta\mathcal{F}}{\delta\mathbf{Q}} \tag{4.3}$$

with complete explicit expression

$$\begin{aligned} H_{\alpha\beta} = A_0&\left[-\left(1-\frac{\gamma(\phi)}{3}\right)Q_{\alpha\beta} + \gamma(\phi)\left(Q_{\alpha\mu}Q_{\mu\beta} - \frac{1}{3}\delta_{\alpha\beta}Q_{\nu\mu}Q_{\mu\nu}\right) - \gamma(\phi)Q_{\alpha\beta}Q_{\gamma\nu}Q_{\mu\nu}\right] \\ &- W\left((\partial_\alpha\phi)(\partial_\beta\phi) - \frac{\delta_{\alpha\beta}}{3}(\partial_\mu\phi\partial_\mu\phi)\right) \\ &+ \frac{\varepsilon}{12\pi}\left(E_\alpha E_\beta - \frac{1}{3}\delta_{\alpha\beta}E^2\right) - 4Kq_0\varepsilon_{\alpha\gamma\delta}\partial_\gamma Q_{\delta\beta} - K\partial_\gamma^2 Q_{\alpha\beta} + 4Kq_0^2 Q_{\alpha\beta}. \end{aligned} \tag{4.4}$$

The explicit calculus of the various terms of the molecoular field is treated in [6].
The concentration scalar field ϕ is described by the Cahn-Hilliard equation:

$$\partial_t\phi + \partial_\alpha(\phi u_\alpha) = D\nabla^2\mu \tag{4.5}$$

In the end there are the continuity equation and Navier-Stokes equation for the total density field n and the velocity field $\mathbf{u}$:

$$\nabla\cdot\mathbf{u} = 0 \tag{4.6}$$

$$n(\partial_t + u_\beta \partial_\beta) u_\alpha = \partial_\beta \sigma^{total}_{\alpha\beta} \tag{4.7}$$

in which $\sigma^{total}_{\alpha\beta}$ contains the viscous, the liquid crystal and the interface terms presented in Chapter 1. This set of coupled equations were solved numerically through hybrid Lattice Boltzmann Method for liquid crystals described in Chapter 3.

4.3 Phase diagram of cholesteric liquid crystals

In order to choose wisely the numerical values for the parameters of the system in the computer simulations, the phase diagram of cholesteric liquid crystals, shown in Fig. 4.1, must be kept in mind. This phase diagram of [127], was obtained in the case of the study of liquid crystal blue phases under electric field and used as guide in the choice of the paramaters of the simulations. It is defined by the three following parameters:

$$\kappa = \sqrt{\frac{108 K q_0^2}{A_0 \gamma}} \tag{4.8}$$

$$\tau = \frac{27(1 - \gamma/3)}{\gamma} \tag{4.9}$$

$$e^2 = \frac{27\varepsilon}{32\pi A_0 \gamma} E_\alpha E_\alpha \tag{4.10}$$

where κ is the chirality which is related to q_0 and so to the cholesteric pitch and tells how much the system is twisted, τ is the reduced temperature and e^2, related to the electric field $\mathbf{E}$, is the effective field strength.
Looking the left panel in Fig. 4.1 if $\gamma = 3$ (for $\gamma_c = 2.7$ there is coexistence of isotropic-nematic phases, if $\gamma_c < 2.7$ there is the isotropic phase, for $\gamma_c > 2.7$ there is the cholesteric one), $\tau = 0$ and so $\kappa \approx 0.5$ and this value was chosen as treshold to mark the separation between cholesteric phase from the BPI one. Therefore the parameters of the simulations A_0, the bulk constant, the elastic constant K, and the inverse of the pitch $q_0 = 2\pi/p_0$ with p_0 pitch of the helix were chosen following this criterion.

4.4 Initial conditions

In the computer simulations, a cholesteric droplet with radius $R = 32$ lattice sites is accomodated at the center of a periodic lattice in all directions with dimensions $L_x = 1 \times L_y = 128 \times L_z = 128$. The set of values is: $\alpha_\phi = 0.07$, $\kappa_\phi = 0.14$, $A_0 = 1$, $K = 0.03$, $\Gamma = 1$, $\eta = 1.67$, $D = 0.05$, $\xi = 0.7$, $\varepsilon = 41.4$ and $|W| = 0.04$. This values of the parameters are expressed in simulation units and can be mapped in SI units

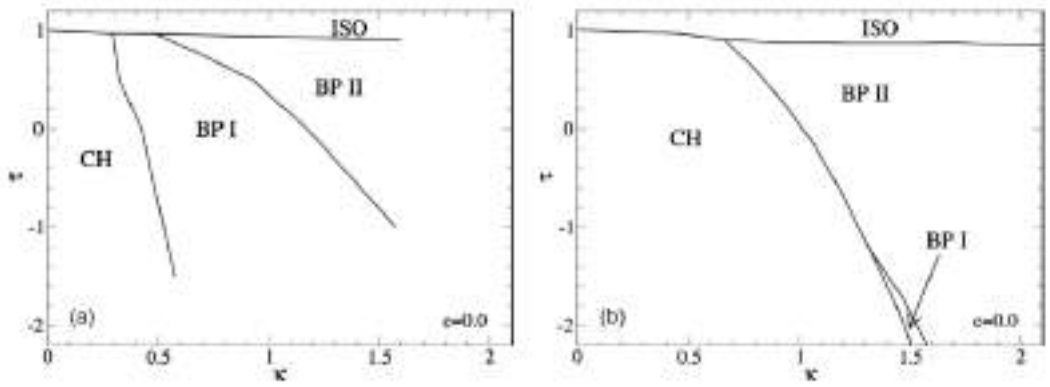

Figure 4.1: Phase diagram in the chirality-temperature plane with $e = 0$ which marks the division of the cholesteric, isotropic, BPI and $BPII$ phases [127].

in the following way: $\Delta x = 1 \sim 0.1\mu m$, $\Delta t = 1 \sim 1\mu s$, $n = 2 \sim 10^3 kgm^{-3}$, $K = 10^{-2} \sim 10^{-11} N$, $W = 10^2 \sim 10^6 Jm^{-2}$, $R = 10 \sim 1 - 10\mu m$ and $\varepsilon \sim \mathbf{E} \sim 1V/\mu m$ [6, 44, 128, 129].
As a measure of the relative size of the droplet with respect to the chiral pitch it can be introduced the following adimensional quantity [51]

$$N = 2R/p_0 \tag{4.11}$$

with R radius of the droplet and p_0 pitch of the helix. It represents the number of 2π turns of the helix in a droplet of radius R. Alternatively, remembering in Chapter 2 that the two directions of the director are equivalent ($\mathbf{n} = -\mathbf{n}$), the same parameter can rewritten as

$$N = 4R/p_0 \tag{4.12}$$

which corresponds to the number of π turns or twists of the helix in the same droplet. The concentration field ϕ and the $\mathbf{Q}$ tensor components are set to zero outside the droplet. Inside the droplet, instead, ϕ has been set equal to a value $\phi_0 = 2$ and the five components have been chosen in order to accomodate the cholesetric helix with helical axis parallel to the horizontal y direction. The components are:

$$Q_{xx} = (c_0 - c_1/2)cos(2q_0 y) + c_1/2, \tag{4.13}$$

$$Q_{yy} = -2c_1, \tag{4.14}$$

$$Q_{xz} = -(c_0 - c_1/2)sin(2q_0 y) \tag{4.15}$$

where $c_0 = 0.546$, $c_1 = 0.272$ while $Q_{xy} = Q_{yz} = 0$.

4.5 Droplets at equilibrium

Each simulation is run for 4×10^5 time-steps, until the droplet is completely equilibrated. This is determined by looking at the relaxation behavior of the free energy towards a constant minimum value. In Fig. 4.2 a set of equilibrium configurations obtained in absence of surface anchoring (top row) and by imposing either tangential anchoring (middle row) or homeotropic anchoring (bottom row) is shown. Two cases are considered: the first one with $q_0 = 2\pi/64$ giving a helical phase with $N = 2\pi$ twists (left column) and the second one obtained with $q_0 = 2\pi/32$ and hence a helical phase with $N = 4\pi$ twists (right column of Fig. 4.2). The figure shows a clear dependence of the equilibrium configuration both on the anchoring and on the number of twists accommodated inside the droplet. As expected, for very weak anchoring the director field orients itself continuously at the boundary to satisfy the natural curvature of the droplet. Hence the resulting equilibrium configurations are defect-free (Fig. 4.2-(a)-(d)). For strong anchoring, frustration between the cholesteric order inside the droplet and the imposed direction at the surface is present and equilibrium configurations with defects are expected [6, 51, 128]. Defects can result either from sharp changes in orientation of the director in the interior of the droplet, or due to conflict with the anchoring close to the boundary. Their number and position also depend on the anchoring direction and strength, as well as on the number N of cholesteric twists in the droplet. As reported in Chapter 2, defects in cholesterics are usually classified into $\lambda^{\pm m}$, $\tau^{\pm m}$, $\chi^{\pm m}$ defect lines (with m topological charge) and twist disclinations [31, 32]. While disclination lines of type $\chi^{\pm m}$ requires a full 3D system and are not observed here, $\lambda^{\pm m}$ and $\tau^{\pm m}$ defects appear. Fig. 4.8 reports the most typical combinations of λ and τ defects encountered in the simulations.

The λ defect, for example, emerges in Fig. 4.2-(b) and the first row of Fig. 4.3. Instead, for a τ defect the director field is singular, so that the (in-plane nematic) orientational order drops at the core (Fig. 4.3 second row). As a consequence, the location of τ defects can be detected numerically and visible by the "brown" spots encircled in red in the pictures. On the contrary, λ defects are more difficult to detect exactly andmust be recognized "by eye".
In the case of strong tangential anchoring and $N = 2$ (Fig. 4.2-(b)) the helical structure bends significantly in a circular fashion forming a quasi-planar configuration with the director field that escapes into the third dimension only in proximity of the droplet center forming a λ^{+1} disclination.
If, on the other hand, the number of twists increases to $N = 4$, the twist energy is too large to be overcome by the bending one and the configuration with the minimal free energy has four defects with topological charge $-1/2$ (lying fully in the yz plane) and three regions of topological charge $+1$ (the stretched stripes in which

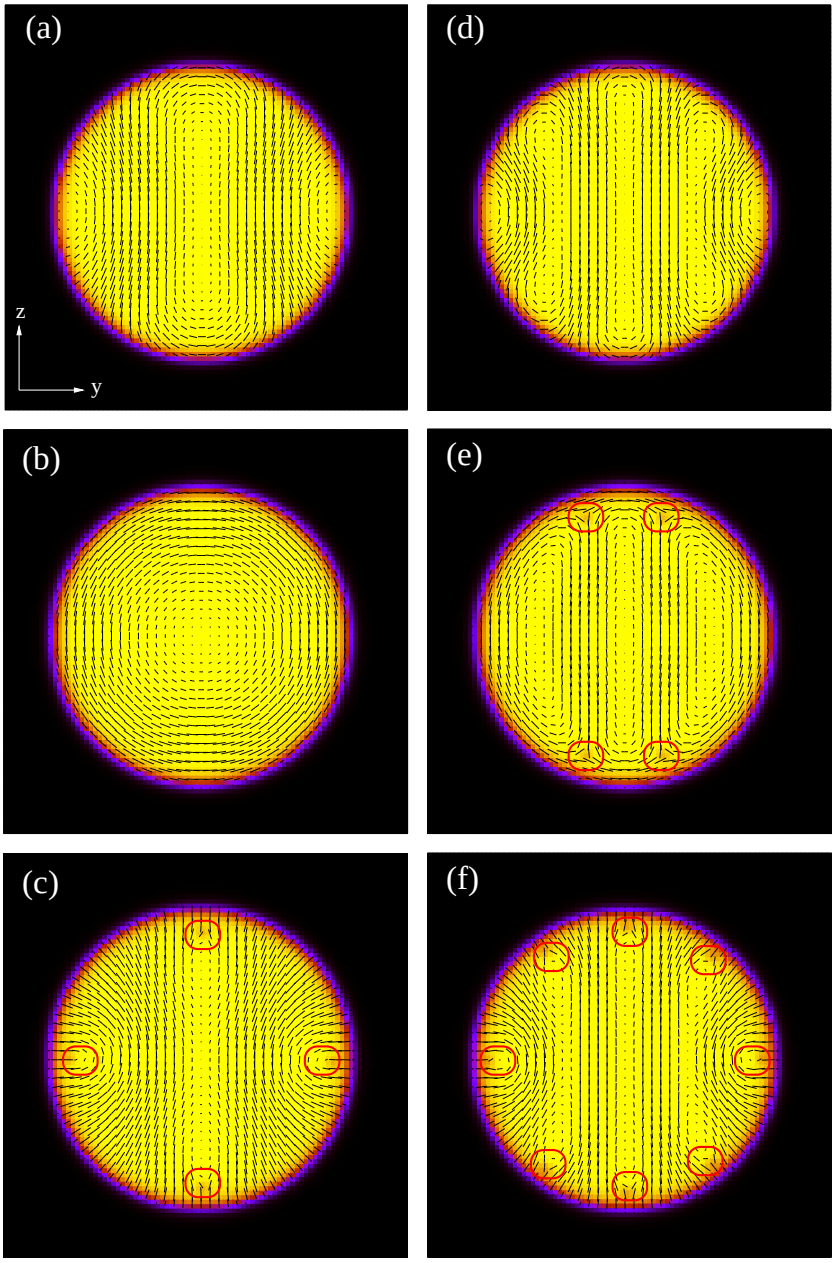

Figure 4.2: Equilibrium configurations (taken at simulation time $t = 4 \times 10^5$) of a cholesteric droplet in an isotropic fluid. The radius of the droplet is $R = 32$ lattice units and the cholesteric pitch is $q_0 = 2\pi/64$ ((a)-(b)-(c)) and $q_0 = 2\pi/32$ ((d)-(e)-(f)). In (a) and (d) no anchoring is set, in (b) and (e) strong tangential anchoring is set while in (c) and (f) strong homeotropic anchoring is chosen. Topological defects, formed nearby the surface (namely τ and twist disclinations), are highlighted with red circles. The color map represents the largest eigenvalue of the $\mathbf{Q}$ tensor and ranges from 0 (the black region outside the droplet) to $\simeq 0.33$ (the yellow region inside the droplet). The color map applies to all figures.

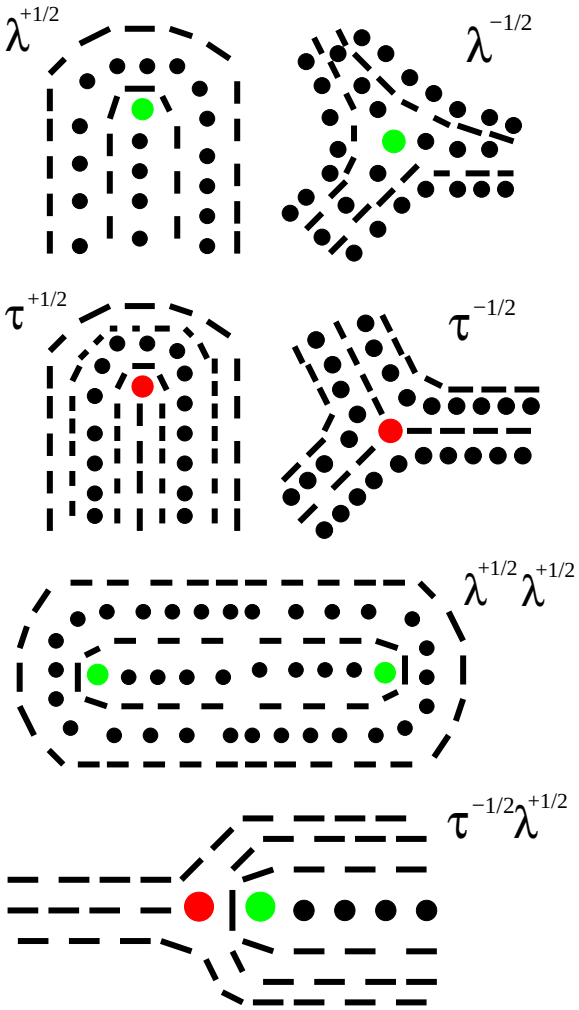

Figure 4.3: Schematic representation of topological defects $\lambda^{\pm m}$ and $\tau^{\pm m}$ and their combination found in most of our simulations. Black dots and lines represent the local director field, perpendicular to and on the plane, respectively. Unlike green dots, the red ones correspond to a real singularity of the director field [51].

the director lies along the x direction, (Fig. 4.2-(e))[1].
In Fig. 4.2-(c) the equilibrium configuration with homeotropic anchoring and $N = 2$ is shown. In this case a thin $+1$-charge region forms in the center of the droplet (along the diameter in the north/south direction), and is sustained by two twist disclinations of charge $-1/2$ firmly anchored at the interface (also represented in Fig. 4.3, fourth row). On both sides of this region, the director displays two symmetric splay-bend deformations in order to accommodate the orientation imposed by the homeotropic surface anchoring. This determines the formation of two further defects, $\tau^{1/2}$ disclinations, located symmetrically along the equator. As required of any $2D$ pattern with these boundary conditions, the total topological charge is therefore again $+1$ [130–132]. Finally when $N = 4$, two more $+1$-charge regions appear symmetrically located with respect to the central one, and eight disclinations form nearby the interface. Two of these are $\tau^{1/2}$ disclinations (those along the equator) whereas the remaining ones are twist disclinations of charge $-1/2$. In proximity of the two $\tau^{1/2}$ defects, the strong bend distortions of the director field protrude well inside the center of the droplet, especially for $N = 2$.

4.6 Switching on-off of a DC electric field

In this section the switching on-off dynamics of a continuous electric field is described. Starting from the equilibrated droplet configurations described in the previous section, a uniform electric field whose direction is either parallel (along the horizontal y axis) or perpendicular (along vertical z axis) to the helical axis is first switched on and the dynamics of the defects is studied until the system reaches a steady state (ON state). Then the field is switched off towards a zero field (OFF) final state. The electric field is of type $E = \Delta V L$ with potential ΔV chosen in order to produce an appreciable variation in the dynamics of defects and also low enough to prevent the complete destruction of the helix and the consequent nematization of the droplet. At first the results for a droplet with no anchoring (defect-free droplet) are presented then moving to the cases in which homogeneous and homeotropic strong anchoring are set.

4.6.1 W=0, free anchoring

Fig. 4.2-(d) deals with the case where a cholesteric phase with $N = 4$ is embedded in a droplet of radius R. Since $W = 0$ the director field at the droplet surface is free to rotate and no defects are present. When, in this case, an electric field is switched on along the helix (y-axis), the director field gradually aligns along the same direction by following a complex dynamics involving the formation and annihilation

[1]From this point for brevity a $+1$ λ-region can indicate a λ^{+1} defect or a pair of $\lambda^{+1/2}$ defects.

of defect pairs. In steady state (when the field is ON) the droplet is oriented almost completely to yield a 2D nematic state – the exception is the equatorial line in which the director field is oriented out of the plane (Fig 4.4-(c)). When the electric field is switched off (Fig. 4.4-(d)-(f)) the director relaxes to the initial (field-off) equilibrium cholesteric arrangement but with the helix axis now oriented along the z-axis. A further ON-OFF cycle, in which the field is first switched on along the z-direction, drives the system back to the initial equilibrium state (Fig. 4.4-(a)). The OFF states are of course equivalent as they differ solely by a rotation of the helical axis, and indeed the values of the field-off free-energy configurations are equal (Fig. 4.5).

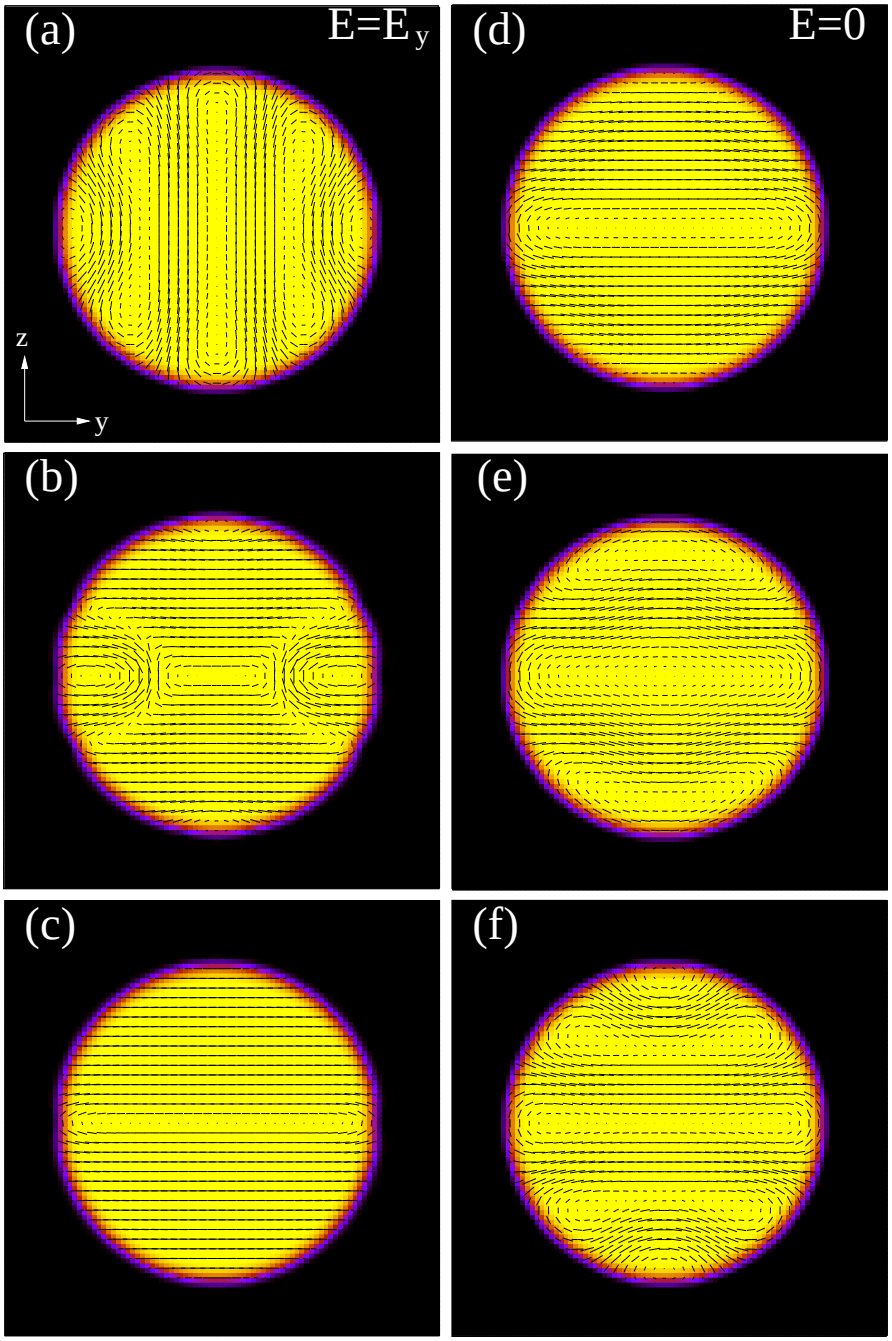

Figure 4.4: Switching dynamics of a cholesteric droplet with $N = 4$ under an electric field applied along the y-direction with $\Delta V = 5$ and $W = 0$ (no anchoring). The field is ON in (a) ($t = 4 \times 10^5$), (b) ($t = 4.05 \times 10^5$) and (c) ($t = 7 \times 10^5$) and OFF in (d) ($t = 7.01 \times 10^5$), (e) ($t = 7.05 \times 10^5$) and (f) ($t = 10^6$). Here t is the simulation time. In particular (c) and (f) represent steady states achieved when the electric field is ON and OFF, respectively. After one switching cycle the director reacquires a cholesteric arrangement with the helix axis parallel to the direction of the electric field.

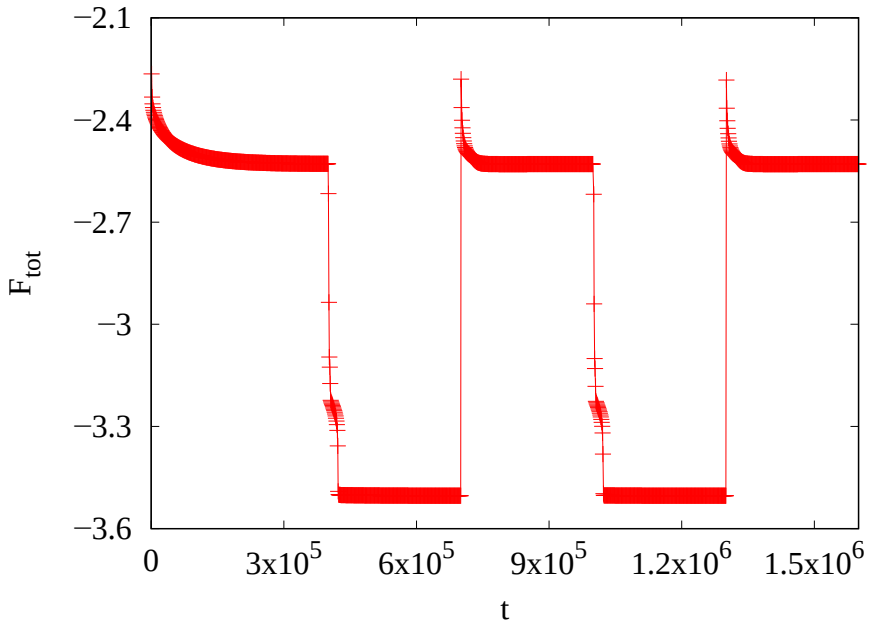

(a)

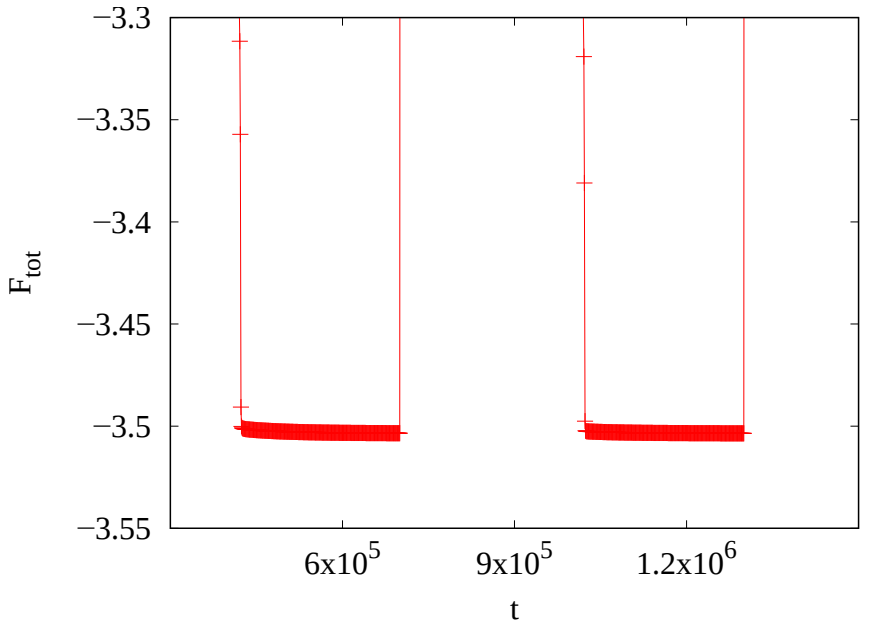

(b)

Figure 4.5: Total free-energy vs simulation time for the case $W = 0$ and $N = 4$ (a). The field is switched on at $t = 4 \times 10^5$ and switched off at $t = 7 \times 10^5$ during the first cycle. During the second cycle it is switched on at $t = 1 \times 10^6$ and off at $t = 1.3 \times 10^6$. Here t is the simulation time. In the inset (b) the two minima of the free-energy are equal.

4.6.2 W=0.04, tangential anchoring

The case of strong tangential anchoring is now discussed.
The two equilibrium starting configurations are those reported in Fig 4.2-(b)-(e) with cholesteric helices respectively of $N = 2$ and $N = 4$ twists. In both cases $\Delta V = 3$. The case $N = 2$ (Fig. 4.2-(b)) is akin to that of a simple nematic droplet. In fact, regardless of the direction of the applied electric field, the director, in the ON steady state, aligns almost everywhere along it, the only exception being a thin stripe passing through the centre of the droplet, in which it orients out of the plane, along the x-direction. When the electric field is switched off, the system relaxes back quite rapidly to the initial field-off equilibrium state as shown in Fig. 4.6 with final elastic energies equal to the ones of the initial equilibrium configuration as reported in Fig. 4.7.

A richer behaviour is observed for the cholesteric phase with $N = 4$ and when the electric field is applied along the helix (y) axis (Fig. 4.8). During the ON dynamics, as the director starts to align along the direction of the electric field, the four defects abandon the droplet surface and move towards the inner region of the droplet. While the director field near the droplet surface remains almost everywhere tangential, inside the droplet it undergoes pronounced symmetric bend distortions that move along the y axis in opposite directions (Fig. 4.8-(a)-(b). At the steady state the bend distortions are confined near the interface and in between the defects, while the director is almost fully parallel to the y-direction in the bulk, with the exception of the equatorial line and of the opposite sides of the in-plane topological defects, in which it is oriented off plane (Fig. 4.8-(c)). These patterns are associated with three $+1$-charge regions. In the ON steady state the initial equilibrium helical order (with axis along the y-direction) has been replaced by a novel arrangement in which a cholesteric-like structure, with the axis now along the z-direction, emerges.

When the field is switched off, the director gradually relaxes towards a new steady state in which the helical arrangement is almost restored. While the position of the in-plane defects remains overall unaltered with respect to that achieved at the ON state, the position of the three $+1$-charge regions is restored almost in the configuration they had in the equilibrium field-off state, as they follow the rearrangement of the director field. This new OFF state is metastable, as it is characterised by an elastic free energy higher than that of its equilibrium counterpart (Fig. 4.9). The higher value of the free energy achieved by this OFF steady state is due to the additional elastic energy necessary to bend the director in proximity of the defects.

If the electric field is switched along the z-direction, the dynamics observed is overall less rich than the previous case. $\Delta V = 5$ was chosen, as for lower values of the electric field the effects on the defects dynamics are really negligible. After the electric field is switched on, the in-plane defects are soon pushed towards the interface

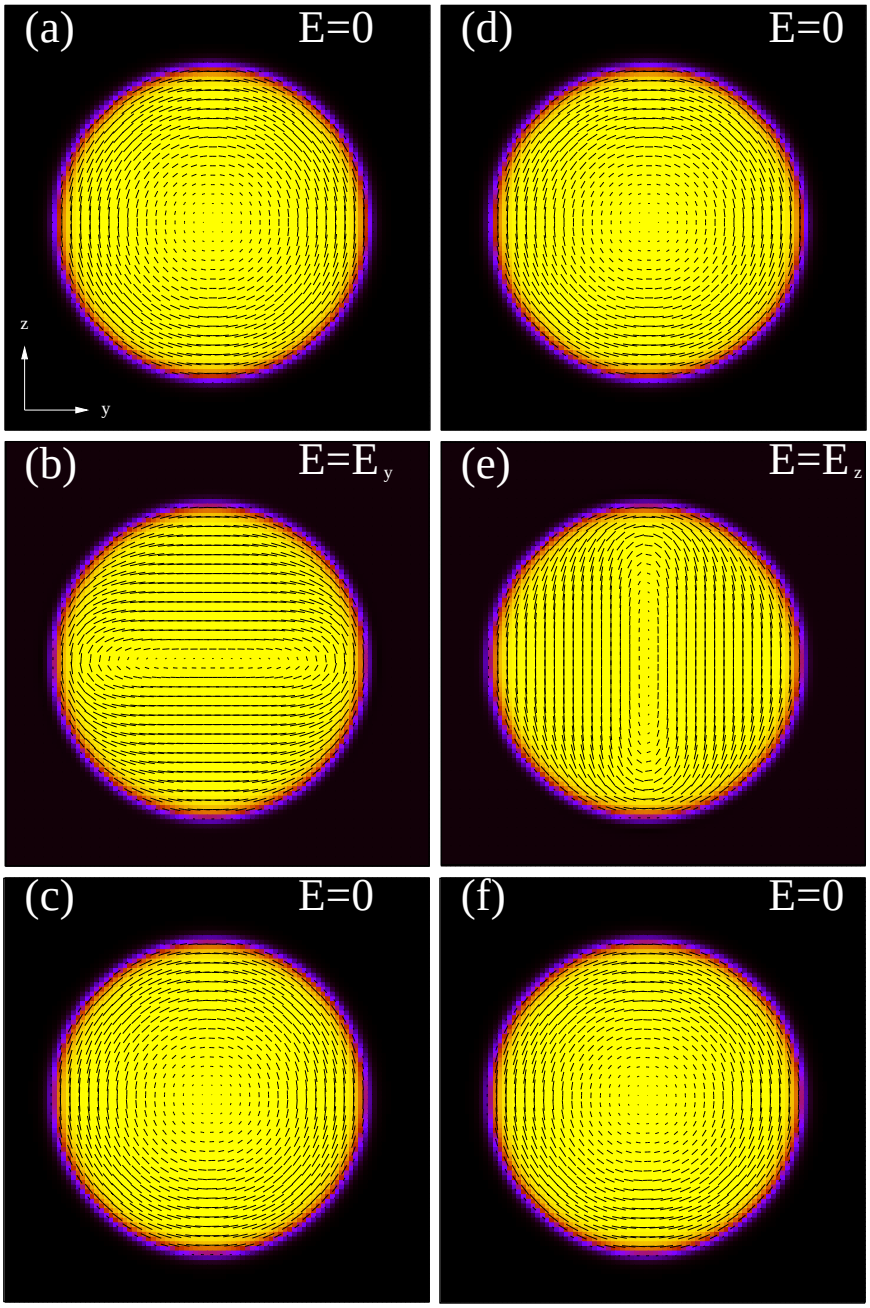

Figure 4.6: Switching dynamics of a cholesteric droplet with $N = 2$ under an electric field applied along the y ((a)-(c) and z direction ((d)-(f)) with $\Delta V = 3$ and $W = 0.04$ (strong tangential anchoring). (a)-(d) ($t = 4 \times 10^5$), the field is ON in (b)-(e) ($t = 7 \times 10^5$) and OFF in (c)-(f) ($t = 10^6$) where t is the simulation time. The final states (c) and (f) are equal to the initial state (a).)

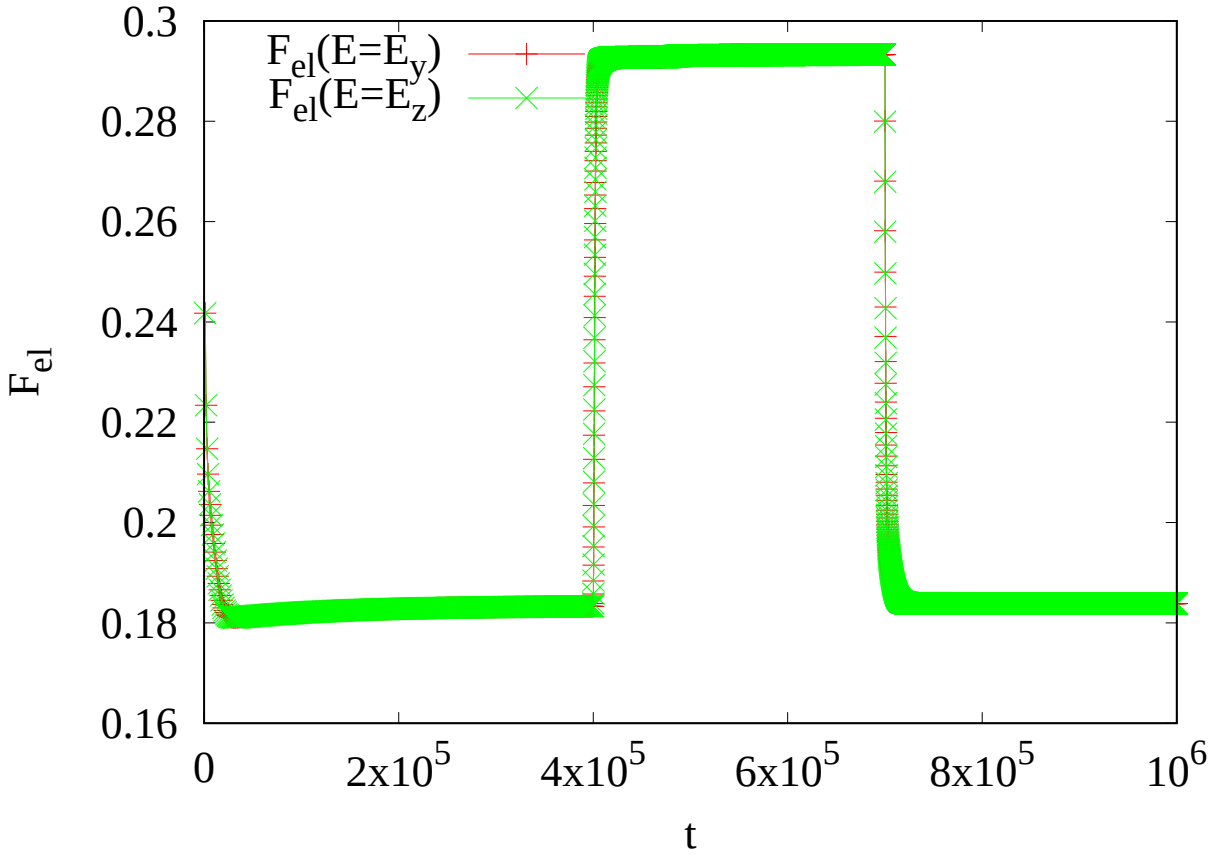

Figure 4.7: Elastic free energy of the droplet during a switching dynamics, with the electric field applied along y-direction (red curve, plusses) with voltage $\Delta V_y = 3$ and along the z-direction (green, crosses) with voltage $\Delta V_z = 3$, both for $N = 2$ ($q_0 = 2\pi/64$) and strong tangential anchoring ($W = 0.04$). The field is switched on at simulation time $t = 4 \times 10^5$ and switched off at $t = 7 \times 10^5$. The final elastic free energies for both cases are equal the one of the equilibrium.

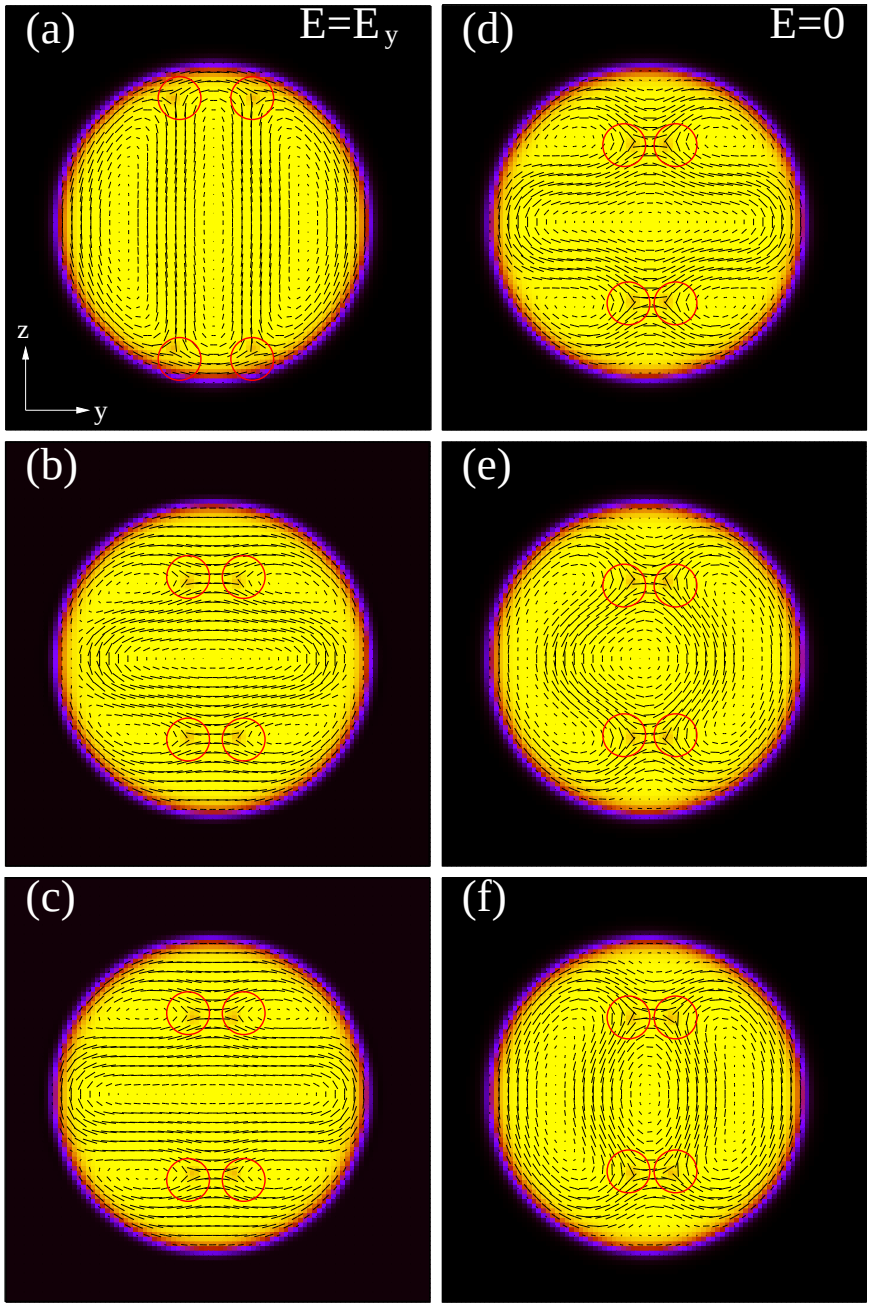

Figure 4.8: Switching dynamics of a cholesteric droplet with $N = 4$ under an electric field applied along the y-direction with $\Delta V = 3$ and $W = 0.04$ (strong tangential anchoring). The field is ON in (a) ($t = 4 \times 10^5$), (b) ($t = 4.5 \times 10^5$) and (c) ($t = 7 \times 10^5$) and OFF in (d) ($t = 7.05 \times 10^5$), (e) ($t = 7.5 \times 10^5$) and (f) ($t = 10^6$), where t is the simulation time. In particular (c) and (f) represent steady states achieved when the electric field is ON and OFF, respectively. At the end of the cycle the droplet is stuck into a novel metastable state achieved through a complex internal rearrangement of the topological defects.

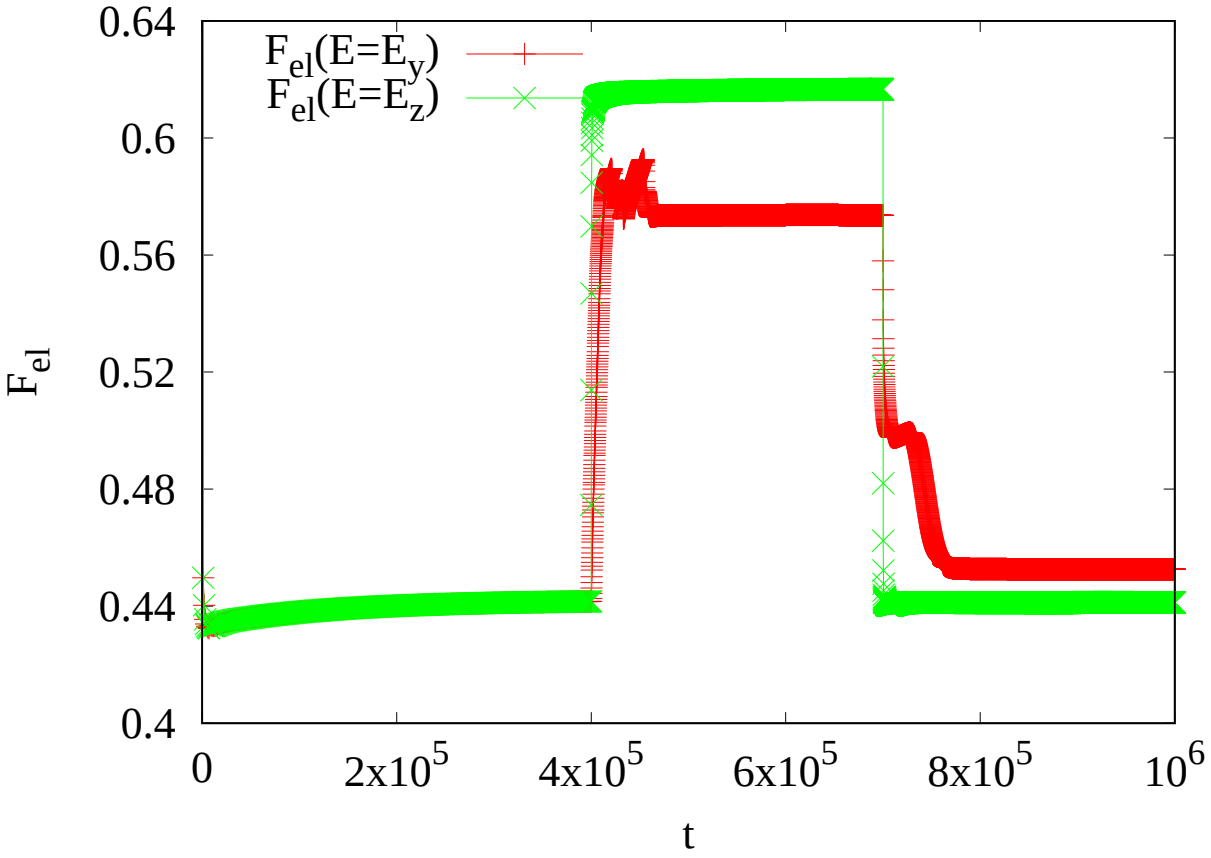

Figure 4.9: Elastic free energy of the droplet during a switching dynamics, with the electric field applied along y-direction (red curve, plusses) with voltage $\Delta V_y = 3$ and along the z-direction (green, crosses) with voltage $\Delta V_z = 5$, both for $N = 4$ ($q_0 = 2\pi/32$) and strong tangential anchoring ($W = 0.04$). The field is switched on at simulation time $t = 4 \times 10^5$ and switched off at $t = 7 \times 10^5$. In the former case the final field-off state has higher elastic free-energy than the initial one.

of the droplet as the director aligns parallel to the z-direction, while the $+1$-charge regions slightly stretch along the field direction. When the field is switched off the in-plane defects migrate back to the initial position driving the system to a new final metastable state (Fig. 4.9), whose director arrangement is similar to the initial equilibrium state.

4.6.3 W=-0.04, homeotropic anchoring

A much richer phenomenology is observed when the surface anchoring is homeotropic. In the case with $N = 2$ where the defect arrangement of the equilibrium configuration (Fig 4.2-(c)) is simpler. Its switching on-off dynamics is reported in Fig. 4.10 when the electric field is applied along the y-direction. During the first half cycle in which the electric field is on (Fig. 4.10-(a)-(c)), while the director aligns along the direction of **E**, a temporary in-plane defect of charge -1 emerges at the centre of the droplet. This defect is unstable and later on it splits into two twist disclinations of charge $-1/2$ each. The initial $+1$-charge region switches to two separate double twist regions, separated by a hyperbolic hedgehog in the centre (whose topological charge is -1). Due to the alignment of the director field along the direction of **E** the defects near the surface change their topological charge and their nature. The two $\tau^{1/2}$ defects along the equator became two twist disclinations of charge $-1/2$, whereas the two twist disclinations of charge $-1/2$ (located along the north/south direction) turn into two $\tau^{1/2}$ defects. Although the switching-off protocol has negligible effects on the defect dynamics, it favours the formation of two large symmetric splay-bend deformations spanning the whole droplet (Fig. 4.10-(d)-(f)). The defects nearby the interface return to their initial field-off configuration whereas those in the bulk turn into two fully in-plane $-1/2$ defects.
The case with $N = 4$ starts from an equilibrium configuration characterised by a large number of defects, which makes the switching dynamics more complex due to the onset of new metastable states. This is expecially true when the electric field ($\Delta V = 5$) is applied along the helix axis (Fig. 4.11). Indeed after the field is switched on (Fig. 4.11-(a)-(c)), the director undergoes a complex reorientation dynamics ending with an almost fully nematic ON state (along the y-direction) decorated with several defects. In particular several pairs of twist disclinations of charge $-1/2$ are anchored to $+1$-charge regions (and usually are pinned there by $\lambda^{+1/2}$ defects immediately nearby each of the defect). These structures span the bulk of the droplet, while two $\tau^{1/2}$ disclinations are stuck at the interface. After the field is switched off (Fig. 4.11-(d)-(f)), the liquid crystal relaxes towards a new metastable state in which some defects cluster deep inside the droplet while the remaining ones are located close to the interface. The director, in turn, develops a more intricate profile, in which pronounced bend distortions in the vicinity of the defects are spaced out by $+1$-charge regions.
If the field, instead, is applied along the z-direction, a less complex, but more intriguing dynamics is observed. During the ON dynamics, while the director progressively aligns along the direction of the electric field, the defects located symmetrically in the north and south part of the droplet move towards its centre, leaving a characteristic straight stripe signature which identifies regions where the director lies along the x-direction (Fig. 4.12-(a)-(c)). If the electric field is strong

enough the final ON state is an almost nematic phase aligned along the z-direction, in which a central stripe with out-of-plane director orientation is sustained by two twist disclinations of charge $-1/2$. The two $\tau^{1/2}$ defects that survive in the ON state are those located along the equatorial line, whose position was unaffected by the switching on dynamics (Fig. 4.12-(c)). During the switching OFF relaxation (Fig. 4.12-(d)-(f)), the two defects inside the droplet move back to the interface while the director gradually relaxes into a final state in which splay-bend distortions emerge as a result of the strong homeotropic anchoring. Regardless of the direction of the applied field, after one cycle the liquid crystal gets stuck into a metastable state, whose elastic free-energy is higher than the equilibrium one (Fig. 4.13) and is very similar to the equilibrium one for $N = 2$ (Fig. 4.2-(e)).

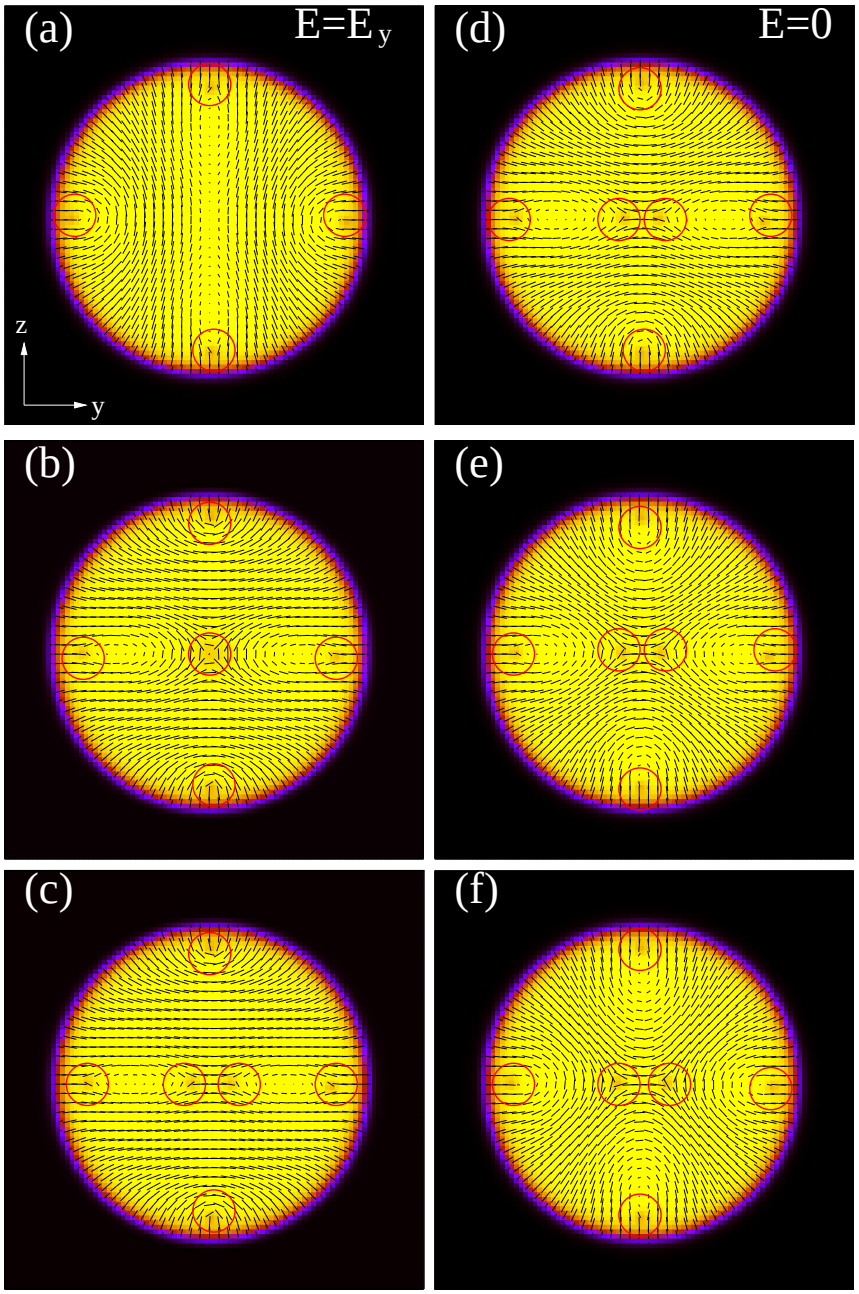

Figure 4.10: Switching dynamics of a cholesteric droplet with $N = 2$ under an electric field applied along the y-direction with $\Delta V = 2.5$ and $W = -0.04$ (homeotropic anchoring). The field is ON in (a) ($t = 4 \times 10^5$), (b) ($t = 4.15 \times 10^5$) and (c) ($t = 7 \times 10^5$) and OFF in (d) ($t = 7.02 \times 10^5$), (e) ($t = 7.08 \times 10^5$) and (f) ($t = 10^6$), where t is the simulation time. In particular (c) and (f) represent steady states achieved when the electric field is ON and OFF, respectively. After one switching cycle two in-plane $-1/2$ defects form in the centre of the droplet sustained by intense bend distortions induced by the surface homeotropic anchoring.

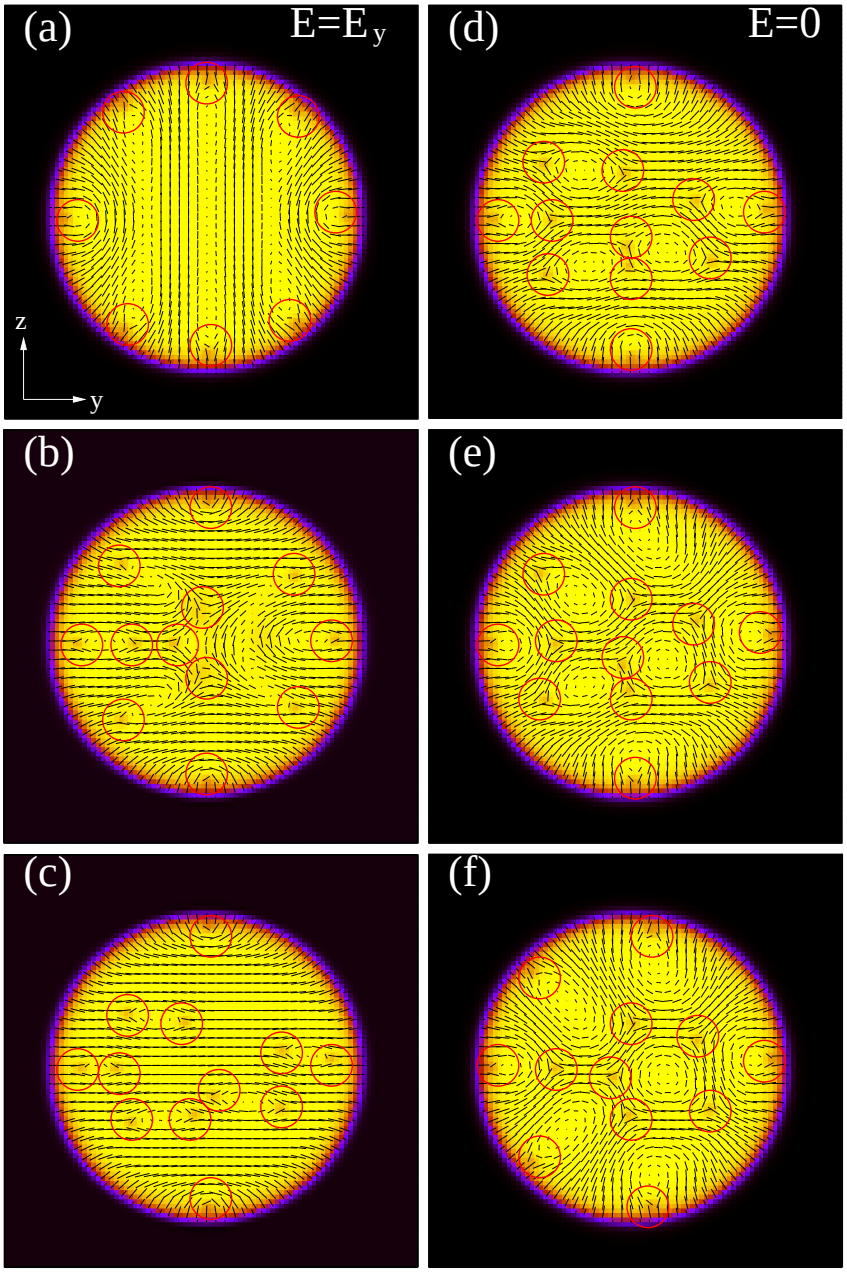

Figure 4.11: Switching dynamics of a cholesteric droplet with $N = 4$ under an electric field applied along the y-direction with $\Delta V = 5$ and $W = -0.04$ (strong homeotropic anchoring). The field is ON in (a) ($t = 4 \times 10^5$), (b) ($t = 4.03 \times 10^5$) and (c) ($t = 7 \times 10^5$) and OFF in (d) ($t = 7.01 \times 10^5$), (e) ($t = 7.08 \times 10^5$) and (f) ($t = 10^6$), where t is the simulation time. In particular (c) and (f) represent steady states achieved when the electric field is ON and OFF, respectively. A complex dynamics is observed during the entire switching cycle. The initial symmetric defect arrangement is destroyed by the electric field and, during the off dynamics, the droplet relaxes towards a new metastable state with several defects.

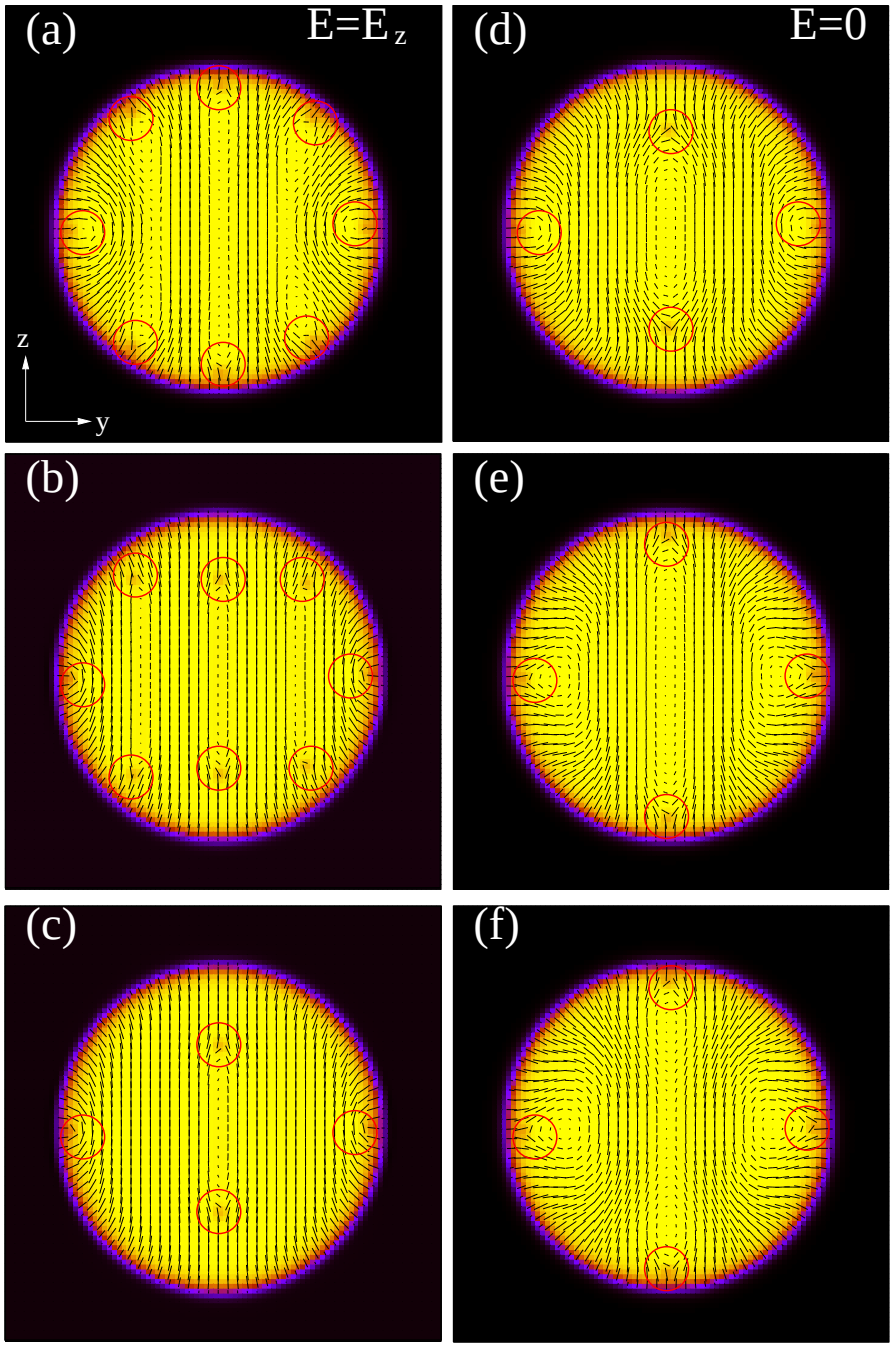

Figure 4.12: Switching dynamics of a cholesteric droplet with $N = 4$ under an electric field applied along the z-direction with $\Delta V = 5$ and $W = -0.04$ (homeotropic anchoring). The field is ON in (a) ($t = 4 \times 10^5$), (b) ($t = 4.1 \times 10^5$) and (c) ($t = 7 \times 10^5$) and OFF in (d) ($t = 7.01 \times 10^5$), (e) ($t = 7.08 \times 10^5$) and (f) ($t = 10^6$), where t is the simulation time. The defect dynamics is overall simpler than the previous case (Fig. 4.11); indeed a cholesteric-like fashion of the director field is obtained after one switching cycle.

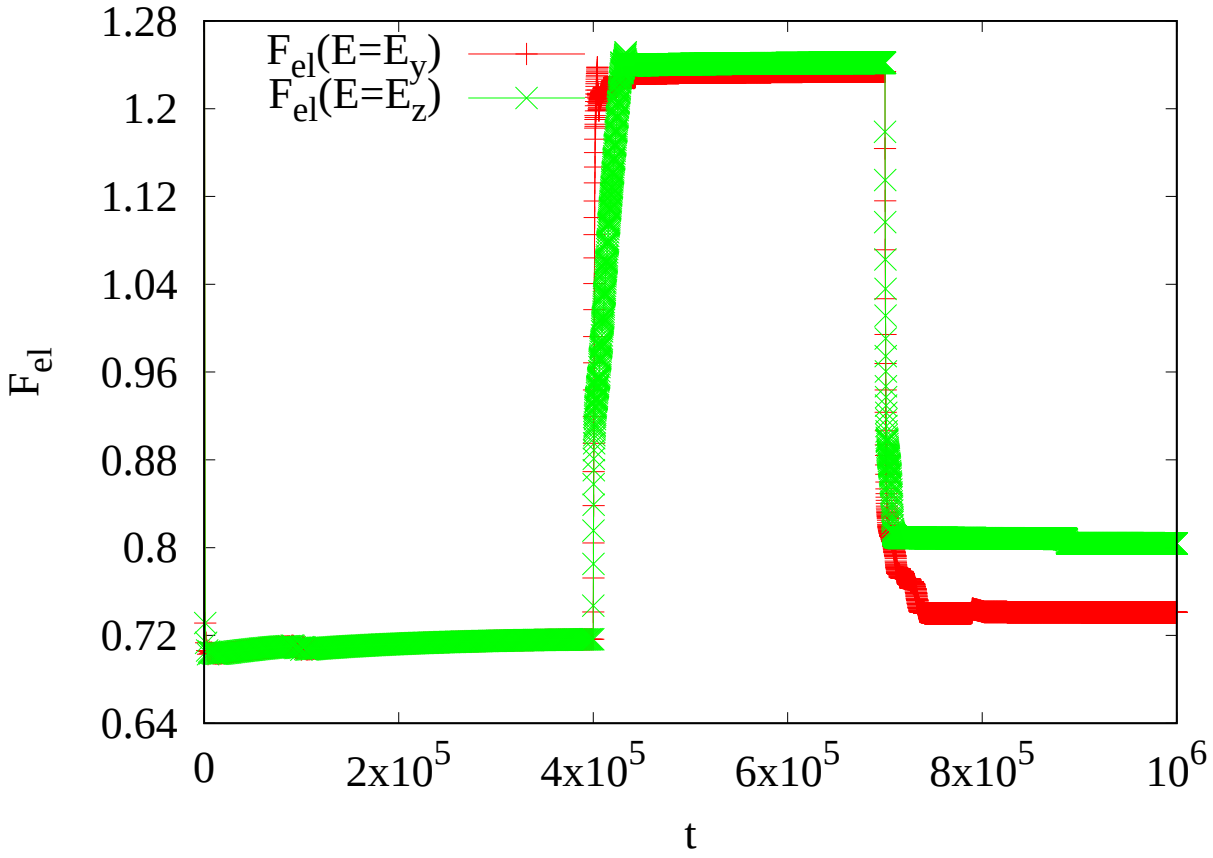

Figure 4.13: Elastic free energy of the system when a uniform electric field is switched along y-direction (red curve) with voltage $\Delta V_y = 5$ and along the z-direction (green) with voltage $\Delta V_z = 5$, both for $N = 4$ ($q_0 = 2\pi/32$) and strong homeotropic anchoring ($W = -0.04$). The field is switched on at simulation time $t = 4 \times 10^5$ and switched off at $t = 7 \times 10^5$. The field-off states (before and after one switching cycle) have different values in both cases.

4.7 Nematization thresholds study

As reported in Chaper 2, the elastic constant is related to the elastic distortions of the liquid crystal but also is related to the resistance of the liquid crystal under the action of electric fields. The higher the value of the elastic constant, the higher will be the threshold to destroy the cholesteric helix and to nematize the system.
It is known in literature that if the magnetic reaches a critical value or treshold it can unwound the helix and the cholesteric liquid crystal becomes a nematic. These results present in literature were obtained by experiments with choelesteric samples subjected to an external magnetic field perpendicular or parallel to the helix [30, 31] and the relation between the critical acting magnetic field with the elastic constant is of kind

$$H_c \sim k_2^{\frac{1}{2}} \tag{4.16}$$

where k_2 is the elastic constant related to the twist distortions.
The purpose of this kind of simulations, in the case of cholesteric liquid crystal droplet, was to find the electric field tresholds for different values of the elastic constants for fixed values of the anchoring strengths and pitches of the helix and discover the relation between the electric treshold with the elastic constant working always in one constant approximation.
The elastic constants were varied in the range $[10^{-4}; 10^{-1}]$ in the simulations, with anchorings $|W| = 0.04$, $W = -0.1$, $W = 0.4$, $W = 0$, always keeping in mind the phase diagram of liquid crystals to ensure the permanence in the correct cholesteric region.
The plots of the thresholds as function of the elastic constants for fixed values of the pitch and anchoring strength are reported in Fig. 4.14 and 4.15 for both cases $N = 4$ ($q_0 = 2\pi/32$) and $N = 2$ ($q_0 = 2\pi/64$) for both the directions of the electric field. A possible reason is the fact that in the first case, the field must destroy two twists of the helix instead of four as in the second case.
The thresholds for $N = 2$, in Fig. 4.15-(a)-(b) for the electric field along the y and the z directions respectively, are slightly lower than the ones for $N = 4$, Fig. 4.14-(a)-(b). Another difference is the fact that the cases for homeotropic anchoring nematize more easily than the correspondent tangential cases. The limiting case of $W = 0$ seems to be intermediate between the extremal cases of tangential and homeotropic ones. A crude physical explanation for this behaviuor can be the following: the effect of the electric field is the alignment of the director in the same direction (for positive dielectric constant) and then the field must be strong enough to destroy the helix. Thus if the anchoring of the director on the droplet is homeotropic, the director is already "partially aligned" with the field and so the value of the voltage to nematize the cholesteric is lower than the corresponding tangential case. In this situation in fact the director lies on the surface of the droplet and so the electric field has to be stronger in order to let the director to go out the

surface, to align with the field and to destroy the cholesteric helix. The particular case of $W = 0$ is characterized by the fact that the **Q** tensor is decoupled from the intarface of the droplet and the director is free to reorganize in the droplet assuming an intermediate structure "partially tangential" and "partially homeotropic". Fits of the simulation data with the relation

$$aK^b \tag{4.17}$$

of the elastic constant K with parameters a and b to be fitted were performed. All the values of the parameters are contained in Table 4.1, for $N = 4$, and Table 4.2, for $N = 2$. For fixed anchoring and pitch, there is no big difference between the threshold values for the field along the y and the z directions; instead the factors which surely influence the variations of the values are the type of pitch and the type of anchoring.

W	a_y	b_y	a_z	b_z
0	17.5594	0.29174	30.5737	0.373217
0.04	41.7276	0.417452	44.911	0.432591
0.4	40.8096	0.417452	44.241	0.427791
-0.04	24.6439	0.432882	24.0987	0.426673
-0.1	25.2599	0.439411	24.0096	0.426899

Table 4.1: Fit parameters for various anchoring for helical pitch $q_0 = 2\pi/32$. a_y, b_y, a_z, b_z are respectively the fitted coefficients; the subscript y or z refers to the case of electric field switched along the y or z directions.

W	a_y	b_y	a_z	b_z
0	13.5476	0.286681	24.1122	0.355319
0.04	35.5689	0.414693	35.0191	0.409268
0.4	35.5689	0.414693	35.8414	0.417557
-0.04	9.23196	0.335771	9.89511	0.342129
-0.1	9.56097	0.343773	11.4406	0.384937

Table 4.2: Fit parameters for various anchoring for helical pitch $q_0 = 2\pi/64$. a_y, b_y, a_z, b_z are respectively the fitted coefficients; the subscript y or z refers to the case of electric field switched along the y or z directions.

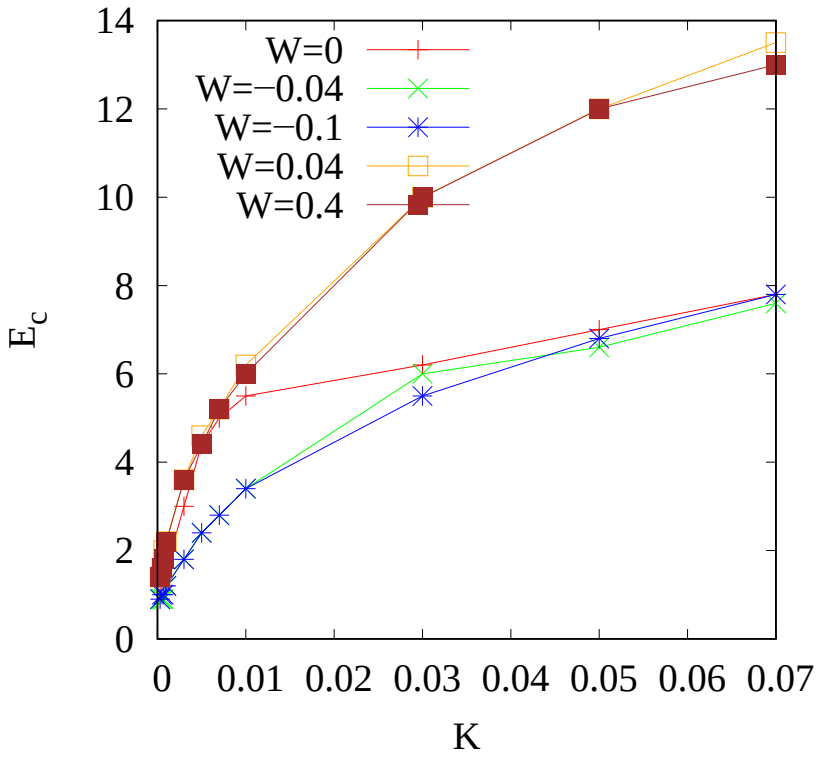

(a)

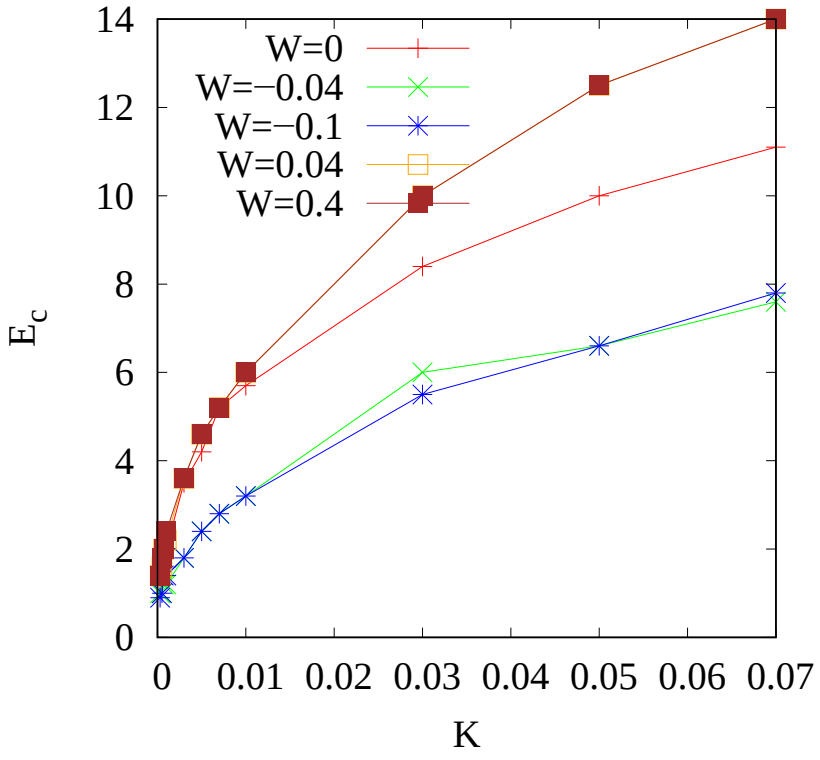

(b)

Figure 4.14: Nematizing tresholds for pitch $q_0 = 2\pi/32$ as function of the elastic constant K if the electric field is switched along y-direction (a) or z-direction (b).

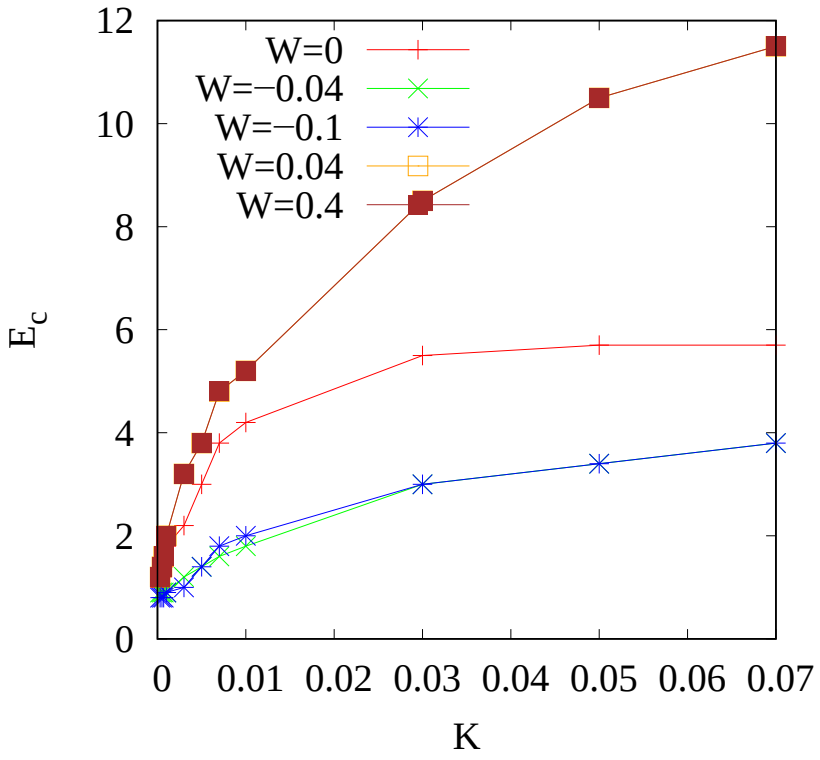

(a)

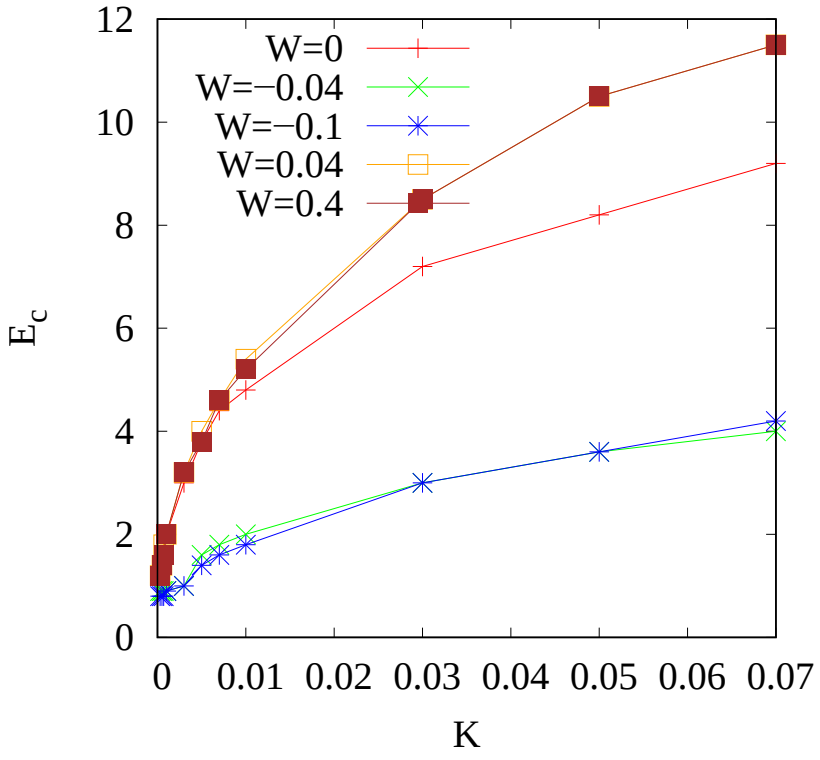

(b)

Figure 4.15: Nematizing tresholds for pitch $q_0 = 2\pi/64$ as function of the elastic constant K if the electric field is switched along y-direction (a) or z-direction (b).

4.8 Switching dynamics for a cholesteric channel

This section analyzes the role played by the curvature of the boundary in the switching dynamics by looking at the simpler case of a cholesteric phase confined between straight walls and comparing the results with the analogous cases of a droplet.
The two parallel walls were located at $z = 0$ and $z = 64$ lattice units instead along the y-direction periodic boundary conditions were considered. The equilibrium configuration corresponds to a full cholesteric phase (namely $\phi \simeq \phi_0$ everywhere) with helix axis along the y-direction and $N = 4$ (Fig. 4.16-(a)). Strong tangential anchoring has been set at the walls as well as no-slip condition for the fluid velocity ($\mathbf{u}_w = 0$). Because of the conflict orientation between the cholesteric phase at the boundary and the tangential anchoring, this set up favours the formation of eight defects of topological charge $-1/2$ pinned at the walls and four $+1$-charge regions in the bulk (each of these has two $\lambda^{+1/2}$ defects at its boundary). Differently from the droplet of Fig. 4.2-(a), the planar wall set up can accomodate all the eight defects expected for a helix with $N = 4$ twist. When the field is switched on along the y-direction, defects located on opposite sides approach each other, as the director aligns parallel to **E** by starting from the wall and then penetrating into the bulk (Fig. 4.16-(b)). The defect motion persists until they get stuck roughly at the middle of the cell (Fig. 4.16-(c)-(d)), by which time each has rotated by almost 90°. When the field is switched off (Fig. 4.16-(e)-(h)), the defects rotate and migrate back towards the wall; however they get stuck before reaching it, so that the cholesteric only partially recovers its twisted arrangement. This is because there is not enough driving force to twist the director field close to the walls, where there is strong tangential anchoring.

Therefore, while within the droplet, of Fig. 4.8, a cholesteric order is restored almost completely after a switching cycle (Fig. 4.8-(h)), with flat walls this is not the case: in this case, curvature facilitates going back to the equilibrium (field off) pattern. The equilibrium elastic free energy of the two cases (droplet vs flat planes) is different (Fig. 4.17 and Fig. 4.9): in particular, lower values of the free energy are reported for flat walls, as weaker distortions are formed there. Indeed, the presence of regions of different orientation of the director field (due to the presence of topological defects) appears to be more favoured within higher curvature domains.
Another comparison was performed between the case of Fig. 4.18 with the case of the channel with homeptropic anchoring to walls in Fig. 4.12.
At first in the equilibrium case of Fig. 4.18 the homeotropic condition of the director to the walls favours the formation of eight twist disclinations (four per wall) of charge $-1/2$ and four central λ regions of charge $+1$. The swithching on of a field along the z direction with voltage $\Delta V = 5$ determines the complete destruction of

the defects and consequent nematization of the channel with director everywhere parallel to the vertical axis. After the switching off of the field the system reshapes and acquire a distorted structure defect free.
In this case the curvature of the system is important because the droplet of Fig. 4.12 resists to complete nematization and preserves its cholesteric structure with defects, the channel becomes nematic with elastic free energy lower than the case of the droplet (Fig 4.19 and Fig. 4.12).

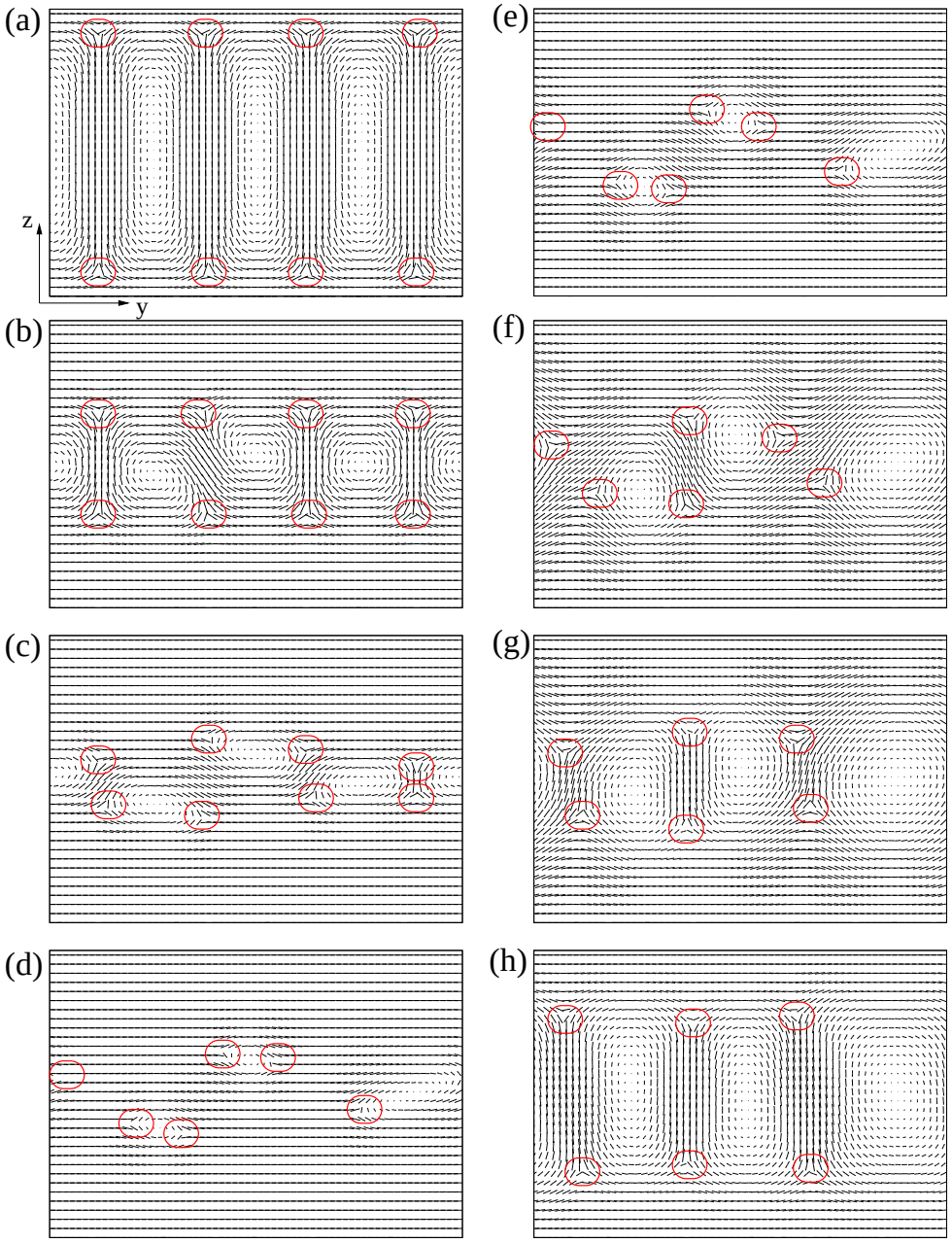

Figure 4.16: Switching dynamics of a cholesteric liquid crystal confined between two flat solid walls and under an electric field applied along the y-direction, with $\Delta V = 3$, strong tangential anchoring to the walls, $L_z = 64$ and $L_y = 128$. The field is ON in (a) ($t = 10^5$), (b) ($t = 1.05 \times 10^5$), (c) ($t = 1.1 \times 10^5$) and (d) ($t = 4 \times 10^5$) and OFF in (e) ($t = 4.01 \times 10^5$), (f) ($t = 4.05 \times 10^5$), (g) ($t = 4.1 \times 10^5$) and (h) ($t = 7 \times 10^5$), where t is the simulation time. In particular (d) and (h) represent steady states achieved when the electric field is ON and OFF, respectively. After one switching cycle a cholesteric arrangment is almost restored in the bulk of the cell, but not close to the boundaries.

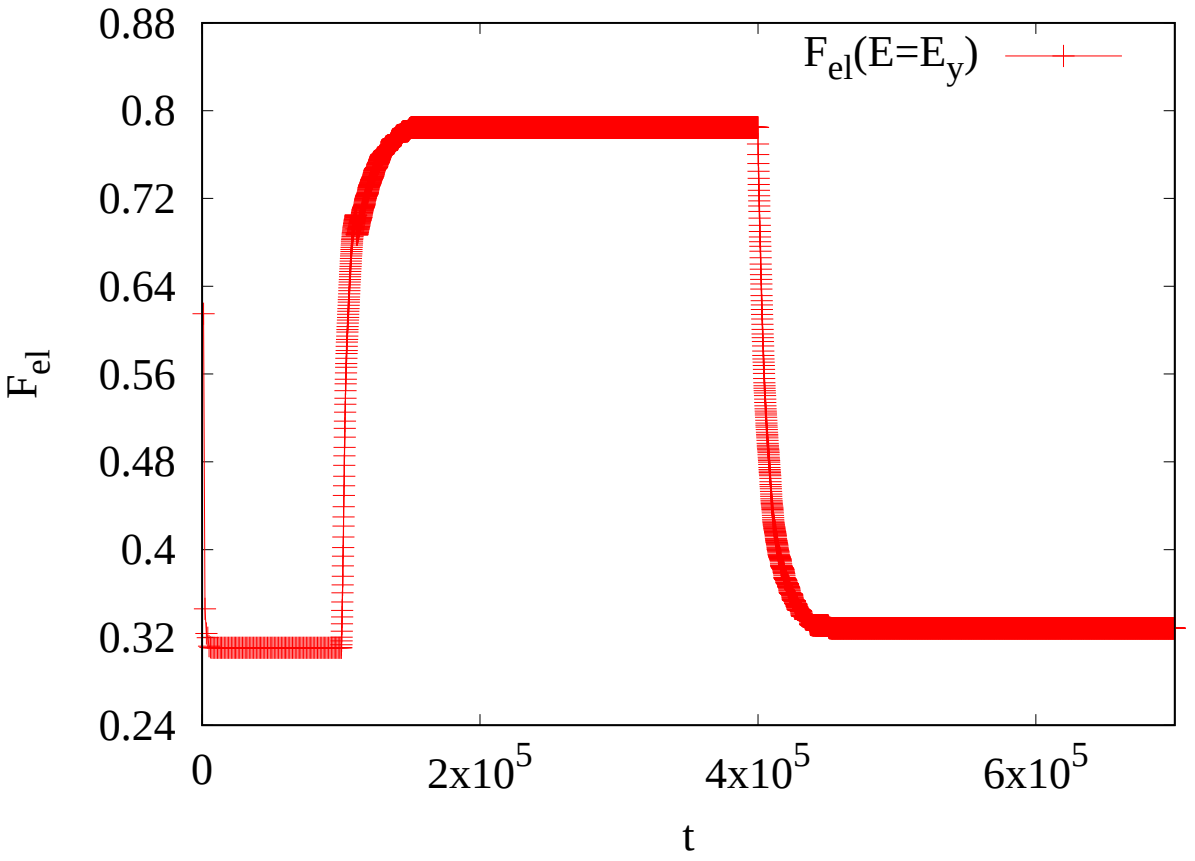

Figure 4.17: Elastic free energy of cholesteric liquid crystal when confined between flat walls. The electric field is switched on along the y-direction (with $\Delta V_y = 3$) at simulation time $t = 10^5$, and switched off at $t = 4 \times 10^5$.

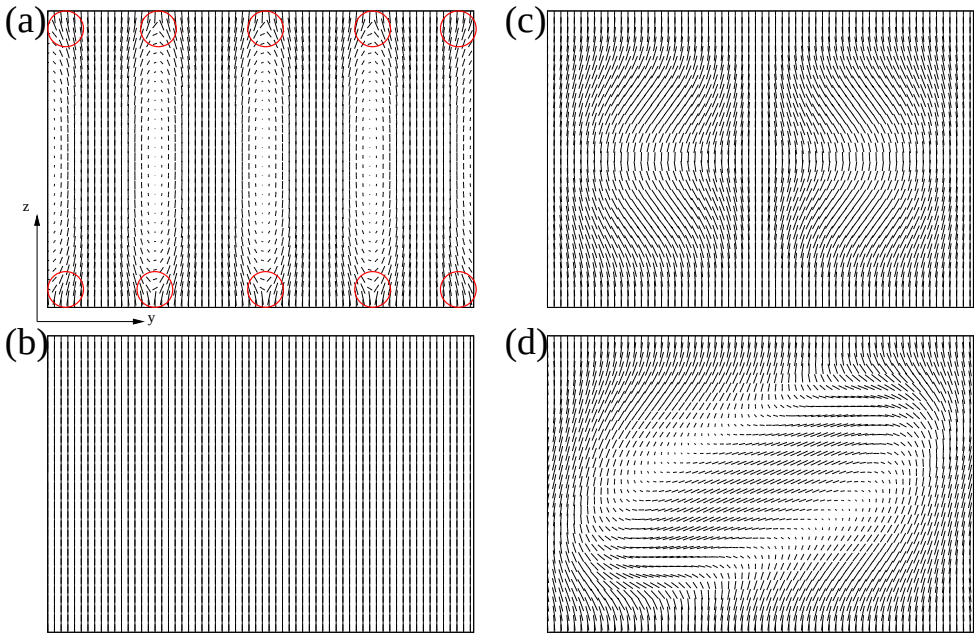

Figure 4.18: Switching dynamics of a cholesteric liquid crystal confined between two flat solid walls and under an electric field applied along the z-direction, with $\Delta V = 5$, strong homeotropic anchoring to the walls, $L_z = 64$ and $L_y = 128$. (a) ($t = 10^5$), (b) ($t = 4 \times 10^5$) field ON, (c) ($t = 5 \times 10^5$) and (d) ($t = 7 \times 10^5$) field OFF where t is the simulation time. The field in this situation nematizes the structure.

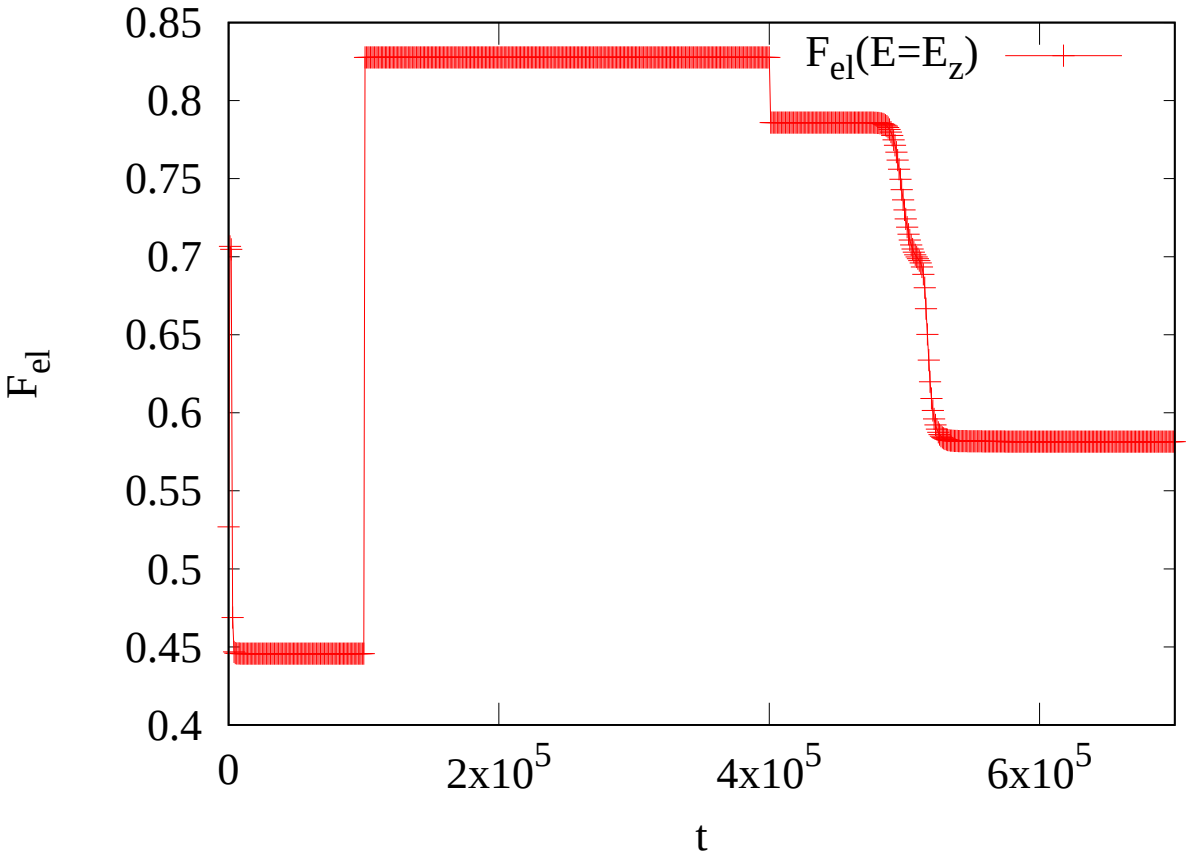

Figure 4.19: Elastic free energy of cholesteric liquid crystal when confined between flat walls. The electric field is switched on along the z-direction (with $\Delta V_z = 5$) at simulation time $t = 10^5$, and switched off at $t = 4 \times 10^5$.

4.9 Effect of a rotating electric field

In this section the dynamics in presence of a time-dependent non-uniform, periodically rotating electric field at constant frequency ω is introduced. This is achieved by setting

$$E_y = -\Delta V_y sin(\omega t)/L_y, \qquad E_z = \Delta V_z cos(\omega t)/L_z, \tag{4.18}$$

with ω frequency, which determines a counterclockwise rotation.
Applying a rotating field is another way of achieving the Lehmann effect, also called electric Lehmann effect, which arises due to a torque term, proportional to $\mathbf{n} \times \mathbf{E}$, in the expression of the molecular field of the Leslie-Erickes theory which wasn't treated in this study [133]. Fig. 4.20 and Fig. 4.21 show the dynamics of a cholesteric droplet subject to a rotating electric field with $\Delta V_y = \Delta V_z = 4$, $\omega = 5 \times 10^{-3}$ and with strong tangential anchoring at the droplet surface. The initial configuration is the equilibrium one reported in Fig. 4.2-(e) for a cholesteric phase with $N = 4$ and helix axis along the y-direction. Under the action of the electric field the four defects, initially located at the droplet surface (Fig. 4.20-(a)) start to rotate counterclockwise (Fig. 4.20-(b)) and then move towards the centre of the droplet. The $+1$ charge regions also reshape, and the cholesteric layers temporarily align along a common direction (Fig. 4.20-(c)) and then merge. The electric field, in turn, tends to destroy the initial cholesteric order, and to favour the formation of regions in which the director is aligned along its direction (Fig. 4.20-(c)-(d)), except nearby the interface where strong anchoring keeps the director fixed. The corresponding velocity field is reported in Fig. 4.20-(e)-(h) characterized by a vortex pattern that is almost negligible at the droplet centre and higher in proximity of the interface.
If homeotropic anchoring is set on the surface, with $\omega = 10^{-3}$, the equilibrium state has eight defects at the droplet surface (Fig. 4.2-(f)) and three $+1$-charge regions in its bulk. This structure leads to a more complex dynamics under a rotanting electric field (Fig. 4.21-(e)-(h) right column). If it rotates counterclockwise, defects near the interface rotate coherently but, unlike the previous case, they remain close to the interface and reduce first to six and finally to four. Interestingly though, a twisted-like arrangement is still observed during a rotation; regions in which the director is almost fully aligned are spaced out by $+1$-charge regions with λ defects, where the director escapes out of the plane. This structure appears periodically during the rotation, approximately after each half turn of the director field.
The case for $N = 2$ and tangential anchoring of Fig. 4.22-(a)-(d) left column is trivial because starting from the original equilibrium configuration, of Fig. 4.2-(b), with central λ^{+1} region, the rotating field splits the defect in a $+1$-region which periodically rotates in time.
In the analogous case for homeotropic anchoring of Fig. 4.22-(e)-(h) right column

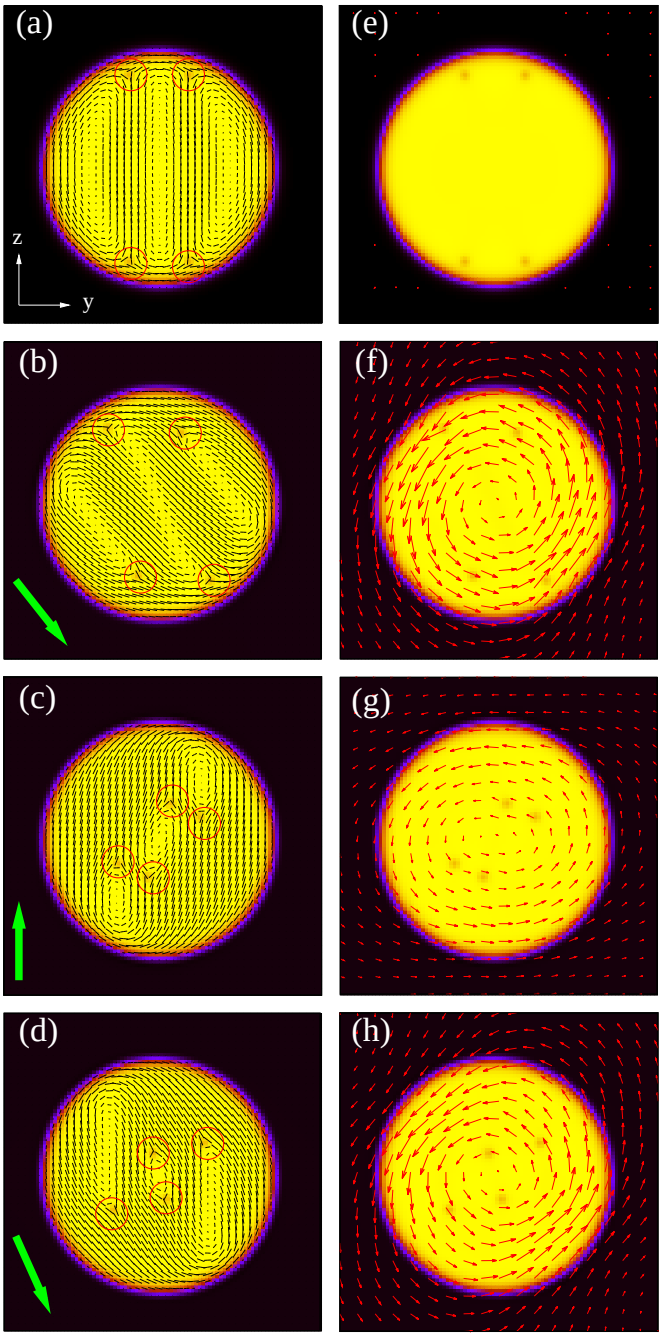

Figure 4.20: Dynamics of a cholesteric droplet (with $N = 4$) under a counter-clockwise rotating electric field. The reduced potential is with $\Delta V_y = \Delta V_z = 4$, $\omega = 5 \times 10^{-3}$ and $W = 0.04$ (strong tangential anchoring). The left column displays director and defect dynamics; the right column displays the velocity field. The green arrow indicates the direction of the electric field. Corresponding simulation times are $t = 4 \times 10^5$ for (a)-(e), $t = 4.1 \times 10^5$ for (b)-(f), $t = 4.3 \times 10^5$ for (c)-(g), and $t = 4.75 \times 10^5$ for (d)-(h).

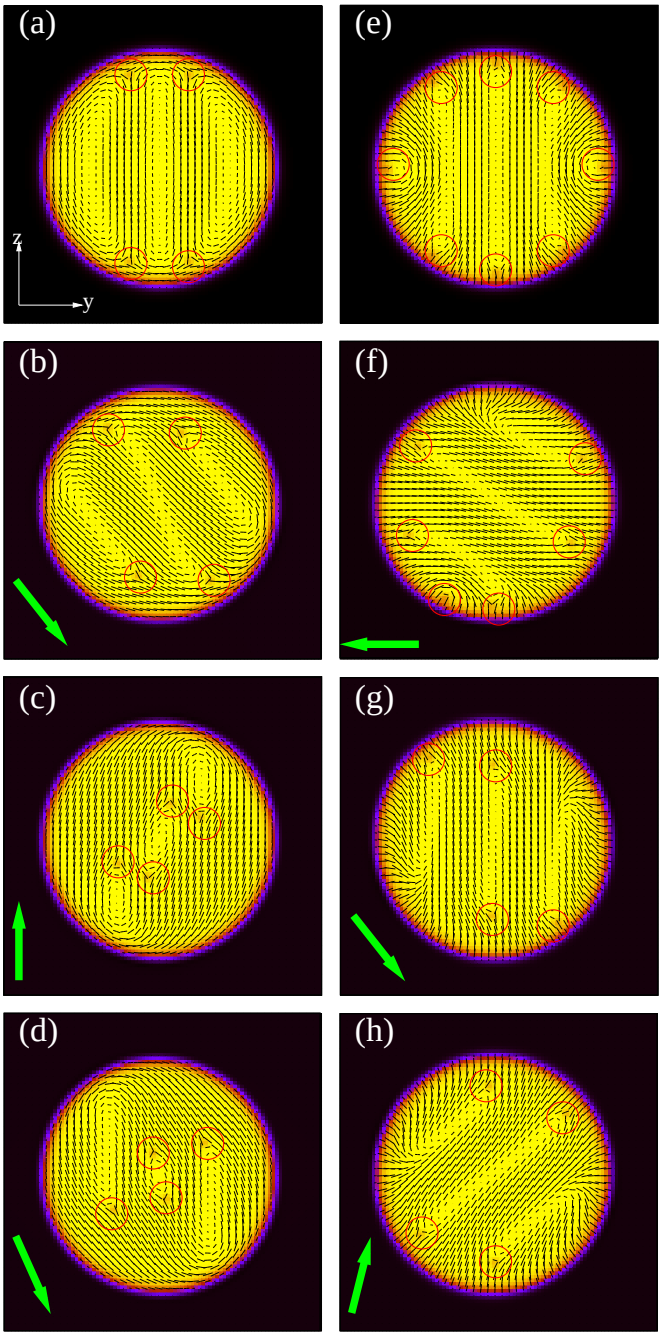

Figure 4.21: Dynamics of a cholesteric droplet under a counterclockwise rotating electric field. The left column (a)-(d) refers to the case for $N = 4$ and $W = 0.04$ for frequency $\omega = 5 \times 10^{-3}$ and the right column (e)-(h) for $N = 4$ and $W = -0.04$ for frequency $\omega = 10^{-3}$. The reduced potential is with $\Delta V_y = \Delta V_z = 4$. The green arrow indicates the direction of the electric field. Corresponding simulation times, for left column, are $t = 4 \times 10^5$ for (a), $t = 4.1 \times 10^5$ for (b), $t = 4.3 \times 10^5$ for (c) and $t = 4.75 \times 10^5$ for (d). For the right column $t = 4 \times 10^5$ for (e), $t = 4.5 \times 10^5$ for (f), $t = 5.6 \times 10^5$ for (g) and $t = 7 \times 10^5$ for (h). t is in simulation time.

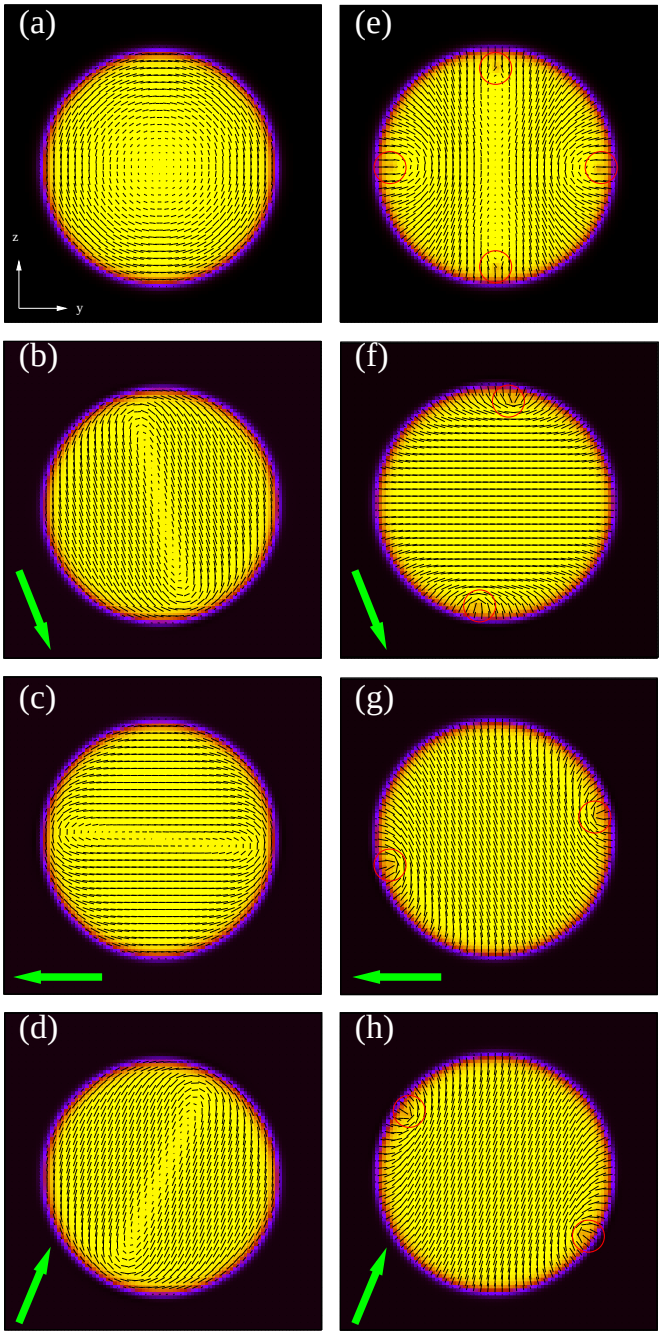

Figure 4.22: Dynamics of a cholesteric droplet under a counterclockwise rotating electric field. The left column (a)-(d) refers to the case for $N = 2$ and $W = 0.04$ and the right column (e)-(h) for $N = 2$ and $W = -0.04$ both for frequencies $\omega = 10^{-3}$. The reduced potential is with $\Delta V_y = \Delta V_z = 4$. The green arrow indicates the direction of the electric field. Corresponding simulation times, for both columns, are $t = 4 \times 10^5$ for (a), $t = 4.5 \times 10^5$ for (b), $t = 5.6 \times 10^5$ for (c) and $t = 7 \times 10^5$ for (d). t is in simulation time.

the field destroys the helix turning the bulk into a nematic and leaving only the two $\tau^{+1/2}$ extremal defects which rotate periodically in time.
A quantitative analysis related to the rotating electric field consisted in computing the angular velocity of the droplet, ω^*, as function the frequency ω of the electric field as

$$\omega^* = \frac{\int dV \phi \mathbf{r} \times \mathbf{u}}{\int dV \phi r^2} \tag{4.19}$$

where $\mathbf{r}$ is the vector position of a lattice site respect to the center of mass of the droplet calculated as follows

$$\mathbf{r}_{CM}(t) = \frac{\sum_{ijk} \phi_{ijk} \mathbf{r}(t)}{\sum_{ijk} \phi_{ijk}} \tag{4.20}$$

where i, j, k are the indexes of a lattice site and the sum is performed inside the droplet.
In Fig. 4.23-(a)-(b) the curves for all the cases are shown with Fig. 4.23-(b) showing an inset for $N = 4$ for $|W| = 0.04$ and $N = 2$ for $W = -0.04$. In all the cases shown there is a general trend to rise reaching a maximum value for approximately $\omega = 10^{-2}$ as sign that the droplet rotates faster increasing the frequency of the field but then, for higher frequencies ($\omega > 10^{-2}$), inertia dominates and the droplet doesn't rotate fast with the field or doesn't rotate anymore. The case for $N = 2$ and $W = 0.04$ of Fig. 4.23-(a) seems to be the fastest case with values of ω^* one order of magnitude greater than the case for $N = 4$ and $W = 0.04$. This could be crudely explained with the fact that the case $N = 2$ with $W = 0.04$ the structure of the topological defects is simple consisting in the starting λ^{+1} defect which splits in the $+1$ region and for higher frequencies ($\simeq 10^{-2}$) the bulk structure is practically nematic. The homeotropic cases are also slower than the correspondent tangential cases; this difference could be crudely explained in terms of a permeation-like effect. Indeed a vortex flow field, typically tangential nearby the interface, would encounter a larger resistance (namely an increased viscosity) if strong surface homeotropic anchoring is set rather than tangential due to the conflict bewtween the local direction of the velocity field and that of the director. A deeper investigation in this analysis could be done exploring the role of the defects during the rotation and how much they can affect the rotation. As long as the case $N = 2$ for $W = 0.04$ seems a bit different from the other cases a starting analysis could consist in repeating the computation of ω^* for the case of an initially nematic droplet, which after the equiliration, is set in rotation.

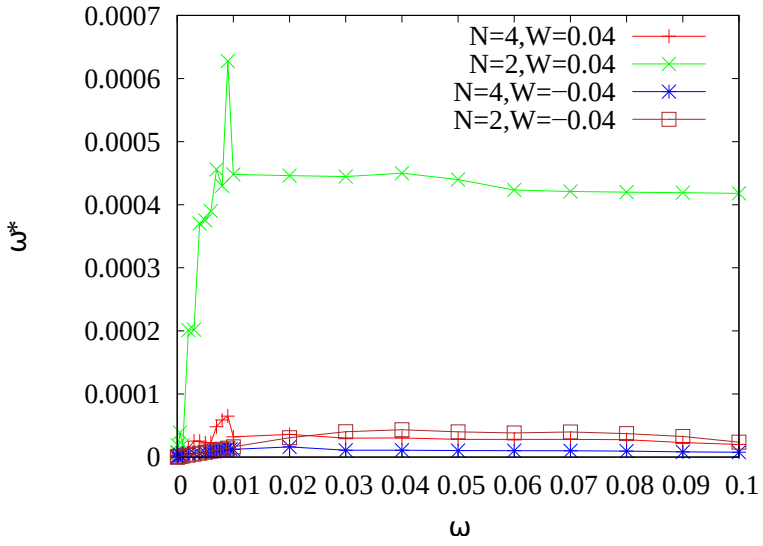

(a)

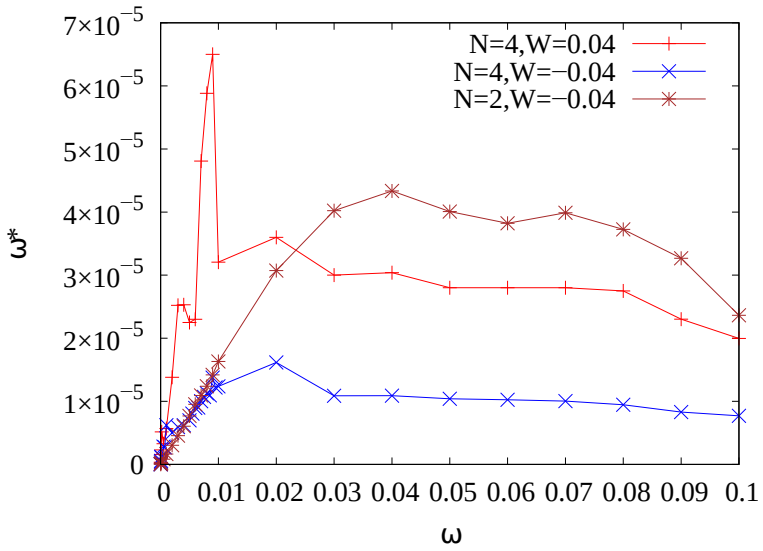

(b)

Figure 4.23: Angular velocity ω^* of a rotating cholesteric droplet as function of the frequency ω of the rotating field for the cases considered $N = 2, 4$ and $|W| = 0.04$ (a) and inset (b) for $N = 4, |W| = 0.04$ and $N = 2, W = -0.04$.

4.9.1 Periodicity of topological defects with rotating field

In general, as described in Chapter 2, the director of the liquid crystal aligns with the direction of the field (for positive dielectric constant) which can reorganize topological defects present in the system and if the intensity of the field is "critical", it can destroy the helix and forms a nematic structure aligned with the direction of the field. Thus if the electric field is rotating it is natural to think that the director and also topological defects rotate as consequence of the interaction with the field. In the particular case of a droplet in which a cholesteric liquid crystal is placed inside it with a certain number of twists ($N = 2, 4$ considered) and type and intensity of the anchoring of the director ($|W| = 0.04$), one could ask if the topological defects, during the dynamics, could follow or not the rotating field and rotate with the same frequency or behave in a different way. So the goal of this section is to explore and find these kinds of different behaviours.
The analysis of the periodicity of topological defects was performed considering an "easy" direction of the electric field (for example the vector of the rotating field which is horizontal or vertical) and looking the successive director configurations in time. As long as for frequencies greater than $\omega = 10^{-2}$ the inertia dominates in the rotation of the droplet, the frequencies chosen to study the periodicity of the defects were $\omega = 10^{-3}, 5 \times 10^{-3}$ and 10^{-2} which respectively correspond to a period of the rotating field of $T = 2\pi/\omega = 3.6 \times 10^5, 7.2 \times 10^4$ and 3.6×10^4 timesteps of the simulation. The interval time of the simulations was chosen to be approximately 2×10^6 timesteps.
In general for values of frequencies of $\omega = 10^{-3}$ and $N = 4$ and $N = 2$ twists of the cholesteric helix for $|W| = 0.04$, the system reaches a situation in which topological defects form periodic structures which reappear in time with the same period of the rotating field. The most interesting and particular cases correspond to $N = 4$ with $|W| = 0.04$ for frequencies of the rotanting $\omega = 5 \times 10^{-3}$ and $\omega = 10^{-2}$. In these cases three different behaviours are recognizable:

- the system is periodic for a time, then non periodic and in the end becomes periodic again,
- the system becomes periodic after a transient where is non periodic,
- the system is characterized by topological defects with an intrinsic periodicity not equal to the one of the rotating electric field.

The first case considered is for $N = 4$, $W = 0.04$ and frequency of the field $\omega = 5 \times 10^{-3}$. This case corresponds to the first mentioned situation.
The system at time $t = 4 \times 10^5$ is relaxed with structure portraied in Fig. 4.2-(e). Then a rotating field with components of Eq. (4.18) is switched on and the droplet rotates. Times $t = 4.31 \times 10^5$, $t = 5.03 \times 10^5$ and $t = 7.19 \times 10^5$ of Fig. 4.24-(a), (b) and (c) correspond respectively to the first time of electric field pointing upwards, first period and fourth periods. These states are characterized by four defects of charges $-1/2$ and three λ regions of charges $+1$ which rotate in the time and in particular the λ regions reshape in time. Fig. 4.24-(b)-(c) are characterized by a couple of defects $-1/2$ which is exchanged with a couple of twist disclinations of charge $-1/2$. At time $t = 1.367 \times 10^6$ of Fig. 4.24-(d), the rotating field has performed 13 periods, and only two defects of charge $-1/2$ survive with two λ regions, instead of the original three, leaving always the total charge unchanged equals $+1$. This structure of Fig. 4.24-(d) repeats periodically three periods of the field and then the system renters in a non periodic regime in which different configurations of the director and defects apper. One of these corresponds to time $t = 1.943 \times 10^6$, the 21st period od the field, of Fig. 4.24-(e) characterized by two defects of charge $-1/2$ close each other and two $+1$ regions symmetrically disposed respect to the two ones. Then at time $t = 2.591 \times 10^6$ of Fig. 4.24-(f), the 29th period of the field, the same structure of time $t = 1.367 \times 10^6$ of Fig. 4.24-(d) reppear and repeats for three more periods of the electric field.
The case for $N = 4$, $W = 0.04$ and frequency of the rotating field $\omega = 10^{-2}$ of Fig. 4.25, assuming as reference direction of the rotating field the horizontal direction pointing to the left, corresponds to the second mentioned situation. The system after the relaxation, switching on the rotating field, initially evolves passing through a series of different configurations which are non periodic with the field and finally reaches a situation from which the rotation becomes periodic. Fig. 4.25-(a), (b), (c), (d) and (e) represent the system at times $t = 4.05 \times 10^5$ (first configuration with field pointing to the left), $t = 6.21 \times 10^5$ (sixth period of the field), $t = 6.93 \times 10^5$ (eighth period of the field), $t = 7.29 \times 10^5$ (nineth period of the field) and $t = 7.65 \times 10^5$ (tenth period of the field) respectively. The general structure sees four encircled topological defects of charge $-1/2$ alternated by three $+1$ regions rotating in the time and moving inside the droplet with the $+1$ regions which continuosly reshape elongating in the time. The topological total charge is $+1$. When the system reaches the time $t = 1.161 \times 10^6$ of Fig. 4.25-(f), correspondent to 21st period of the rotating field, the four defects of charge $-1/2$ vanish and only one λ region of charge $+1$ remain which repeats periodically 34 times until the end of the interval time of the simulation.
The cases for $N = 4$, $W = -0.04$ and frequencies $\omega = 5 \times 10^{-3}$ and $\omega = 10^{-2}$ represented in Fig. 4.26 and Fig. 4.27 respectively deal with the last mentioned situation in which the system rotates because of the field generating configurations

which are non periodic in time but possess an "intrinsic" periodicity which is different from the one of the applied field. The system initially relaxes until time $t = 4 \times 10^5$ portraied in Fig. 4.2-(f) and then the rotating field is switched on. Fig. 4.26-(a), (b), (c), (d), (e) and (f) correspond to times $t = 7.19 \times 10^5$ (fourth period of the rotating field), $t = 7.91 \times 10^5$ (fifth period of the rotating field), $t = 8.63 \times 10^5$ (sixth period of the rotating field), $t = 1.223 \times 10^6$ (eleventh period of the rotating field), $t = 2.015 \times 10^6$ (22nd period of the rotating field), $t = 2.087 \times 10^6$ (23rd period of the rotating field) respectively. In Fig. 4.26-(a), (b), (c), (d) and (f) the two extremal original $\tau^{+1/2}$ defects, two couples of twist-disclinations alternated by $+1$ λ regions are recognizable. In Fig. 4.26-(e) instead three $\tau^{+1/2}$ defects appear. In particular they seem to be distributed at two sides of the droplet alternated by a region in which the director seems to be nematic pointing towards the direction of the field. In this situation the system seems to have an intrinsic periodicity of the topological defects of about $T^{'} = 2.16 \times 10^5$, after which the defects reapper identically, against the peridicity of $T = 7.2 \times 10^4$ of the applied rotating field. Fig. 4.26-(d) there are four λ $+1$ regions which become three in Fig. 4.26-(e) and two again in Fig. 4.26-(f).
Fig. 4.27-(a), (b), (c), (d), (e), (f) correspond to times $t = 6.93 \times 10^5$ (eighth period of the rotating field), $t = 7.29 \times 10^5$ (nineth period of the rotating field), $t = 7.65 \times 10^5$ (tenth period of the rotating field), $t = 8.01 \times 10^5$ (eleventh period of the rotating field), $t = 8.37 \times 10^5$ (twelveth period of the rotating field) and $t = 8.73 \times 10^5$ (thirtheenth period of the rotating field) respectively. In Fig. 4.27-(a)-(b) originnaly there are four $+1$ λ regions with six twist disclinations of charge $-1/2$. In Fig. 4.27-(c) there are only two λ $+1$ regions plus two new $\tau^{+1/2}$ extremal defects, one on the left and the other on the right. In Fig. 4.27-(d) one $\tau^{+1/2}$ defect has vanished and changed by a λ $+1$ region. A similar situation of Fig. 4.27-(c)-(d) repeats also in Fig. 4.27-(e)-(f). This case is characterized by an intrinsic periodicity $T^{'} = 8.64 \times 10^5$. The configurations shown reappear of $T^{'} = 8.64 \times 10^5$.

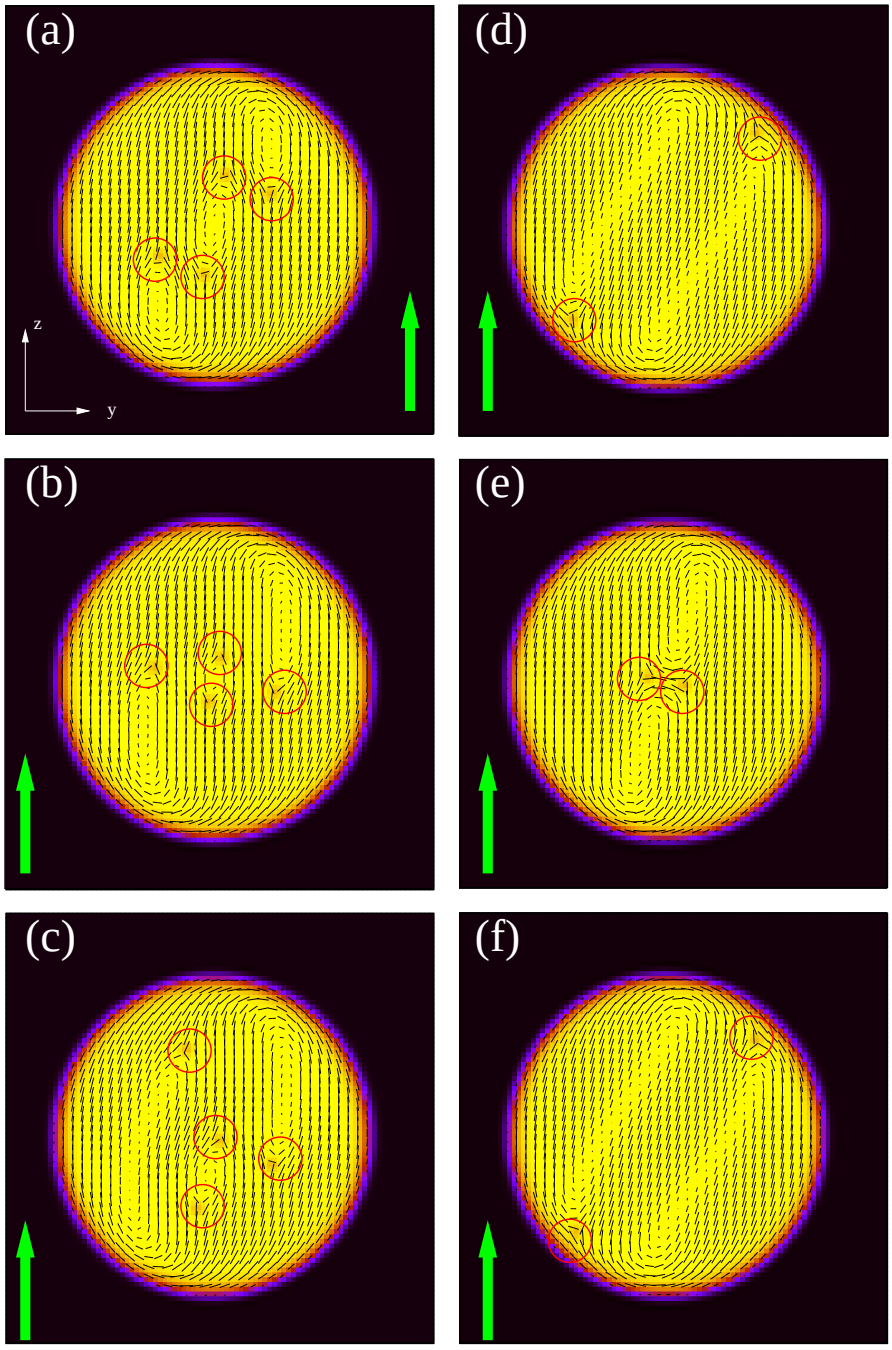

Figure 4.24: Dynamics of a cholesteric droplet (with $N = 4$) under a counter-clockwise rotating electric field. The reduced potential is with $\Delta V_y = \Delta V_z = 4$, $\omega = 5 \times 10^{-3}$ and $W = 0.04$ (strong tangential anchoring). The green arrow indicates the direction of the electric field. Corresponding simulation times are $t = 4.31 \times 10^5$ for (a), $t = 5.03 \times 10^5$ for (b), $t = 7.19 \times 10^5$ for (c) , $t = 1.367 \times 10^6$ for (d), $t = 1.943 \times 10^6$ for (e) and $t = 2.591 \times 10^6$ for (f) with t simulation time.

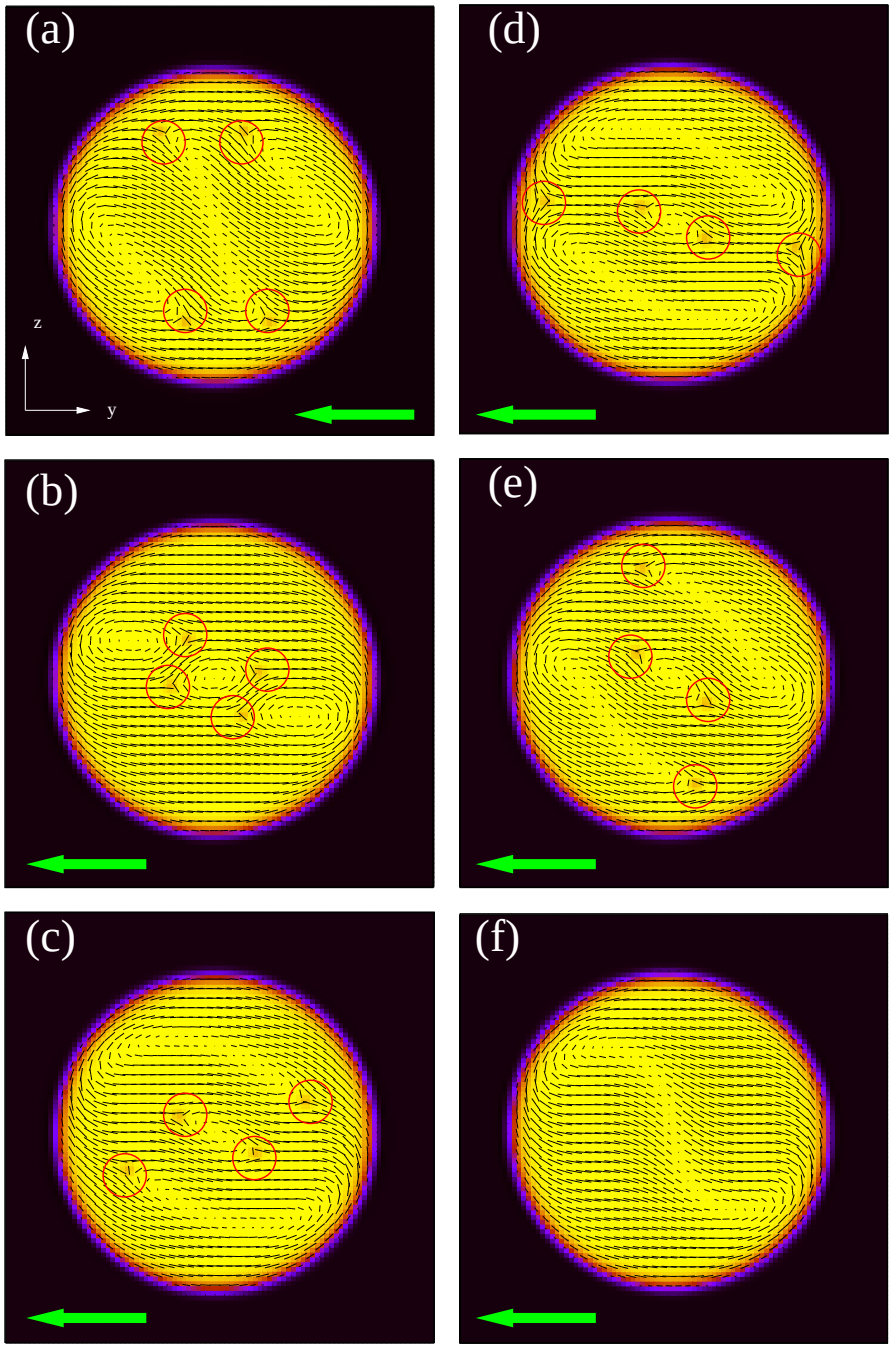

Figure 4.25: Dynamics of a cholesteric droplet (with $N = 4$) under a counterclockwise rotating electric field. The reduced potential is with $\Delta V_y = \Delta V_z = 4, \omega = 10^{-2}$ and $W = 0.04$ (strong tangential anchoring). The green arrow indicates the direction of the electric field. Corresponding simulation times are $t = 4.05 \times 10^5$ for (a), $t = 6.21 \times 10^5$ for (b), $t = 6.93 \times 10^5$ for (c) , $t = 7.29 \times 10^5$ for (d), $t = 7.65 \times 10^5$ for (e) and $t = 1.161 \times 10^6$ for (f) with t simulation time.

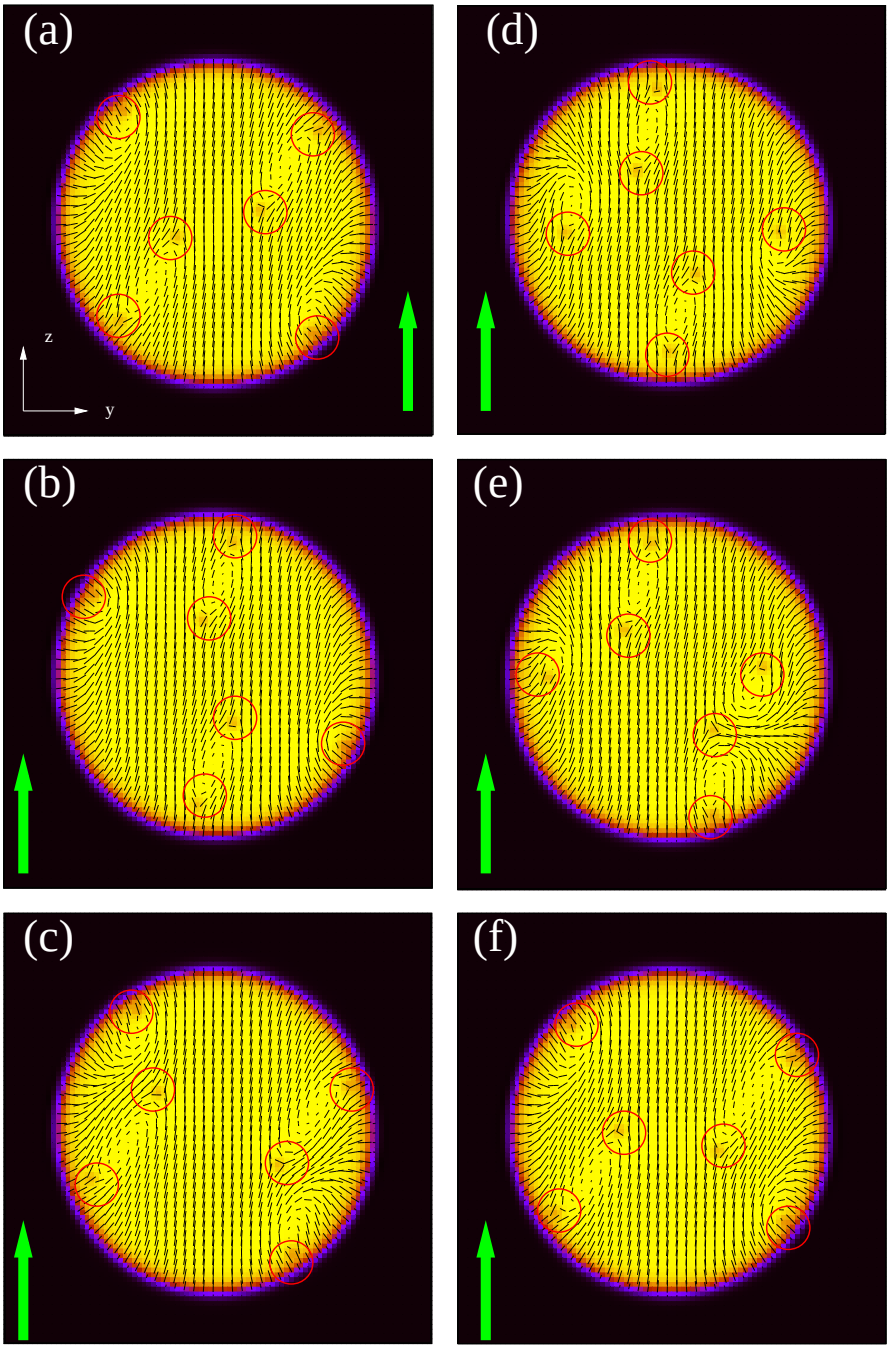

Figure 4.26: Dynamics of a cholesteric droplet (with $N = 4$) under a counter-clockwise rotating electric field. The reduced potential is with $\Delta V_y = \Delta V_z = 4$, $\omega = 5 \times 10^{-3}$ and $W = -0.04$ (strong homeotropic anchoring). The green arrow indicates the direction of the electric field. Corresponding simulation times are $t = 7.19 \times 10^5$ for (a), $t = 7.91 \times 10^5$ for (b), $t = 8.63 \times 10^5$ for (c) , $t = 1.223 \times 10^6$ for (d), $t = 2.015 \times 10^6$ for (e) and $t = 2.087 \times 10^6$ for (f) with t simulation time.

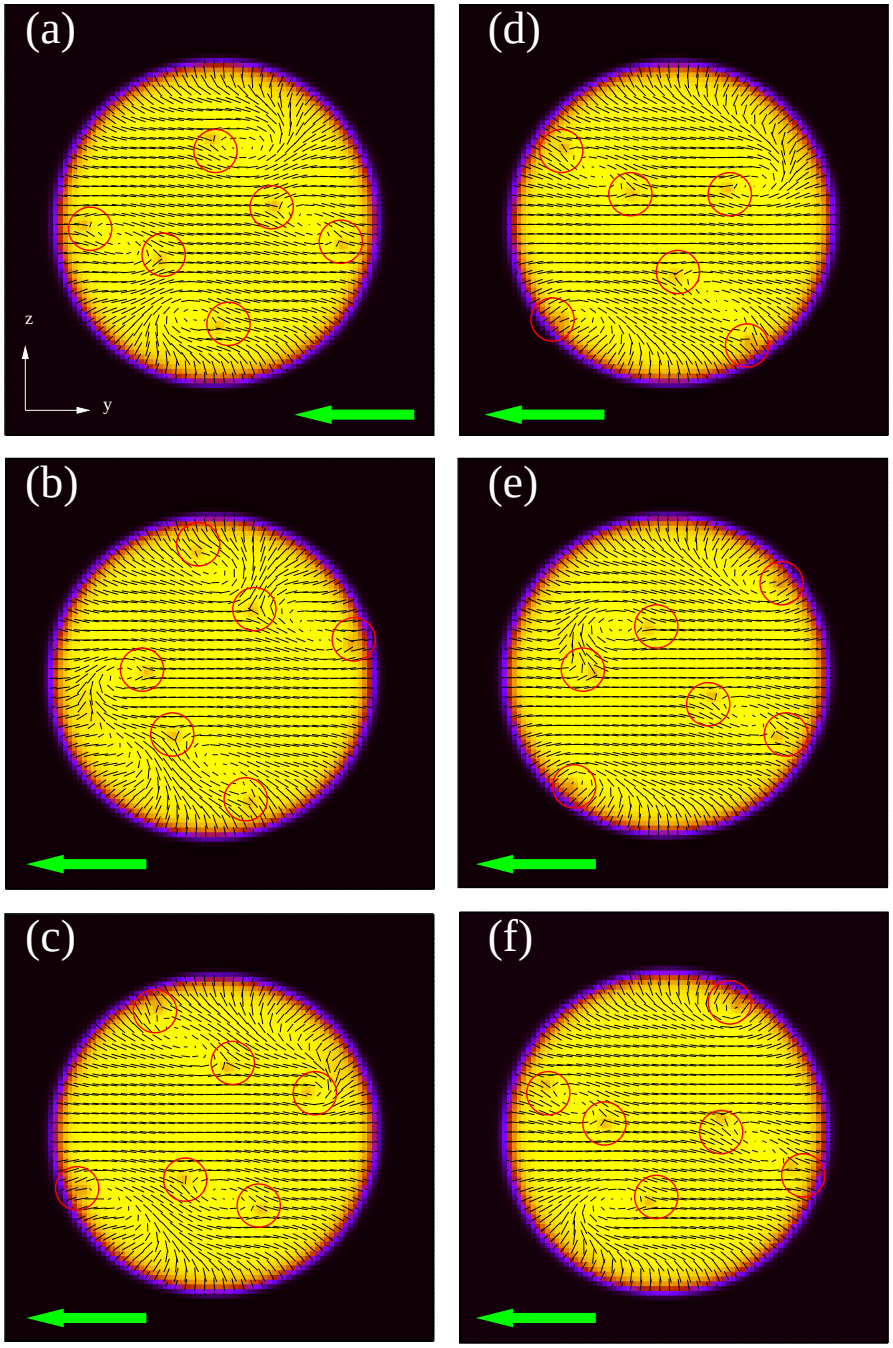

Figure 4.27: Dynamics of a cholesteric droplet (with $N = 4$) under a counterclockwise rotating electric field. The reduced potential is with $\Delta V_y = \Delta V_z = 4, \omega = 10^{-2}$ and $W = -0.04$ (strong homeotropic anchoring). The green arrow indicates the direction of the electric field. Corresponding simulation times are $t = 6.93 \times 10^5$ for (a), $t = 7.29 \times 10^5$ for (b), $t = 7.65 \times 10^5$ for (c) , $t = 8.01 \times 10^5$ for (d), $t = 8.37 \times 10^5$ for (e) and $t = 8.73 \times 10^5$ for (f) with t simulation time.

4.10 Two interacting rotating droplets

In this section the dynamics of two cholesteric liquid crystal droplets in isotropic phase with surfactant under rotating electric fields is briefly discussed.
The results which are introduced here deal with a study in preparation "*Interacting rotating cholesteric liquid crystal droplets*". The goal of this paper is to study a system of two and more cholesteric liquid crystal droplets subjected to rotating electric fields and analyzing the mutal interactions. This study can be thought as an expansion of the first study of the single cholesteric droplet already analyzed in the paper "*Switching dynamics in cholesteric liquid crystal emulsions*", J. Chem. Phys. **147**, 064903 (2017).
This system differs from the one of "*Switching dynamics in cholesteric liquid crystal emulsions*" for the presence of a component of surfactant, to prevent the coalescence of the droplets, in the free energy functional $\mathcal{F} = \int f dV$ with

$$\begin{aligned} f &= \frac{a}{4}\phi^2(\phi-\phi_0)^2 + \frac{(\kappa_\phi+\kappa_c c)}{2}|\nabla\phi|^2 + c\ln c \\ &+A_0\left[\frac{1}{2}\left(1-\frac{\gamma(\phi)}{3}\right)Q_{\alpha\beta}^2 - \frac{\gamma(\phi)}{3}Q_{\alpha\beta}Q_{\beta\gamma}Q_{\gamma\alpha} + \frac{\gamma(\phi)}{4}(Q_{\alpha\beta}^2)^2\right] \\ &+\frac{K}{2}\left[(\partial_\beta Q_{\alpha\beta})^2 + (\varepsilon_{\alpha\zeta\delta}\partial_\zeta Q_{\delta\beta} + 2q_0 Q_{\alpha\beta})^2\right] \\ &+W(\partial_\alpha\phi)Q_{\alpha\beta}(\partial_\beta\phi) - \frac{\varepsilon}{12\pi}E_\alpha Q_{\alpha\beta}E_\beta. \end{aligned} \tag{4.21}$$

In this free energy functional c represents the concentration of surfactant coupled to $\nabla\phi$ with a linear relation

$$\frac{(\kappa_\phi+\kappa_c c)}{2}|\nabla\phi|^2 \tag{4.22}$$

with coefficient $\kappa_c < 0$ which favours a migration of surfactant towards the interface of the droplet [134, 135]; the term $c\ln c$ is an entropic term added in the functional to ensure consistency to the model. The concentration of surfactant evolves in time through the following equation

$$\partial_t c + \nabla\cdot(c\mathbf{u}) = \nabla\cdot[L(c)\nabla\mu_c] \tag{4.23}$$

where $L(c) = D^{'}c$ with $D^{'}$ diffusion coefficient of the surfactant. This way of coupling the surfactant to the scalar field ϕ and the equation for c were taken from [136]. The other equations of this system, the continuity, the Navier-Stokes equation, the Beris-Edwards and the Cahn-Hilliard equations are the same for the system of the single droplet and are always numerically solved with hybrid Lattice Boltzmann method described in Chapter 3.
The system consists in a quasi-2D square periodic lattice with dimensions $L_x =$

$1 \times L_y = 250 \times L_z = 250$ in order to accommodate two droplets and the component of surfactant which migrates to the interfaces of the two droplets used to avoid a possible coalescence of the two ones. The parameters used for the study of this system are the same used for the study of the single droplet: $\alpha_\phi = 0.07$, $\kappa_\phi = 0.14$, $\kappa_c = -1.3$, $A_0 = 1$, $K = 0.03$, $\Gamma = 1$, $\eta = 1.67$, $D = 0.05$, $D^{'} = 0.1$, $\xi = 0.7$, $\varepsilon = 41.4$ and $|W| = 0.04$.
The initial conditions of the system consist in two droplets placed at half-height of the lattice with a horizontal distance of about 84 lattice sites between the two centers of mass with $\phi = 2$ inside the droplet and $\phi = 0$ outside; the surfactant instead is initially set $c = 0.02$ all over the lattice. The cholesteric liquid crystal is always accommodated inside each droplet with helix along the horizontal y direction with components of (4.13)-(4.15) and 0 outside.
Starting with these initial conditions the system at first relaxes approximately at time $t = 4 \times 10^5$. Fig. 4.28 shows the surfactant which migrates at interfaces of the two droplets at equilibirum for $t = 4 \times 10^5$. Fig. 4.29-(a), instead, shows the diretor structure of the two cholesteric droplets at the same time.

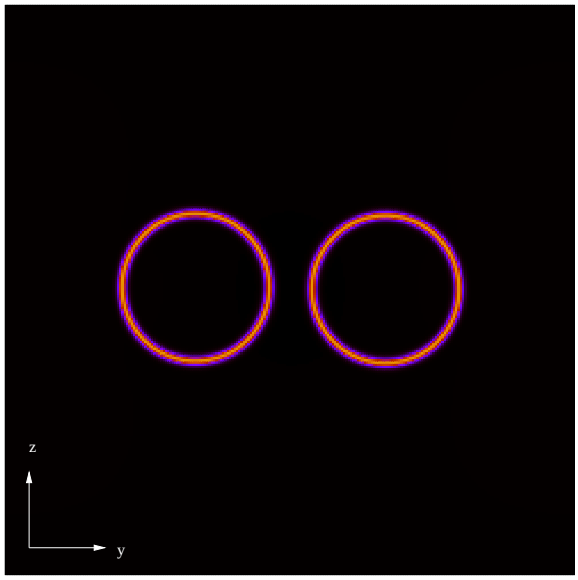

Figure 4.28: Contour plot of the concentration of surfactant for the two droplets at equilibrium at $t = 4 \times 10^5$. The choice of $\kappa_c = -1.3$ favours the migration of the surfactant to the interfaces of the two droplets. The yellow color of the rings around the droplets corresponds to a value of $c = 0.025$ instead the dark region to a value of $c = 0.0195$.

After the relaxation of the system, a rotating electric field with the same components of (4.18) is switched on and the two droplets rotate. However this new case introduces a new kind of interaction: the two droplets rotate around their own cen-

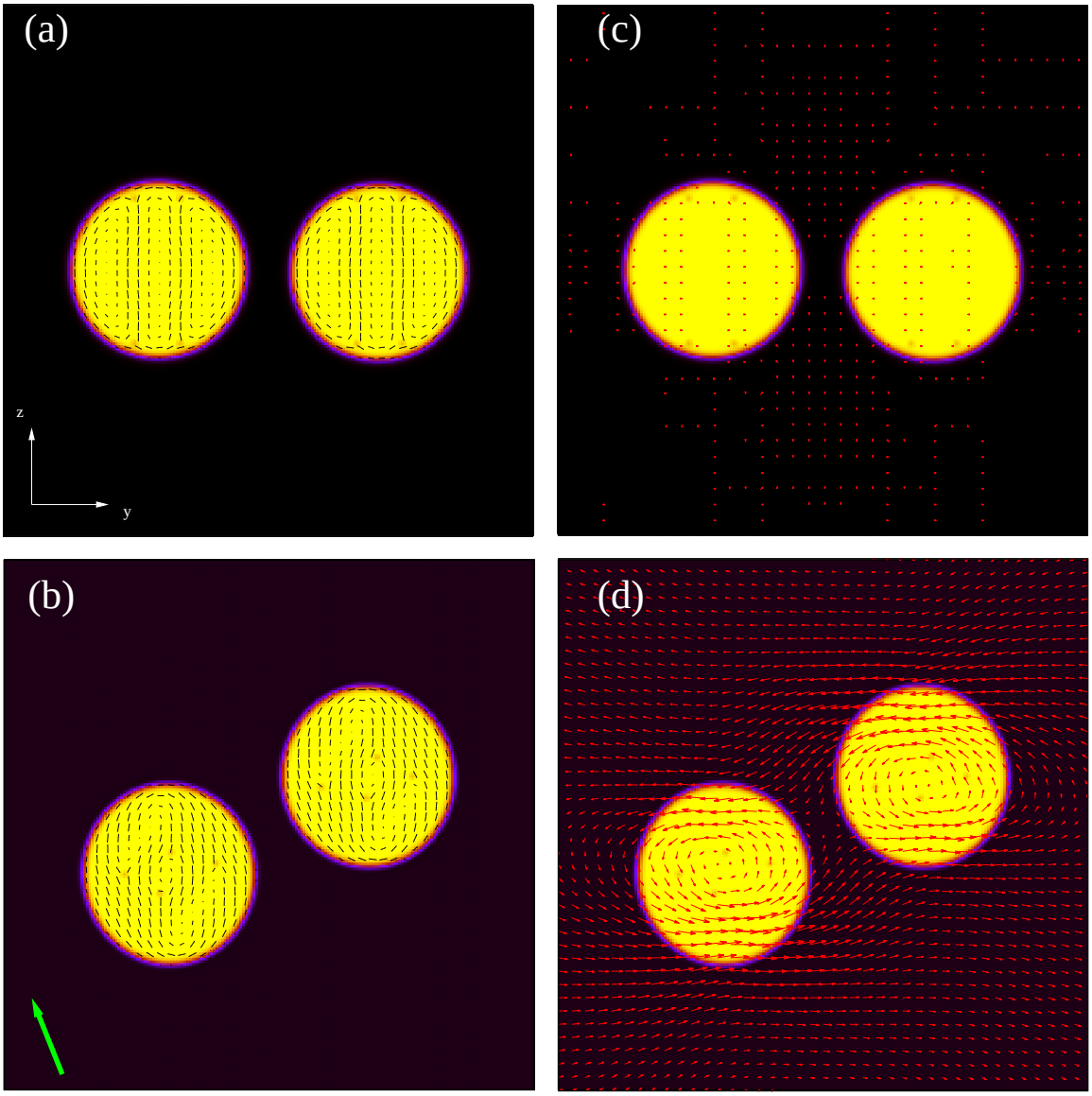

Figure 4.29: Cholesteric droplets with $N = 4$, $W = 0.04$, frequency of the field $\omega = 10^{-2}$ and reduced potential $\Delta V_y = \Delta V_z = 7.84$. Left column (a)-(b) displays the droplets with the director field at times $t = 4 \times 10^5$ (a) and $t = 6.5 \times 10^5$ (b). The right column the droplets with the velocity field for correspondent times. The green arrow indicates the direction of the rotating field. t is in simulation units.

ter of mass but also they start to rotate each other around a common center which approximately correspond to the center of the lattice. Fig. 4.29-(d) shows the two rotating droplets at time $t = 6 \times 10^5$; Fig. 4.29-(c) shows the two vortices inside each droplet which interact each other and determine a mutual rotation of the two droplets. So the quantitative analysis which was performed and which is reported here, consisted in computing the angular velocity of rotation of the single droplet with the relation (4.19)

$$\omega^* = \frac{\int dV \phi \mathbf{r} \times \mathbf{u}}{\int dV \phi r^2} \tag{4.24}$$

and also computing the angular velocity of rotation of the the axis joining the two centers of mass of the two droplets with

$$\omega^{**} = \frac{d\theta}{dt} \tag{4.25}$$

with θ angle the axis forms with the horizontal y direction as function of the frequency ω of the applied field.
These two plots are represented in Fig. 4.30-(a)-(b) for the case of $N = 4$, $W = 0.04$ and $V = 7.84$.
The peculiarity of this process is the fact that it seems to have a threshold. For fixed frequency of the applied field, each droplet rotate but the common rotation is visibile only for frequencies of the field $\omega \geq 10^{-3}$. Fig. 4.30-(a) shows the two superposed curves of the angular velocity of each droplet. Like the case of the single one there is an initial region of low frequecies ($\omega \leq 10^{-2}$) in which the ω^* rises. The faster the rotating field, the faster the rotation of the single droplet. In the region of higher frequencies ($\omega \geq 10^{-2}$) the two curves seems to decrease as signature that inertia starts to dominate the dynamics.
Fig. 4.30-(b) shows the angular velocity of rotation of the axis which joins the two centers of mass of the two droplets. Even in this case there is a region of low frequencies ($\omega \leq 10^{-2}$) in which ω^{**} rises reaching a maximum value and then decreases as consequence of the rising of the inertia in the system. The ω^{**} is also one order of magnitude less than the correspondent ω^*.

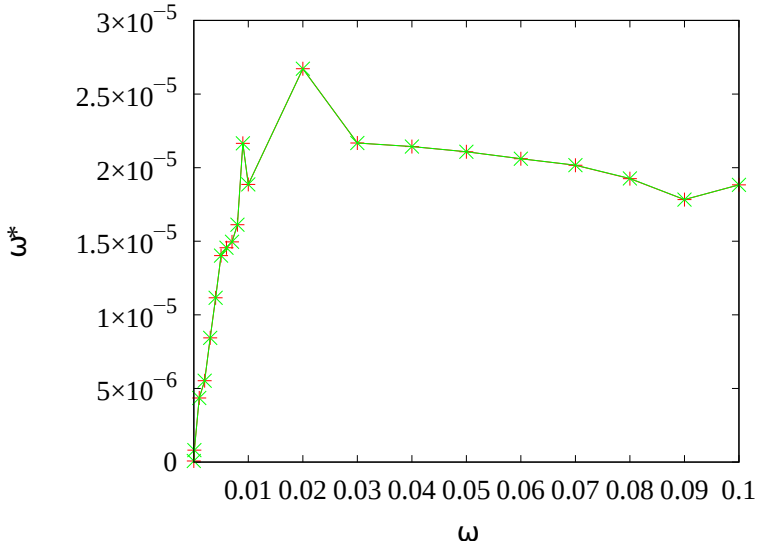

(a)

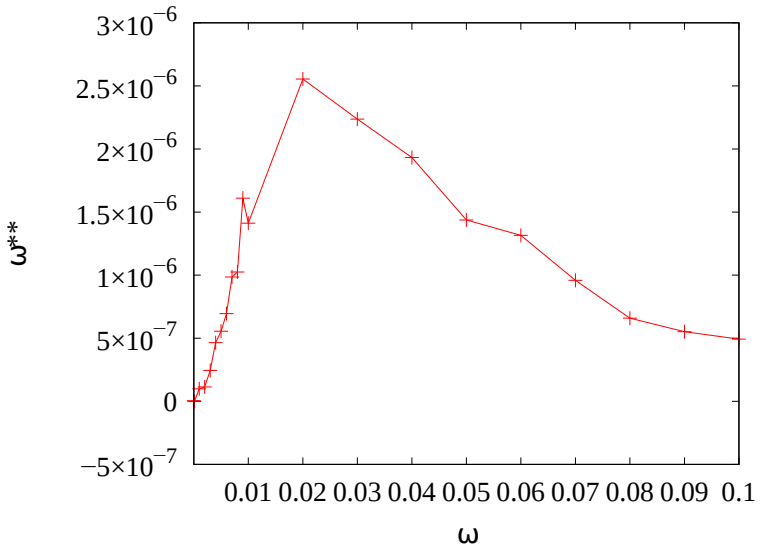

(b)

Figure 4.30: Angular velocity of each droplet as function of the frequency of the applied field (a) and angular velocity of rotation of the axis of the two centers of mass of the two droplets as function of frequency of the applied field (b) for $N = 4$, $W = 0.04$.

4.11 Summary

In this Chapter the results of the study of a cholesteric liquid crystal droplet in isotropic host under electric fields have been collected.
Factors like elasticity of the material, type of anchoring, cholesteric helix encapsulated in the droplet and presence of external fields can cause the rise of topological defects whose dynamics is studied. Two typical situations have been considered: the one consisting in the switching on-off of a continuous electric field and the application of a rotating one. In general the switching on-off of the field causes a reorganization of the defects and the director in the bulk of the droplet and if the field is particularly strong can destroy every defect and the helix turning the cholesteric into a nematic. As regards the rotating electric field, a quantitative analysis was performed computing the angular velocity of the rotating droplet as function of the applied field and observing the existence of a regime of high frequencies in which inertia of the droplet starts to dominate.
The final part of the Chapter presented the initial results of a new kind of study consisting in the analysis of the interactions between two interacting cholesteric droplets under rotating electric fields with the presence of the surfactant which avoids the coalescence between the two droplets. In particular an interesting interatction seems to emerge consisting in a common rotation of the two droplets around a common centre and also a threshold value of the frequency of the field below which the effects is absent. The future goal of this study will consist to explore deeper this kind of interaction for the homeotropic anchoring and other values of the cholesteric pitch also investigating the interactions between more than two droplets.

Chapter 5

Cholesteric emulsion under shear

This chapter describes briefly the dynamics of a cholesteric emulsion represented by an isotropic droplet in cholesteric host under shear.
The results presented in this paper represent a part of a new paper in preparation, "*Shear dynamics of an inverted cholesteric emulsion*", for the journal *Fluids*. The goal of the paper is to investigate the dynamics of a direct (cholesteric droplet in isotropic phase) and an inverted emulsion (isotropic droplet in cholesteric host) for different conditions of anchoring of the director on the droplet and the walls, different pitches of the choelsteric helix, different directions of the helix and different shear rates. In particular it is known in literature the phenomenon known as permeation consisting in an enormous increase in the viscosity of the cholesteric liquid crystal under shear parallel to the helix which is one of the goals of the paper.
The results presented in this Chapter deal with the case of an isotropic droplet in a cholesteric channel with helix parallel to the horizontal direction subjected to a symmetric shear parallel to the helix that slightly distorts the droplet. In the Chapter the configurations of the director and the velocity for different times will be presented discussing the evolution of the system until the achievement of the stationary state. In general the shear distorts the droplet and also reorganizes the topological defects in the cholesteric phase. The sections of the three components are also showed.

5.1 Numerical model

The system, consisting in an isotropic droplet in the liquid crystal host, is described by the free energy functional $\mathcal{F} = \int f dV$ with f

$$\begin{aligned} f &= \frac{a}{4}\phi^2(\phi-\phi_0)^2 + \frac{\kappa_\phi}{2}|\nabla\phi|^2 \\ &+ A_0\left[\frac{1}{2}\left(1-\frac{\gamma(\phi)}{3}\right)Q_{\alpha\beta}^2 - \frac{\gamma(\phi)}{3}Q_{\alpha\beta}Q_{\beta\gamma}Q_{\gamma\alpha} + \frac{\gamma(\phi)}{4}(Q_{\alpha\beta}^2)^2\right] \\ &+ \frac{K}{2}\left[(\partial_\beta Q_{\alpha\beta})^2 + (\varepsilon_{\alpha\zeta\delta}\partial_\zeta Q_{\delta\beta} + 2q_0 Q_{\alpha\beta})^2\right] \\ &+ W(\partial_\alpha\phi)Q_{\alpha\beta}(\partial_\beta\phi) + \frac{W_0}{2}(Q_{\alpha\beta}-Q_{\alpha\beta}^0)^2 \end{aligned} \tag{5.1}$$

also used in the previous study [8]. As reported in Chapter 2 the term

$$\frac{W_0}{2}(Q_{\alpha\beta}-Q_{\alpha\beta}^0)^2 \tag{5.2}$$

describes the energetic cost to anchor the director to the rigid walls of the system with constant strength W_0 and $Q_{\alpha\beta}^0$ which is the value of the **Q** tensor to the walls. The dynamic equations which describe the system are the same of Chapter 4 and are always solved through computer simulations with hybrid Lattice Boltzmann method.

5.2 Initial conditions

As already mentioned in Chapter 4, the choice of the parameters in the computer simulations must be wise in order to be sure to stay in correct cholesteric region of the phase-diagram reported in Fig. 4.1.
In the computer simulations, an isotropic droplet with radius $R = 32$ lattice sites is accomodated at the center of a lattice with rigid horizontal walls with dimensions $L_x = 1 \times L_y = 300 \times L_z = 100$. The set of values is: $\alpha_\phi = 0.07$, $\kappa_\phi = 0.14$, $A_0 = 1$, $K = 0.03$, $\Gamma = 1$, $\eta = 1.67$, $D = 0.05$, $\xi = 0.7$, $|W| = 0.04$ and $W_0 = 0.4$. This values of the parameters are expressed in simulation units. The quantity

$$N = L/p_0 \tag{5.3}$$

with L characteristic lenght of the system (if the helix is along the horintal y direction it is $L = L_y$) and p_0 pitch of the helix represents the number of 2π turns of the director along the lenght L. The concentration field ϕ and the $\mathbf{Q}$ tensor components are set to zero inside the isotropic droplet. Outside the droplet, instead, ϕ has been set equal to a value $\phi_0 = 2$ and the five components have been chosen in order to accomodate the cholesteric helix with helical axis parallel to the horizontal y direction as Eq. (4.13)-(4.15) of Chapter 4. The components of the $\mathbf{Q}$ tensor in the cholesteric phase, $Q^0_{\alpha\beta}$, at the top wall $z = L_z$, are:

$$Q^0_{xx} = c_2(sin(\theta_z)sin(\theta_z)cos(\theta_{xy})cos(\theta_{xy}) - 1/3), \tag{5.4}$$

$$Q^0_{xy} = c_2(sin(\theta_z)sin(\theta_z)cos(\theta_{xy})sin(\theta_{xy}) - 1/3), \tag{5.5}$$

$$Q^0_{yy} = c_2(sin(\theta_z)sin(\theta_z)sin(\theta_{xy})sin(\theta_{xy}) - 1/3), \tag{5.6}$$

$$Q^0_{xz} = c_2(sin(\theta_z)cos(\theta_z)cos(\theta_{xy})), \tag{5.7}$$

$$Q^0_{yz} = c_2(sin(\theta_z)cos(\theta_z)sin(\theta_{xy})), \tag{5.8}$$

with $c_2 = 0.5$, $\theta_z = 0$ the angle the director forms with the vertical z axis and $\theta_{xy} = \pi/2$ tha angle with the x axis. The same conditions apply also for the bottom wall $z = 0$. These conditions are suitable to ensure a perpendicular anchoring of the director to the two walls.

5.3 Channel of isotropic fluid

In this section the situation of a channel of isotropic fluid is considered setting initially $\phi = \mathbf{Q} = 0$ in the whole system. The system then evolves and reaches an initial equilibrium at time $t = 10^5$ represented in Fig. 5.1-(a). The the two horizontal rigid walls at $z = 0$ and $z = L_z$ are set symmetrically in motion with

a shear rate $\dot{\gamma} = 2u/L_z$ being $|u| = 0.002$. The sheared system then evolves in time and reaches a final stationary state represented in Fig. 5.1-(c) correspondent at time $t = 2 \times 10^5$. The panel of Fig. 5.1 represent the velocity field which exhibit the typical pattern of a sheared system with velocity which is maximum at the two moving walls and zero at the centre of the channel [4, 137]. This is also visible in Fig. 5.2 in which the three section of the components of the velocity field are plotted as functions of the vertical coordinate z. The x and z components are zero instead the y component of the velocity has a linear trend being zero at half height of the lattice and maxima, in absolute value, the two walls. After the relaxation, which is achieved at time $t_i = 10^5$, and the application of the shear, the system arrives in a final stationary state at time $t_f = 2 \times 10^5$; so the interval time $\Delta t = t_f - t_i = 10^5$ is now assumed as unit time for the successive studies.

5.4 Isotropic droplet in cholesteric channel

In this section the results of the simulation of an isotropic droplet in a cholesteric liquid crystal host is discussed.
In this case an isotropic droplet or radius $R = 32$ is placed at the center of the channel in which a cholesteric liquid crystal with $N = 4$ twists and homeotropic anchoring on both the droplet and the walls is accommodated with $W = -0.04$ and $W_0 = 0.4$.
Fig. 5.3 reports the configurations of the droplet in the time. The presence of the two confining walls determine an equilibrium structure in Fig. 5.3-(a) for time $t = 4 \times 10^5$ characterized by three twist disclinations on each wall with topological charge $-1/2$, two defects of charge $-1/2$ at each side of the droplet along the equatorial line and three λ regions each of charge $+1$. The total topological charge is -1.
After time $t = 4 \times 10^5$, a symmetric shear is applied moving the two walls with velocity $|v| = 0.002$.
The imposed shear causes a reorganization of the structure of the channel; in fact, only four twist disclinations survive, two $\tau^{+1/2}$ defects appear at each wall, the defects at the two poles of the droplet rotate, two couples of twist disclinations at the two opposite parts of the droplet alternated by a λ region and a defect, on the right, in which the director enters in the plane of charge -1. The droplet also starts to slightly elongate in the direction of the shear [138], Fig. 5.3-(b), for time $t = 6 \times 10^5$). After some time the twist disclinations at the walls turn into two defects of charge $-1/2$ (Fig. 5.3-(c) for time $t = 8 \times 10^5$), at the center of the channel the λ stretches and in the end the droplet reaches the stationary state of Fig. 5.3-(d) for $t = 1.4 \times 10^6$. The time requested by this kind of system to reach the final stationary state, expressed in Δt units of the previous section, is $t = 14\Delta t$.

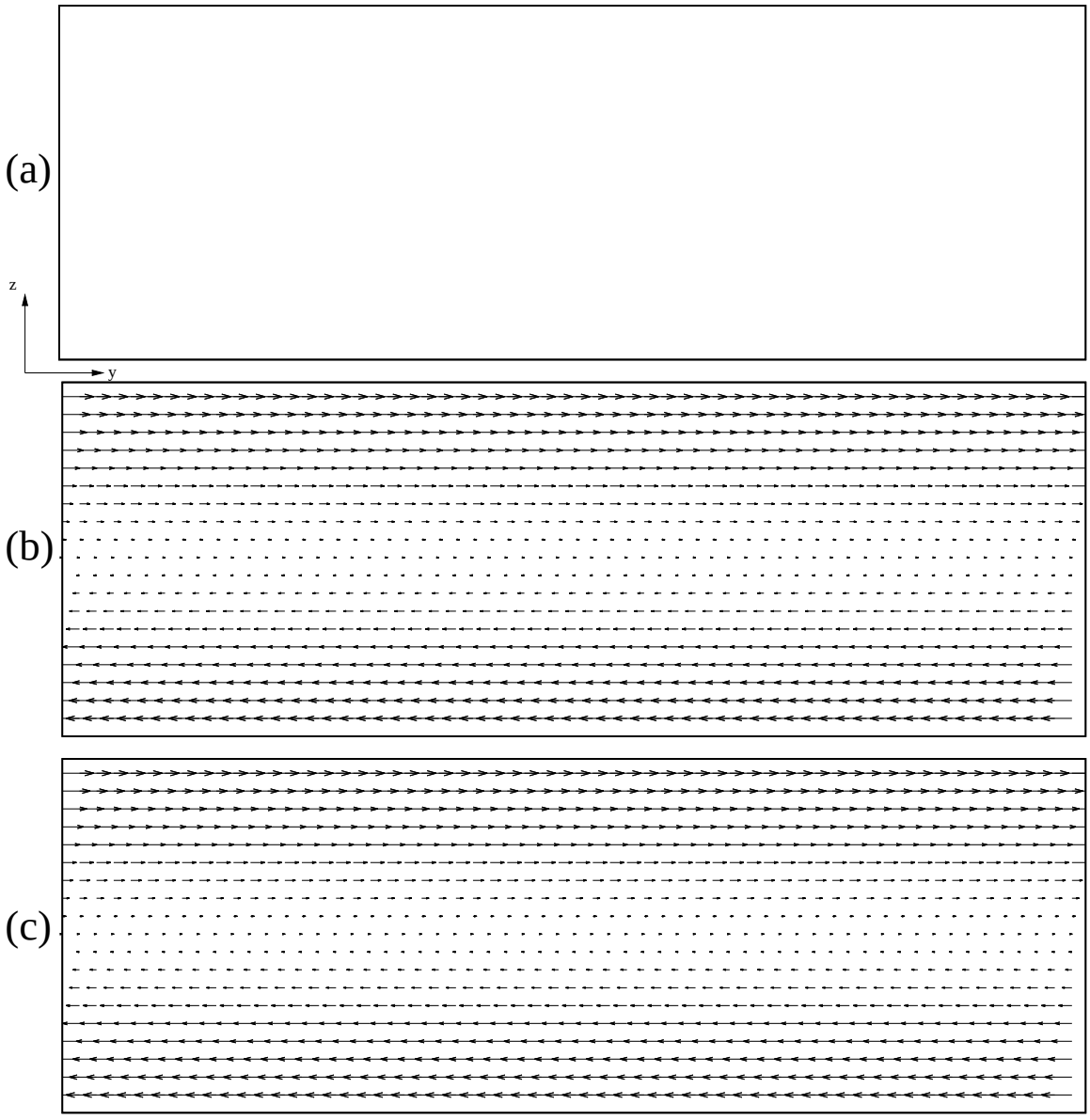

Figure 5.1: Velocity field configurations of a channel of isotropic fluid for times $t = 10^5$ at equilibrium (a), $t = 1.5 \times 10^5$ (b) and $t = 2 \times 10^5$ (c) where shear is active.

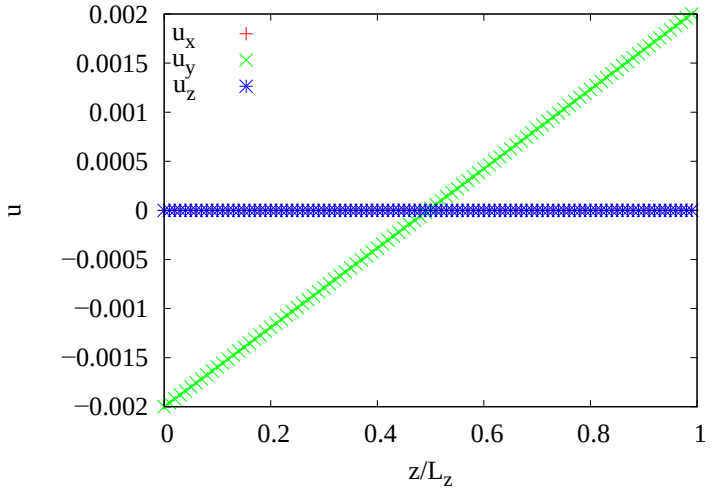

Figure 5.2: Sections of the three components of the velocity fields as function of the vertical coordinate z obtained fixing the value of $y = L_y/2$.

Fig. 5.4 shows the plot of the droplet with superposed velocity fields for the correspondent times of Fig. 5.3. The plots show a velocity field which is intense near the moving walls and form a vortex inside the droplet [8].
Fig. 5.5 shows the sections of three components of the velocity field calculated at $y = L_y/6$, $y = L_y/2$ and $y = 5L_y/6$. The profiles for $y = L_y/6$ and $y = 5L_y/6$ show a parabolic trend for u_z similar to the one in [139] as signature of a little permeation effect. The profiles of u_y and u_z for $y = L_y/2$ seem a bit distorted due to the presence of the interface of the droplet which induces elastic distortions in the cholesteric phase which change the velocity profile.

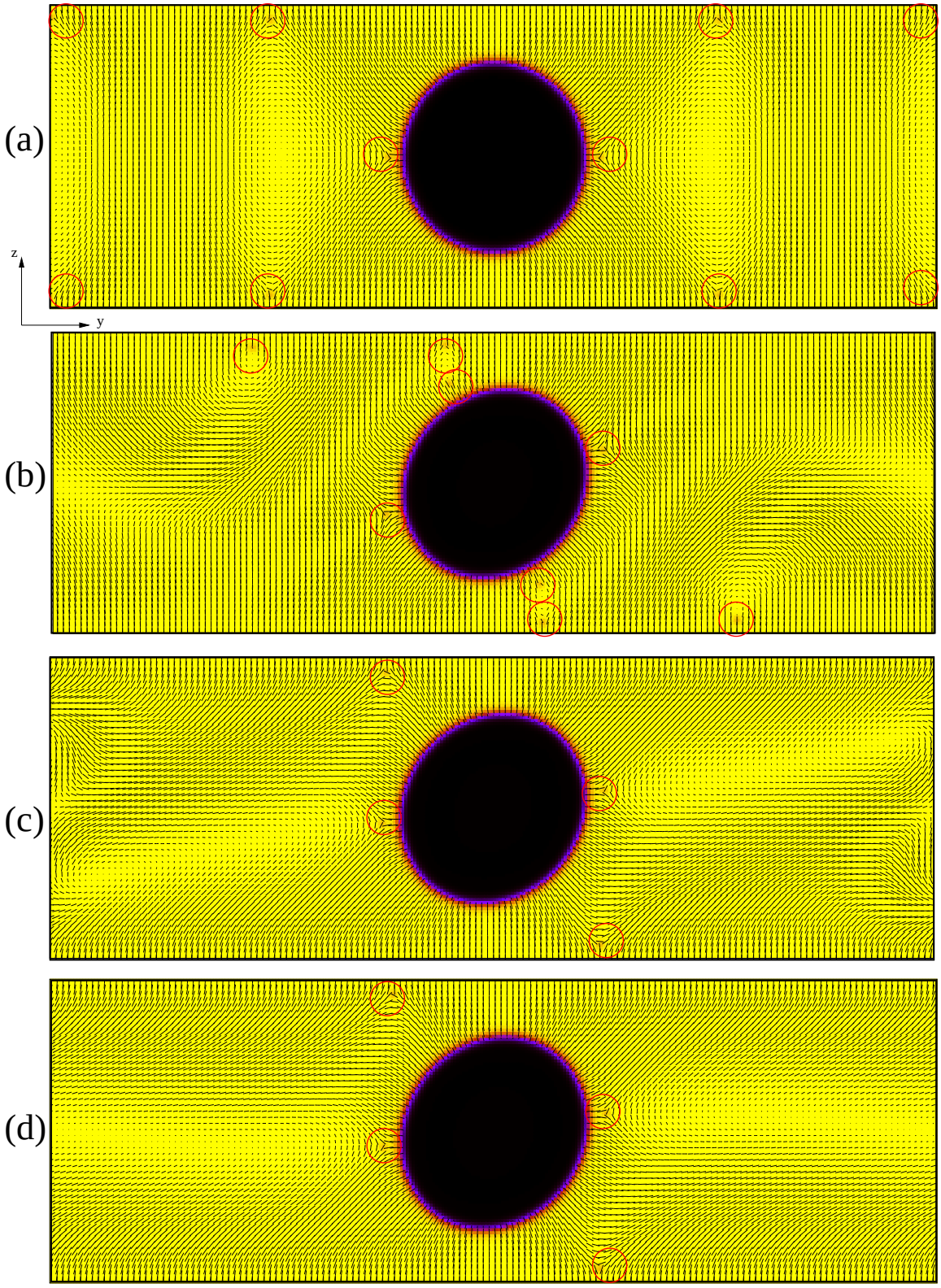

Figure 5.3: Configurations of an isotropic droplet in a cholesteric liquid crystal host for $N = 4$, $W = 0.04$ and $W_0 = 0.4$ with superposed the director field. The topological defects are highlighted with red circles. The times are $t = 4 \times 10^5$ the equilibrium (a), $t = 6 \times 10^5$ (b), $t = 8 \times 10^5$ (c) and $t = 1.4 \times 10^6$ (d) when shear is active. The color map represents the largest eigenvalue of the $\mathbf{Q}$ tensor and ranges from 0 (violet region inside the droplet) to 0.33 (yellow region outside the droplet). t is in simulation units.

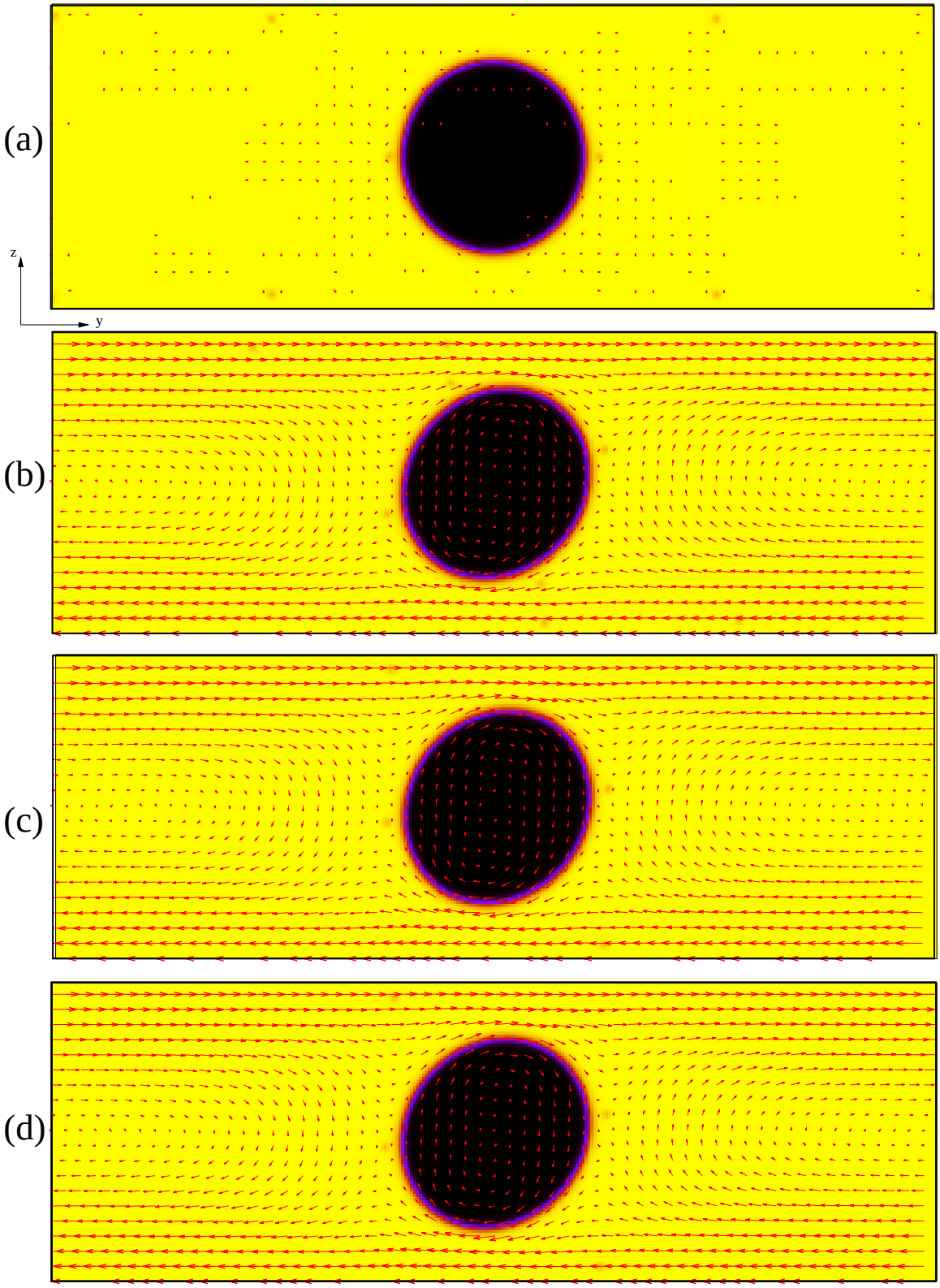

Figure 5.4: Configurations of an isotropic droplet in a cholesteric liquid crystal host for $N = 4$, $W = 0.04$ and $W_0 = 0.4$ with superposed the velocity field. The times are $t = 4 \times 10^5$ the equilibrium (a), $t = 6 \times 10^5$ (b), $t = 8 \times 10^5$ (c) and $t = 1.4 \times 10^6$ (d) when shear is active. The color map represents the largest eigenvalue of the $\mathbf{Q}$ tensor and ranges from 0 (violet region inside the droplet) to 0.33 (yellow region outside the droplet). t is in simulation units.

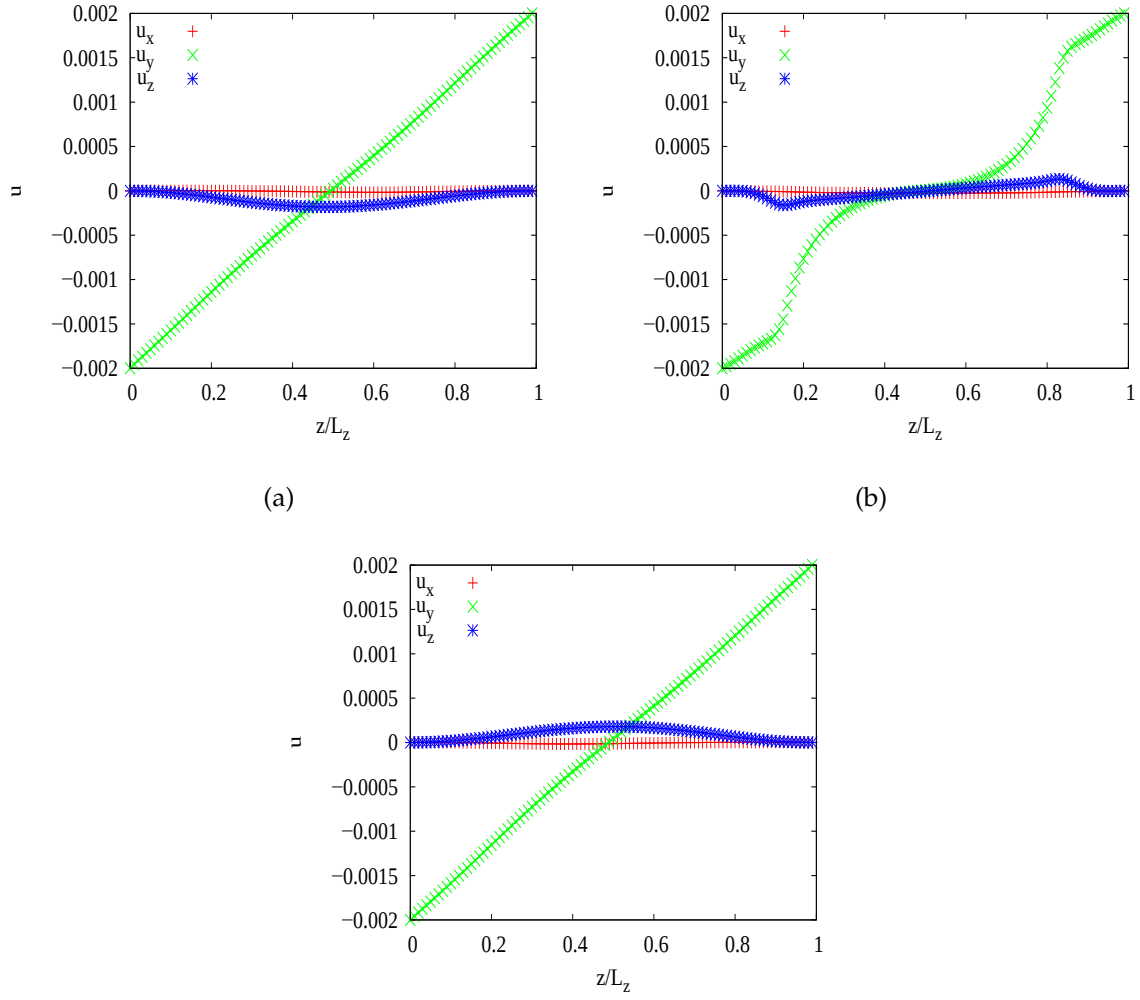

(a)

(b)

(c)

Figure 5.5: Sections of the three components of the velocity field for $y = L_y/6$ (a), $y = L_y/2$ (b) and $y = 5L_y/6$ (c).

5.5 Summary

In this chapter the first results of the simulations of a cholesteric emulsion under shear were collected. These results belong to the paper in preparation "*Shear dynamics of an inverted cholesteric emulsion*".
The case of an isotropic channel and the isotropic droplet in choelesteric phase were considered. The future studies will consist in analyze deeper the behaviour of the droplet under shear for different types of anchoring and directions of the helix. A quantitative calculus which can be performed following [8] consists in evaluating the Taylor deformation parameter, D, as function of the capillary number C_a varying the shear rates. An important effect of cholesteric is the permeation consisting in an enormous increase of the viscosity when a shear is applied along the direction of the helix. Thus starting from these initial results the future simulations will be focused on these directions.

Chapter 6

Self-propelled droplets through Marangoni effect

In this Chapter the main results of the self-propelled motion of a single and a couple of droplets through Marangoni effect, contained in the paper "*Lattice Boltzmann study of chemically-driven self-propelled droplets*", are collected.
At first the basic concepts like the surface tension and the surfactants are introduced; then the Marangoni effect is described. It is a physical effect consisting in the rise of a tangential force to an interface, which separates different fluids, due to an imbalance in the surface tension of the system which then results in the moviment of the fluid. In the case treated in the Chapter, a key ingredient to generate the imbalance in the surface tension is an anisotropy of the concentration of surfactant present in the system.
After that, the numerical model of a self-propelled droplet is introduced and then the results of the simulations. At first for the equilibrium case is considered and then the dynamic case when a chemical reaction scheme of production and consumption of the surfactant in the system is implemented to generate the propulsion due to the Marangoni effect. Choosing the production of the surfactant in an internal circular region of the droplet and consuming it in the system creates the requested imbalance in the surface tension which then generates the Marangoni flow which causes the moviment of the droplet.
In the final part of the Chapter the case for two droplets is considered in different geometries in order to investigate the mutual interactions. The cases of two self-propelled droplets is considered and also the cases in which one of the two is motionless. The typical geometries which are presented consist in two approaching collinear droplets, two approaching non collinear ones and two vertical droplets.

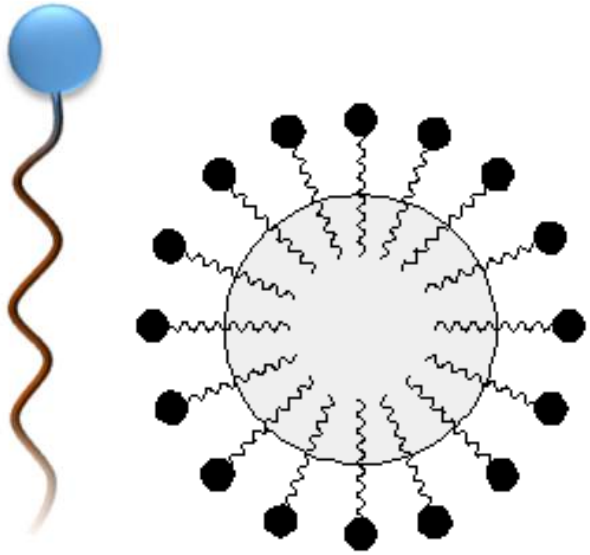

(a) (b)

Figure 6.1: (a) Schematic view of a single surfactant molecule and organization of surfactant molecules in water solutions (b).

6.1 Surface tension and surfactants

The surface tension, σ, is defined as the energy per unit area or a force per unit lenght to contract the interface with relation

$$\sigma = \partial F / \partial A \tag{6.1}$$

where $F = E - TS$ is the Helmholtz free energy with E internal energy, T temperature, S entropy and A the area of which the surface contracts.
For liquids in general the surface tension is a decreasing function of the temperature [140].
Surfactants are particular materials which have the property to spread at interfaces of systems and lower the surface tension [29, 141].
From a chemical point of view surfactant molecules are tipically amphiphilic which means that they possess hydrophilic groups, which "love" water, chemically bonded to lypophilic groups, which "hate" water. An example of a surfactant molecule consists in a hydrocarbon chain of 8-20 carbon atoms of lenght, also called surfactant "tail" linked to the hydrophilic "head" as shown in Fig. 6.1-(a). Fig. 6.1-(b) shows a typical structure in water solution which sees the polar heads of the surfactant molecules near the water and the hydrophilic tails inside the structure.

6.2 The Marangoni effect

Spatial variations in the surface tension at liquid-gas interface, for example, result in added tangential stresses at the interface and hence a surface tractive force that acts on the adjoining fluid, giving rise to fluid motions in the underlying bulk of the liquid. This motion induced by tangential gradients of surface tension is usually termed *Marangoni effect* after scientist C. Marangoni whose initial work on this theme appeared in 1871. This spatial gradients in the surface tension may arise from a variety of causes, including spatial variations at the interface in temperature, in surface concentration of a tensio-active substance like the surfactants or in electric charge. The resulting flows are termed respectively, thermocapillary flow, diffusiocapillary flow and electrocapillary flow [140, 142, 143].
The analytical expression which relates the tangential force to the gradient of the surface tension is

$$\mathbf{f} = \nabla\sigma. \tag{6.2}$$

The fact that the force is in the same direction of the gradient means that the force and so the flow, near the interface, is directed in the verse of higher surface tension as shown in Fig. 6.2 . However, due to the incompressibility of the fluid, a bulk motion of the fluid in the opposite direction arises [144].

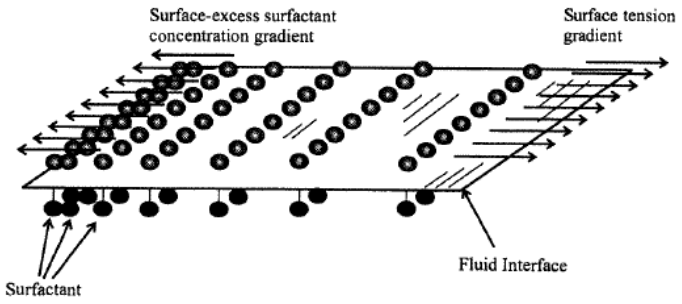

Figure 6.2: The Marangoni effect in the case of anisotropy of surfactant which results in a gradient in the surface tension. As long as surfactants lower the surface tension, the highest tension occurs in those regions where the surfactant density is lower; thus the restoring force acts in the opposite direction to the surfactant density gradient [144].

An interesting example of the Marangoni effect in everyday life is the so called "tears of wine"- the formation and motion of drops of wine and other spirits in the internal walls of a glass observed since the early history of humanity and also cited in the Bible. Myths talked of "tears" but the scientific and physical explanation

of the phenomenon can be searched in surface tension gradients arising due to the evaporation of alcohol from the mixture with the water in the thin part of the meniscus where wine wets the glass surface- this in turn generates a gradient in surface tension and drives the fluid upward leading he formation of tears of wine [145] as shown in Fig. 6.3.

(a) (b)

Figure 6.3: Schematic view of the phenomenon of the "tears of wine". When ethanol evaporates from the thinner region of the meniscus, a surface tension gradient is generated and the liquid climbs the glass spontaneously forming a film and then, thanks to gravity, tears. (b) Photo of a glass of wine with the "tears of wine" [145, 146].

Another example in which the Marangoni effect is visible is the soap boat [147] as shown in Fig. 6.4. If a small floating object such as a toothpick is placed on a water surface with one end dipped in soap, the surface tension at the clean end is greater than that at consiquently propels the object away from the soap.

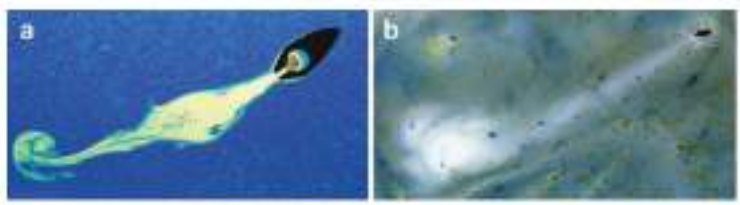

Figure 6.4: Marangoni propulsion of a "soap boat" and "Microvelia". The latter releases a small amount of surfactant and the resulting surface tension gradient propels it forward.

A similar mechanism is used by water walker insects to propel. Billard and Bruyant

(1905) observed this when terrestrial insects accidentally fell onto water surface. In fact releasing a surfactant, it was able to propel itself forward and up the meniscus bordering land and return to its preferred terrestrial environment. Marangoni propulsion of the rove beetle was observed with also other semi-acquatic insects for example *Microvelia* and *Velia*. The composition of the rove beetle's secreted surfactant was analyzed and it resulted with low solubility in water and reduced the surface tension from 72 to 49 dynes/cm with peak speeds, during the Marangoni propulsion for Microvelia, of approximately 17cm/s [147].

6.2.1 The Marangoni effect for droplets

Various studies were performed in the past considering different variants like a droplet under temperature gradient [148] and with surfactants due to chemical reactions that establish an anisotropy which causes the rise of the Marangoni flow [136, 146, 149–162]. In [146], for example, authors perform studies on self-propelled droplets through Marangoni effect induced by an imbalance in the surface tension created by an anisotropy in the concentration of surfactant in the system. Fig. 6.5 shows the mechanism of moviment of the droplet.
As shown in Fig. 6.5-(top), if the concentration of surfactant is isotropic around the droplet there will be no gradient in the surface tension and thus no motion will occur. In order to observe the motion of the droplet, the key ingredient is creating an anisotropy in the concentration of surfactant. This can be achieved in two different ways shown respectively in the center and the bottom of Fig. 6.5.
In the former case, the anisotropy is created manually inducing the surfactant to be more concentrated at one side of the droplet than the other and this results in the Marangoni flow which points in the verse of the side with less surfactant molecules (higher value of surface tension). The latter case corrisponds to a situation in which a chemical reaction, for example the bromination of the surfactant, determines the formation of inert products (the black circles in Fig. 6.5-(center)) which accumulate at one side of the droplet and thus creating again an imbalance in the surface tension which results in the Marangoni flow always pointing in the verse of higher surface tension. The bottom of Fig. 6.5 is the scheme of the flow of the self-propelled droplet: points A and B in this case are stagnation points with surface tension is A higher than B, the black lines represent the direction of the Marangoni flow instead the big arrow indicates the verse of the motion of the droplet.
Various are also the experimental realization of self-propelled droplets using oil or water ones [163–172]. An experiment which will be described is [163] and is shown in Fig. 6.6.
In this experiment oil droplets are considered which exhibit self-propelled motion consuming a hydrolyzable surfactant as "fuel" which is supplied by the acqueous

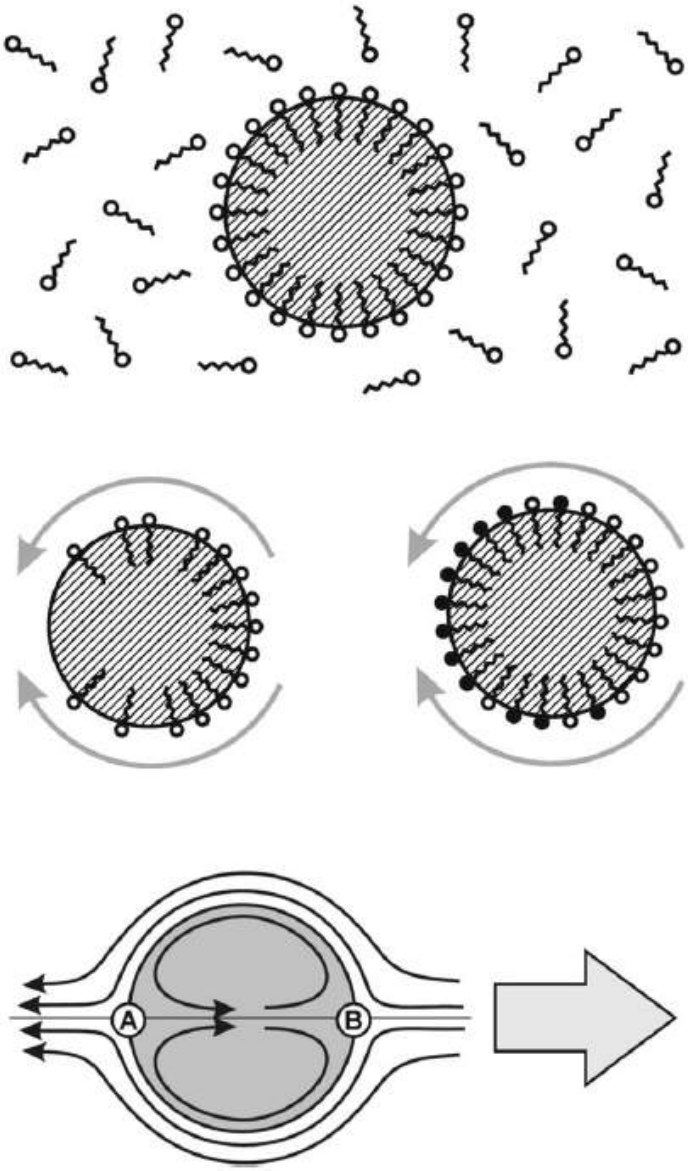

Figure 6.5: Top panel: surfactant molecules isotropically distributed around a droplet. Central panel: surfactant concentration becomes inhomogeneous (left) or a chemical reaction has occurred; the grey arrows indicate the verse of the Marangoni flow pointing in the direction of higher surface tension. Bottom panel: flow field of a droplet with points A and B with surface tension in A higher than B and; Marangoni flow indicated by the black lines and the big arrow which indicates the direction of motion of the droplet [146].

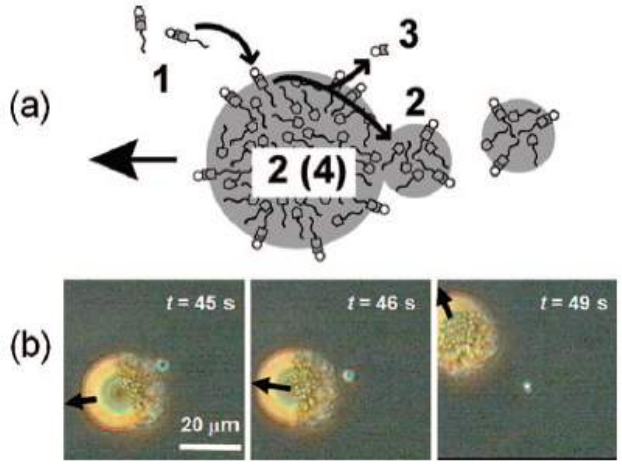

Figure 6.6: (a) Self-propelled oil droplet consuming "fuel" surfactant and producing "waste" oily droplets at the trailing edge. (b) Snapshots of of consequent moviment of the droplet which moves in the verse of the black arrow pushing the waste tiny droplet backwards and expelling it [163].

dispersion. After mixing acqueous dispersion of fuel surfactant N-(4-[3-[trimethylammonio]ethoxy]benzylidene)-4-octylaniline bromide), most of the floating droplets, with diameters in the range 10-140μm move autonomously with initial speeds of 3-40μms^{-1}. The origin of the self-propelled motion consists of three stages. In the first one, the hydrolysis of the fuel occurs at the surface of the oil droplet containing the catalyst. A fluctuation rate of the hydrolysis leads to the symmetry-breakege of the oil droplet and the products of the recation accumulates in the most reactive sites. In the second step the symmetry-breakage of the oil droplet causes an imbalance in the interfacial tension between the product accumulaing sites and the nonaccumulating sites, and the lateral moviment of the product is evoked at the surface of the oil droplet through the Marangoni instability. Another aspect is the fact that the lipophilic products generated by the hydrolysis of the surfactant aggregate forming tiny droplets as waste. The interfacial energy of the leading edge of the oil droplet becomes lower than the of the trailing edge and this is accompained by the motion of the droplet. In the last stage, the leading edge of the droplet continue to take additional fuel surfactant converting it into lipophilic product as the droplet moves. Meanwhile, the products of the reaction that aggregated forming tiny droplets are pushed backwards of the droplet and then released. Authors of the work observe that until the environment is rich of fuel surfactant the moviment continues with the droplet which sustains its unidirectional self-moviment consuming the fuel surfactant.

The practical applications on the self-propelled motion of droplets and particles in general are various and here some of them will be briefly mentioned. Sometimes literature uses terms like "smart devices" and "dream nanomachines" [173] to indicate the power and the potentiality of these systems and possible intense use in a future.
These applications go from the monitoring and water remediation [174–176], transport of a cargo [177, 178], extraction of rare-earth metal ions [179] to medical applications [180–182].
The self-propelled droplet via Marangoni effect induced by an anisotropy of the concentration of the surfactant established by a chemical reaction can be viewed as an interesting example of "active" system. The Active Matter is an interdisciplinary branch of research which studies "active" systems which exhibit self-propelled motion converting the energy supplied directly, isotropically and independently at the level of the individual constituents from a form into another. The key aspects which make "active " these systems is the fact that they are force free and constantly out of equilibrium as long as they continuosly convert the energy [153, 183, 184]. The self-propelled droplet through Marangoni effect is thus an active system because constantly converts chemical energy deriving by the chemical reactions of the surfactant into mechanical energy and so motion.

6.3 The squirmer model

The world of microorganisms, due to the little size of these kind of organisms, is characterized by low values of the Reynolds number[1] defined as

$$R_e = \frac{nLv}{\eta}. \tag{6.3}$$

where v and L are the velocity and the dimension of the organims, n is the density of the fluid and η is the dynamical viscosity. It represents the ratio between the inertil forces and the viscous ones. If it is low it means that inertia is negligible and instead the viscous forces dominate.
This fact has important consequences because the Navier-Stokes equation which is the equation for the velocity field of a fluid becomes simpler in the form of the Stokes equation

$$\nabla p = \eta \nabla^2 \mathbf{u} + f, \qquad \nabla \cdot \mathbf{u} = 0 \tag{6.4}$$

This equations are linear and more tractable mathematically.
In [150] it is shown how with the model of the self-propelled droplet due to Marangoni

[1] For low values it means $R_e << 1, \simeq 10^{-4}$.

effect it is possible to mimick the locomotion of this microorgnanisms. Another common model widely used is the so called *squirmer model*.
The squirmer model represents a particular class of swimmers particulary used because they admit exact solution and because this model can help in taking into account the hydrodynamic effects [149, 185–195]. This model was first introduced by Lighthill and Blake [196, 197]. It consists in a spherical particle with a prescribed tangential velocity distribution on its surface assuming absent the radial component of the velocity. The polar velocity is expressed as expansion of the Legendre polynomials

$$u(\theta) = \sum_{n=1}^{\infty} B_n \frac{2}{n(n+1)} sin\theta P_n^{'}(cos\theta) \tag{6.5}$$

where the coefficient B_n can depend on time.
In the simplest approximation $B_n = 0$ with $n > 2$, the only coefficient that are really important are the first and second order. So the expression above becomes

$$u(\theta) = B_1 sin\theta + \frac{1}{2} B_2 sin2\theta \tag{6.6}$$

B_1 and B_2 have both a precise physical meaning. B_1 in the squirmer model is related to the physical velocity of motion of the swimmer as

$$\mathbf{u} = \frac{2}{3} B_1 \tag{6.7}$$

instead the coefficient B_2 is related to the stresslet or force dipole[2]
From B_1 and B_2 it is possible to build an adimensional parameter

$$\beta = B_2 / B_1. \tag{6.8}$$

This ratio can have a sign and its value determines the type of swimmer.
If $\beta > 0$ the squirmer is called *puller* or *polar contractile squirmer* since it pulls the fluid inwards along its body axis; algae like *Chlamydomonas reinhardtii* are examples of pullers. If, instead, $\beta < 0$ the squirmer is a *pusher* or *polar extensile squirmer* since it pushes fluid outwards along its body axis.
Two limiting cases are represented by $\beta = 0$ ($B_2 = 0$) and $\beta = \infty$ ($B_1 = 0$). The former case correspond to a neutral squirmer which develops a potential flow; in absence of stress the features of propulsion are analogous to the transport of a charged colloid under electric fields [187]. Tha latter case, instead, corresponds to a "shaker" e.g. a microorganism which does not propel but puts the fluid in motion shaking it [187–189, 191].

[2]The stresslet is the singular solution of the Stokes equation associated with no net force or moment to the fluid.

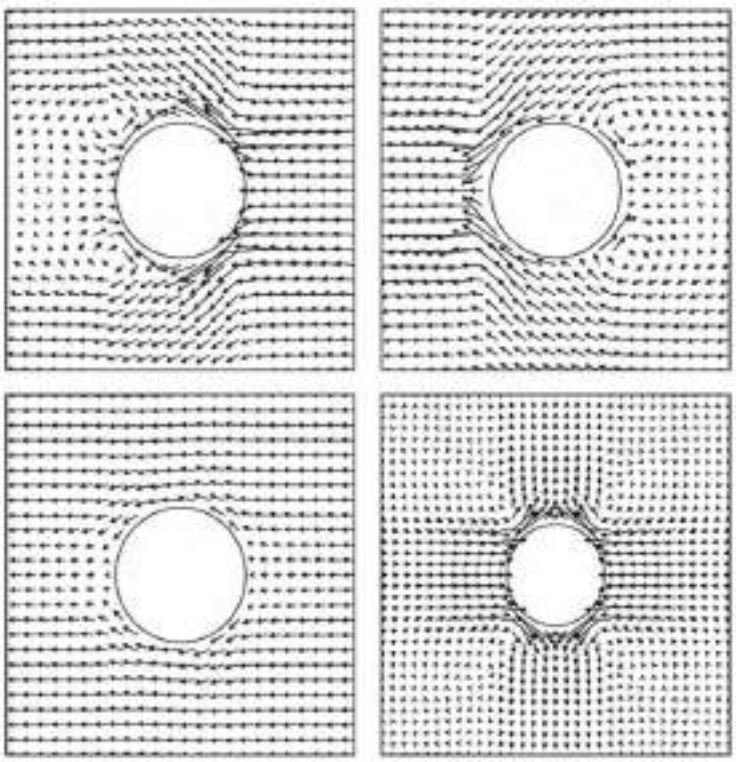

Figure 6.7: Flow streamlines of a polar contractile squirmer or puller, $\beta > 0$), (top left); polar extensile squirmer or pusher, $\beta < 0$, (top right); neutral squirmer, $\beta = 0$ (bottom left); shaker, $\beta = \infty$ (bottom right) . The velocity fields are shown in the squirmer frame of reference [187].

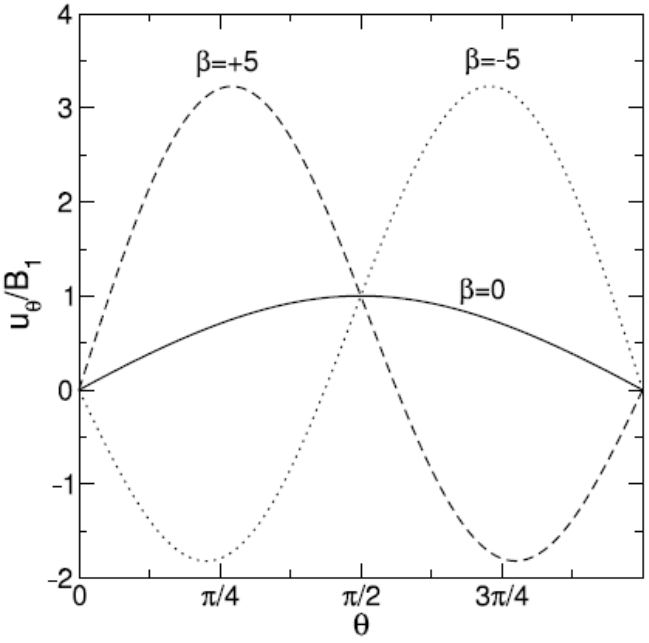

Figure 6.8: Polar velocity $u(\theta)$ as function of the polar angle θ on the surface of the squirmer for a puller ($\beta > 0$), a pusher ($\beta < 0$) and for a neutral squirmer ($\beta = 0$) [189].

Fig. 6.7 reports all the types of squirmers and their typical velocity pattern, in the squirmer moving frame, and Fig. 6.8 shows the polar velocity $u(\theta)$ for a puller, pusher and a neutral squirmer.

6.4 Numerical model of a self-propelled droplet

The systems consists in a ternary fluid mixture with free energy functional like the one used by authors in [136]

$$\mathcal{F} = \int d\mathbf{r} \left[nT \ln n + f_{GL}(\phi) + \frac{B(c)}{2}(\nabla\phi)^2 + c \ln c \right], \tag{6.9}$$

where ϕ is the local concentration difference of two immiscible components of the mixture, c is the concentration of surfactant (the third component), T is the temperature, assumed fixed in the following, and n is the total density of the mixture. The term depending on n gives rise to the ideal gas pressure $p^i = nT$ which does not affect the phase behavior. The free-energy density $f_{GL}(\phi) = \frac{a}{2}\phi^2 + \frac{b}{4}\phi^4$ corresponds to the polynomial part of a Ginzburg-Landau free energy describing the bulk properties of the system [9]. The coefficient b is always positive while a allows to discriminate between a disordered ($a > 0$) mixture and an ordered one ($a < 0$), where the two components coexist with equilibrium values $\phi = \pm\phi^{eq}$ being $\phi^{eq} = \sqrt{-a/b}$ [14]. The interfacial properties of the mixture are controlled by the gradient term where the coupling $B(c)$ is assumed globally positive with expression $B(c) = B_0 + B_1 c$. The coefficient B_1 determines whether the surfactant migrates to the interface ($B_1 < 0$) or away from it in the bulk ($B_1 > 0$) [134, 135]. The logarithmic term $f_0 = c \ln c$ arises from the translational entropy of the dilute amphiphilic component [136].
The time-evolution of ϕ is described by the convection-diffusion equation

$$\partial_t \phi + \nabla \cdot (\phi \mathbf{u}) = \nabla^2 \mu_\phi \tag{6.10}$$

where μ_ϕ is the chemical potential with expression

$$\mu_\phi = \frac{\delta \mathcal{F}}{\delta \phi} = a\phi + b\phi^3 - B(c)\nabla^2\phi - B_1 \nabla\phi \cdot \nabla c. \tag{6.11}$$

The dilute component c of surfactant obeys a convection-diffusion equation as well

$$\partial_t c + \nabla \cdot (c\mathbf{u}) = \nabla \cdot [L(c)\nabla\mu_c] \tag{6.12}$$

where $L(c) = Dc$ and D is the diffusion coefficient for the surfactant. The quantity μ_c is the chemical potential of the surfactant

$$\mu_c = \frac{\delta \mathcal{F}}{\delta c} = \ln c + 1 + \frac{B_1}{2}(\nabla\phi)^2. \tag{6.13}$$

In the right hand side of (6.12) the linear dependence of $L(c)$ is necessary for a dilute component [136]. The concentrations ϕ and c are coupled to the local

velocity $\mathbf{u}$ of the whole fluid which obeys the Navier-Stokes equation

$$\partial_t(nu_\beta) + \partial_\alpha(nu_\alpha u_\beta) = -\partial_\alpha P_{\alpha\beta} + \partial_\alpha \left\{ \eta \left(\partial_\alpha u_\beta + \partial_\beta u_\alpha - 2\frac{\delta_{\alpha\beta}}{d}\partial_\gamma u_\gamma \right) + \zeta\delta_{\alpha\beta}\partial_\gamma u_\gamma \right\} \tag{6.14}$$

where η and ζ are the shear and bulk viscosities respectively and d is the dimensionality of the system ($d = 2$ in this case). The fluid mass density n satisfies the continuity equation

$$\partial_t n + \nabla \cdot (n\mathbf{u}) = 0. \tag{6.15}$$

$P_{\alpha\beta}$ is the pressure tensor of the system. Its expression is obtained by

$$P_{\alpha\beta} = \left[\phi\frac{\delta\mathcal{F}}{\delta\phi} + c\frac{\delta\mathcal{F}}{\delta c} + n\frac{\delta\mathcal{F}}{\delta n} - f(\phi, c) \right] \delta_{\alpha\beta} + D_{\alpha\beta} \tag{6.16}$$

where $D_{\alpha\beta}$ has to ensure the general equilibrium condition $\partial_\alpha P_{\alpha\beta} = 0$ [14]. It turns out that $P_{\alpha\beta} = p_0\delta_{\alpha\beta} + B(c)\partial_\alpha\phi\partial_\beta\phi$ with

$$p_0 = p^i + \frac{a}{2}\phi^2 + \frac{3b}{4}\phi^3 - B(c)\phi\nabla^2\phi - B_1\phi\nabla c\cdot\nabla\phi + c - \frac{B_0}{2}\nabla\phi\cdot\nabla\phi. \tag{6.17}$$

The self-propelled motion of the droplet can be achieved adding a source term $A\Theta(R - |\mathbf{r} - \mathbf{r}_P|)$ and a consumption one $-\gamma(c - c_0)$ to the Eq. (6.12) of the surfactant concentration. The source term with coefficient $A > 0$ mimicks the production of surfactant in a circular region, centered in $\mathbf{r}_P$ inside the droplet, of radius R, Θ being the Heaviside step function. The second term, instead, promotes a reduction of c with rate $\gamma > 0$, c_0 being the minimum value of c all over the system. Equations (6.10), (6.12), (6.14) and (6.15) were solved numerically by using a hybrid method described in details in Chapter 3. In the following paragraphs the main results of the simulations starting from the equilibrium initial analysis and then moving to the study of the self-propelled motion of a single-droplet and the interactions between two droplets.

6.5 Equilibrium properties of the system

In this section the relaxation towards equilibrium of a planar sharp interface separating the phases of a binary fluid mixture is considered. The study is performed on a lattice of size $L_x = L_y = 128\Delta x$ where periodic boundary conditions are set. Thermodynamic parameters are $a = -b = -0.001$, $D = 0.1$, $\Delta x = \Delta t_{LB} = 1$, $\tau = \Delta t_{LB}$. In this case $\gamma = A = 0$ to neglect production and consumption contributions of the surfactant. In Fig. 6.9 the profiles of ϕ and c at several simulation times are shown, when $B_0 = 0.006$ and $B_1 = -0.05$, in order to favour the migration of the surfactant (initially set to $c_i = 0.1$ everywhere) to the interface from the bulk.

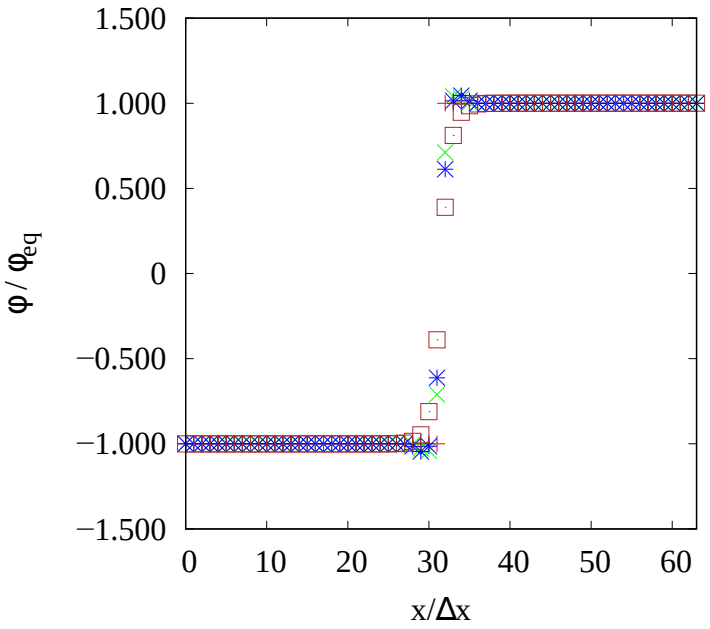

(a)

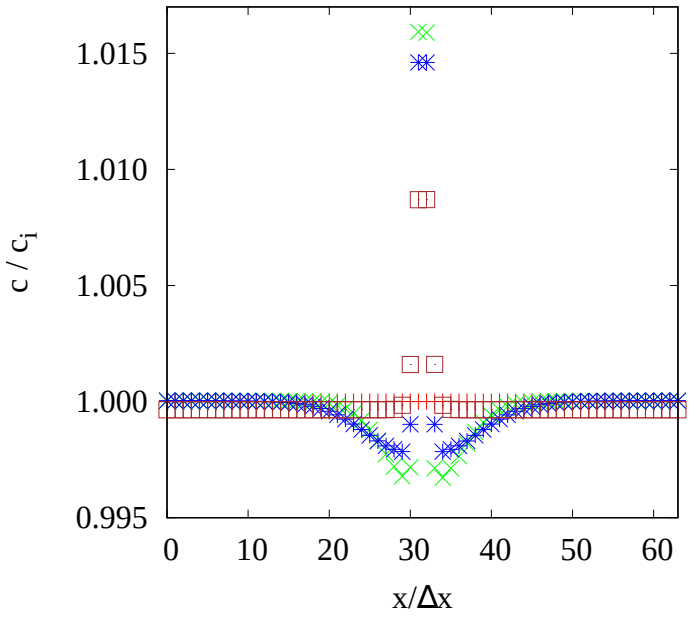

(b)

Figure 6.9: Concentration profiles of ϕ (a) and c (b) across the system for $B_0 = 0.006$ and $B_1 = -0.05$ at times $t/\Delta t_{LB} = 0$ (+), 10^2 ($\times$), 2×10^2 ($*$), 2×10^5 ($\square$).

The concentration ϕ correctly relaxes to its expected equilibrium profile [14, 198], given by

$$\phi(x) = \phi^{eq} \tanh\left(\frac{2x}{\xi}\right) \tag{6.18}$$

where ξ is the interface width, whereas the surfactant gradually moves towards the interface where a peak in the concentration is found. This is created at early times and lasts until full equilibration (namely when $\nabla\mu_\phi = \nabla\mu_c = 0$ and $\partial_\alpha P_{\alpha\beta} = 0$) is achieved. In line with these results, a good agreement is also found between the theoretical and the numerical values of the surface tension obtained for several values of B_0 and B_1 (Table 6.1). For a planar interface along the x direction, the former is calculated as [136]

$$\sigma_{th} = \int B(c)\left(\frac{\partial\phi}{\partial x}\right)dx, \tag{6.19}$$

whereas the numerical value is computed from [3]

$$\sigma_{num} = \int (f(\phi, c) - f(\phi^{eq}, c))dx, \tag{6.20}$$

where $f(\phi, c)$ is the free-energy density of a system with planar interface and $f(\phi^{eq}, c)$ is the free-energy density of a homogeneous system without interface.
By keeping B_0 fixed, the value of the surface tension is lower when $B_1 < 0$ due to the accumulation of surfactant at the interface. As expected, by increasing B_0 the surface tension increases if B_1 is kept negative. Fitting the theoretical relation of Eq. (6.18) with the simulation data, it was also possible to compute numerically the interface width ξ with values collected in Table 6.1. Then the relaxation towards equilibrium of a circular droplet of radius $R = 32\Delta x$ with the same parameter set, as a test case of a system with interface not aligned with lattice links was considered. Fig. 6.10 shows the contour plot of the concentrations ϕ of the system when $B_0 = 0.006$ and $B1 = -0.05$. Instead Fig. 6.11 shows the contour plot of the concentration c of surfactant when $B1 = 0.05$ Fig. 6.11-(a) with surfactant which has escaped in the bulk and when $B1 = -0.05$ Fig.6.11-(b) with surfactant migrated at the interface of the droplet.

B_0	B_1	σ_{th}	σ_{num}	ξ
0.003	-0.01	0.00128	0.00129	3.90
0.003	0.01	0.00185	0.001856	5.57
0.006	-0.01	0.00208	0.00208	6.23
0.006	0.01	0.00248	0.00249	7.38
0.006	-0.03	0.00159	0.00160	4.80
0.006	0.03	0.00283	0.00284	8.35
0.006	-0.05	0.00086	0.00086	2.57
0.006	0.05	0.00314	0.00314	9.21
0.01	-0.01	0.00283	0.00283	8.35
0.01	-0.05	0.00208	0.00208	6.23
0.01	-0.08	0.00127	0.00128	3.83
0.08	-0.05	0.00915	0.00932	21.66
0.08	-0.1	0.0089	0.0089	20.78
0.08	-0.6	0.0043	0.0041	12.11

Table 6.1: Comparison of theoretical, σ_{th}, the numerical values, σ_{num}, of the surface tension and interface width, ξ, for a planar interface with different values of B_0 and B_1.

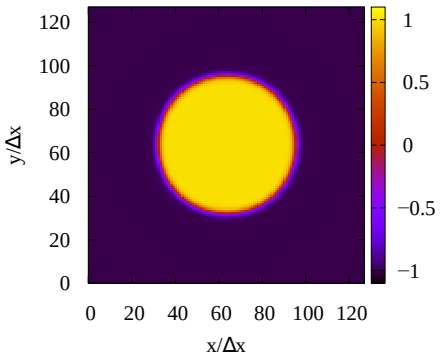

Figure 6.10: Contour plot of the concentration field ϕ for $B_0 = 0.006$ and $B_1 = -0.05$.

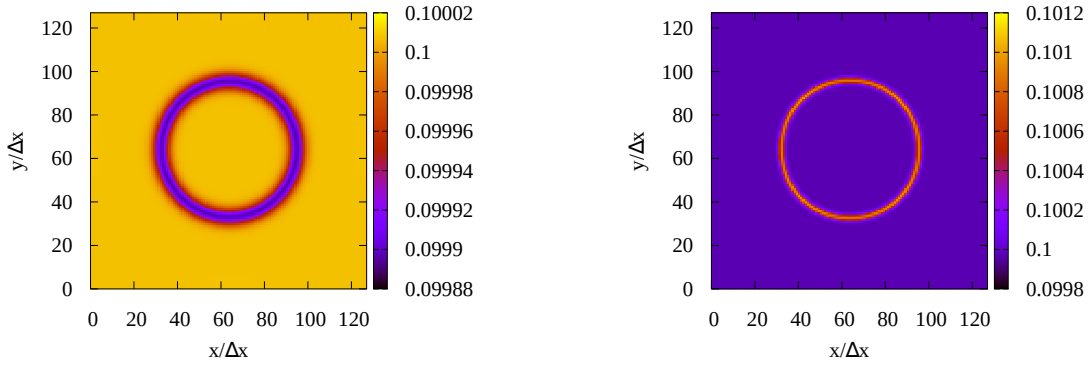

Figure 6.11: Contour plots of the concentration field c for $B_1 = 0.05$ and for $B_1 = -0.05$.

6.6 Single self-propelled droplet

In this section the study of the self-propelled motion of a droplet in the system is analyzed. The results which will be presented refer to values $B_0 = 0.006$ by $B_1 = \pm 0.05$; in this case the system consists in a rectangular box with dimensions $L_x = 512\Delta x$ and $L_y = 256\Delta x$ enclosed among rigid walls in order to be sure that periodic effects could not affect the motion of the droplet. The relaxation time was reduced to the value $\tau = 0.6\Delta t_{LB}$ in order to reduce the viscosity. A droplet of radius $R = 32\Delta x$ is initially placed at the center of the lattice with initial constant value of surfactant, $c_i = 0.1$, all over the system. At first the system equilibrated until approximately $t/\Delta t_{LB} = 2 \times 10^5$ and then the terms of consumption and production of surfactant in equation (6.12) were switched on. As introduced before, the consumption of surfactant happens in the whole system with value c_0 as the minimum of c all over the lattice and consumption rate $\gamma = 1.5 \times 10^{-3}$ whereas the production of surfactant happens in a circular region inside the droplet. In particular the coefficent A, that controls the strenght of production, was chosen time dependent with $A(t) = A_0 t$ being $A_0 = 0.5 \times 10^{-10}$. The choice of the values γ and A is not casual but convenient in order to ensure a considerable movement of the droplet and to prevent its breaking. In fact, if the system produces surfactant too fast, the stability condition $B(c) > 0$ is violated and the droplet breaks up. In this sense the presence of a consumption term, which attenuates the production of surfactant, is important. The internal region of surfactant production has been defined in this way: a circular region was chosen fixing the center in the point (x_P, y_P) with $x_P = x_{CM} + 20\Delta x$ and $y_P = y_{CM}$ with the center of mass (x_{CM}, y_{CM})

of the droplet given by [14]

$$\mathbf{r}_{CM}(t) = \frac{\sum_{ij} \phi_{ij} \mathbf{r}_{ij}(t)}{\sum_{ij} \phi_{ij}} \tag{6.21}$$

where the indexes i and j denote the lattice sites and the sum is calculated under the constraint $\phi_{ij} \geq 0$. The x-coordinate of the extremal point ($x_{EXTR}, y_{EXTR} = y_P = y_{CM}$) which indicates the interface of the droplet, has been calculated trough bilinear interpolation assuming that the interface is located at $\phi = 0$. The radius of the region of production of surfactant was simply calculated as the difference $|x_{EXTR} - x_P|$.
The competition between the two actions of production and consumption of surfactant creates a gradient of the surface tension being its value in the leading (point B) smaller than in the trailing edge (point A) (Fig. 6.12). Thus the Marangoni flows which results, is directed from B to A resulting in the movement of the droplet to the right as denoted by the thick long white arrows. Fig. 6.12 shows the contour plot of the surfactant in the system for the cases $B_1 < 0$ (surfactant which migrates to the interface of the droplet) and $B_1 > 0$ (surfactant which migrates away from the interface of the droplet) with the region of production in the right part of the droplet (interface with black circle). The velocity field is superimposed in the plot. Fig. 6.13 shows the x component of the center of mass of the droplet for the cases $B_1 < 0$ and for $B_1 > 0$ for values $|B_1| = 0.05$ in the time interval $[2 \times 10^5 \Delta t_{LB}; 2 \times 10^6 \Delta t_{LB}]$. In both cases th droplet starts from the middle of the lattice ($L_x/2 = 256\Delta x$, $L_y/2 = 128\Delta x$) and moves to the right. These two cases have the same set of parameters and same mechanism of production and consumption of surfactant. In the plot it is clear that in the case $B_1 < 0$ the motion is more robust than the counterpart $B_1 > 0$; for this reason the latter case was neglected and the attention was focused only on the case $B_1 < 0$ in order to study the interactions between two droplets. As the motion is horizontal along the x direction the y component of the center of mass remains almost constant in the time and for simplicity it has not been reported.
Fig. 6.14 represents the panels of the configurations of the droplet for different times ((a) $t = 5 \times 10^5$, (b) $t = 10^6$, (c) $t = 1.5 \times 10^6$ and (d) $t = 2 \times 10^6$) with concentration field ϕ and the velocity field. Fitting the numerical data of $u(\theta)$ using Eq. (6.6) it was possible to obtain the plots of Fig. 6.15 of the polar velocities for both cases $B_1 > 0$ and $B_1 < 0$. The behaviour of $u(\theta)$ resembles, at least on a qualitative level, the one expected for pusher-like particles of Fig. 6.8.
For the single self-propelled droplet a set of simulations in the time interval $[2 \times 10^5; 2 \times 106]$ was performed considering various distances of the droplet by the upper wall in order to detect the influence of the wall in the motion. Fig. 6.16 shows the trajectories of the droplet for various distances from the wall quantified by the extremal point of the droplet. As shown in Fig. 6.16, when the droplet

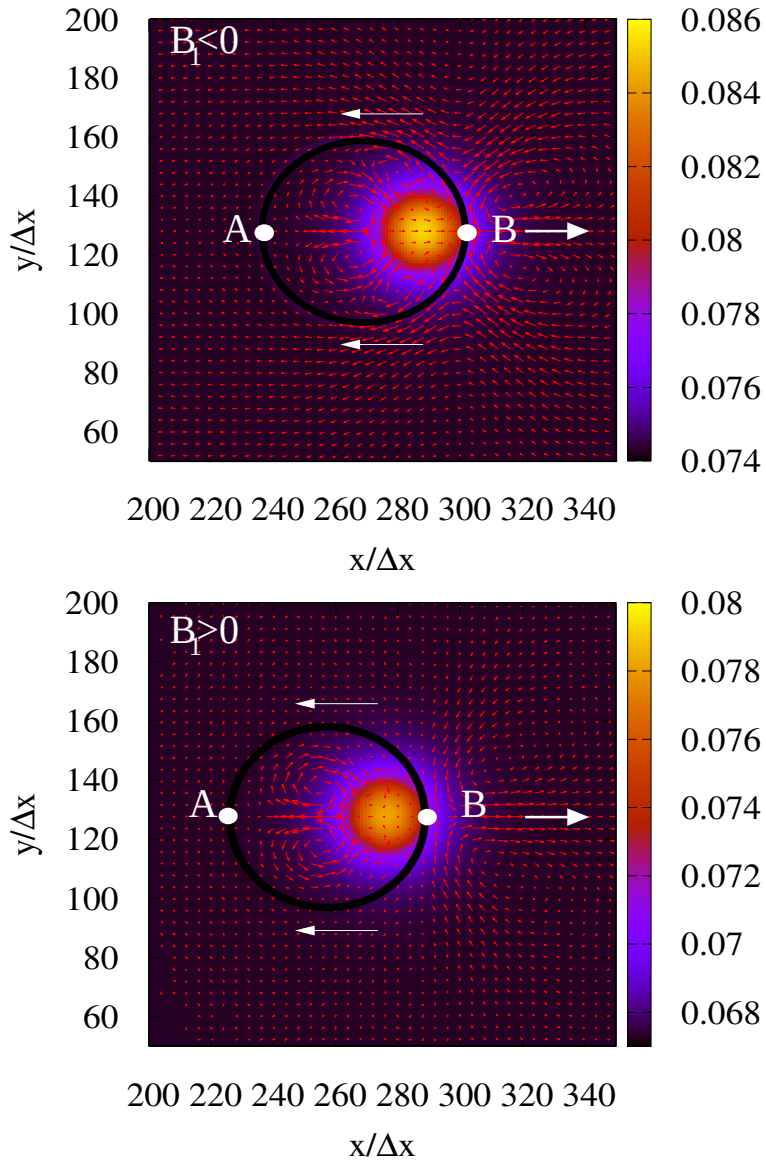

Figure 6.12: Contour plot of the concentartion field c of the surfactant with the velocity field superimposed (in the moving frame of the droplet) when $B_1 < 0$ (top panel) and $B_1 > 0$ (bottom panel). The time is $t/\Delta t_{LB} = 6 \times 10^5$ for both cases. The production and the consumption of surfactant start at time $t/\Delta t_{LB} = 2 \times 10^5$. The black external circle indicates the interface of the droplets assumed at $\phi = 0$ while the little one the region of production of surfactant. A and B indicate the two extremal points of the droplet with surface tension in A greater than in B. The thin arrows indicate the direction of the Marangoni flow coincident with the gradient of surface tension instead the thick arrows on the right indicate the direction of motion of the droplet.

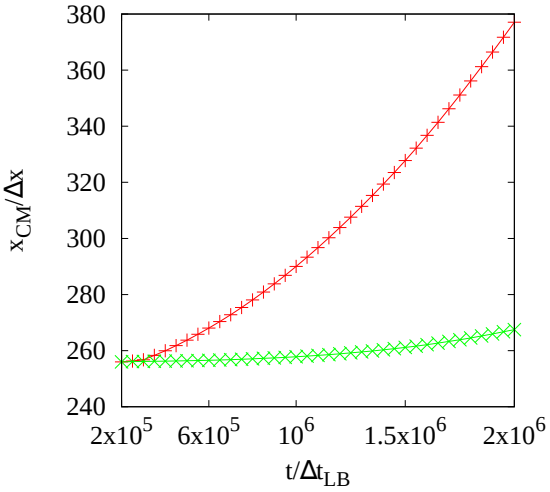

Figure 6.13: x component of the center of mass of the droplet as a function of the time for $B_1 < 0$ $(+)$ and for $B_1 > 0$ $(\times)$ and value $|B_1| = 0.05$ in the time interval $[2 \times 10^5 \Delta t_{LB}; 2 \times 10^6 \Delta t_{LB}]$. The droplet starts from the middle of the lattice $(L_x/2 = 256\Delta x, L_y/2 = 128\Delta x)$ and moves to the right in increasing abscissa.

is "too close" to the wall (for example when the initial center of mass has coordinate $y_{CM} = 192\Delta x$), it moves for the already described Marangoni effect but it also experiments a vertical moviment due to the repulsion from the upper wall. Continuing to rise the distance of the droplet from the wall, the influence becomes more and more negligible.

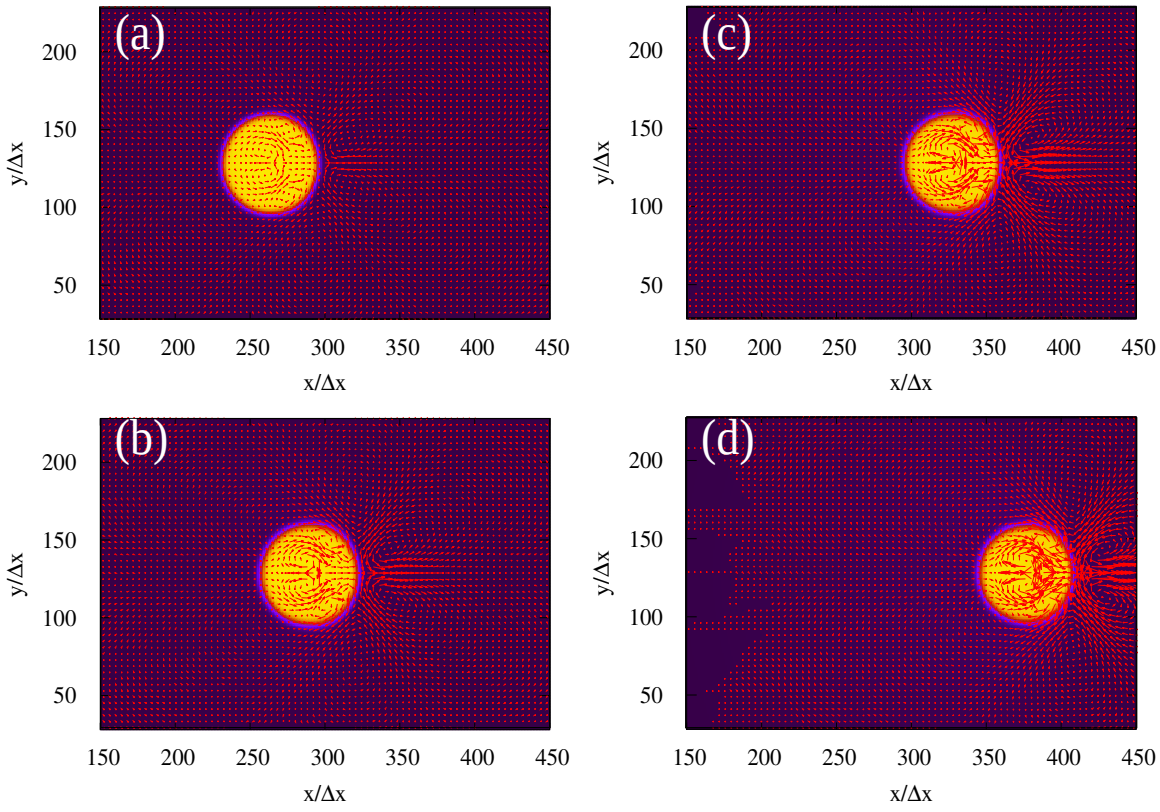

Figure 6.14: Successive configurations of the concentration field ϕ with superposed velocity field of the seld-propelled droplet for times $t/t_{LB} = 5 \times 10^5$ (a), $t/t_{LB} = 10^6$ (b), $t/t_{LB} = 1.5 \times 10^6$ (c) and $t/t_{LB} = 2 \times 10^6$ (d).

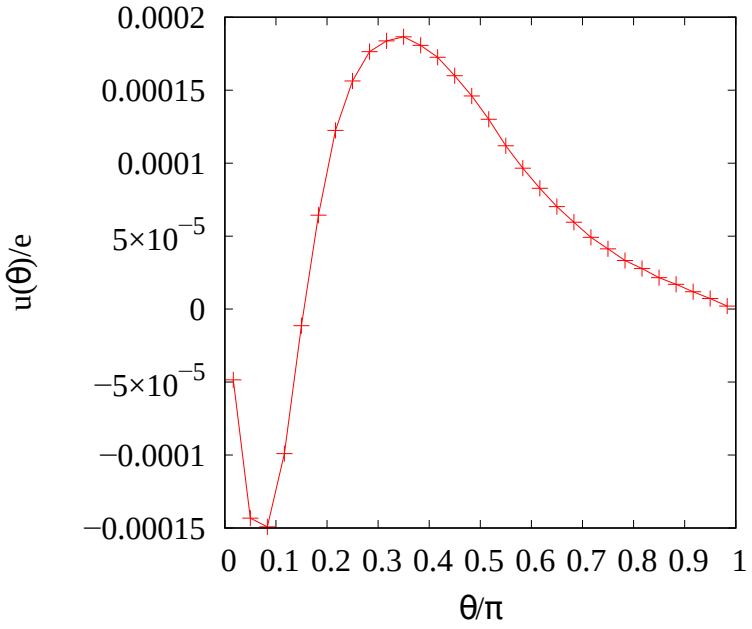

(a)

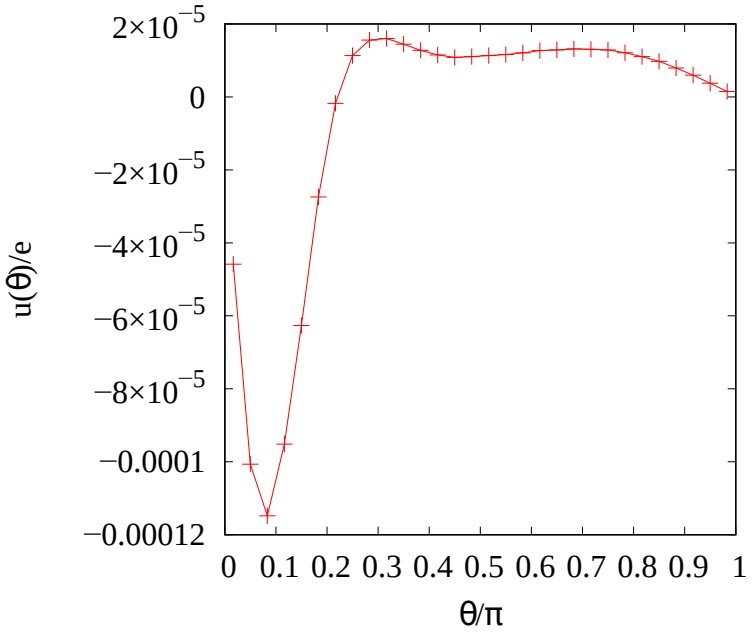

(b)

Figure 6.15: Polar velocity $u(\theta)$ as a function of the polar angle θ for the case $B_1 < 0$ (a) and $B_1 > 0$ (b). These curves are at time $t/\Delta t_{LB} = 6 \times 10^5$.

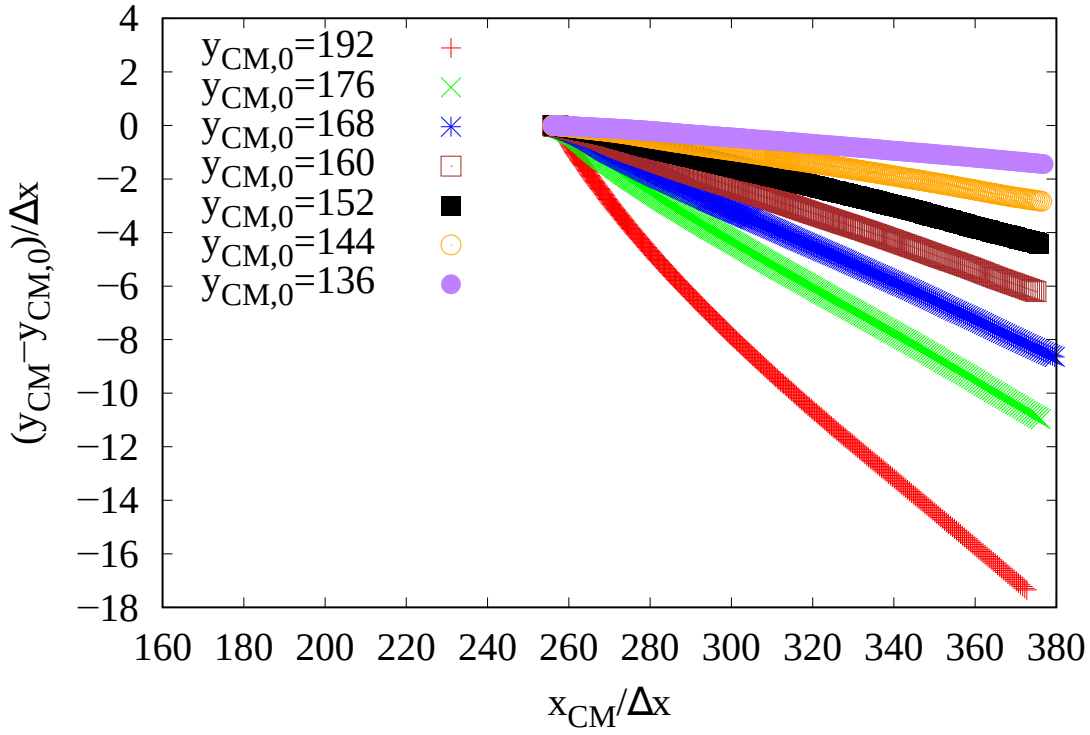

Figure 6.16: Trajectories of the droplet for various distances by the upper wall. In the vertical axis the vertical componenents of the center of mass of the y_{CM} have been rescaled by $y_{CM,0}$ the initial equilibrium value of the vertical component of the center of mass.

6.7 Two interacting self-propelled droplets

After the description of the motion of a single active droplet, the interactions between two droplets are considered. Different system realizations using both active and passive droplets were treated starting from the previous case of study of two of them in [152]. The adjective "passive" indicates the fact that in such a droplet the production of surfactant is missing thus inhibiting the Marangoni effect.

6.7.1 Colliding collinear droplets

The case sees two collinear droplets of radius $R_0 = 32\Delta x$ located on the same horizontal line in a lattice of size $L_x = 512\Delta x$, $L_y = 256\Delta x$. They are placed at distance $|x_{cm,1}(t_i) - x_{cm,2}(t_i)| = d_x(t_i) = 6R_0$, where $(x_{cm,1}, y_{cm,1})$ and $(x_{cm,2}, y_{cm,2})$ are the coordinates of the centers of mass of the droplets. The same set of parameters used in the case of the isolated active droplet is adopted here as well. The system is initially relaxed up to $t_i \simeq 2 \times 10^5 \Delta t_{LB}$; afterwards production and consumption terms of the surfactant are switched on.
At early times, the velocity field generated by each droplet resembles that seen in Fig. 6.17, with four vortices inside the droplets and other four ones located in their front, arranged into a fourfold symmetry. Due to the initial relatively large distance between them, the hydrodynamic interaction mediated by the external passive fluid is negligible (Fig. 6.17-(a)). However, as the droplets move against each other driven by the inhomogeneity of the surfactant distributions, a compression of the four vortices formed in the fluid in between is observed. In addition a further quadrupolar field is clearly visible in the system. Here two vortices are located on top of each droplet outside them and the other two are placed at their bottom (Fig. 6.17-(b)). The structure of the velocity field inside each droplet instead displays the typical four vortices, again triggered by a Marangoni-like effect, although now more intense than that seen at early times. The relative motion persists up to a time t_f when a balance between the repulsion induced by the flow between the droplets and an attraction due to Marangoni effect is achieved. This occurs, for the specific simulation considered, at distance $d_x(t_f) \simeq 3.3R_0$ with $t_f/\Delta t_{LB} \simeq 1.585 \times 10^6$. The dynamics is overall simpler if the active droplet on the right is replaced with a passive one (Fig. 6.17-(c)-(d)). In this case only the active droplet on the left is self-propelled along the increasing x-axis. While initially the interaction between the two droplets is negligible (Fig. 6.17-(c)), when the active one approaches the passive one the fluid flow generated by the former pushes the latter rightwards, which is hence simply advected by the fluid (Fig. 6.17-(d)). In order to better appreciate the effect of the surfactant, also the collision of two passive droplets, driven by a constant external force acting on each of them (Fig 6.17-(e)-(f)) was included. The external force acts on the density inside the droplets and is di-

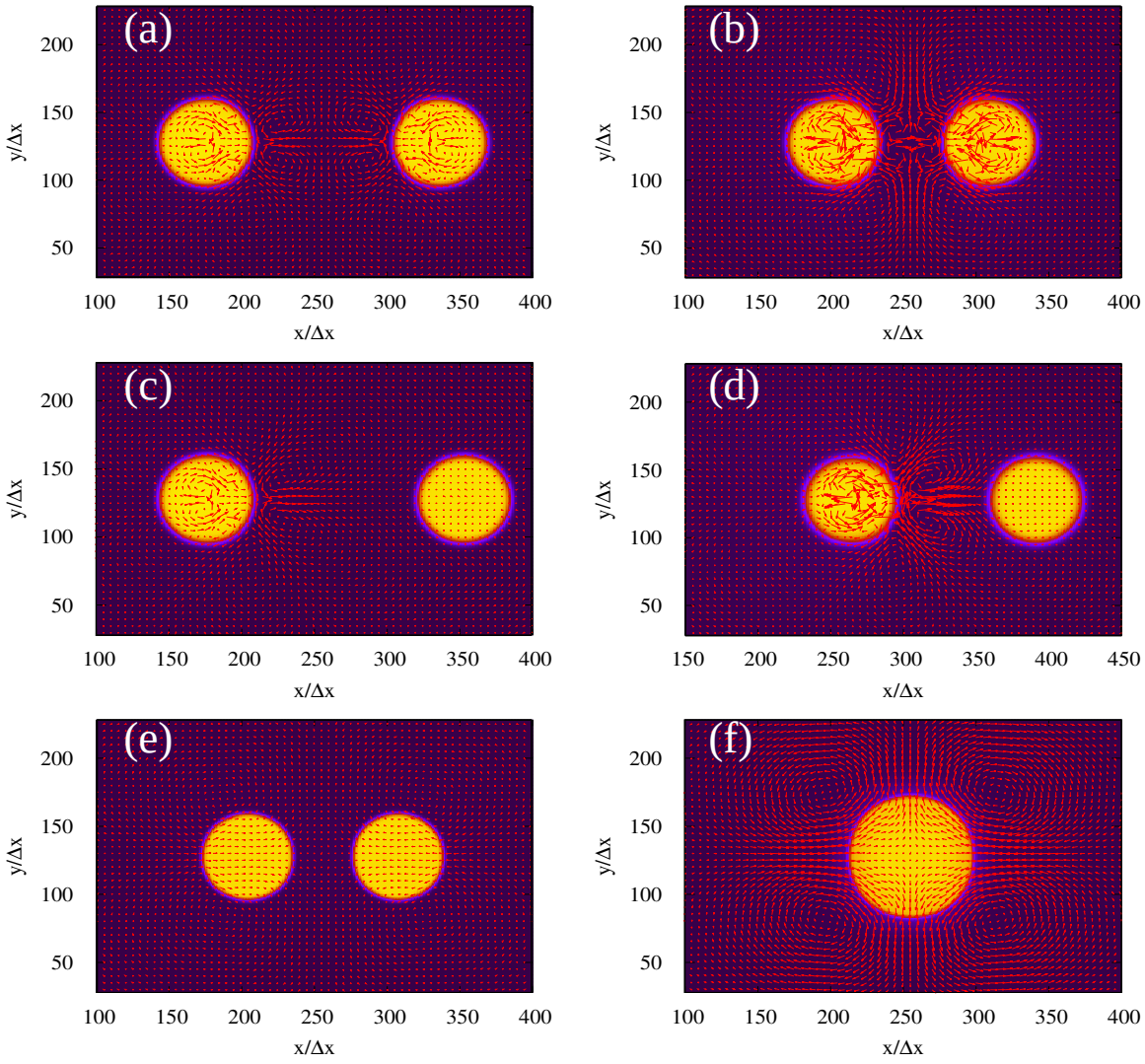

Figure 6.17: Contour plots of the concentration field ϕ for two active colliding collinear droplets ((a)-(b)), active left droplet towards passive right droplet ((c)-(d)) and two passive colliding droplets ((e)-(f)). The velocity field is also shown. The whole lattice is $[512\Delta x \times 256\Delta x]$. In the first case the two active droplets initially approach each other ((a) $t/\Delta t_{LB} = 7 \times 10^5$), but, when a balance between the repulsion generated by intermediate hydrodynamic flow and the attraction due to a Marangoni-like effect is achieved, the reciprocal motion ceases ((b), $t/\Delta t_{LB} = 1.585 \times 10^6$). In the second case the active droplet moves towards the passive immobile one ((c), $t/\Delta t_{LB} = 7 \times 10^5$) and, when they come sufficiently close, the former pushes the latter to the right ((d), $t/\Delta t_{LB} = 2.2 \times 10^6$). In the third case the two passive colliding droplets are subject to an external force ((e), $t/\Delta t_{LB} = 7 \times 10^5$) applied on each of them parallel to the x-axis and along opposite directions, with the same magnitude. They finally coalesce into a larger droplet ((f), $t/\Delta t_{LB} = 1.04 \times 10^6$). The color scale is the same as in Fig. 6.10.

rected rightwards ($\mathbf{F^{ext}} = |F|\mathbf{x}$, being $\mathbf{x}$ a unit vector, directed along the increasing x-axis) if applied at the droplet on the left and leftwards if applied at the droplet on the right ($\mathbf{F^{ext}} = -|F|\mathbf{x}$). The force, with magnitude $|F| \sim 10^{-8} n(\Delta x)^2/\Delta t_{LB}$, acts until the droplets move with a speed similar to that of the self-propelled ones. Unlike the previous cases, here the velocity field is largely parallel to the x-axis, the direction along which the forces are applied. These push the droplets against each other until they coalesce into a bigger one (Fig. 6.17-(f)) as no surfactant (impeding the coalescence) is present in the system. Hence even in a relatively simple realization of a system with two droplets, the dynamics can be dramatically different and ultimately be affected by the nature of the droplets considered. In particular an inhomogeneous production of surfactant migrating towards the interface of the droplet may either drive the system to a non-motile steady state (if both droplets are active) or render motile a passive droplet if this is close enough with an active one.

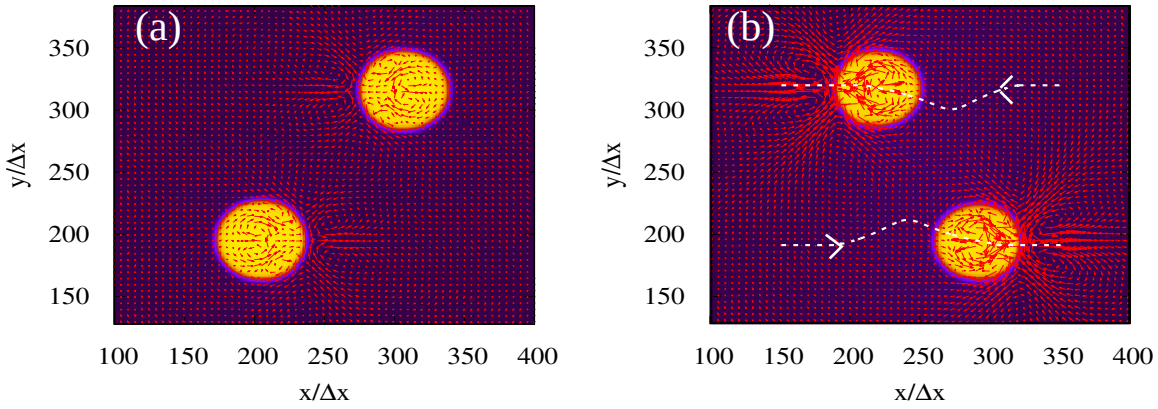

Figure 6.18: Contour plots of the concentration field ϕ for two active vertically shifted colliding droplets. The velocity field is also shown. The configurations are at times $t/\Delta t_{LB} = 7 \times 10^5$ (a) and $t/\Delta t_{LB} = 2 \times 10^6$ (b) and the trajectory is also shown. The whole lattice is $L_x = 512\Delta x \times L_y = 512\Delta x$. The two active droplets are initially attracted by each other ((a), $t/\Delta t_{LB} = 7 \times 10^5$) and, when close enough, they are scattered away along their own direction. The color scale is the same as in Fig. 6.10.

6.7.2 Colliding non collinear droplets

The dynamics is even more intriguing in a modified setup in which the droplets are vertically shifted. More specifically, two droplets of radius $R_0 = 32\Delta x$ are placed at $d_x(t_i) = 6.25R_0$ and at $d_y(t_i) = 4R_0$, in a lattice of size $L_x = 512\Delta x$, $L_y = 512\Delta x$ (Fig. 6.18-(a)).
At first both droplets are active, the upper one moving leftwards and the lower one moving rightwards (Fig. 6.18-(a)). While at an early stage the velocity field formed in the fluid between the droplets (along a direction joining their centers of mass) favours their mutual attraction (Fig. 6.18-(a)), later on (see the trajectories in Fig. 6.18-(b)), after the droplets achieve a minimal vertical distance (estimated roughly $d_{y,min} \simeq 3R_0$), it induces a reciprocal repulsion, as clearly visible from the direction of the velocity field formed between the droplets when they pass each other (Fig. 6.18-(b)). After the scatter occurs, the droplets move along their own direction at an almost constant speed. It must be emphasized that no rotation of droplets occurs since the region of surfactant production is fixed inside the droplet and does not follow its direction of motion. This behavior has been observed for values of vertical separation $3.5R_0 \leq d_y(t_i) \leq 4R_0$, whereas for lower values the attraction is strong enough to overcome the resistance to coalescence mediated by the surfactant.
If the upper active droplet is replaced with a passive one, the dynamics is not too dissimilar from the previous case. Here the active droplet on the left acquires

motion rightwards and, when close enough with the passive one, attracts it downwards (Fig. 6.19-(a)-(c)), until a minimal vertical separation of $d_{y,min} \simeq 2.8R_0$ is achieved. Later on, when the two droplets are almost vertically aligned, the velocity field created by the active droplet repels the passive one, which slightly shifts leftwards, whereas the active one continues its motion rightwards, along the dashed trajectory indicated in Fig. 6.19-(d). The main difference with the case discussed in Fig. 6.18 is that the droplets get even closer although at much longer times, as a weaker mutual interaction is now due to only one source. Also in this case this behavior holds as long as $3.5R_0 \leq d_y(t_i) \leq 4R_0$, whereas for lower values droplets coalesce.

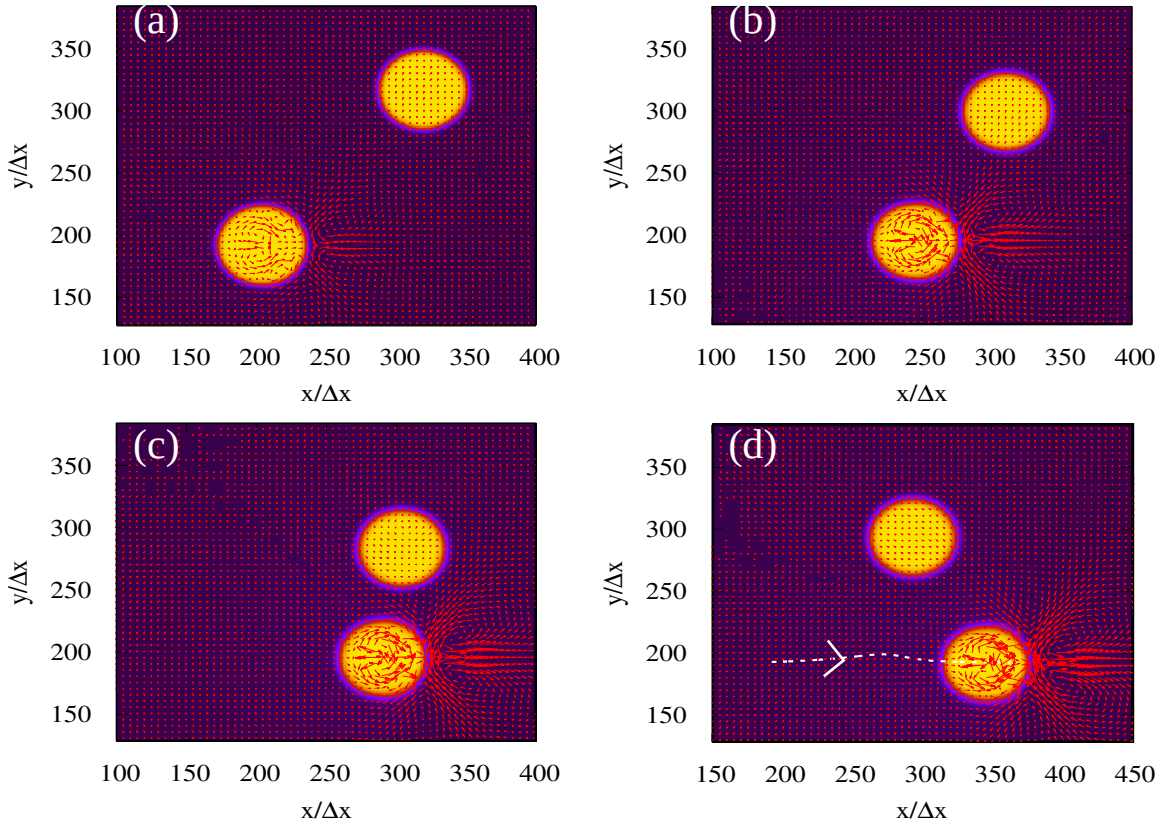

Figure 6.19: Contour plots of the concentration field ϕ for an active and a passive vertically shifted colliding droplets. The velocity field is also shown. The configurations are taken at times $t/\Delta t_{LB} = 7 \times 10^5$ (a), $t/\Delta t_{LB} = 1.6 \times 10^6$ (b), $t/\Delta t_{LB} = 2.3 \times 10^6$ (c) and $t/\Delta t_{LB} = 3 \times 10^6$ (d). The lattice size is $L_x = 512\Delta x$, $L_y = 512\Delta x$. The left active droplet moves towards the passive one ((a)-(b)) and when close enough, it initially attracts and then repels the passive one ((c)-(d)). Later on, the active droplet continues its motion to the right along the dashed trajectory, leaving the passive droplet on its left (d). The color scale is the same as in Fig. 6.10.

6.7.3 Vertically aligned droplets

Finally the case of two droplets vertically aligned, with $d_y(t_i) = 2.5R_0$ and $d_x(t_i) = 0$ (Fig. 6.20) is considered. If both droplets are active (Fig. 6.20-(a)-(b)), the velocity field formed in between favours their reciprocal repulsion and a drift along the vertical direction, whereas that generated inside each droplet and in their front drags them along the positive x-axis. Droplets move initially slightly faster along the x-direction rather than along the y-one, but when they get at a vertical distance of $d_y \simeq 4.2R_0$, the speed along the y-axis progressively diminishes as the repulsion becomes negligible. This geometry slightly resembles that studied by Gompper et. al. [190] in which the interaction between two pullers is investigated.
If the upper droplet is passive (Fig. 6.20-(c)-(d)), the flow field created by the active one first pushes it upwards and afterwards drags it slightly backwards. The motion of the active droplet proceeds almost unaltered rightwards along the trajectory indicated in Fig. 6.20-(d), and the repulsion with the passive one becomes negligible at $t \simeq 2.35 \times 10^6 \Delta t_{LB}$, when the vertical separation is roughly $d_y \simeq 3.2R_0$.

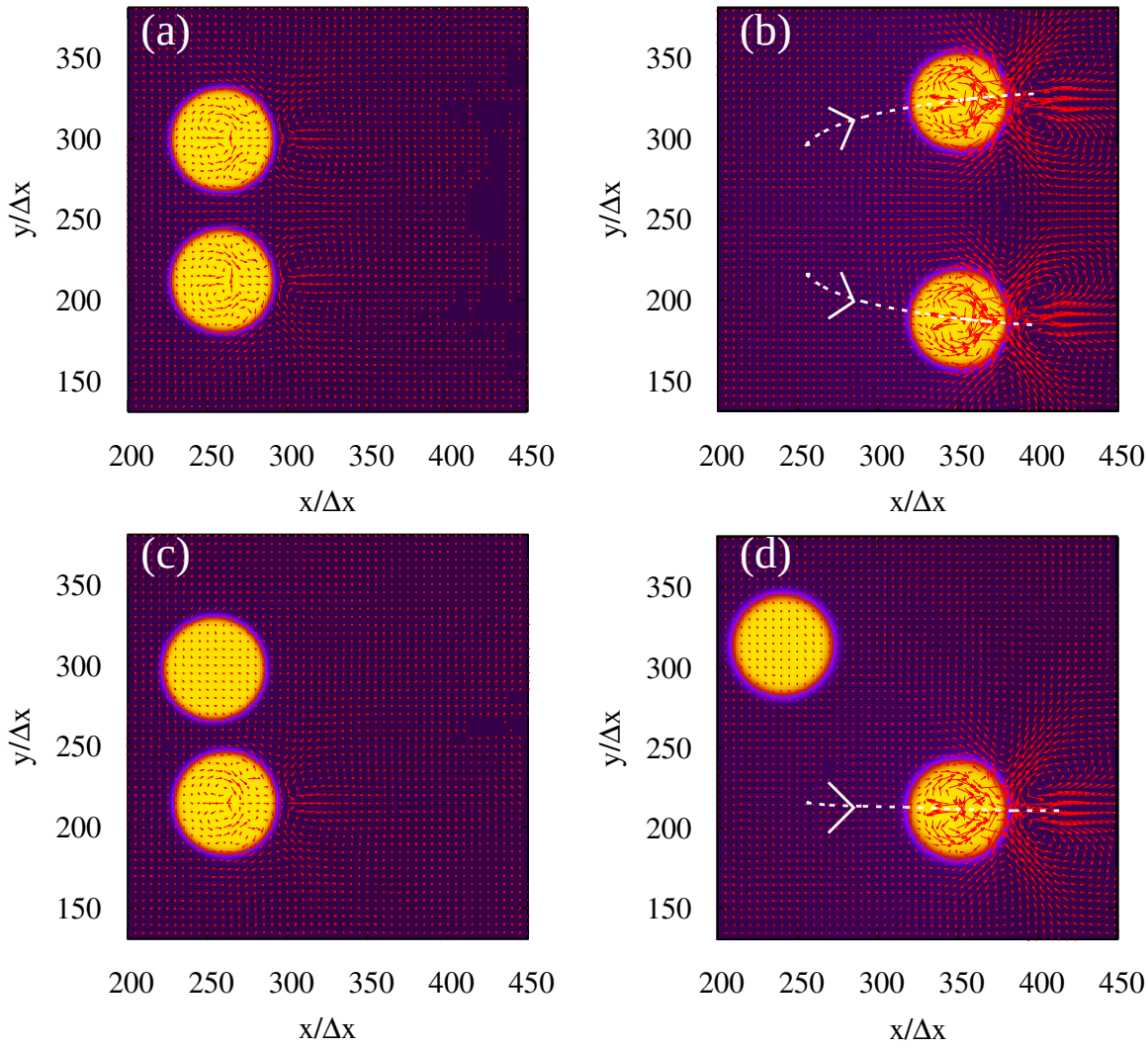

Figure 6.20: Contour plots of the concentration field ϕ for two active equiverse droplets ((a)-(b) and active lower droplet and passive upper droplet ((c)-(d)). The velocity field is also shown. The lattice size is $L_x = 512\Delta x \times L_y = 512\Delta x$. In the first case the two active droplets initially repel each other and move rightwards ((a), $t/\Delta t_{LB} = 5 \times 10^5$) along the direction indicated by the dashed lines ((b), $t/\Delta t_{LB} = 2 \times 10^6$). In the second case the active lower droplet repels the upper passive one, which now drifts backwards ((c), $t/\Delta t_{LB} = 5 \times 10^5$), and moves rightwards as in the previous case ((d), $t/\Delta t_{LB} = 2.35 \times 10^6$). The color scale is the same as in Fig. 6.10.

6.8 Summary

In this Chapter the Marangoni effect was introduced with the description of the results of the study of self-propelled droplets of the paper "*Lattice Boltzmann study of chemically-driven self-propelled droplets*". At first the basic concepts of the Marangoni effect in general were exposed and then moved to the description of the studies on droplets with brief introduction of the squirmer model.
After that the results of the work were analyzed in detail starting at first by the results of the equilibrium case of the system when the production and the consumption of surfactant are absent and then moving to the characterization of the motion of a single self-propelled droplet.
In the final part of the Chapter, the cases dealing with two interacting self-propelled droplets exploring active and passive situation in different geometries. In general different ways of placing the droplets in the system can lead to different interactions between them depending wheter they are both active or one of them is passive and doesn't produce surfactant.

Conclusions

In this thesis droplets of complex fluids and liquid crystals have been analyzed through computer simulations.
In these numerical studies the hybrid Lattice Boltzmann method, described in Chapter 3, has been adopted; the adjective "hybrid" is due to the fact that the hydrodynamic equations such as the continuity and the Navier-Stokes equations are solved in the standard way, instead the equations for the order parameter and other scalar fields are solved apart with a finite-difference scheme. In the case of fluid mixtures the order parameter is scalar and corresponds to the concentration field, defined as difference between the concentrations of the mixture, which evolve through the convection-diffusion equation. Instead the order parameter for liquid crystals is a symmetric and traceless tensor which evolve through the Beris-Edwards equation. The whole thermodynamics of the system, following the Ginzburg-Landau approach, is encoded in a free energy functional in which all the energetic terms are present and by which quantities like the chemical potential and the pressure tensor can be extracted and calculated. All these aspects were presented in Chapter 1.
One important result, presented in the Chapter 4, after a general presentation of the liquid crystals in Chapter 2, deals with the study of a quasi-bidimensional cholesteric liquid crystal droplet in isotropic phase under electric fields published on *The Journal of Chemical Physics* with title *"Switching dynamics in cholesteric liquid crystal emulsion"*. The goal of the work was to explore the dynamics of topological defects of the cholesteric droplet for different situations with different pitches of the helix, different types of anchoring of the director on the droplet and different types of electric fields. Topological defects are regions where the order parameter of liquid crystals is not well defined and the local orientation of the director is ambiguous and can rise for the combinations of various factors like elasticity of the material, type of anchoring, cholesteric helix encapsulated in the pitch, ecc. At first, the equilibrium configurations of the cholesteric droplets were presented and then the application of the field was considered. Two situations were considered: the switching on-off of a continuous electric field and a rotating electric field.
In the former case after the relaxation of the system, a field along the horizontal (parallel to the direction of the helix) or the vertical (perpendicular to the helix) di-

rection was applied letting the system to evolve towards a first intermediate state and then switched off in order to observe if the system regained or not the original equilibrium structure. In general, the electric field is an important way to reorganize the topological defects in the cholesteric droplet; in particular, if the intensity of the field reaches a "critical" value it is possible that it removes all the defects and destroys the cholesteric order turning the droplet into a nematic one. So the simulations of the switching on-off dynamics of a continuous electric field were enforced finding the threshold values of the field (both for the horizontal and the vertical directions) as function of the elastic constant for various anchorings. In general the more elastic is the liquid crystal, the more intense the field must be in order to destroy the cholesteric helix and to turn the droplet into a nematic. The homeotropic anchoring is also more sensistive to an external field and nematize more easier than the correspondent tangential case.
In the case of the rotating electric field, switched on after the system has relaxed, the droplet and the defects rotate in the time. Two studies in this case were performed: the evaluation of the angular velocity of the droplet as function of the frequency of the applied field and the study of the periodicity of the topological defects. In the first case, the angular velocity of the rotating droplet was calculated varying the frequency of the applied field for various pitches and anchorings. The plots suggest that for low frequencies of the field ($\omega \leq 10^{-2}$) there is an increase in the angular velocity of the droplet as increasing the frequency of the applied field. In other words the faster is the rotating field, the faster is the rotation of the droplet. For higher frequencies ($\omega \geq 10^{-2}$) inertia starts to dominate and the dynamics of the rotating droplet seems to be slower or the droplet doesn't rotate anymore. As long as the rotating electric field has a periodicity, it could be reasonable to ask if the topological defects follow this periodicity and appear periodically as the electric field. Considering various pitches of the helix and anchorings, three interesting situations were found: a case in which the dynamics of the defects is not periodic but after a certain time becomes periodic, then is not periodic and in the end periodic again, a case in which the dynamics of the defects is periodic with the field after a transient and the case in which the dynamics of the topological defects shows a own periodicity different form the one of the field.
The final part of Chapter 4 contains also the initial results of a new system consisting in two cholesteric liquid crystal droplets with surfactant under rotating electric fields of the work in preparation "*Interacting rotating cholesteric liquid crystal droplets*". The presence of surfactant is important to avoid the coalescence of the two droplets. After the switching on of the rotating field, the droplets rotate around their own center of mass but also interact each other rotating around a common centre. The peculiarity of this effect is the fact that it seems to require a threshold value of the frequency of the applied field to be observed ($\omega \simeq 10^{-3}$) and below which the common rotation of the two droplets is not visible anymore.

In Chapter 6 the self-propelled motion of a simple fluid droplet, of the paper "*Lattice Boltzmann study of chemically-driven self-propelled droplets*", was treated first introducing the basic concepts of the Marangoni effect with brief references on the squirmer model used to simulate microorganisms and the Active Matter which studies systems which convert energy from a form into another. The system studied consists in a ternary fluid mixtures of a fluid droplet in another one with surfactant. At first the equilibrium properties of the system with the analysis of the one-dimensional profiles of the concentration fields, the surface tension and the interface lenght were performed. Then the results of the self-propelled motion of a single droplet and then the interaction of a couple of droplets were considered. In the case of the single droplet the Marangoni effect was achieved inserting terms of production and consumption of surfactant. In particular the surfactant was produced inside a circular region internally tangent to the droplet which causes an imbalance in the surface tension to the two sides of the droplet and in the end the droplet moves. In the final part of Chapter 6 the interactions of two self-propelled droplets were considered exploring different geometries and also different types of droplets. Both the cases of two self-propelled droplets and one self-propelled and the other motionaless were analyzed. In general different ways of placing the droplets into the lattice and the zone of surfactant inside the droplet can lead to different interactions also depending if two active droplets or active-passive ones are considered.
Now it should be possible to mark new possible routes to the future research.
At first the two works, "*Interacting rotating cholesteric liquid crystal droplets*" briefly mentioned in Chapter 4 and "*Shear dynamics of an inverted cholesteric emulsion*" of Chapter 5, should be completed. At the end of Chapter 4 the system of two choelesteric liquid crystal droplets with surfactant under rotating electric fields will be investigted deeply. As mentioned, this systems is characterized by the fact that under a threshold value of the frequency of the field no mutual interaction is visible. Instead, if the frequencies are larger than this treshold value, the two droplets start to move and rotate each other around a common centre also rotating around their center of mass. A future study will consist in exploring this interaction for other cases of the anchoring of the director and also for other pitches of the helix. Another interesting aspect could be considering the interactions of more than two droplets in various geometries.
As regards the inverted cholesteric liquid crystal emulsion, the future studies will consist in exploring the opposite situation of a cholesteric droplet in isotropic host and computing quantitatively other quantities such as the tilt angle of the droplet and the Taylor deformation parameter related to the distortion of the droplet. An important effect typical of cholesteric is the permeation effect consisting in an enormous increase of the viscosity caused by the shear applied along the direction of the helix. This will be another future goal of this work.

Other possible future projects for liquid crystals can be the following ones.
In this thesis a quasi-bidimensional system for the cholesteric droplet was considered and it could be interesting studying a full three-dimensional cholesteric droplet under electric fields. In a three-dimensional system it should be possible to observe the χ line defect which wasn't observed in the bidimensional counterpart. Certainly the most important fact is the difficulty to simulate a full three-dimensional system for the huge requirement of computational resources and the great amount of time. It will be mandatory a parallelization of the code.
Same future studies can be performed on the self-propelled motion of a droplet both in the full three-dimensional case or remaining in bidimensional case it could be performed the study of "lots" ($\simeq 10^2$) of self-propelled droplets with an analysis of the collective effects.

Appendix A

Continuum limit of Lattice Boltzmann for fluid mixtures

In this appendix it will be shown how, performing Chapman-Enskog expansion, it is possible to obtain the continuity and Navier-Stokes equation [97].
In $D2Q9$ model the coefficients ω_i of equation (3.19) of Chapter 3 are

$$\omega_0 = 4/9; \qquad \omega_{1-4} = 1/9; \qquad \omega_{5-8} = 1/36. \tag{A.1}$$

A, B_α, $C_{\alpha\beta}$ are functions of F_α and are related to the moments of F_i through

$$\sum_{i=0}^{8} F_i = A, \qquad \sum_{i=0}^{8} e_{i\alpha} F_i = B_\alpha, \qquad \sum_{i=0}^{8} e_{i\alpha} e_{i\beta} F_i = c_s^2 A \delta_{\alpha\beta} + \frac{1}{2}[C_{\alpha\beta} + C_{\beta\alpha}]. \tag{A.2}$$

The continuum limit is performed through a multiscale expansion in the Knudsen number ε

$$\partial_t = \varepsilon \partial_{t1} + \varepsilon^2 \partial_{t2}, \tag{A.3}$$

$$\partial_\beta = \varepsilon \partial_{\beta 1}, \tag{A.4}$$

$$f_i = f_i^{(0)} + \varepsilon f_i^{(1)} + \varepsilon^2 f_i^{(2)}, \tag{A.5}$$

$$F_\alpha = \varepsilon F_{\alpha 1}; \qquad A = \varepsilon A_{\alpha 1}; \qquad B_\alpha = \varepsilon B_{\alpha 1}; \qquad C_{\alpha\beta} = \varepsilon C_{\alpha\beta 1}. \tag{A.6}$$

The Knudsen number ε is defined as the ratio between two different length scales:

$$\varepsilon = \frac{\lambda}{L} \tag{A.7}$$

where L is a macroscopic length of the system and λ is the molecular mean free path. If $\varepsilon << 1$ an hydrodynamic approach is correct and Navier-Stokes equation can be considered, instead if $\varepsilon \sim 1$, the microscopic details become important and

need to be taken into account. It is also important to bear in mind these useful tensorial relations [3]:

$$\sum_i e_{i\alpha} = 0, \tag{A.8}$$

$$\sum_i e_{i\alpha} e_{i\beta} = 2e^2 \delta_{\alpha\beta} + 4e^2 \delta_{\alpha\beta}, \tag{A.9}$$

$$\sum_i e_{i\alpha} e_{i\beta} e_{i\gamma} = 0, \tag{A.10}$$

and

$$\sum_i e_{i\alpha} e_{i\beta} e_{i\gamma} e_{i\delta} = 2e^4 \delta_{\alpha\beta\gamma\delta} + (4e^2 \Delta_{\alpha\beta\gamma\delta} - 8e^4 \delta_{\alpha\beta\gamma\delta}) \tag{A.11}$$

being

$$\Delta_{\alpha\beta\gamma\delta} = \delta_{\alpha\beta}\delta_{\gamma\delta} + \delta_{\alpha\gamma}\delta_{\beta\delta} + \delta_{\alpha\delta}\delta_{\beta\gamma}. \tag{A.12}$$

Through a series expansion of the Boltzmann equation

$$f_i(\mathbf{r} + \mathbf{e}_i \Delta t, t + \Delta t) - f_i(\mathbf{r}, t) = -\Delta t \frac{f_i - f_i^{eq}}{\tau} + \Delta t F_i(\mathbf{r}, t) \tag{A.13}$$

with

$$f_i^{eq} = A^\sigma + B^\sigma e_{i\alpha} u_\alpha + C^\sigma u^2 + D^\sigma (e_{i\alpha} u_\alpha)^2 \tag{A.14}$$

where A, B, C, D are coefficients in the expression of f_i^{eq} and the index $\sigma = 0, 1, 2$ if the center of the elementary cell ($\sigma = 0$ if $i = 0$) or the first neighbour sites ($\sigma = 1$ if $i = 1, 2, 3, 4$) or the second neighbour sites ($\sigma = 2$ if $i = 5, 6, 7, 8$) are considered, one obtains:

$$\Delta t (e_{i\beta}\partial_\beta + \partial_t) f_i + \frac{\Delta t^2}{2} (e_{i\beta}\partial_\beta + \partial_t)^2 f_i = \Delta t F_i - \Delta t \frac{f_i - f_i^{eq}}{\tau} \tag{A.15}$$

or

$$\Delta t (e_{i\beta}\partial_\beta + \partial_t) f_i + \frac{(\Delta t)^2}{2} (e_{i\beta} e_{i\gamma} \partial_\beta \partial_\gamma + \partial_t^2 + e_{i\beta}\partial_\beta \partial_t) f_i = \Delta t F_i - \Delta t \frac{f_i - f_i^{eq}}{\tau}. \tag{A.16}$$

Simplyfing the Δt's and through a Knudsen expansion (A.3)-(A.6)it is

$$\begin{aligned} &(\varepsilon e_{i\beta}\partial_{\beta 1} + \varepsilon \partial_{t1} + \varepsilon^2 \partial_{t2})(f_i^{(0)} + \varepsilon f_i^{(1)} + \varepsilon^2 f_i^{(2)}) + \\ &+ \frac{\Delta t}{2} [e_{i\beta} e_{i\gamma} \varepsilon^2 \partial_{\beta 1} \partial_{\gamma 1} + (\varepsilon \partial_{t1} + \varepsilon^2 \partial_{t2})^2 + \varepsilon e_{i\beta} \partial_{\beta 1} (\varepsilon \partial_{t1} + \varepsilon^2 \partial_{t2})] \\ &\times (f_i^{(0)} + \varepsilon f_i^{(1)} + \varepsilon^2 f_i^{(2)}) \\ &= \varepsilon F_{i1} - \frac{f_i^{(0)} + \varepsilon f_i^{(1)} + \varepsilon^2 f_i^2 - f_i^{eq}}{\tau}. \end{aligned} \tag{A.17}$$

Neglecting terms higher than order two, after some algebra one obtains:

$$O(\varepsilon^0) : f_i^{(0)} = f_i^{eq} \tag{A.18}$$

$$O(\varepsilon) : (e_{i\beta}\partial_{t1} + \partial_{t1})f_i^{(0)} = -\frac{1}{\tau}f_i^{(1)} + F_{i1} \tag{A.19}$$

$$O(\varepsilon^2) : \partial_{t2}f_i^{(0)} + (e_{i\beta}\partial_{\beta 1} + \partial_{t1})f_i^{(1)} + \frac{\Delta t}{2}(\partial_{t1}^2 f_i^{(0)} + e_{i\beta}e_{i\gamma}\partial_{\beta 1}\partial_{\gamma 1}f_i^{(0)} + 2e_{i\beta}\partial_{\beta 1}\partial_{t1}f_i^{(0)}) = -\frac{f_i^{(2)}}{\tau} \tag{A.20}$$

Thanks to (A.18) or (A.19) and (A.20) $f_i^{(0)} = f_i^0$. It is also:

$$\sum_i f_i = \sum_i f_i^{eq} = n \rightarrow \sum_i (f_i^{(0)} + \varepsilon f_i^{(1)} + \varepsilon^2 f_i^{(2)}) = n \tag{A.21}$$

from which

$$\sum_i f_i^{(1)} = \sum_i f_i^{(2)} = 0. \tag{A.22}$$

Also it is

$$\sum_i f_i^{eq} e_{i\alpha} = nu_\alpha = \sum_i f_i e_{i\alpha} + m\Delta t F_\alpha = \sum_i f_i^{(0)} e_{i\alpha} + \varepsilon \sum_i f_i^{(1)} e_{i\alpha} + \varepsilon^2 \sum_i f_i^{(2)} + \varepsilon m \Delta t F_{1\alpha} \tag{A.23}$$

from which one obtains

$$\sum_i f_i^{eq} e_{i\alpha} = \sum_i f_i^{(0)} e_{i\alpha}, \tag{A.24}$$

$$\sum_i f_i^{(1)} e_{i\alpha} = -m\Delta t F_{1\alpha}, \tag{A.25}$$

$$\sum_i f_i^{(2)} e_{i\alpha} = 0. \tag{A.26}$$

The continuity equation

Developing products in (A.19) and applying ∂_{t1}, one obtains:

$$\partial_{t1}^2 f_i^0 + e_{i\beta}\partial_{\beta 1}\partial_{t1} f_i^0 = -\frac{1}{\tau}\partial_{t1} f_i^{(1)} + \partial_{t1} F_{i1}, \tag{A.27}$$

applying $e_{i\gamma}\partial_{t1}$ to (A.19) one obtains:

$$e_{i\gamma}\partial_{\gamma 1}\partial_{t1} f_i^0 + e_{i\beta}e_{i\gamma}\partial_{\beta 1}\partial_{\gamma 1} f_i^0 = -\frac{1}{\tau}e_{i\gamma}\partial_{\gamma 1} f_i^{(1)} + e_{i\gamma}\partial_{\gamma 1} F_{i1}. \tag{A.28}$$

Subtracting the (A.28) from (A.27) it is:

$$\partial_{t1}^2 f_i^0 = e_{i\beta}e_{i\gamma}\partial_{\beta 1}\partial_{\gamma 1} f_i^0 - \frac{1}{\tau}\partial_{t1} f_i^{(1)} + \frac{1}{\tau}e_{i\gamma}\partial_{\gamma 1} f_i^{(1)} + \partial_{t1} F_{i1} - e_{i\gamma}\partial_{\gamma 1} F_{i1} \tag{A.29}$$

whih substituted in (A.20) allows to get

$$\begin{aligned} \partial_{t2} f_i^0 + \partial_{t1} f_i^1 + \frac{\Delta t}{2}e_{i\beta}e_{i\gamma}\partial_{\beta 1}\partial_{\gamma 1} f_i^0 - \frac{\Delta t}{2\tau}\partial_{t1} f_i^{(1)} + \frac{\Delta t}{2\tau}e_{i\gamma}\partial_{\gamma 1} f_i^{(1)} \\ + \frac{\Delta t}{2}(\partial_{t1} F_{i1} - e_{i\gamma}\partial_{\gamma 1} F_{i1}) + e_{i\beta}\partial_{\beta 1} f_i^{(1)} + \frac{\Delta t}{2}e_{i\beta}e_{i\gamma}\partial_{\beta 1}\partial_{\gamma 1} f_i^0 + \\ \Delta t e_{i\beta}\partial_{\beta 1}\partial_{t1} f_i^0 = -\frac{f_i^{(2)}}{\tau}. \end{aligned} \tag{A.30}$$

From (A.19) it follows

$$\partial_{t1} f_i^0 = -e_{i\beta}\partial_{\beta 1} f_i^0 - \frac{1}{\tau} f_i^{(1)} + F_{i1} \tag{A.31}$$

from which, multiplying by $\Delta t e_{i\beta}e_{i\gamma}$, one obtains

$$\Delta t e_{i\beta}\partial_{\beta 1}\partial_{t1} f_i^0 = -\Delta t e_{i\beta}e_{i\gamma}\partial_{\beta 1}\partial_{\gamma 1} f_i^0 - \frac{\Delta t}{\tau}e_{i\beta}\partial_{\beta 1} f_i^{(1)} + \Delta t e_{i\beta}\partial_{\beta 1} F_{i1} \tag{A.32}$$

which substituted in (A.30) leads to

$$\begin{aligned} \partial_{t2} f_i^0 + \partial_{t1} f_i^{(1)} + \frac{\Delta t}{2}e_{i\beta}e_{i\gamma}\partial_{\beta 1}\partial_{\gamma 1} f_i^0 - \frac{\Delta t}{2\tau}\partial_{t1} f_i^{(1)} + \frac{\Delta t}{2\tau}e_{i\beta}\partial_{\gamma 1} f_i^{(1)} + \\ \frac{\Delta t}{2}(\partial_{t1} F_{i1} - e_{i\gamma}\partial_{\gamma 1} F_{i1}) + e_{i\beta}\partial_{\beta 1} f_i^{(1)} + \frac{\Delta t}{2}e_{i\beta}e_{i\gamma}\partial_{\beta 1}\partial_{\gamma 1} f_i^0 \\ -\Delta t e_{i\beta}e_{i\gamma}\partial_{\beta 1}\partial_{\gamma 1} f_i^0 - \frac{\Delta t}{\tau}e_{i\beta}\partial_{\beta 1} f_i^1 + \Delta t e_{i\beta}\partial_{\beta 1} F_{i1} = -\frac{1}{\tau} f_i^{(2)} \end{aligned} \tag{A.33}$$

and after some algebra

$$\begin{aligned}\partial_{t2} f_i^0 + \partial_{t1} f_i^{(1)} - \frac{\Delta t}{2\tau}\partial_{t1} f_i^{(1)} + \frac{\Delta t}{2\tau} e_{i\gamma}\partial_{\gamma 1} f_i^{(1)} + e_{i\beta}\partial_{\beta 1} f_i^{(1)} \\ -\frac{\Delta t}{\tau} e_{i\beta}\partial_{\beta 1} f_i^{(1)} = -\frac{1}{\tau} f_i^{(2)} - \frac{\Delta t}{2}(\partial_{t1} F_{i1} - e_{i\gamma}\partial_{\gamma 1} F_{i1}).\end{aligned} \tag{A.34}$$

By summing on the index i the (A.19), through $nu_\alpha = \sum_i f_i e_{i\alpha} + mF_\alpha \Delta t$, with m to be determined, and (A.24) and remembering that $\sum_i f_i^0 = n$, one obtains

$$\partial_{t1} n + \partial_{\beta 1}(nu_\beta) = A_1 \tag{A.35}$$

which is the continuity equation at first order only if $A_1 = 0$ and so that $A = 0$. Now by multiplying the (A.19) for $e_{i\alpha}$ and summing on index i, assuming $B_{1\alpha} = \lambda F_{1\alpha} = \sum_i F_{i1} e_i$ one obtains

$$\partial_{t1}(nu_\alpha) + \partial_{\beta 1}(nu_\alpha u_\beta) + \partial_{\beta 1}\left(\frac{c^2}{3} n\delta_{\alpha\beta}\right) = \frac{m}{\tau} F_{1\alpha}\Delta t + \lambda F_{1\alpha} \tag{A.36}$$

where the third term of the left-hand side of equation has been obtained expliciting in the sum the (A.14) and utilizing the second tensorial relation of (A.8)-(A.11), the (A.36) is the equation of the first order momentum with the condition

$$\lambda + \frac{m}{\tau}\Delta t = 1. \tag{A.37}$$

Summing over i the (A.34), it is

$$\begin{aligned}\partial_{t2} n - \frac{\Delta t}{2\tau}\partial_{\gamma 1}(-mF_{1\gamma}\Delta t) + \partial_{\gamma 1}(-mF_{1\gamma}\Delta t) \\ = -\frac{\Delta t}{2}[\partial_{t1} A_1 + \partial_{\gamma 1}(\lambda F_{1\gamma})]\end{aligned} \tag{A.38}$$

which, with conditions (A.37) and $A_1 = 0$, becomes

$$\partial_{t2} n + \frac{\Delta t}{2\tau}\partial_{\gamma 1}(mF_{1\gamma}\Delta t) - \partial_{\gamma 1}(mF_{1\gamma}\Delta t) = -\frac{\Delta t}{2}\left(1 - m\frac{\Delta t}{2}\right)\partial_{\gamma 1} F_{1\gamma} \tag{A.39}$$

or

$$\partial_{t2} n = \Delta t\left(m - \frac{1}{2}\right)\partial_{\gamma 1} F_\gamma. \tag{A.40}$$

Summig the latter with (A.35) (with $A = 0$) and after some algebra, one obtains

$$\partial_t n + \partial_\beta(nu_\beta) = \Delta t\left(m - \frac{1}{2}\right)\partial_\gamma F_\gamma \tag{A.41}$$

which is exactly the continuity equation if

$$m = \frac{1}{2}. \tag{A.42}$$

The Navier-Stokes equation

Multiplying the (A.34) with $e_{i\alpha}$ and summing on i, after some algebra it is

$$\partial_{t2}(nu_\alpha) + \left(1 - \frac{\Delta t}{2\tau}\right)\partial_{\beta 1}\sum_i e_{i\alpha}e_{i\beta}f_i^{(1)} = -\frac{\Delta t}{4}\partial_{\gamma 1}(C_{1\alpha\gamma} + C_{1\gamma\alpha}). \tag{A.43}$$

It is necessary to find an explicit expression for $f_i^{(1)}$:

$$\begin{aligned}\sum_i e_{i\alpha}e_{i\beta}f_i^{(1)} &= \sum_i e_{i\alpha}e_{i\beta}[-\tau\partial_{t1}f_i^0 - \tau e_{i\gamma}\partial_{\gamma 1}f_i^0 + \tau F_{i1}] \\ &= -\tau\partial_t\sum_i e_{i\alpha}e_{i\beta}f_i^0 - \tau\partial_{\gamma 1}\sum_i e_{i\alpha}e_{i\beta}e_{i\gamma}f_i^0 + \tau\sum_i e_{i\alpha}e_{i\beta}F_{i1}\end{aligned} \tag{A.44}$$

expliciting f_i^0 through (A.14) and exploiting the tensorial properties (A.8)- (A.11) the latter becomes

$$\begin{aligned}\sum_i e_{i\alpha}e_{i\beta}f_i^{(1)} &= -\tau\partial_{t1}\left[\frac{c^2}{3}n\delta_{\alpha\beta} + nu_\alpha u_\beta\right] \\ -\tau\partial_{\gamma 1}\left[\frac{c^2}{3}n(u_\gamma\delta_{\alpha\beta} + u_\alpha\delta_{\beta\gamma} + u_\beta\delta_{\alpha\gamma}\right] &+ \tau\sum_i e_{i\alpha}e_{i\beta}F_{i1}.\end{aligned} \tag{A.45}$$

From the left-hand side

$$\partial_{t1}n = -\partial_{\beta 1}(nu_\beta) \tag{A.46}$$

$$\partial_{t1}(nu_\alpha) = -\partial_{\gamma 1}\left(\frac{c^2}{3}n\delta_{\alpha\gamma} + nu_\alpha u_\gamma\right) + F_{1\alpha} \tag{A.47}$$

which substituted in (A.45) gives

$$\begin{aligned}&\sum_i e_{i\alpha}e_{i\beta}f_i^{(1)} = -\tau\times \\ &\left[\frac{c^2}{3}\partial_{\beta 1}(nu_\alpha) + \frac{c^2}{3}\partial_{\alpha 1}(nu_\beta) + nu_\alpha\partial_{t1}u_\beta - u_\beta\partial_{\gamma 1}\left(\frac{c^2}{3}n\delta_{\alpha\beta} + nu_\alpha u_\beta\right) + u_\beta F_{1\alpha} - \sum_i e_{i\alpha}e_{i\beta}F_{i1}\right].\end{aligned} \tag{A.48}$$

From the derivative expansion $\partial_{t1}(nu_\alpha)$ one can obtain

$$\begin{aligned}n\partial_{t1}u_\beta &= \partial_{t1}(nu_\alpha) + u_\beta\partial_{\gamma 1}(nu_\gamma) \\ &= -\partial_{\gamma 1}\left(\frac{c^2}{3}n\delta_{\beta\gamma} + nu_\beta u_\gamma\right) + F_{1\beta} + u_\beta\partial_{\gamma 1}(nu_\gamma)\end{aligned} \tag{A.49}$$

which multiplied to the left for u_α becomes

$$nu_\alpha \partial_{t1} u_\beta = -u_\alpha \partial_{\gamma 1}\left(\frac{c^2}{3} n\delta_{\beta\gamma} + nu_\beta u_\gamma\right) + u_\alpha F_{1\beta} + u_\alpha u_\beta \partial_{\gamma 1}(nu_\gamma). \tag{A.50}$$

Once substitued in (A.48), one obtains

$$\sum_i e_{i\alpha} e_{i\beta} f_i^{(1)} = -\tau \times \left[\frac{c^2}{3} n(\partial_{\beta 1} u_\alpha + \partial_{\alpha 1} u_\beta) - \partial_{\gamma 1}(nu_\alpha u_\beta) + u_\beta F_{1\alpha} + u_\alpha F_{1\beta} - \sum_i e_{i\alpha} e_{i\beta} F_{i1}\right] \tag{A.51}$$

in which the second term in parentesis can be neglected since it is of third order in the velocity u. Substituting this result in (A.43), it is

$$\partial_{t2}(nu_\alpha) + \left(1 - \frac{\Delta t}{2\tau}\right) \partial_{\beta 1} \left\{-\tau \left[\frac{c^2}{3} n(\partial_{\beta 1} u_\alpha + \partial_{\alpha 1} u_\beta) + u_\beta F_{1\alpha} + u_\alpha F_{1\beta} - \sum_i e_{i\alpha} e_{i\beta} F_{i1}\right\}\right] = -\frac{\Delta t}{4} \partial_{\gamma 1}(C_{1\alpha\gamma} + C_{1\gamma\alpha}). \tag{A.52}$$

With some algebra and choosing for $C_{1\alpha\beta}$

$$C_{1\alpha\beta} = \left(1 - \frac{\Delta t}{2\tau}\right)(u_\alpha F_{1\beta} + u_\beta F_{1\alpha}) \tag{A.53}$$

the (A.52) becomes

$$\partial_{t2}(nu_\alpha) = \frac{c^2}{3}\left(\tau - \frac{\Delta t}{2}\right) \partial_{\beta 1}[n(\partial_{\beta 1} u_\alpha + \partial_{\alpha 1} u_{\beta 1})] \tag{A.54}$$

which is the second order momentum equation which added to the equation for the first order momentum (A.36) allows to get

$$\begin{aligned} \partial_t(nu_\alpha) + \partial_\beta(nu_\alpha u_\beta) &= -\partial_\beta\left(\frac{c^2}{3} n\delta_{\alpha\beta}\right) + F_\alpha + \nu\partial_\beta[n(\partial_\beta u_\alpha + \partial_\alpha u_\beta)]) \\ &= -\partial_\beta(c^2 P_{\alpha\beta}) + \nu[n(\partial_\beta u_\alpha + \partial_\alpha u_\beta)] \end{aligned} \tag{A.55}$$

which is exactly the Navier-Stokes equation with viscosity

$$\nu = \frac{c^2}{3}\left(\tau - \frac{\Delta t}{2}\right) \tag{A.56}$$

or alternatively

$$\eta = nc_s^2 \Delta t \left(\frac{\tau}{\Delta t} - \frac{1}{2} \right) \tag{A.57}$$

with second viscosity $\zeta = \frac{2}{d}\eta$ and pressure tensor defined by

$$-\partial_\beta (c^2 P_{\alpha\beta}) = -\partial_\beta (p\delta_{\alpha\beta}) + F_\alpha. \tag{A.58}$$

Using the expressions for A, B_α, $C_{\alpha\beta}$, the force term becomes

$$F_i = \left(1 - \frac{\Delta t}{2\tau} \right) \omega_i \left[\frac{e_{i\alpha} - u_\alpha}{c_s^2} + \frac{(e_{i\alpha} u_\alpha) e_{i\alpha}}{c_s^4} \right] F_\alpha. \tag{A.59}$$

with F_α of order $O(\varepsilon)$.
In [48] it is shown that also for liquid crystals in the continuum limit the continuity and Navier-Stokes equations are obtained with viscosity $\eta = n\tau/3$.

Bibliography

[1] G. Toth, C. Denniston, and J.M. Yeomans. "Hydronamics of Topological Defects in Nematic Liquid Crystals". *Phys. Rev. Lett.* **88**, 105504 (2002).

[2] M.E. Cates, O. Heirich, D. Marenduzzo, and K. Stratford. "Lattice Boltzmann simulations of liquid crystalline fluids: active gels and blue phases". *Soft Matter* **5**, 3791-3800 (2009).

[3] G. Gonnella and J.M. Yeomans. "Using the Lattice Boltzmann Algorithm to Explore Phase Ordering Fluids" (2008).

[4] L.D. Landau and E.M. Lifšits. *Meccanica dei fluidi*. Editori Riuniti University press, (2013).

[5] A. Beris and B.J. Edwards. *Thermodynamics of Flowing Systems*. Oxford University Press, Oxford, (1994).

[6] N. Sulaiman, D. Marenduzzo, and J.M. Yeomans. "Lattice Boltzmann algorithm to simulate isotropic-nematic emulsion". *Phys. Rev. E* **74**, 041708 (2006).

[7] A. Tiribocchi, O. Heinrich, J.S. Lintuvuori, and D. Marenduzzo. "Switching hydrodynamics in liquid crystal devices:a simulation perspective". *Soft Matter* **10**, 4580 (2014).

[8] A. Tiribocchi, M. Da Re, D. Marenduzzo, and E. Orlandini. "Shear dynamics of an inverted nematic emulsion". *Soft Matter* **12** (2016).

[9] J. Bray. "Theory of Phase Ordering Kinetics". *Adv. Phys.* **43**, 357 (1994).

[10] S.R. de Groot and P. Mazur. *Non-equilibrium thermodynamics*. Dover Publications, Inc. New York, (2011).

[11] L. Peliti. *Appunti di meccanica statistica*. Bollati Boringheri, (2003).

[12] J.W. Cahn and E. Hilliard J. "Free Energy of a Nonuniform System. I. Interfacial Free Energy". *J. Chem. Phys.* **28**, 258 (1958).

[13] A.J.M. Yang, P.D. Fleming III, and J.H. Gibbs. "Molecular theory of surface tension". *J. Chem. Phys.* **64**, 3732 (1976).

[14] A. Tiribocchi, N. Stella, G. Gonnella, and A. Lamura. "Hybrid Lattice Boltzmann Model for Binary Fluid Mixtures". *Phys. Rev. E* **80**, 026701 (2009).

[15] R. Evans. "The nature of the liquid vapour interface and other topics in the statistical mechanics of non-uniform, classical fluids". *Adv. Phys.* **28**, 143 (1979).

[16] K. Stratford, O. Henrich, J.S. Lintuvuori, M.E. Cates, and D. Marenduzzo. "Self-assembly of colloid-cholesteric composites provides a possible route to switchable optical materials". *Nat. Comm.* **5**, 3954 (2014).

[17] J.H. Kim, M. Yoneya, and H. Yokoyama. "Tristable nematic liquid-crystal device using micropatterned surface alignment". *Nature* **420** (2002), pp. 159–162.

[18] W. Cao, A. Munoz, P. Palfy-Muhoray, and B. Taheri. "Lasing in a three-dimensional photonic crystal of the liquid crystal blue phase II". *Nat. Mater.* **1** (2002), pp. 111–113.

[19] P. Etchegoin. "Blue phases of cholesteric liquid crystals as thermotropic photonic crystals". *Phys. Rev. E* **62**, 1 (2000).

[20] Y. Hisakado, H. Kikuchi, T. Nagamura, and T. Kajiyama. "Large Electro-optic Kerr Effect in Polymer-Stabilized Liquid-Crystalline Blue Phases". *Adv. Mater.* **17**, 1 (2005).

[21] M.F. Moreira, C.S. Carvalho, W. Cao, C. Bailey, B. Taheri, and P. Palffy-Muhoray. "Cholesteric liquid-crystal laser as an optic fiber-based temperature sensor". *Appl. Phys. Lett.* **85**, 14 (2004).

[22] H. Iwai, J. Fukasawa, and T. Suzuki. "A liquid crystal application in skin care cosmetics". *Int. J. Cosmetic Science* **20** (1998), pp. 87–102.

[23] W. Zhang and L. Liu. "Study on the formation and properties of liquid crystal emulsion in cosmetic". *JCDSA* **3** (2013), pp. 139–144.

[24] I.I. Smalyukh, Y. Lansac, N. A.Clark, and R.P. Trivedi. "Three-dimensional structure and multistable optical switching of triple-twisted particle-like excitations in anisotropic fluids". *Nat. Mater.* **9** (2010).

[25] H.F. Gleeson, A. Wood T, and M. Dickinson. "Laser manipulation in liquid crystals:an approcah to microfluidics and micromachines". *Phyl. Trans. R. Soc. A* **364** (2006), pp. 2789–2805.

[26] V. Borsch, Y.K. Kim, J. Xiang, M. Gao, A. Jakli, V.P. Panov, J.K Vij, C.T. Imrie, M.G. Tamba, G.H. Mehl, and O.D. Lavrentovich. "Nematic twist-bend phase with nanoscale modulation of molecular orientation". *Nat. Comm.* **4**, 2635 (2013).

[27] Z. Parsouzi, S.M. Shamid, V. Borschch, P.K. Challa, A.R. Baldwin, M.G. Tamba, C. Welch, G.H. Mehl, J.T. Gleeson, A. Jakli, O.D. Lavrentovich, D.W. Allender, J.V. Selinger, and S. Sprunt. "Fluctuation Modes of a Twist-Bend Nematic Liquid Crystal". *Phys. Rev. X* **6**, 021041 (2016).

[28] P. Oswald and P: Pieranski. *Nematic and Cholesteric Liquid Crystals*. Taylor and Francis, (2005).

[29] R.G. Larson. *The Structure and Rheology of Complex Fluids*. Oxford University Press, (1999).

[30] P.G. de Gennes and J. Prost. *The Physics of Liquid Crystals*. Clarendon Press, 2nd edition, Oxford, (1993).

[31] S. Chandrasekhar. *Liquid Crystals*. Cambridge University Press. 2nd edition, Cambridge, (1977).

[32] M. Kleman and O.D. Lavrentovich. *Soft Matter Physics:An introduction*. Springer-Verlag, (2001).

[33] A.M. Figueiredo Neto and S.R.A. Salinas. *The Physics of Lyotropic Liquid Crystals*. Oxford University Press, (2005).

[34] P.M. Chaikin and T.C. Lubensky. *Principles of condensed matter physics*. Cambridge University Press, (1995).

[35] J.D Martin, C.L. Keary, T.A Thornton, M.P Novotnak, J.W Knutson, and J.C.W Folmer. "Metallotropic liquid crystals formed by surfactant templating of molten metal halides". *Nat. Mater.* **5** (2006).

[36] D.J. Gardiner, W.K. Hsiao, S.M. Morris, P.J.W. Hands, T.D. Wikinson, I.M. Hutchings, and H.J. Coles. "Printed photonic arrays from self-organized chiral nematic liquid crystals". *Soft Matter* **8** (2012), pp. 9977–9980.

[37] M. Humar and I. Muševic. "3D microlasers from self-assembled cholesteric liquid-crystal microdroplets". *Optic Express* **18**, 26 (2010).

[38] P. Oswald, J. Baudry, and S. Pirkl. "Static and dynamic properties of cholesteric fingers in electric field". *Phys. Rep.* **337** (2000), pp. 67–96.

[39] D.C. Wright and N.D. Mermin. "Crystalline liquids: the blue phases". *Rev. Mod. Phys.* **61** (1989).

[40] E. Karatairi, B. Rozic, Z. Kutnjak, V. Tzitzios, G. Nounesis, G. Cordoyiannis, J. Thoen, and C. Glorieux. "Nanoparticle-induced widening of the temperature range of liquid-crystalline blue phases". *Phys. Rev. E* **81**, 041703 (2010).

[41] H. Kikuchi, M. Yokota, Y. Hisakado, H. Yang, and T. Kajiyama. "Polymer-stabilized liquid crystal blue phases". *Nat. Mater.* **1** (2002), pp. 64–68.

[42] H.J. Coles and M.N. Pivnenko. "Liquid crystal 'blue phases' with a wide temperature range". *Nature* **436** (2005), pp. 997–1000.

[43] A. Tiribocchi. "Modellizzazione e analisi del ruolo dell'idrodinamica nei cristalli liquidi e nelle miscele di fluidi". Ph.D. Thesis. Università degli Studi di Bari Aldo Moro, (2011).

[44] A. Tiribocchi, G. Gonnella, D. Marenduzzo, and E. Orlandini. "Switching dynamics in cholesteric blue phases". *Soft Matter* **7**, 3295 (2011).

[45] http://www.personal.kent.edu/ bisenyuk/liquidcrystals/index.html.

[46] http://gizmodo.com/390255/samsung-develops-new-blue-phase-lcd-panel-for-tvs.

[47] https://arxiv.org/abs/1409.3542.

[48] C. Denniston, E. Orlandini, and J.M. Yeomans. "Lattice Boltzmann simulations of liquid crystal hydrodynamics". *Phys. Rev. E* **63**, 056702 (2001).

[49] P. Poulin and D.A. Weitz. "Inverted and multiple nematic emulsions". *Phys. Rev. E* **57**, 1 (1998).

[50] G. Foffano, J.S. Lintuvuori, A. Tiribocchi, and D. Marenduzzo. "The dynamics of colloidal intrusions in liquid crystals: a simulation perspective". *Liquid Crystal Review* **2**, 1 (2014).

[51] D. Seč, T. Porenta, M. Ravnik, and S. Žumer. "Geometrical frustration of chiral ordering in cholesteric droplets". *Soft Matter* **8**, 11982 (2012).

[52] S. Čopar. "Topology and geometry of nematic braids". *Phys. Rep.* **538** (2014), pp. 1–37.

[53] A. Tiribocchi, M.E. Cates, G. Gonnella, D. Marenduzzo, and E. Orlandini. "Flexoelectric switching in cholesteric blue phases". *Soft Matter* **9**, 4831 (2013).

[54] C. Denniston and J.M. Yeomans. "Flexoelectric surface switching of bistable nematic devices". *Phys. Rev. Lett.* **87**, 27 (2001).

[55] S. Succi. *The Lattice Boltzmann Equation for Fluid Dynamics and Beyond*. Clarendon Press Oxford, (2001).

[56] R. Benzi, S. Succi, and M. Vergassola. "The Lattice Boltzmann Equation : Theory and Applications". *Phys. Rep.* **222**, 3 (1992), pp. 145–197.

[57] S. Chen and G.D. Doolen. "Lattice Boltzmann method for fluid flows". *Annu. Rev. Fluid Mech.* **329**, 30 (1998).

[58] B. Dunweg and A.J.C. Ladd. "Lattice Boltzmann Simulations of Soft Matter Systems". *Adv. Polym. Sci.* **221**, 89 (2009).

[59] R.R. Nourgaliev, T.N. Dinh, T.G. Theofanous, and D. Joseph. "The Lattice Boltzmann equation method : theoretical interpretation, numerics and implications". *Int. J. Multiphase Flow* **29**, 17 (2003).

[60] V.M. Kendon, J.C. Desplat, P. Blandon, and M.E. Cates. "3D spinodal decomposition in the inertial regime". *Phys. Rev. Lett.* **83**, 576 (1999).

[61] A. Calì, S. Succi, A. Cancelliere, R. Benzi, and M. Gramignani. "Diffusion and hydrodynamic dispersion with the Lattice Boltzmann method". *Phys. Rev. A* **45**, 5771 (1992).

[62] Q.J. Kang, D.X. Zhang, and S.Y. Chen. "Unified lattice Boltzmann method for flow in multiscale porous media". *Phys. Rev. E* **66**, 056307 (2002).

[63] F.J. Alexander, S. Chen, and J.D. Sterling. "Lattice Boltzmann thermodynamics". *Phys. Rev. E* R2249 (1993).

[64] Y. Chen, H. Ohashi, and O. Akiyama. "Two-Parameter thermal lattice BGK model with a contrallable Prandtl number". *J. Sci. Comp.* **12**, 169 (1997).

[65] S. Chen, H. Chen, D. Martinez, and W. Mattheus. "Lattice Boltzmann model for simulation of magnetohydrodynamics". *Phys. Rev. Lett.* **67**, 3776 (1991).

[66] S. Succi, M. Vergassola, and R. Benzi. "Lattice Boltzmann scheme for two-dimensional magnetohydrodynamics". *Phys. Rev. A* **43**, 4521 (1991).

[67] W. Schaffenberger and Hanslmeier. "Two-dimensional lattice Boltzmann model for magnetohydrodynamics". *Phys. Rev. E* **6**, 046702 (2002).

[68] S. Succi and R. Benzi. "Lattice Boltzmann equation for quantum mechanics". *Physica D* **69** (1993), pp. 327–332.

[69] D. Lapitski and P. Dellar. "Convergence of a three-dimensional quantum lattice Boltzmann scheme towards solutions of the Dirac equation". *Phyl. Trans. R. Soc. A* **369**, 2155 (2011).

[70] F. Fillion-Gourdeau, H.J. Hermann, M. Mendoza, S. Palpacelli, and S. Succi. "Formal analogy between the Dirac equation in its Majorana form and the discrete-velocity version of the Boltzmann kinetic equation". *Phys. Rev. Lett.* **111**, 160602 (2013).

[71] J.I. Cirac and P. Zoller. "Quantum Computations with cold trapped ions". *Phys. Rev. Lett.* **74**, 20 (1995).

[72] A. Mezzacapo, M. Sanz, L. Lamata, I.L. Egusquiza, S. Succi, and E. Solano. "Quantum simulator for transport phenomena in fluid flows". *Sci. Rep.* **5**, 13153 (2015).

[73] M. Mendoza, Boghosian, Herrmann, and S. Succi. "Fast Lattice Boltzmann Solver for Relativistic Hydrodynamics". *Phys. Rev. Lett.* **105**, 014502 (2010).

[74] M. Mendoza, H. Herrmann, and S. Succi. "Preturbulent regimes in graphene flow". *Phys. Rev. Lett.* **106**, 156601.156601 (2011).

[75] S. Succi, M. Mendoza, F. Mohseni, and I. Karlin. "Relativistic lattice kinetic theory: Recent developments and future prospects". *Eur. Phys. J. Special Topics* **223** (2014), pp. 2177–2188.

[76] X. He and L.S. Luo. "Theory of the lattice Boltzmann method: From the Boltzmann equation to the lattice Boltzmann equation". *Phys. Rev. E* **56**, 6811 (1997).

[77] S. Sachedv and M. Muller. "Quantum criticality and black holes". *J. Condens. Matter* **21**, 164216 (2009).

[78] J. Maldacena. "The Large-N Limit of Superconformal Field Theories and Supergravity". *Int. J. Theor. Phys.* **38**, 1113 (1999).

[79] G. Policastro, D.T. Son, and A.O. Starinets. "Shear Viscosity of Strongly Coupled $N = 4$ Supersymmetric Yang-Mills Plasma". *Phys. Rev. Lett.* **87**, 8 (2001).

[80] P.M. Chesler, H. Liu, and A. Adams. "Holographic Vortex Liquids and Superfluid Turbolence". *Science* **341**, 368 (2013).

[81] J. Yepez, G. Vahala, L. Vahala, and M. Soe. "Superfluid Turbulence from Quantum Kelvin Wave to Classical Kolmogorov Cascades". *Phys. Rev. Lett.* **103**, 084501 (2009).

[82] O. Heinrich, D. Marenduzzo, and M.E. Cates. "Domain growth in cholesteric blue phases : Hybrid lattice Boltzmann simulations". *Comput. Math. Appl.* **59** (2010), pp. 2360–2369.

[83] S. Succi. "Lattice Boltzmann 2038". *Europhys. Lett.* **109**, 50001 (2015).

[84] U. Frisch, B. Hasslacher, and Y. Pomeau. "Lattice-Gas Automata for the Navier-Stokes equation". *Phys. Rev. Lett.* **56**, 14 (1986).

[85] G.R. McNamara and G. Zanetti. "Use of the Boltzmann Equation to Simulate Lattice-Gas Automata". *Phys. Rev. Lett.* **61**, 20 (1988).

[86] F.J. Higuera and S. Succi. "Simulating the Flow around a Circular Cylinder with a Lattice Boltzmann Equation". *Europhys. Lett.* **8**, 6 (1989), pp. 517–521.

[87] F.J. Higuera, S. Succi, and R. Benzi. "Lattice Gas Dynamics with Enhanced Collisions". *Europhys. Lett.* **9**, 4 (1989), pp. 345–349.

[88] P.L. Bhatnagar, E.P. Gross, and M. Krook. "A Model for Collision Processes in Gases. I. Small Amplitude Processes in Charged and Neutral One-Component Systems". *Phys. Rev.* **94**, 3 (1954).

[89] Y.H. Qian, D. d'Humieres, and P. Lallemand. "Lattice BGK Models for Navier-Stokes Equation". *Europhys. Lett.* **17**, 6 (1992), pp. 479–484.

[90] H. Chen, S. Chen, and W. Mattheus. "Recovery of the Navier-Stokes Equations using a lattice-gas Boltzmann equation". *Phys. Rev. A* **45**, R5339 (1992).

[91] A.K. Gunstensen, D.H. Rothman, S. Zaleski, and G. Zanetti. "Lattice Boltzmann model of immiscible fluids". *Phys. Rev. A* **43**, 4320 (1991).

[92] E.G. Flekkoy. "Lattice Bhatnagar-Gross-Krook models miscible fluids". *Phys. Rev. E* **47**, 4247 (1993).

[93] E. Orlandini, M.R. Swift, and J.M. Yeomans. "A Lattice Boltzmann Model of Binary-Fluid Mixtures". *Europhys. Lett.* **32**, 6 (1995), pp. 463–468.

[94] M.R. Swift, E. Orlandini, W.R. Osborn, and J.M. Yeomans. "Lattice Boltzmann simulations of liquid-gas and binary fluid systems". *Phys. Rev. E* **54**, 5 (1996).

[95] M.R. Swift, W.R. Osborn, and J.M. Yeomans. "Lattice Boltzmann simulations of nonideal fluids". *Phys. Rev. Lett.* **75**, 830 (1995).

[96] X. Shan and H. Chen. "Simulation of nonideal gases and liquid-gas phase transitions by the lattice Boltzmann multiphase models". *Europhys. Lett.* **49**, 2941 (1994).

[97] Z. Guo, C. Zheng, and B. Shi. "Discrete lattice effects on the forcing term in the lattice Boltzmann method". *Phys. Rev. E* **65**, 046308 (2002).

[98] M. Sbragaglia, H. Chen, X. Shan, and S. Succi. "Continuum free-energy formulatio for a class of lattice Boltzmann multiphase models". *Europhys. Lett.* **86**, 24005 (2009).

[99] S.M. Fielding. "Role of inertia in nonequilibrium steady states of sheared binary fluids". *Phys. Rev. E* **77**, 021504 (2008).

[100] J.C. Strickwerda. *Finite Difference Schemes and Partial Differential Equations*. Chapman and Hall, New York, (1989).

[101] A. Tiribocchi, A. Piscitelli, G. Gonnella, and A. Lamura. "Pattern study of the thermal phase separation for binary fluid mixtures". *International Journal of Numerical Methods for Heat and Fluid Flow* **21** (2011), pp. 572–583.

[102] Q. Zou and X. He. "On the pressure and velocity boundary conditions for the Lattice Boltzmann BGK model". *Physics of Fluids* **9**, 1591 (1997).

[103] G. Kahler, F. Bonelli, G. Gonnella, and A. Lamura. "Cavitation inception of a van der Waals fluid at a sack-wall obstacle". *Physics of Fluids* **27**, 123307 (2015).

[104] C. Denniston, D. Marenduzzo, E. Orlandini, and J.M. Yeomans. "Lattice Boltzmann algorithm for three-dimensional liquid-crystal hydrodynamics". *Phyl. Trans. R. Soc. A* **362**, 1745-1754 (2004).

[105] Y. Geng, D. Seč, P.L. Almeida, O. Lavrentovitch, S. Žumer, and M.H. Godinho. "Liquid crystals necklaces: cholesteric drops threated by thin cellulose fibres". *Soft Matter* **9**, 33 (2013), pp. 7879–8074.

[106] J. Bajc, P.P Crooker, and S. Žumer. "Chiral Nematic Liquid Crystal Droplets". *Liquid Crystals Today* **7**, 3 (1997).

[107] D. Seč, S. Čopar, and S. Žumer. "Topological zoo of free-standing knots in confined chiral nematic fluids". *Nat. Comm.* **5** (2014).

[108] T. Orlova, S.J. Abhoff, T. Yamaguchi, N. Katsonis, and E. Brasselet. "Creation and manipulation of topological states in chiral nematic microspheres". *Nat. Comm.* **6** (2015).

[109] D. Svensek, H. Pleiner, and H.R. Brand. "Inverse Lehmann effects can be used as a microscopic pump". *Phys. Rev. Lett.* **78**, 021703 (2008).

[110] J. Ignes-Mullol, G. Poy, and P. Oswald. "Continuous rotation of achiral nematic liquid crystal droplets driven by heat flux". *Phys. Rev. Lett.* **117**, 057801 (2016).

[111] P. Oswald and S. Pirkl. "Lehmann rotation of cholesteric helix in droplets oriented by an electric field". *Phys. Rev. E* **89**, 022509 (2014).

[112] G. Poy and P. Oswald. "Do Lehmann cholesteric droplets subjected to a temperature gradient rotate as rigid bodies?" *Soft Matter* **12** (2016), pp. 2604–2611.

[113] A. Dequidt, G. Poy, and P. Oswald. "Generalized drift velocity of a cholesteric texture in a temperature gradient". *Soft Matter* **12** (2016), pp. 7529–7538.

[114] P. Oswald and A. Dequidt. "Measuremets of the continuous Lehmann rotation of cholesteric droplets subjected to a temperature gradient". *Phys. Rev. Lett.* **100**, 217802 (2008).

[115] R.H. Brand, H. Pleiner, and D. Svensek. "Lehmann effect and rotatoelectricity in liquid crystalline systems made of achiral molecules". *Phys. Rev. E* **88**, 024501 (2013).

[116] P. Oswald and G. Poy. "Lehmann rotation of cholesteric droplets : Role of the sample thickness and of the concentration of chiral molecules". *Phys. Rev. E* **91**, 032502 (2015).

[117] J. Yoshioka, I. Fumiya, Y. Suzuki, H. Takahashi, H. Takizawa, and Y. Tabe. "Director/barycentric rotation in cholesteric droples under temperature gradient". *Soft Matter* **10** (2014), pp. 5869–5877.

[118] T. Yamamoto, M. Kuroda, and M. Sano. "Three-dimensional analysis of thermo-mechanically rotating cholesteric liquid crystal droplets under a temperature gradient". *Europhys. Lett.* **109**, 46001 (2015).

[119] P. Oswald. "About the Leslie explanation of the Lehmann effect in cholesteric liquid crystals". *Eurphys. Lett.* **97**, 36006 (2012).

[120] P. Oswald. "Lehmann rotation of cholesteric droplets subjected to a temperature gradient: Role of the concentration of chiral molecules". *Eur. Phys. J. E* **28** (2009), pp. 377–383.

[121] P. Oswald and A. Dequidt. "Direct measurement of the thermomechanical Lehmann coefficient in a compensated cholesteric liquid crystal". *Europhys. Lett.* **83**, 16005 (2008).

[122] A. Dequidit and P. Oswald. "Lehmann effect in compensated liquid crystals". *Europhys. Lett.* **80**, 26001 (2007).

[123] P. Oswald. "Leslie thermomechanical power in diluted cholesteric liquid crystals". *Europhys. Lett.* **108**, 36001 (2014).

[124] P. Oswald. "Microscopic vs. macroscopic origin of the Lehmann effect in cholesteric liquid crystals". *Eur. Phys. J. E* **35**, 10 (2012).

[125] A. Dequidt and P. Oswald. "Does the electric Lehmann effect exist in cholesteric liquid crystals?" *Eur. Phys. J. E* **24** (2007), pp. 157–166.

[126] A. Dequidt, A. Zywocinski, and P. Oswald. "Lehmann effect in a compensated cholesteric liquid crystal : Experimental evidence with fixed and gliding boundary conditions". *Eur. Phys. J. E* **25** (2008), pp. 277–289.

[127] O. Heinrich, D. Marenduzzo, K. Stratford, and M.E. Cates. "Thermodynamics of blue phases in electric fields". *Phys. Rev. E* **81**, 031706 (2010).

[128] A. Tiribocchi, G. Gonnella, D. Marenduzzo, E. Orlandini, and F. Salvadore. "Bistable Defect Structures in Blue Phase Device". *Phys. Rev. Lett.* **107**, 237803 (2011).

[129] A. Tiribocchi, G. Gonnella, D. Marenduzzo, and E. Orlandini. "Swicthing and defect dynamics in multistable liquid crystal devices". *Appl. Phys. Lett.* **97**, 143505 (2010).

[130] O.D. Lavrentovich. "Topological defects in dispersed words and worlds around liquid crystals, or liquid crystal drops". *Liq. Cryst.* **24**, 1 (1998), pp. 117–125.

[131] M. Kleman and J. Friedel. "Disclinations, dislocations, and continuous defects: A reappraisal". *Rev. Mod. Phys.* **80**, 1 (2008).

[132] R.D. Kamien. "The geometry of soft materials: a primer". *Rev. Mod. Phys.* **74**, 4 (2002).

[133] H.P. Padmini and N.V. Madhusudana. "Electromechanical effect in cholesteric mixtures with a compensation temperature". *Liq. Cryst.* **14**, 497 (1993).

[134] A. Lamura, G. Gonnella, and J.M. Yeomans. "A lattice Boltzmann model of ternary fluid mixtures". *Europhys. Lett.* **45**, 3 (1999), pp. 314–320.

[135] A. Lamura, G. Gonnella, and J.M. Yeomans. "Modelling the dynamics of amphiphilic fluids". *Int. J. Mod. Phys. C* **9**, 8 (1998), pp. 1469–1478.

[136] S. Yabunaka, T. Ohta, and N. Yoshinaga. "Self-propelled motion of a fluid droplet under chemical reaction". *J. Chem. Phys.* **136**, 074904 (2012).

[137] E. Guyon, J.P. Hulin, L. Petit, and C.D. Mitescu. *Physical Hydrodynamics*. Oxford University Press, (1991).

[138] J.M. Rallison. "The deformation of small viscous drops and bubbles in shear flows". *Annu. Rev. Fluid Mech.* **16** (1984), pp. 45–66.

[139] D. Marenduzzo, E. Orlandini, and J.M. Yeomans. "Permeative flows in cholesterics: Shear and Poiseuille flows". *J. Chem. Phys.* **124**, 204906 (2006).

[140] R.F. Probstein. *Physicochemical Hydrodynamics An introduction*. John Wiley & Sons, Inc., (2002).

[141] R.A.L Jones. *Soft Condensed Matter*. Oxford University Press, (2002).

[142] V.G. Levich and V.S. Krylov. "Surface-Tension-Driven Phenomena". *Annu. Rev. Fluid Mech.* **1** (1969), pp. 293–316.

[143] J.L. Anderson. "Colloid Transport by Interfacial Forces". *Annu. Rev. Fluid Mech.* **21** (1989), pp. 61–99.

[144] A. Nepomnyashchy, M.G. Velarde, and P. Colinet. *Interfacial phenomena and convection*. Chapman & Hall/Crc, (2002).

[145] R. Krechetnikov. "Thermodynamics of chemical Marangoni-driven engines". *Soft Matter* **13** (2017).

[146] S. Herminghaus, C. Maas, C. Kruger, S. Thutupalli, L. Goehring, and C. Bahr. "Interfacial mechanisms in active emulsions". *Soft Matter* **10** (2014), pp. 7008–7022.

[147] J.W.M. Bush and D.L. Hu. "Walking on Water: Biolocomotion at the Interface". *Annu. Rev. Fluid Mech.* **38** (2006).

[148] N.O. Young, J.S. Goldstein, and M.J. Block. "The motion of bubbles in a vertical temperature gradient". *J. Fluid Mech.* **6**, 3 (1959).

[149] M. Schmitt and H. Stark. "Marangoni flow at droplet interface: Three-dimensional solution and applications". *Physics of Fluids* **28**, 012106 (2016).

[150] S. Thutupalli, R. Seeman, and S. Herminghaus. "Swarming behaviour of simple model squirmers". *New J. Phys.* **13**, 073021 (2011).

[151] M. Schmitt and H. Stark. "Swimming active droplet: A theoretical analysis". *Europhys. Lett.* **101**, 44008 (2013).

[152] S. Yabunaka and N. Yoshinaga. "Collision between chemically driven self-propelled drops". *J. Fluid Mech.* **806** (2016).

[153] S. Ramaswamy. "The Mechanics and Statistics of Active Matter". *Annu. Rev. Condens. Matter Phys.* **1** (2010).

[154] R. Seeman, J.B. Fleury, and C. Maas. "Self-propelled droplets". *Eur. Phys. J. Special Topics* **225** (2016).

[155] C. Maas, C. Kruger, S. Herminghaus, and C. Bahr. "Swimming droplets". *Annu. Rev. Condens. Matter Phys.* **7** (2016).

[156] N. Yoshinaga. "Spontaneous motion and deformation of a self-propelled droplet". *Phys. Rev. E* **89**, 012913 (2014).

[157] N. Yoshinaga, K.H. Nagai, Y. Sumino, and H. Kitahata. "Drift instability in the motion of a fluid droplet with a chemically reactive surface driven by Marangoni flow". *Phys. Rev. E* **86**, 016108 (2012).

[158] K. Furtado, C.M. Pooley, and J.M. Yeomans. "Lattice Boltzmann study of convective drop motion driven by nonlinear chemical kinetics". *Phys. Rev. E* **78**, 046308 (2008).

[159] C. Kruger, C. Bahr, S. Herminghaus, and C. Maas. "Dimensionality matters in the collective behaviour of active emulsions". *Eur. Phys. J. E* **39**, 64 (2016).

[160] M. Schmitt and H. Stark. "Active Brownian motion of emulsion droplets: Coarsening dynamics at the interface and rotational diffusion". *Eur. Phys. J. E* **39**, 80 (2016).

[161] S. Thutupalli and S. Herminghaus. "Tuning active emulsion dynamics via surfactants and topology". *Eur. Phys. J. E* **36**, 91 (2013).

[162] C. Kruger, G. Klos, C. Bahr, and C. Maas. "Curling Liquid Crystal Microswimmers: A Cascade of Spontaneaous Symmetry Breaking". *Phys. Rev. Lett.* **117**, 048003 (2016).

[163] T. Toyota, N. Maru, M. Hanczyc, T. Ikegami, and T. Sugawara. "Self-propelled Oil Droplet Consuming "Fuel" Surfactant". *J. Am. Chem. Soc.* **131** (2009).

[164] Z. Izri, M.N. van der Linden, S. Michelin, and O. Dauchot. "Self-propulsion of Pure Water Droplets by Spontaneous Marangoni-Stress-Driven Motion". *Phys. Rev. Lett.* **113**, 248302 (2014).

[165] H. Kitahata, N. Yoshinaga, K. Nagai, and Y. Sumino. "Spontaneous motion of a droplet coupled with a chemical wave". *Phys. Rev. E* **84**, 015101(R) (2011).

[166] K. Nagai, Y. Sumino, H. Kitahata, and k. Yoshikawa. "Mode selection in the spontaneous motion of an alcohol droplet". *Phys. Rev. E* **71**, 065301(R) (2005).

[167] T. Banno, Kuroha, and T. Toyota. "pH-Sensitive Self-Propelled Motion of Oil Droplets in the Presence of Cationic Surfactants Containing Hydrolyzable Ester Linkages". *Langmuir* **28** (2012).

[168] T. Ban, T. Yamagami, and Y. Nakata H. Okano. "pH-Dependent Motion of Self-Propelled Droplets due to Marangoni Effect at Neutral pH". *Langmuir* **29** (2013).

[169] T. Toyota, H. Tsuha, K. Yamada, K. Takakura, T. Ikegami, and T. Sugawara. "Listeria-like Motion of Oil Droplets". *Chem. Lett.* **35**, 7 (2006).

[170] Y. Sumino, N. Magome, T. Hamada, and K. Yoshikawa. "Self-Running Droplet: Emergence of Regular Motion from Nonequilibrium Noise". *Phys. Rev. Lett.* **94**, 068301 (2005).

[171] M.M. Hanczyc, T. Toyota, T. Ikegami, N. Packard, and T. Sugawara. "Fatty Acid Chemistry at the Oil-Water Interface: Self-Propelled Oil Droplets". *J. Am. Chem. Soc.* **129** (2007).

[172] G. Zhao, T.H. Seah, and M. Pumera. "External-Energy-Independent Polymer Capsule Motors and Their Cooperative Behavious". *Chem. Eur. J.* **17** (2011), pp. 12020–12026.

[173] G.A. Ozin, I. Manners, S. Fournier-Bidoz, and A. Arsenault. "Dream Nanomachines". *Adv. Mater.* **17** (2005), pp. 3011–3018.

[174] L. Soler and S. Sanchez. "Catalytic nanomotors for environmental monitoring and water remediation". *Nanoscale* **6** (2014), pp. 7175–7182.

[175] M. Zhang, X. Xie, M. Tang, C.S. Criddle, Y. Cui, and S.X Whang. "Magnetically ultraresponsive nanoscavengers for next-generation water purification systems". *Nat. Comm.* **4**, 1866 (2013).

[176] W. Gao, X. Feng, A. Pei, Y. Gu, L. Jinxing, and J. Wang. "Seawater-driven magnesium based Janus micromotors for environmental remediation". *Nanoscale* **5** (2013), pp. 4696–4700.

[177] L. Baraban, M. Tasinkevych, M.N. Popescu, S. Sanchez, S. Dietrich, and O.G. Schmidt. "Transport of cargo by catalytic Janus micro-motors". *Soft Matter* **8**, 48 (2012).

[178] J. Burdick, R. Laocharoensuk, P.M. Wheat, J.D. Posner, and J. Wang. "Synthetic Nanomotors in Microchannel Networks: Directional Microchip Motion and Controlled Manipulation of Cargo". *J. Am. Chem. Soc.* **130** (2008), pp. 8164–8165.

[179] T. Ban, K. Tani, H. Nakata, and Y. Okano. "Self-propelled droplets for extracting rare-earth metal ions". *Nanoscale* **10** (2014), pp. 6316–6320.

[180] T. Patino and S. Sanchez. "Miniaturazied soft bio-hybrid robotics: a tep forward into healthcare applications". *Lab on a Chip* **16** (2016), pp. 3626–3630.

[181] J.R. Baylis, J.H. Yeon, M.H. Thomson, A. Kazerooni, X. Wang, A.E.St. John, E.B. Lim, D. Chien, A. Lee, J.Q. Zhang, J.M. Piret, L.S. Machan, T.F. Burke, N.J. White, and C.J. Kastrup. "Self-propelled particles that transport cargo through flowing blood and halt hemorrhage". *Sci. Adv.* **1**, 9 (2015).

[182] J. Wang and W. Gao. "Nano/Microscale Motors: Biomedical Opportunities and Challenges". *ACS Nano* **6**, 7 (2012), pp. 5745–5751.

[183] S. Ramaswamy. "Active Matter". *J. Stat. Mech.* 054002 (2017).

[184] M.C. Marchetti, J.F. Joanny, S. Ramaswamy, T.B. Liverpool, J. Prost, M. Rao, and R. Aditi Simha. "Hydrodynamics of soft active matter". *Rev. Mod. Phys.* **85** (2013).

[185] A. Zottl and H. Stark. "Emergent behaviour in active colloids". *J. Phys. Condens. Matter* **28**, 253001 (2016).

[186] A. Zottl and H. Stark. "Hydrodynamics Determines Collective Motion and Phase Behaviour of Active Collids in Quasi-Two-Dimensional Confinement". *Phys. Rev. Lett.* **112**, 118101 (2014).

[187] I. Llopis and I. Pagonabarraga. "Hydrodynamic interactions in squirmer motion: Swimming with a neighbour and close to a wall". *J. Non-Newtonian Fluid Mech.* **165** (2010).

[188] D. Giacchè and T. Ishikawa. "Hydrodynamic interaction of two unsteady model microorganisms". *J. Theor. Biology* **267** (2010).

[189] M. Downton and H. Stark. "Simulation model microswimmer". *J. Phys. Condens. Matter* **21**, 204101 (2009).

[190] I. Goetze and G. Gompper. "Mesoscale simulation of hydrodynamic squirmer interaction". *Phys. Rev. E* **82**, 041921 (2010).

[191] A. Evan, T. Ishikawa, T. Yamagichi, and E. Lauga. "Orientational order in concentrated suspensions of spherical microwimmers". *Physics of Fluids* **23**, 111702 (2011).

[192] J.M. Yeomans, D.O. Pushkin, and H. Shum. "An introduction to the hydrodynamics of swimming microorganims". *Eur. Phys. J. Special Topics* **223** (2014), pp. 1771–1785.

[193] F. Alarcon and I. Pagonabarraga. "Spontaneous aggregation and global polar ordering in squirmer sospensions". *J. Mol. Liquids.* **185** (2013), pp. 51–61.

[194] J. Elgeti, R.G. Winkler, and G. Gompper. "Physics of microswimmers-single particle motion and collective behaviour: a review". *Rep. Prog. Phys.* **78**, 056601 (2015).

[195] E. Lauga and T. Powers. "The hydrodynamics of swimming microorganisms". *Rep. Prog. Phys.* **72**, 096601 (2009).

[196] M.J. Lighthill. "On the Squirming Motion of Nearly Spherical Deformable Bodies through Liquids at Very Small Reynolds Numbers". *Comm. Pure Appl. Math.* **109**, 118 (1952).

[197] J.R. Blake. "A spherical envelope approach to ciliary propulsion". *J. Fluid Mech.* **46** (1971).

[198] J.S. Rowlinson and B. Widom. *Molecular Theory of Capillarity*. Dover Publications, Inc., (1982).

Acknowledgements

First of all I sincerely thank Professor Giuseppe Gonnella, my Ph.D. supervisor, for having proposed an interesting field of research, for our discussions and for having taught to me the critical approach to the research and results. My hope is to continue to work with him wherever I'll be in the future. In the same way I want to thank Doctor Antonio Lamura, CNR researcher and my Ph.D. supervisor too, for his constant presence and precious help during the research. I also thank Professor Enzo Orlandini of University of Padua for hosting me during two beautiful and fruitful periods in his Department and his collaboration in the research. Another important people to thank are Doctor Adriano Tiribocchi for his precious help, for our discussions and his kindness and availability and Professor Davide Marenduzzo of University of Edinburgh for his collaboration. I also thank Bari Recas data center and its people and technologists for allowing me to use their computer resources for the simulations without which this thesis would not exist.
I want also thank all the beautiful and hard-working people, I cannot cite name by name for a matter of space, of the Physics Department in Bari: secretaries, tecnicians, researchers, etc. In a way or another I entered in contact with this people and they made me richer in human sense.
Other important people I want to mention and thank are Luigi and Floriana the brothers I never had and also Liana and Benito's beautiful family.
I want also to thank three special Professors who were important in my life and in my scholastic and human growth: Professor Iusi of Italian at the secondary school, Professor Laterza of Italian and Professor Costantini of Maths and Physics at the high school.
An important contribution comes from the family. I deeply thank mum and dad for their constant presence, the love, the support in all senses and most of all patience. They believed in me most of all and they'll always continue to believe in me. I'll always love them whenever I'll be and I'll work!
Last but not least, I thank all my friends that supported me in these three years. My hope is that, wherever we'll be we'll continue to meet each other and that everyone can realize his dreams. My personal dream, in fact, is to continue the scientific research, even if the path is difficult, and to become one day a stable researcher!